Advanced Wavefront Sensing and Astrometric Techniques for the Next Generation of Extremely Large Telescopes

by

Mojtaba Taheri
B.Sc., Sharif University of Technology, 2013
M.Sc., Amirkabir University of Technology, 2015

A Dissertation Submitted in Partial Fulfillment of the Requirements for the Degree of

DOCTOR OF PHILOSOPHY

in the Department of Physics and Astronomy

Advanced Wavefront Sensing and Astrometric Techniques for the Next Generation of Extremely Large Telescopes

by

Mojtaba Taheri
B.Sc., Sharif University of Technology, 2013
M.Sc., Amirkabir University of Technology, 2015

Supervisory Committee

Dr. David R. Andersen, Co-Supervisor
(Department of Physics and Astronomy)

Dr. Kim Venn, Co-Supervisor
(Department of Physics and Astronomy)

Dr. Alan W. McConnachie, Departmental Member
(Department of Physics and Astronomy)

Dr. Jens Bornemann, Member
(Department of Electrical and Computer Engineering)

Supervisory Committee

Dr. David R. Andersen, Co-Supervisor
(Department of Physics and Astronomy)

Dr. Kim Venn, Co-Supervisor
(Department of Physics and Astronomy)

Dr. Alan W. McConnachie, Departmental Member
(Department of Physics and Astronomy)

Dr. Jens Bornemann, Member
(Department of Electrical and Computer Engineering)

ABSTRACT

The new generation of giant ground-based telescopes will see their first light this decade. These state-of-the-art facilities will significantly surpass the resolving power of modern space-based observatories such as the James Webb telescope, thanks to their enormous aperture size and adaptive optics (AO) facilities. Without AO, atmospheric turbulence would degrade the image quality of these enormous telescopes to that of a 50 cm amateur one. These extremely large telescopes (ELTs) will further benefit from a particular branch of AO called multi-conjugate adaptive optics (MCAO), which provides an extremely high resolving power over a much wider field of view as compared to classical AO systems. The design and fabrication of such systems, as well as their optimal use for science operation, pose a great challenge as they are an order of magnitude more complicated than current AO systems. To face such a

challenge, the combined knowledge of MCAO system design and fabrication, working in tandem with scientific insights into new astronomy science cases, is an extremely valuable and essential pairing. This thesis is an effort to not only contribute to the design and fabrication of ELT MCAO facilities, but also provide guidance on the optimal method to utilize these giant telescopes to achieve unprecedented astrometric measurements.

On the instrumentation side, in partnership with the National Research Council of Canada's - Herzberg Astronomy and Astrophysics Institute as well as W.M. Keck Observatory in Hawaii, I was involved in the design and fabrication of a cutting edge new wavefront sensor, which is the eye of an AO system. I performed opto-mechanical design and verification studies for components of the Keck infrared pyramid wavefront sensor (IR-PWFS) as well as the Keck Planet Imager and characterizer (KPIC) instrument, which have both been commissioned and are in science operation. Furthermore, I designed the alignment plan and participated in the modification and alignment operation of a few components on the Keck II adaptive optics bench on the summit of Mauna Kea.

To pave the way for the design verification of future MCAO systems for ELTs, I proposed a new method for an old challenge in the path of AO system design and verification: a flexible method for precise intensity pattern injection into laboratory AO benches. AO benches are the backbone of instrument design and modeling. One of the challenges especially important for the future generation of MCAO systems for ELTs is the verification of the effect of shadowed regions on the primary mirror. During my PhD, I successfully demonstrated the feasibility of a new proposed method to accurately model the telescope pupil. This work was done in partnership with the Laboratoire d'Astrophysique de Marseille (LAM) in France. The method I developed at LAM will be implemented in the AO Lab at NRC Herzberg Astronomy and Astrophysics.

As an observational astronomer, I focused on developing methods for making optimal astrometric measurements with MCAO-enabled telescopes. The expected unparalleled astrometric precision of ELTs comes with many unprecedented challenges that if left unresolved, would jeopardize the success of these facilities as they would not be able to reach their science goals. I used observations with the only available MCAO system in science operation, the Gemini MCAO system on the 8-meter Gemini South telescope in Chile, to develop and verify a pipeline specifically designed for very high-precision astrometric studies with MCAO-fed imagers. I successfully used the

pipeline to provide the precise on-sky differential distortion of the Gemini South telescope and its MCAO facilities by looking deep into the core of globular cluster NGC 6723. Using this pipeline, I produced high quality proper motions with an uncertainty floor of $\sim 45\,\mu$as yr^{-1} as well as measured the proper motion dispersion profile of NGC 6723 from a radius of ~ 10 arcseconds out to ~ 1 arcminute, based on ~ 12000 stars. I also produced a high-quality optical-near-infrared color magnitude diagram which clearly shows the extreme horizontal branch and main-sequence knee of this cluster.

Contents

List of Tables

List of Figures

List of Acronyms

ACS	Advanced Camera for Surveys
AO	Adaptive Optic
CMD	Color-Magnitude Diagram
DM	Deformable Mirror
DVF	Displacement Vector Field
ELT	Extremely Large Telescope
FIU	Fiber Injection Unit
FOV	Field Of View
FSM	Field Steering Mirror(s)
FWHM	Full Width at Half Maximum
GeMS	Gemini Multi-conjugate adaptive optics System
GC	Globular Cluster
GSAOI	Gemini South Adaptive Optics Imager
HAA	Herzberg Astronomy and Astrophysics Research Centre
HST	Hubble Space Telescope
HWHM	Half Width at Half Maximum
IF	Influence Function
IFU	Integral Field Unit
IM	Interactions Matrix
IMBH	Intermediate-Mass Black Hole
IR	Infra Red
ISM	Interferometer Science Fold Mirror
K2AO	Keck 2 Adaptive Optic
KAON	Keck Adaptive optic Notes system
KPIC	Keck Planet Imager and Characteriser
LAM	Laboratoire d'Astrophysique de Marseille
LOOPS	LAM/ONERA Pyramid Sensor bench
LCoS	Liquid Crystal on Silicon
LGS	Laser Guide Star
MCAO	Multi-Conjugate Adaptive Optics
MICADO	Multi-Adaptive Optics Imaging CamerA for Deep Observations
NCPA	None Common Path Aberration
SMS	Secondary Mirror Structure

MEMS	Micro-ElectroMechanical System
NIR	Near Infra Red
NFIRAOS	Narrow-Field Infrared Adaptive Optics System
NGS	Natural Guide Star
NIRC2	Near-InfRared Camera
NIRSpec	Near Infrared Spectrograph
NRC	National Research Council Canada
OAP	Off-Axis Parabola
OOMAO	Object-Oriented Matlab Adaptive Optics toolbox
PWFS	Pyramid WaveFront Sensor/Sensing
PSF	Point Spread Function
RTC	Real-Time Controller
SCAO	Single Conjugate Adaptive Optic
SCExAO	Subaru Coronagraphic Extreme Adaptive Optics
SHWFS	Shack-Hartmann WaveFront Sensors/Sensing
SLM	Spatial Light Modulator
TMT	Thirty-Meter Telescope
TTM	Tip-Tilt Mirror
UVic	University of Victoria
VPD	Vector Point Diagram
WFS	WaveFront Sensor/Sensing

ACKNOWLEDGEMENTS

First and foremost, I wish to thank my supervisors: **Dr. David Andersen**, **Dr. Alan McConnachie**, and **Dr. Kim Venn** for providing me with the brilliant opportunities to further my work in the fields of Astronomical Adaptive Optics, Astrometry, and Industry collaborations through NTCO-CREATE. Thank you for your guidance, mentorship, and for sending me to the Big Island and Marseille, where I gained world-class experience in these areas. Through your support, it has been an amazing journey which has brought me thus far, having discovered and learned so much, and where I see such wonderful vistas ahead.

I am also deeply indebted to **Dr. Peter Wizinowich**, without whose support my collaboration with W.M. Keck Observatory and resulting work would not be possible. I would also like to thank **Scott Lilley** for his supervision and patience in answering my many questions. A big thank you to the entire **Keck AO group and summit operation team**, who were a pleasure to work with. I would also like to extend my sincere thanks to **Dr. Benoit Neichel** (LAM), **Dr. Jean-Francois Sauvage** (LAM), and **Dr. Thierry Fusco** (LAM) for their constructive advice regarding the work which resulted from my collaboration with the Laboratoire d'Astrophysique de Marseille in France, as well as **Dr. Simone Esposito** (INAF) and **Dr. Lorenzo Busoni** (INAF), for hosting me during my very constructive visit of L'Istituto Nazionale di Astrofisica (INAF) in Florence, Italy. I also wish to thank **Dr. Rene Rutten**, **Dr. Gaetano Sivo** and **Dr. Eduardo Marin** for facilitating my visit and presentation at Gemini South Observatory in La Serena, Chile.

Thank you as well to the awesome **AO group at the National Research Council Herzberg Astronomy and Astrophysics Research Centre** for being so supportive throughout my research. A special thanks to **Dr. Jean-Pierre Véran** for all the great discussions, guidance, and kind support he provided. Also, thank you to **Dr. Peter Stetson** for his wise comments and advice throughout my research. My gratitude also extends to my supervisors **Dr. M. Bahmanabadi** and **Dr. M. Khakian**, who throughout my undergrad and masters degree, encouraged and provided me with many opportunities to expand my knowledge and grow. I am also grateful to **Paolo**, **Masen**, and all the other graduate students and postdocs for their support and friendship.

Afnan, thank you for all your love, encouragement, and unwavering support. Thank you for always being there to edit my work and provide invaluable feedback,

while at the same time studying, working, helping others, and lighting up our world with your phenomenal spirit. You are the brightest star in my sky.

My mother, **Parivash**, thank you for having nurtured my curiosity and always being so supportive. When you bought me a 5-inch telescope, did you ever imagine I would be helping to develop a 30-meter one? Thank you for always believing in me. This would never have been possible without you.

Last but not least, thank you to my feathery friend, **Hendooneh** (Watermelon) the lovebird, for your wholehearted love and companionship.

I gratefully acknowledge the generous financial support received through the prestigious Natural Sciences and Engineering Research Council of Canada's (NSERC) scholarship; the New Technologies for Canadian Observatories (NSERC-CREATE NTCO) grant; SIAF President's Beyond Borders Asia Partners - Asia Graduate Supplement; and the Howard Petch and David Strong Research Scholarships.

Some data used in this work was obtained from ACS Globular Cluster Treasury program (PI: Ata Sarajedini, HST Program 10775). Also, observations obtained at the international Gemini Observatory, a program of NSF's NOIRLab, which is managed by the Association of Universities for Research in Astronomy (AURA) under a cooperative agreement with the National Science Foundation. On behalf of the Gemini Observatory partnership: the National Science Foundation (United States), National Research Council (Canada), Agencia Nacional de Investigación y Desarrollo (Chile), Ministerio de Ciencia, Tecnología e Innovación (Argentina), Ministério da Ciência, Tecnologia, Inovações e Comunicações (Brazil), and Korea Astronomy and Space Science Institute (Republic of Korea). Additionally, this work benefited from the support of the WOLF project ANR-18-CE31-0018 of the French National Research Agency (ANR) and the French CNRS INSU-CSAA program. This document has been prepared as part of the activities of OPTICON H2020 (2017-2020) Work Package 1 (Calibration and test tools for AO assisted E-ELT instruments). OPTICON is supported by the Horizon 2020 Framework Programme of the European Commission's (Grant number 730890). This work was supported by the Action Spécifique Haute Résolution Angulaire (ASHRA) of CNRS/INSU co-funded by CNES.

دل گر چه درین بادیه بسیار شتافت
یک موی ندانست و بسی موی شکافت
گرچه ز دلم هزار خورشید بتافت
آخر به کمال ذره‌ای راه نیافت

Although my senses were searching the desert unrelentingly
discovering nothing although finding a lot
my soul was illuminated by a thousand suns
but could never ever touch the perfection of a single atom.
- ***Ibn Sina*** *(ca. 970–1037) - Persian astronomer, physician and writer*

Chapter 1

Introduction

1.1 Astronomy and Scientific Methodology

The scientific methodology is undoubtedly one of the greatest inventions of humankind. The path that systematically empowers humans to learn the laws of nature and use them for their benefit. From the emergence of inductive experimental methods in Ibn al-Haytham's (Alhazen) *Book of Optics* (1021 AD) [91, 2] to the current modern age, our understanding of the workings of nature are obtained based on three main stages of scientific methodology: Observation, Modeling, and Experimentation. The basic definition of a scientist is one who observes the behaviour of a natural phenomena, provides a model for his or her observation, and experiments to find the goodness of fit for the model while endlessly endeavouring to perfect it. Astronomy and astronomers follow the same path. However, observations in astronomy may be deemed somewhat different to other branches of science. With rare exceptions, in astronomy the scientist cannot touch any of the bodies and phenomena of interest as they are typically "astronomically" long distances away. In particular, this limits the meaning of "observation" to "detecting electromagnetic waves" for the majority of branches of astronomy. A few examples of exceptions are the samples Apollo 13 brought from the moon, the study of meteorites, and direct experimentation on a few solar system bodies using robotic probes. For the remaining (and absolute majority) branches of astronomy, the main messenger are waves, mainly[1] electromagnetic waves. Since the beginning of modern astronomy and the very first telescopes, astronomers

[1]There are also other kind of messengers like neutrinos or gravitational waves that provide observations from the universe, but the portion of our knowledge acquired by them is still minimal compared to looking at photons across the electromagnetic spectrum

look at incoming electromagnetic waves in the form of visible light to satisfy pieces of our curiosity and reach beyond the borders of our knowledge.

1.2 Electromagnetic Spectrum and Atmosphere

Astronomers look at the sky not only through the visible spectrum, but through the full electromagnetic spectrum: from very high-frequency, high-energy Gamma-ray photons, to kilometers-long wavelength photons in the radio astronomy domain. Each band of the electromagnetic spectrum carries information about a variety of physical phenomena of the universe. However, our atmosphere, which makes life on Earth possible, poses a challenge to receiving some parts of this spectrum causing the loss of portions of this precious data. Figure 1.1 represents the schematic of transparency of the atmosphere for different regions of the electromagnetic spectrum.

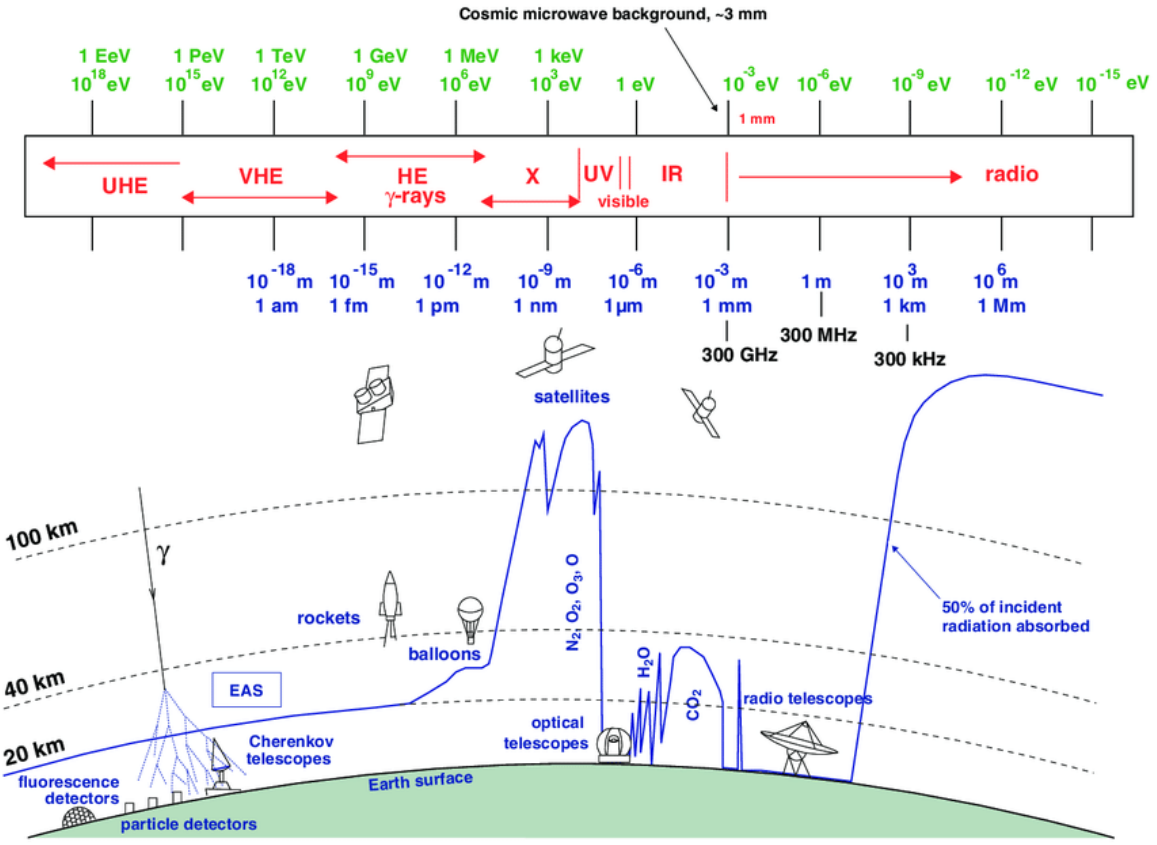

Figure 1.1: A schematic showing different domains of the electromagnetic spectrum and the relative transparency of Earth's atmosphere [57].

In theory, observing from high altitudes or space is ideal. However, it is neither

essential nor practical to place all observatories in space. In some frequency domains, as in radio astronomy, observatories do not have problems with transparency or other effects of the Earth's atmosphere. In other domains, as in the visible spectrum, the transparency of the atmosphere does not pose much of a problem, but the turbulent nature of the atmosphere degrades the image quality of ground-based observatories. Considering the order of magnitude higher cost of space observatories, and also current technical limitations of space missions (i.e. weight and dimensions of the telescope), astronomers have always endeavoured to improve the observing quality of ground-based observatories. They do this by attempting to overcome the challenges posed by the Earth's atmosphere. These efforts are mainly concentrated in the visible and near-infrared (Vis/NIR) domains, were transparency is not the main limitation, but rather the atmospheric optical effects are.

To understand the optical effect of the atmosphere, two phenomena should be considered:

- Our atmosphere is a fluid, whose motion can be best described as turbulent. In contrast with the laminar motion of a fluid, the motion of each particle in the turbulent regime of a fluid is not coherent, but rather is chaotic and consists of many eddies.

- The refractive index of the air that makes up our atmosphere is a function of pressure and temperature.

The non-laminar flow, in addition to the natural thermal gradient of the atmosphere, means turbulent vertical temperature gradients and non-uniform structures with temperature differences exist within the atmosphere. Combining this knowledge with the dependency of the refractive index on temperature, one can expect that the atmosphere acts as a chaotic layer of matter which is optically active and is changing the path of light that passes through it. This is what actually happens in ground-based systems, yielding a significant limitation on the resolving power of telescopes. To visualize such an effect, one can think of light from a star coming from outer space towards the atmosphere. The wavefront of such a light is similar to a flat sheet of paper in shape after passing a very long distance (see Fig 1.2). The wavefront is the shape of a surface which describes points in an incoming electromagnetic wave, which all have an equal phase. This wavefront initially propagates as a sphere, however when it arrives at Earth, it is well approximated as flattened (see Fig 1.3).

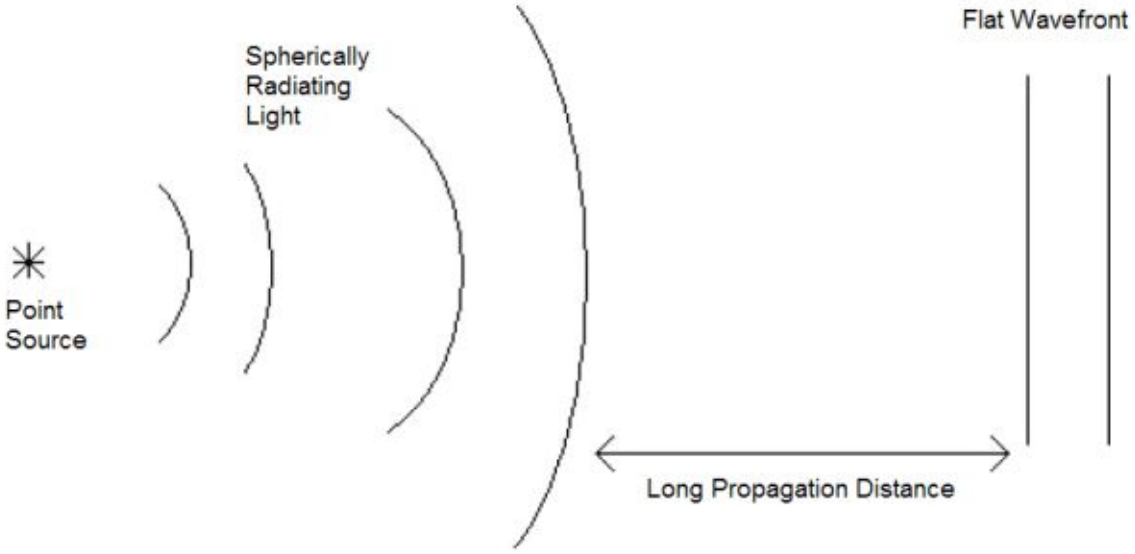

Figure 1.2: A schematic showing the flattening of spherical wavefront propagated over very long distances [103].

Passing through different layers of turbulence, the atmosphere causes the flat wavefront to wrinkle. These wrinkles cause a significant loss in performance, particularly in the Vis/NIR domain of the electromagnetic spectrum.

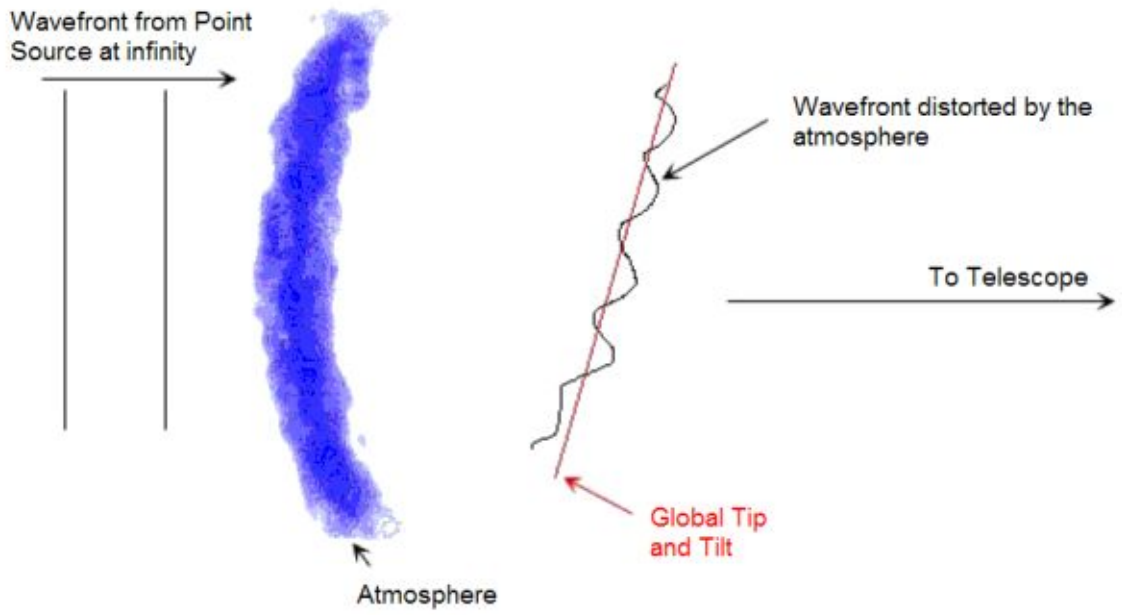

Figure 1.3: A schematic showing the disrupting effect of the atmosphere on the wavefront flatness [103].

1.3 The Resolving Power of Optical Systems

The point-spread function (PSF) of an optical system is defined by the shape of the intensity pattern the optical system provides from a unresolvable object. The smaller the PSF of an optical system, the higher the resolving power of that system. The ideal point-spread function of an optical system is the square modulus of the Fourier transform of the electromagnetic wave coming through its aperture. The shape of a theoretically ideal PSF for an optical system with a circular aperture in the presence of a flat wavefront can be described by an "*Airy*" disk which typically is referred to as "*diffraction-limited*". The width of a PSF of a optical system, no matter the detail of the design, cannot be smaller than the diffraction-limited PSF. Any non-flat features in the shape of the wavefront translate to a broadened PSF, which degrades the performance of the optical system. Therefore, there are only two ways to increase the theoretical limit of the resolving power of an optical system working at a given wavelength:

- Increase the size of the aperture.
- Flatten the input wavefront as much as possible.

The goal of increasing the aperture size of both ground and space-based telescopes has always been a part of astronomical instrumentation. Both the James Webb Space Telescope and the coming generation of giant ground-based telescopes, including the Extremely Large Telescope (ELT) and the Thirty Meter Telescope (TMT), are in line with this endeavour.

To flatten the wavefront, there are only two main practical approaches: build or position the observatory in a place with minimal atmospheric turbulence or compensate for the optical effects of the atmosphere. A good example of the first approach is to place the telescope in space or at the top of a high mountain such as Mauna Kea (home to Gemini, Keck and many other observatories) in Hawaii or Cerro Pachón in Chile (Gemini South and Rubin observatories). In the case of ground-based observatories, correcting the wavefront for the significant atmospheric effects is the responsibility of adaptive optics.

1.4 Adaptive Optics: The Art of Wavefront Flattening

Uncompensated atmospheric turbulence limits the resolving power of ground-based astronomy. One can send a telescope and its instrument suite to space to avoid this limitation, but this solution is many orders of magnitude more costly than ground-based observatories. More importantly, current space launch technologies limit the aperture size of the largest space telescope to be smaller than the aperture of the future generation of extremely large ground-based telescopes by a factor of ~ 5 [16]. If atmospheric turbulence can be well-corrected, ground-based observatories could achieve a factor of 5 times increase in resolving power and a factor of 25 times increase in light-gathering power. Astronomical adaptive optics (AO) systems are therefore an essential technology for ground-based telescopes. Without AO, the resolving power of the largest ground-based telescope would be no better than a 50 cm amateur telescope at a good site.

The advantage of building larger telescopes are two fold: larger light gathering area and increased resolving power, meaning the gathered light will focus in a smaller area. The light gathering power is proportional to D^2, and the two-dimensional size of the PSF is proportional to D^{-2}, where D is the diameter of the telescope aperture. Considering both effects simultaneously, the advantage of increasing the

size of a telescope is proportional to D^4 in the background-limited regime for point sources [42]. However, in the presence of atmospheric turbulence, the D^{-2} relation holds only down to a certain limit which is known as "astronomical seeing". Seeing is the smallest possible PSF size that the atmosphere will allow a large enough telescope to see from a point source. This means that, without AO, increasing the size of the telescope above a certain diameter only brings a D^2 advantage instead of a D^4, which is the main reason why AO is essential in the design of extremely large telescopes.[2]

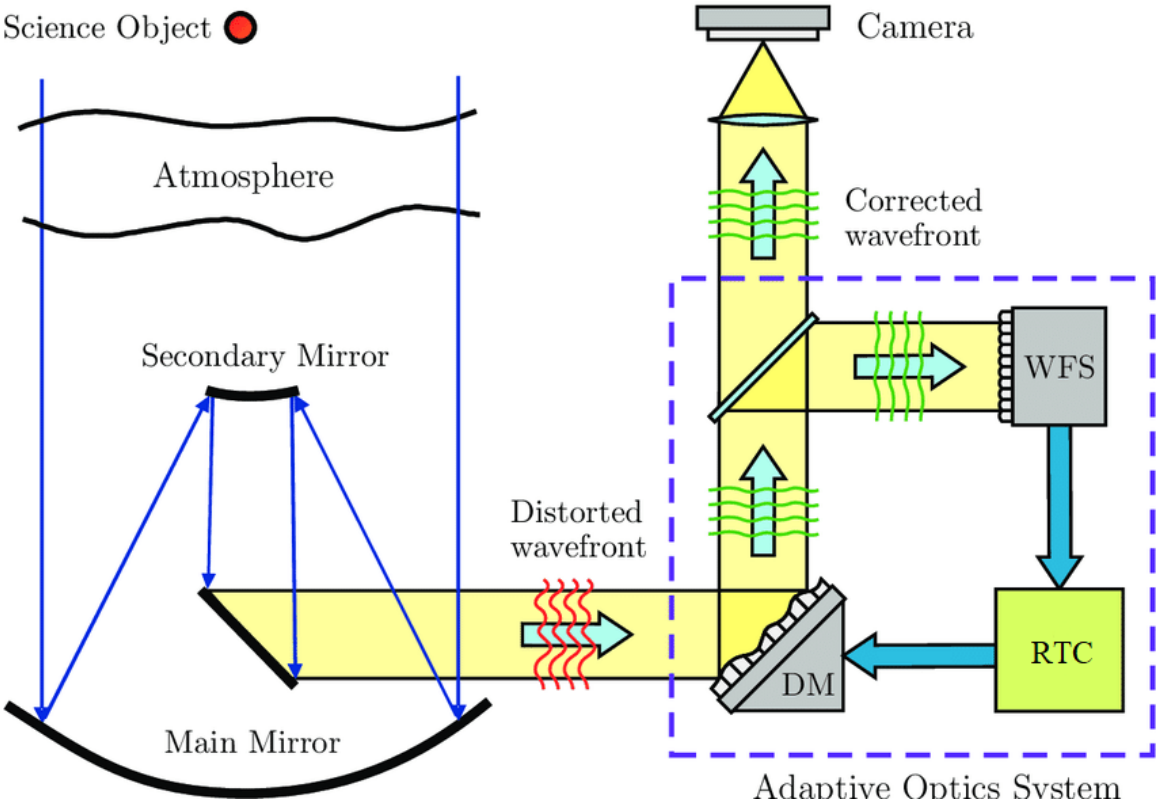

Figure 1.4: A schematic of an AO system (Credit: Lessard [54]).

1.4.1 Main architecture of AO systems

A typical AO system consists of three main subsystems: the wavefront sensor (WFS) measures the wavefront, the deformable mirror (DM) can change shape to compensate for the atmospheric turbulence, and the real-time computer (RTC) which connects the two optical devices by reading in the WFS measurements, then determining and

[2]The limiting size is related to the wavelength of observation and the amount of turbulence in the atmosphere characterised by the Fried parameter [42]. Even for the best sites for observatories in the Vis/NIR domain, this limiting size is well below 1 meter.

applying the appropriate commands for the DM (see Fig 1.4).

Wavefront sensors

The wavefront sensor is the eye of an AO system, responsible for measuring the wavefront shape. The most common types of wavefront sensors in astronomical adaptive optics are Shack-Hartmann [87, 40] and Pyramid [74]. There are other architectures such as the curvature [78] WFS, however they are not as common.

The first and relatively simpler WFS architecture is the Shack-Hartmann sensor. A SHWFS divides the aperture of the telescope into many sub-apertures and measures the angle of incidence of the wavefront for each sub-aperture. This can be done by focusing the light using a lenslet array and tracking the position of each spot formed in the focal plane of the lenslet array. This measurement provides the average slope of the wavefront for each sub-aperture. Integrating slopes over the whole aperture and X,Y axis reconstructs the shape of the incoming wavefront. A schematic of such a WFS system can be seen in Figure 1.5.

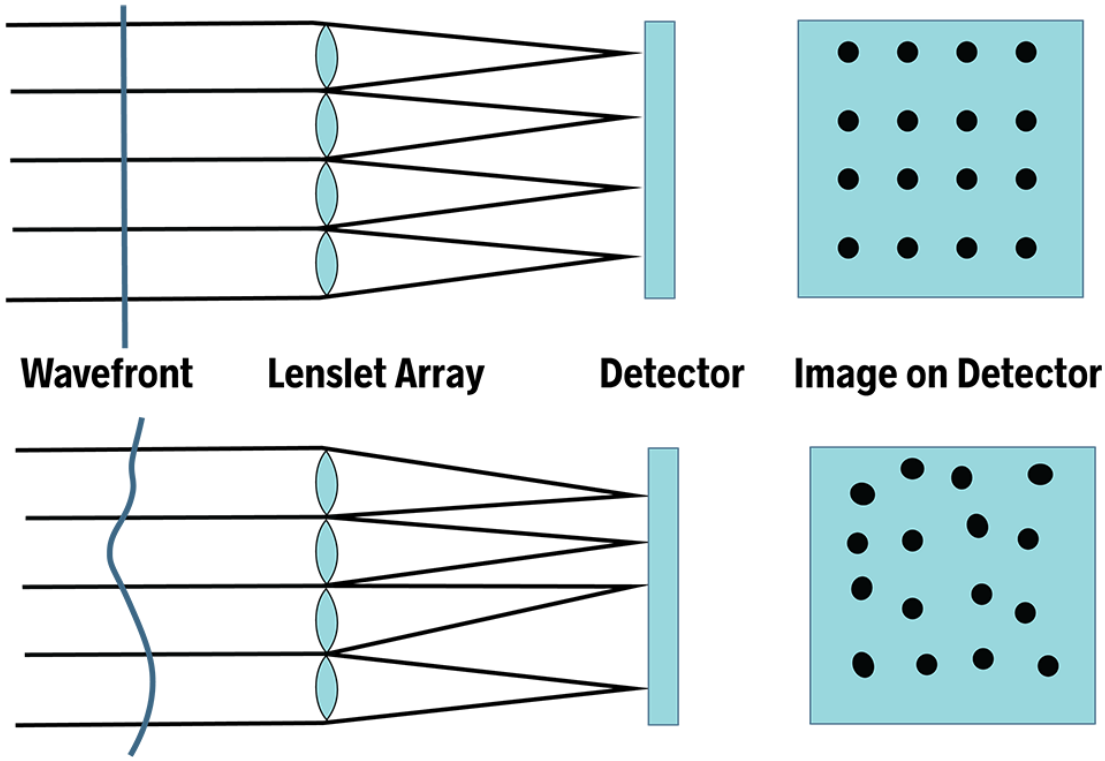

Figure 1.5: This simple schematic is showing the principles of SHWFS. By measuring the displacement of each spot relative to the reference wavefront, it is possible to measure the average gradient vector of the wavefront. (Photo credit: Tokovinin [100])

Pyramid WFS (PWFS) are a more recently developed and more complicated type of wavefront sensor [74]. In this architecture, a pyramid-shaped piece of glass is placed in the focal plane of the telescope, such that the PSF is imaged onto the tip of the pyramid. Re-imaging the pupil plane after passing through the pyramid provides four separate images of the pupil on the WFS detector as shown in Figure 1.6.

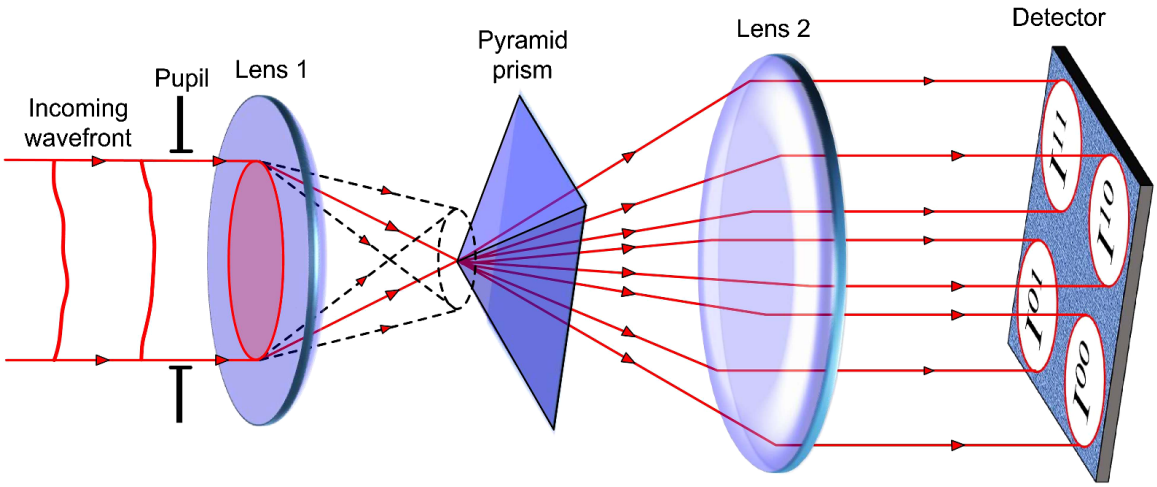

Figure 1.6: Schematic showing the principles of PWFS. (Photo credit: Shatokhina et al. [88])

The pyramid signal, corresponding to the wavefront slopes, can be derived from the intensity of these patterns utilising Equation 1.1.

$$S_x(n,m) = \frac{I_1(n,m)+I_3(n,m)-I_2(n,m)-I_4(n,m)}{\frac{1}{N}\sum_{n,m} I_1(n,m)+I_2(n,m)+I_3(n,m)+I_4(n,m)}$$
$$S_y(n,m) = \frac{I_1(n,m)+I_2(n,m)-I_3(n,m)-I_4(n,m)}{\frac{1}{N}\sum_{n,m} I_1(n,m)+I_2(n,m)+I_3(n,m)+I_4(n,m)} \quad (1.1)$$

$I_i(n,m)$ refers to the intensity in each pupil image at the equivalent pixel location specified by (n,m) and N is the total number of illuminated pixels in an individual image [13]. PWFS converts the phase variation to intensity modulation. Although the pyramid signal resulting from Equation 1.1 is not exactly equal to the slope of the wavefront, it is directly correlated with it. The four-pupil images on the PWFS detector of the Keck II telescope can be seen in Figure 1.7.

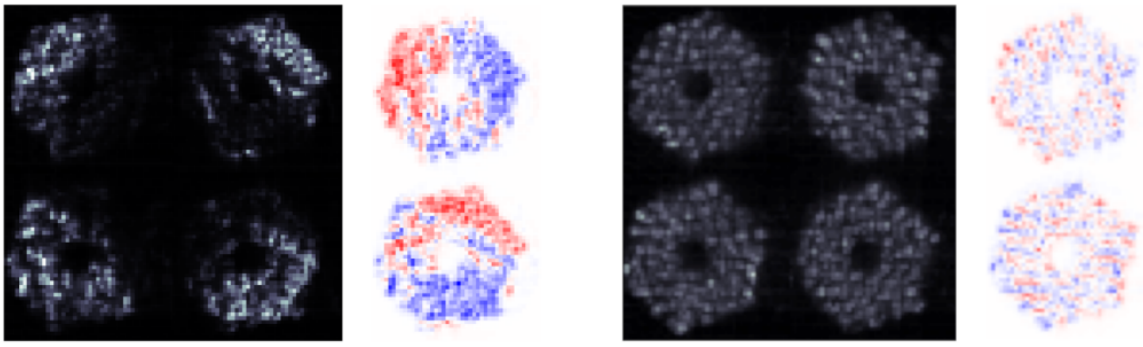

Figure 1.7: The gray scale intensity pattern of the infrared PWFS detector for Keck II telescope. The blue-red patterns are the corresponding pyramid signal. The left side of diagram is the wavefront before correction and the right side is the same system while correction on the wavefront is applied. Note the significantly smoother signal on the right side provided by the AO system wavefront correction. (Photo credit: Bond et al. [13])

Pyramid wavefront sensing has some benefits over SHWFS, mainly in error propagation for sensing low-spatial modes and higher performance for faint guide stars. However, the efficient use of a PWFS is typically more difficult compared to a SHWFS. The linear range of the PWFS is very narrow, so a fast steering mirror is typically used in PWFS systems to modulate the PSF on the top of pyramids, broadening the dynamic range of the measurements which adds to the mechanical complexity of the system. The high sensitivity and limited linear range also makes PWFS more difficult to use in the presence of large non-common path aberrations[3] or highly turbulent atmospheric conditions.

Real-time computer

The Real-time computer (RTC) is responsible for providing the necessary computational power for calculating which commands should be sent to the DM actuators based on the WFS measurements. The atmospheric turbulence pattern changes hundreds of times in a second. This means the whole loop of sensing, calculating the actuator commands, and deforming the DM surface needs to be repeated hundreds of times per second. This leaves just a few milliseconds for the RTC to calculate the necessary commands. Such a systems usually benefits from optimized processing to further decrease the processing time for each instance of the loop.

[3]Non common path aberration or NCPA is referred to as any wavefront aberration source which is in the path of the science detector, but which cannot be seen by the WFS

Deformable mirror

To compensate for the wrinkles of the incoming wavefront, a device that precisely controls the optical path difference over a cross-section of the beam is necessary. Different solutions have been proposed. The most practical and common solution is a deformable mirror. With deformable mirrors, the wavefront is reflected on a reflective surface that has a precise control over its shape. The shape is formed in such a way to mimic the wavefront shape multiplied by -0.5. Reflecting from such a surface will flatten the wavefront as Figure 1.8 schematically represents.

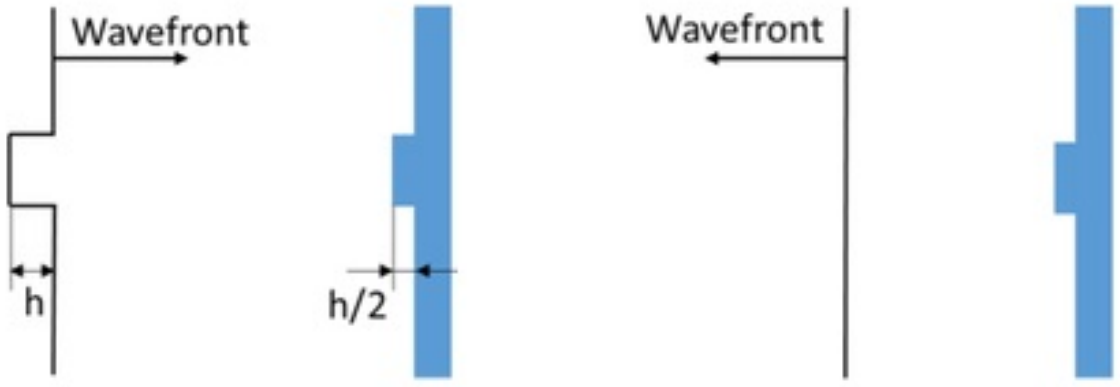

Figure 1.8: The incoming wavefront on left and flattened reflection on the left. Note that the shape of the mirror is the same as the shape of wavefront multiplied by a factor of -0.5. (Photo credit: Nikitin et al. [68])

Among different practical approaches to build such a device, the continuous face-plate concept is the most common one. With such a device, a thin deformable membrane is shaped by an array of mechanical actuators stuck to the backside of the membrane (see Figure 1.9). The resolution and the goodness of the spatial correction that such a DM can provide is related to the density and size of the actuator array as well as the stroke range of each actuator. In addition to the spatial resolution, another important consideration is the response time. The shape of a DM surface must change hundreds of times per second to act fast enough to compensate for atmospheric turbulence.

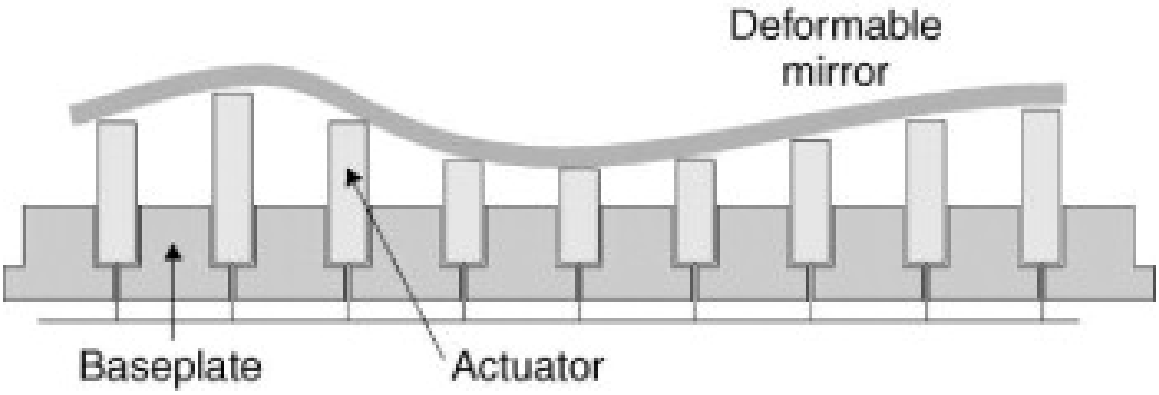

Figure 1.9: Schematic of a DM with continuous faceplate concept. (Photo credit: Pernechele [71])

1.4.2 Single and Multi-Conjugate AO

AO systems come in different architectures with different levels of complexity, depending on the application. A key configuration that is critical for both TMT and ELT is multi-conjugate adaptive optics (MCAO). The desirable aspect of this architecture is its ability to provide uniform correction across a (relatively wide) one arcminute field of view, to be compared to a typical classic AO system that provides efficient correction across a field of view of the order of a few arcseconds [7]. In a classic single conjugate AO (SCAO) system, a single wavefront measurement is made and a single DM corrects for the cumulative effect of all the layers of turbulence in the cylinder of atmosphere between the telescope and the science target. The size of the corrected field is typically $\sim$1 arcsecond and is characterized by the "isoplanatic angle", beyond which the rest of the telescope's field of view is uncorrected. MCAO systems provide a much wider corrected field of view by using multiple wavefront sensors to provide a 3D tomographic wavefront measurement of the cone-shaped volume of atmosphere in front of the telescope. The wavefront is corrected by using multiple DMs (at least two) which are conjugated to turbulence layers at different altitudes, and this provides relatively uniform correction across a wide field of view. Figure 1.10 represents the general structure of classic and MCAO systems.

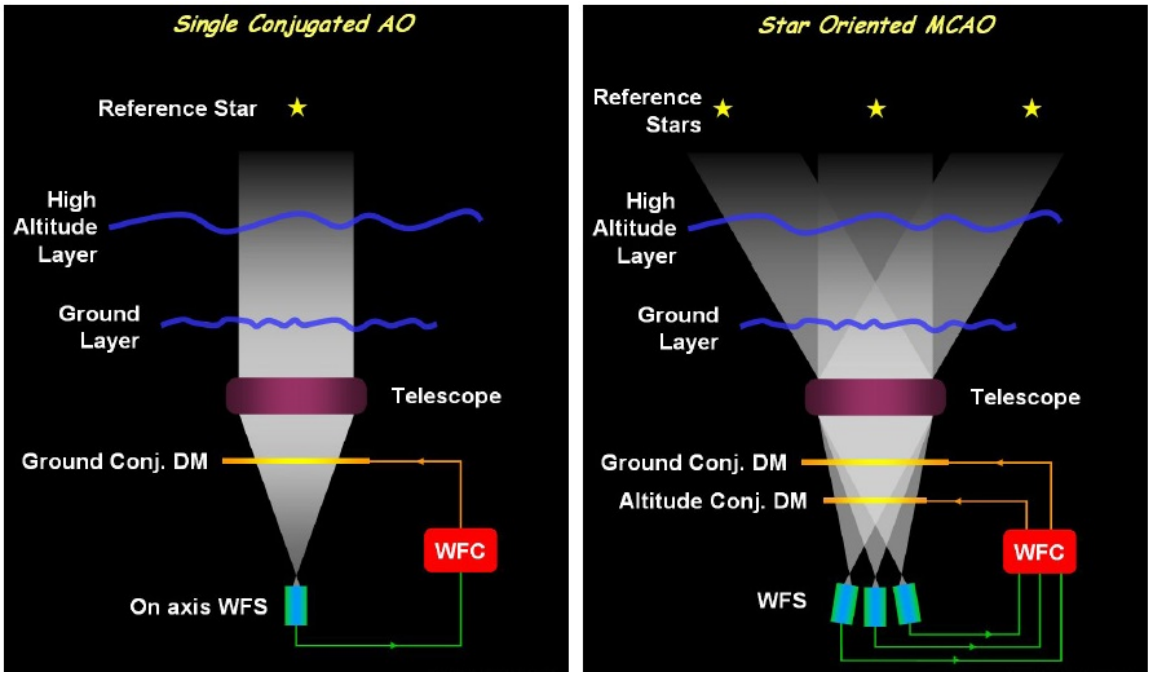

Figure 1.10: The structure of classic and muti-conjugate AO systems. (Photo credit: Marchetti/ESO)

The only MCAO instrument that is currently in regular science operation is at the Gemini South telescope. The Gemini multi-conjugate adaptive optic system (GeMS) and the Gemini South adaptive optic imager (GSAOI) are instruments placed on the Cassegrain focus of this 8-meter facility [33]. GeMS uses a constellation of 5 laser guide stars (LGSs) combined with 3 natural guide stars (NGSs). The LGS constellation provides tomographic information about the turbulence layer in the cone-like volume of atmosphere that is in front of the primary mirror of the telescope. However, LGSs are not sufficient to remove all phase aberration modes as they are blind to low-order phase aberration modes. This causes the "tilt anisoplanatism" problem which is well described and addressed in [34]. Here, NGSs come to help for measuring and calibrating low-order phase aberration modes like tilt/tip and focus. The real time controller (RTC) then processes the information gathered from the 5 LGS + 3 NGS to create a tomographic map of the turbulence. This tomographic map provides the necessary information to drive two deformable mirrors conjugated to altitudes of 0/9 km in the atmosphere. These mirrors provide tomographic wavefront adjustment, which provides the wide field correction advantage in addition to a uniform wavefront correction across the field of view [28, 77]. Figure 1.11 shows the quality difference between seeing limited, classic AO and MCAO performance.

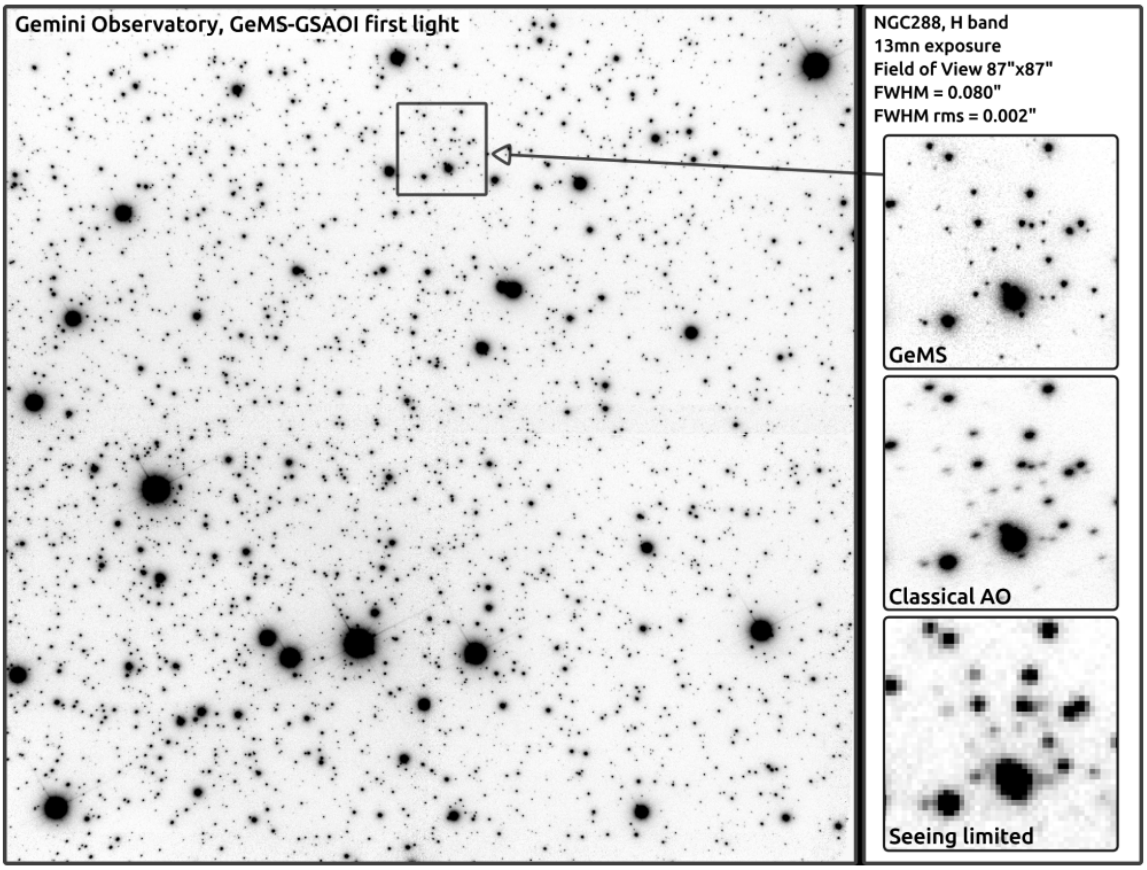

Figure 1.11: NGC288 at H band taken with GeMS. GeMS/MCAO (up), classical AO (middle), and seeing limited case (bottom). (Photo credit: Rigaut et al. [77])

1.4.3 The Science Cases for MCAO and ELTs

A new generation of extremely large ground-based telescopes, the Thirty Meter Telescope (TMT - 30m aperture) [81] and the Extremely Large Telescope (ELT - 39m aperture) [75] will see first light later this decade. These state-of-the art facilities will revolutionize astronomy thanks to their very large apertures, which simultaneously increase their light-gathering ability and resolving power. The key technology that is essential for enabling these advances is adaptive optics. Without this technology, the resolving power of such a giant instrument would degrade to that of a small 50 cm backyard telescope. The current launch technologies limit the aperture size of the largest space telescope to be smaller than the aperture of ELTs by a factor of 5. This translates to 5 times less diffraction-limited resolving power and 25 times less light-gathering power, significantly limiting the possible critical science cases (see Figure 1.12).

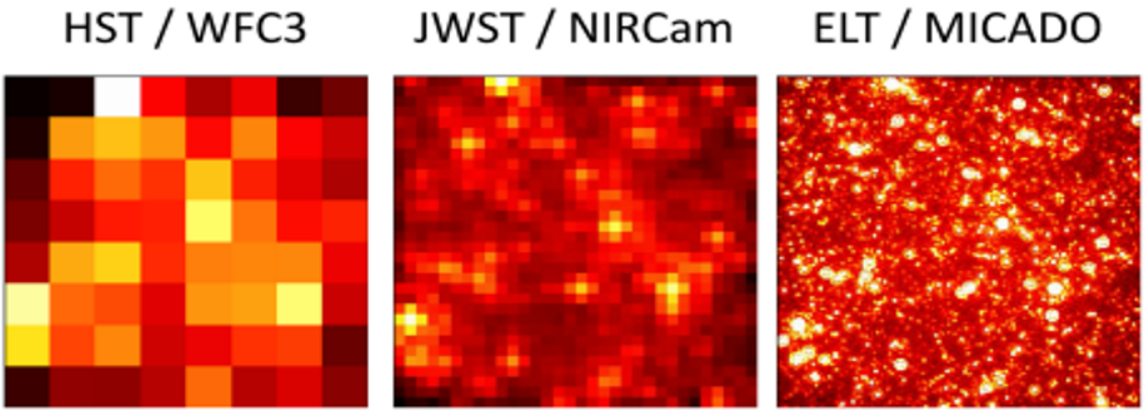

Figure 1.12: NGC 4472 in the Virgo Cluster seen by HST, JWST (James Webb Space Telescope, 6.5 meter space-based telescope), and ELT/MICADO. Note the significantly improved resolving power of ELT using its MCAO imager, MICADO. (Photo credit: Davies et al. [26])

The wealth of science available makes ground-based ELTs and astronomical AO an important focus and research priority for the future of astronomy. ELTs will exploit MCAO technology to provide revolutionary astronomical imaging, covering 100 times larger AO-corrected area per image compared to classical AO systems. Using MCAO technology, the expected resolving power of ELTs will be more than ten-fold that of the Hubble Space Telescope (HST). Furthermore, when ELTs receive their first MCAO-corrected light in 2027, their resolving power will be a five-fold improvement over the current generation of cutting-edge telescopes, such as the European Very Large Telescope (VLT) telescopes in the Atacama Desert.

The European Southern Observatory (ESO) is investing approximately € 1.3 billion (2019) towards the ELT project and the TMT Observatory is about to invest a similar amount for the 30m telescope. The return on this investment will be obtained by achieving critical scientific goals, several of which require high-precision astrometry. Astrometry is a sub-discipline of astronomy which measures the precise positions and tangential motions of astronomical objects. In this field, MCAO systems have the potential to be a premier facility for precision astrometry due to the powerful combination of high-spatial resolution, large field of view, and infrared capabilities. For example, the estimation of the astrometric error of TMT is the extremely small number of $\sim$10 μas [85]. A few examples of critical astrometric science cases are:

- Supermassive black holes: Supermassive black holes present us with a testbed to study general relativity and the remarkable physics of the most extreme

environments. Current AO observations with 8-10 meter class telescopes of the center of the Milky Way and the core of neighboring galaxies are limited by the telescopes' resolving and light-gathering power. For the first time, 30-meter class telescopes will extend our understanding of the space-time topology around a super massive black hole to well within ∼1000 Schwarzchild radii. The immediate surroundings of the black hole at the center of our Galaxy will allow for fundamental tests of "medium field" relativity, including the astrometric signal of prograde general relativity precession [8].

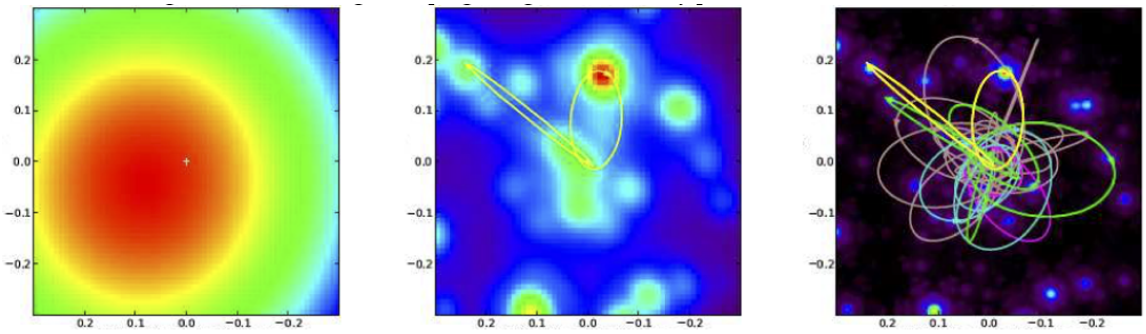

Figure 1.13: Probing the Galactic Center with ELTs. A seeing-limited observation of the 0.6 arcsec region of the Galactic Center (Left), an image with the current Keck adaptive optics capabilities (Middle), and a simulation of the Galactic Center as observed by the future 30 meter class telescopes (Right). The increased resolving and light gathering power of ELTs will expose many fainter and closer probes of the Galactic Center, which is a key for more precise measurements of the mass of the black hole in the core of our galaxy and its dynamics [8]. (Photo credit: Ghez/Weinberg/Morris/Lu)

- Dark matter halos: Dwarf Spheroidal (dSphs) galaxies are believed to be the most dark-matter-dominated objects in existence. Deriving the anisotropy and mass density profile of these objects via high-precision astrometric studies of internal kinematics could provide an ideal test bench for structure formation models. Cosmological N-body simulations suggest that Cold Dark Matter (CDM) halos must have a cuspy density profile in the absence of baryonic effect, whereas rotation curve studies estimated a shallower mass profile. Verifying the presence of these cores/cusps in dSphs using the unprecedented depth and astrometric precision of ELT will not only provide an end to this debate, but also pave the way to confirm the consistency of these theories with ΛCDM and to make a direct test of the most important cosmological models [92].

- Intermediate mass black holes: One of the most interesting topics to study with the novel astrometric abilities of the ELTs is that of Intermediate Mass Black Holes (IMBH). These are black holes with masses of order $10^3 - 10^4\ M_\odot$ are expected in the core of dense star clusters, but their existence has never been observationally confirmed. There are extensive simulations predicting different mass models for globular clusters and the possible existence of the IMBH in the core of these objects, waiting for observational data for validation [25]. Thanks to the unprecedented astrometric potentials of MCAO, ELTs would be able to provide ideal observational evidence to reveal the mysteries hidden in the core of globular clusters [64, 30, 38, 82].

Note that these science cases cannot be addressed with Gaia astrometry due to its much shallower limiting magnitude and also its lack of sensitivity at infrared wavelengths, hence only ELTs will open these science windows. Critical to this science is the determination of residual astrometric errors that act to reduce the precision of astrometric data gathered by these systems, in order to develop methods to correct for them. Astrometry with adaptive optics, and particularly MCAO systems, is not yet a mature field and not all issues associated with it are well understood. Since first light from ELTs is less than a decade away, it is now a priority to carefully study astrometric error sources from MCAO systems and devise methods and solutions to compensate for their effects.

1.5 Thesis Overview

The main focus of this PhD thesis is on improving MCAO systems, by simultaneously improving hardware and developing new data processing techniques. I believe this approach provides valuable insight of the detailed performance of astronomical AO systems as well as knowledge of their optimal use for scientific applications.

In Chapter 2, I focus on my collaboration with W. M. Keck Observatory as well as the National Research Council of Canada to develop new wavefront sensing approaches. The details of my participation of design and development of the new infrared pyramid wavefront sensor for the Keck II telescope and leading the design and fabrication of the very high-order Shack-Hartmann sensor at NRC Facilities is explained in this chapter.

In Chapter 3, the details of the laboratory method I developed for emulating the

spider shadow on laboratory benches is explained. Studying such an effect on the performance of AO systems is an essential step for the future MCAO facilities of ELTs to reach their wavefront residual error budget requirements. The method I proposed allows the injection of high-precision shadow patterns into the pupil plane of laboratory AO benches using an spatial light modulator (SLM) device which has not previously been available. The alternative methods are significantly more difficult to apply, less accurate, and in some cases limited by current mechanical fabrication technologies i.e. 3D printed masks. In addition to testing the feasibility of the proposed approach on the LOOPS bench in partnership with the Laboratoire d'Astrophysique de Marseille (LAM), I re-designed the advanced wavefront bench at NRC facilities to accommodate this new solution.

In Chapter 4, I shift my focus from hardware improvements to the data processing and scientific applications of the future MCAO systems. Many sensitive science cases for the new ELTs depend upon their astrometric precision. The performance of the MCAO system improves the resolving power of these telescopes over a relatively wide FoV. However, MCAO also can introduce field distortion, which if not considered carefully, will jeopardize foreseen science applications. I led the development of a statistical method in the form of an astronomical pipeline, designed to reduce the distortion field of MCAO-aimed observations to the level comparable to space-based data. Details of the methodology, observations, and results are explained in this chapter.

Finally, in Chapter 5, the results and achievements of this thesis are summarized.

Chapter 2

Design and Implementation of New Wavefront Sensors

I provided the optical and mechanical design of, and verified performance of, multiple components which were later commissioned in the Keck IR-PWFS and KPIC instrument. Some material of Section 2.2 is closely based on a technical report KAON-1178 [55] by Taheri (2017). I provided optical modeling and performance analysis of the FSM system as well as calculated the motion function of each mirror. Some material of Section 2.3 is closely based on a technical report KAON-1179 [95] published by Lilley and Taheri (2017). Here I provided an alignment plan for the replacement and bench modification procedure, assembled new opto-mechanical components, and assisted in the replacement and installation of new components on the K2AO bench on Keck II telescope. Also some material from Section 2.2 and 2.3 are published in a paper by Bond co-authored by Taheri (2020) [13], a paper by Ragland co-authored by Taheri (2019) [80] and a paper by Lilley co-authored by Taheri (2018) [56]. A paper closely based on Section 2.4 is submitted for publication in 2022. I led the entire development process, including the opto-mechanical design of the device and multiple custom-made components, as well as design and performance verification tests and analysis of results.

2.1 Introduction

Wavefront sensors (WFSs) are an essential part of any AO system. The two WFSs most widely used in astronomy are Shack-Hartmann and Pyramid wavefront sensors.

In this chapter, I present my work on the design and development of science grade implementations of both types of these devices, first for the new IR-PWFS for the Keck II telescope, and secondly for a new very-high order SHWFS for use at NRC facilities.

The first step to reducing the effect of turbulence in the atmosphere is to build on sites with minimum turbulence. This is one of the main reasons that most observatories are built on the summits of high mountains. The mountain of Mauna Kea is situated in the middle of the Pacific Ocean. Its summit is at the altitude of 4207 meters above sea level, and it features a relatively gentle slope on its foothills. These factors make the summit of Mauna Kea one of the best places on earth for hosting observatories, and it is for this reason that the Keck Observatory is located there in the company of other large ground-based observatories (see Figure 2.1).

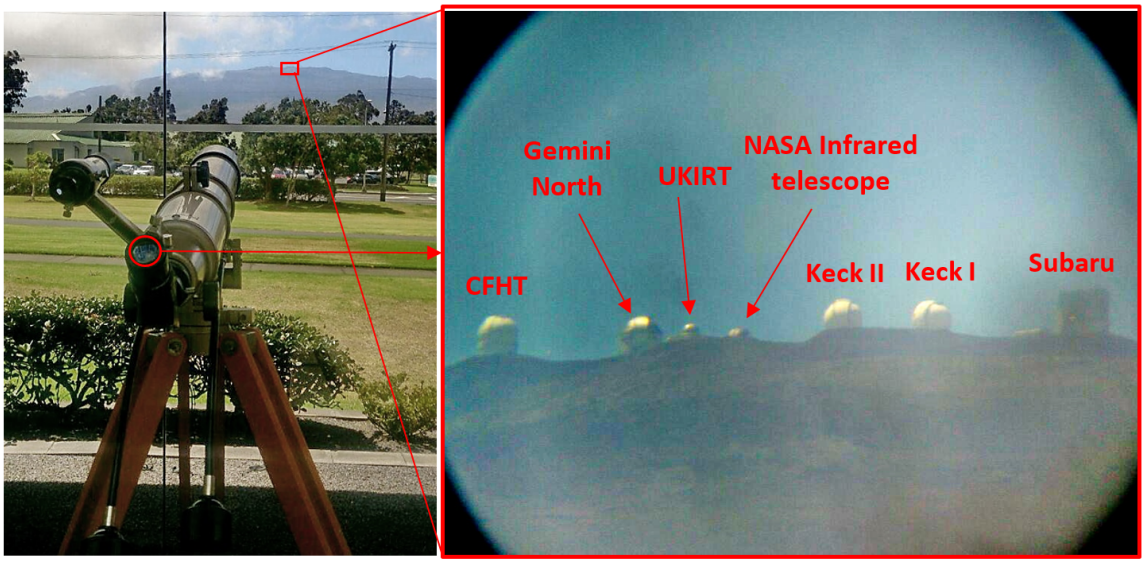

Figure 2.1: Summit of Mauna Kea as seen via a small telescope from Keck headquarters in Waimea. (Photo: Mojtaba Taheri)

The W.M. Keck Observatory operates two 10-meter class telescopes at the top of Mauna Kea in Hawaii, making it the largest telescope aperture currently active in science operation (see Figure 2.2). Keck Observatories have always been at the cutting edge of astronomical instruments and supporting technologies like adaptive optics. The first implementation of adaptive optics technology on a 10m-class telescope was made on the Keck II telescope in 1999, improving the angular resolution of observations to 10 times better than seeing-limited observations [105]. Since then, the Keck Observatory has always been one of the pioneers of adaptive optics.

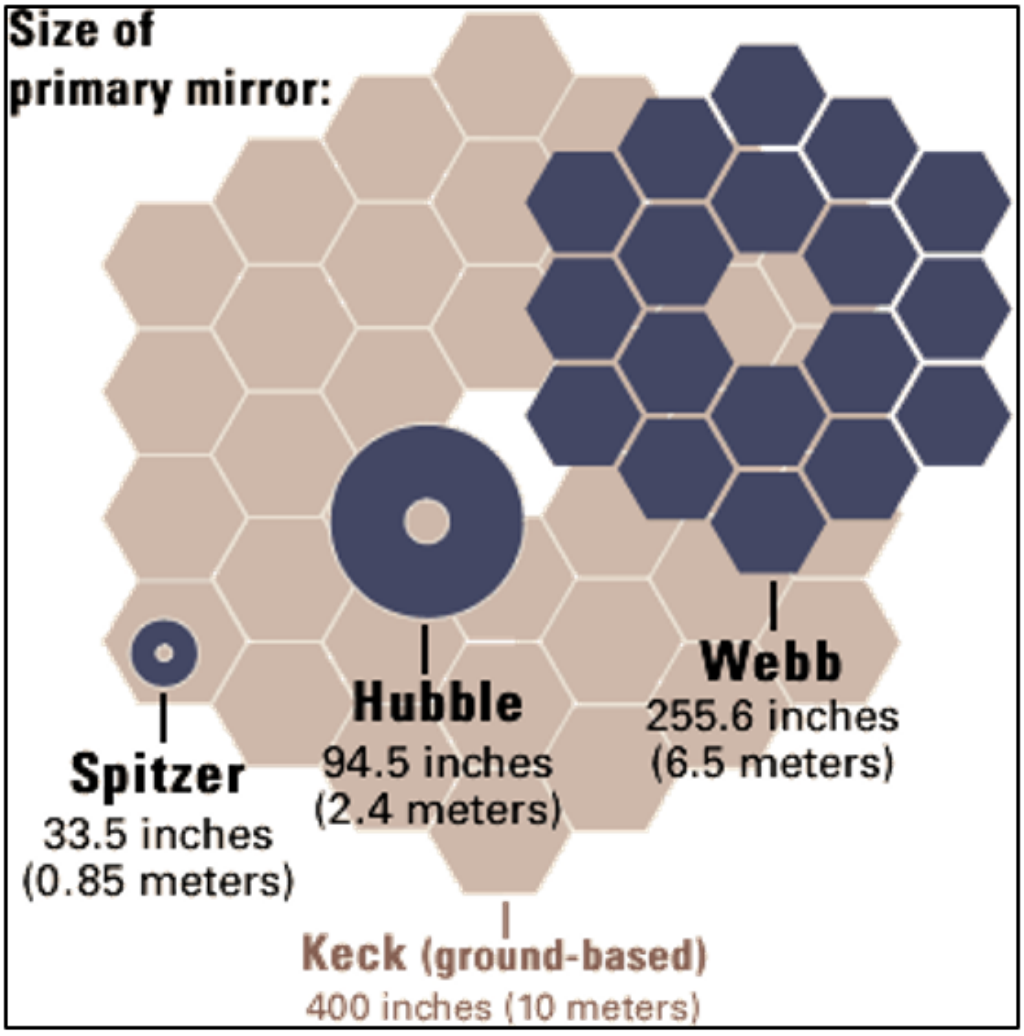

Figure 2.2: Size comparison between Keck primary mirror and famous space telescopes. (Photo: STSCI)

The Keck Observatory implemented a sophisticated infrared pyramid wavefront sensor on the AO bench of the Keck II telescope, commissioned in July 2019 [13]. I worked on various aspects related to the design, development, and installation of this significant WFS upgrade. Figure 2.3 compares the improvement of AO performance between the new IR-PWFS and the previous SHWFS.

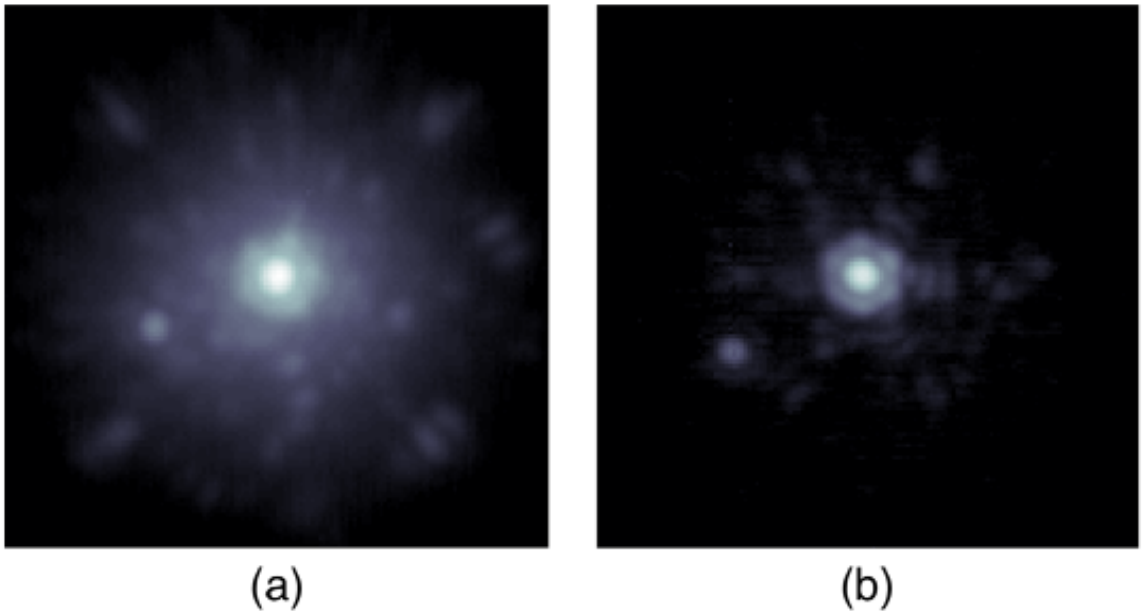

Figure 2.3: K-band images of the system WISEJ0720 - 0846AB (R = 16.9 and H = 9.9) taken with Keck. (a) LGS observation, October 2018 [29]. Seeing $\sim 0.5''$, SR = 22%. (b) PWFS observation, October 2019. Seeing $\sim 0.6''$, SR = 46%. (Photo Credit: C. Bond [13])

There are several science cases, particularly in the field of exoplanet imaging and characterization, which can significantly benefit from wavefront sensing in the infrared. One such example is the case of M-dwarf stars, made particularly desirable for observation due to their potential as hosts of exoplanets. Another example is the case of proto-planetary disks in star forming regions, such as those recently discovered by ALMA [6]. These cooler or dust obscured stars are often faint in the visible, requiring the use of off-axis natural guide stars or laser guide stars for AO observations, both of which do not provide optimal correction for the science target. However, these stars are bright enough to be used as the natural guide star with an IR WFS, with the potential to provide high quality AO correction on-axis. The realisation of these IR sensors is now possible thanks to developments in low noise IR detector technology. The new Keck pyramid wavefront sensor forms part of the larger KPIC instrument. The specific goal of this instrument is to identify new planets via direct imaging and subsequently to characterize these and other known planets using fiber fed spectroscopy. KPIC is used in conjunction with Keck II's facility infrared instruments: NIRC2, an imager with a vortex coronagraph; and NIRSpec, a high resolution sepctrograph. Currently the AO correction is provided by the Keck facility

tip-tilt mirror (TTM) and 349 actuator Xinetics deformable mirror (DM) - 21 × 21 actuators.

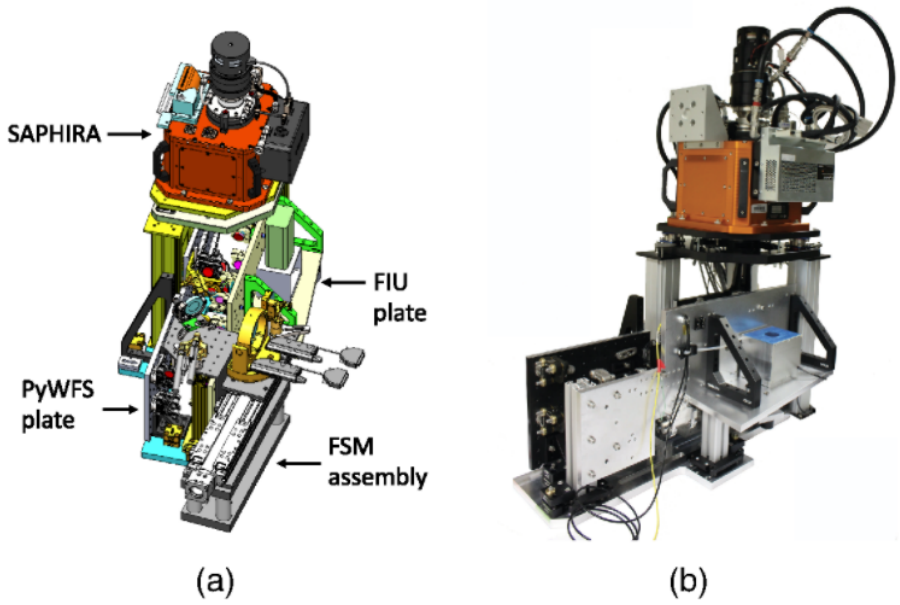

Figure 2.4: (a) CAD drawing of KPIC, including the FSM (field steering mirror) assembly; PWFS and FIU plates; and PWFS (SAPHIRA) camera. (b) KPIC assembled in the laboratory: PWFS plate (black, background); FIU plate (silver, foreground); and SAPHIRA camera (orange casing)(credit: Bond et al [13]).

Figure 2.4 shows a CAD drawing of the PWFS and FIU mechanical design (2.4(a)) and a photograph of the instrument assembled in the laboratory at the Hilo Institute for Astronomy during March 2018 (2.4(b)). The black optical plate in Figure 2.4(b) is the PWFS plate, on which the optics for the PWFS are mounted. Above the two plates is the PWFS camera - the SAPHIRA detector housed in a cryogenic dewar to keep it cooled to the required 85 K. In the CAD drawing the FSM assembly is also shown: a stage and platform on which a set of field steering optics are mounted. These optics are used to pick-off the light from the Keck II AO bench (just before NIRC2) to send to KPIC.

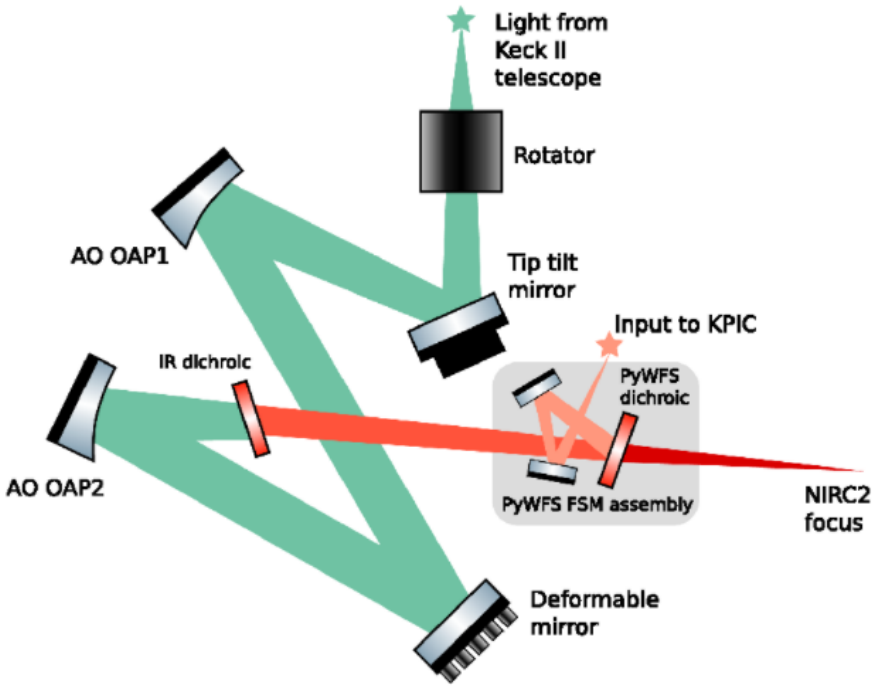

Figure 2.5: Illustration of the Keck II AO bench optics and the pick off (FSM assembly) for the PWFS. (Bond et al [13])

An illustration of the optical layout of the Keck II AO bench is shown in Figure 2.5, up to and including the PWFS FSM assembly (more on my contribution to FSM design in Section 2.2). The visible AO wavefront sensing optics (after reflection from the IR dichroic) are not shown. The KPIC optical layout is presented in the next section. A PWFS consists of a pyramid prism at the focal plane, pupil re-imaging optics and a detector at the pupil plane. For the Keck PWFS the four sided pyramid prism is effectively produced by the use of two rooftop prisms. The two prisms are oriented at right angles to each other with the two vertices almost touching, a concept demonstrated on SCExAO [58, 102, 63]. The advantage of this method is the relative ease in manufacturing a roof prism to the required tolerances, compared to a 4-sided prism. Conventionally PWFSs have utilized a double pyramid to minimize chromatic effects. After the prisms a lens images the four telescope pupils onto a SAPHIRA detector [41].

For the Keck PWFS a minimum sampling of 32 pixels is required to match a future planned upgrade to a MEMS DM with 32 actuators across the pupil. Simulation studies led to the decision to over-sample the wavefront for the Keck PWFS, with 40

pixels across the Keck pupil. The results of further simulations of the Keck PWFS are reported in Section 3.2.1. Figure 2.6 shows an illustration of the Keck PWFS optical design. The input is the beam from the facility AO system, with an f-ratio of 13.66. The following optical relay consists of four off-axis parabolic mirrors (OAPs), providing two pupil planes: one for the PWFS modulator and one for the future higher order MEMS DM (currently populated by a flat mirror). The modulator is a fast steering mirror which moves the PSF around the tip of the pyramid in a certain radius. A field stop restricts the field passed to the PWFS to a diameter of 2″.

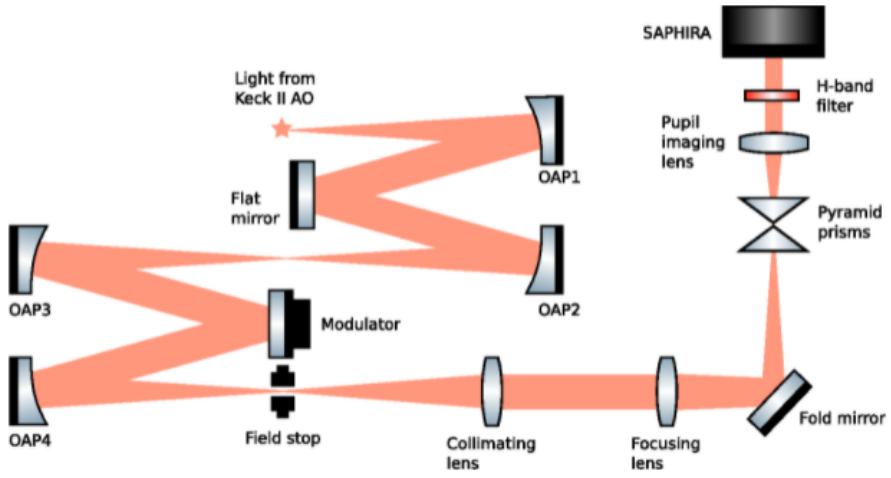

Figure 2.6: Illustration of the layout of the Keck PWFS optics. The system consists of: two OAP relays; a field stop; lenses to provide the correct f-ratio and WFS sampling for the WFS; and two roof-top prisms to act as the four-sided pyramid prism. A filter within the PWFS transmits only H-band light and the SAPHIRA detector is used to image the WFS signal.

2.2 Performed Calculations and Optical Analysis for K2AO PWFS Bench Field Steering Mirrors

The K2 adaptive optic system received its first pyramid wave front sensor (PWFS) combined with a fiber injection unit (FIU) for the Keck Planet Imager and Characterizer (KPIC). These systems are fed using a field steering system providing field steering capability for NGS selection. The field steering mirror system typically con-

sists of a pair of mirrors that gives the observer the ability to move the field over a detector or other instrument without having to move the telescope itself. In this instance, the PWFS system needed to have a steering ability since there is usually an angular separation between the science target and the wavefront sensing target (NGSs in this case). One of my contributions to the success of IR-PWFS at Keck was to optically analyze the system to understand the precise relation between the angle each mirror should be positioned for a given WFS target in the field of view. In the absence of the field distortion, calculations for how the steering mirrors should rotate are simply geometric. However, I found that higher degree calculations of distortion were necessary to satisfy the designed accuracy requirements for the instrument.

This FSM system contains two mirrors and a dichroic allowing simultaneous operation along with a NIRC2 instrument. The dichroic reflects H and J band and passes the longer wavelengths (mainly K, L and M band) to NIRC2. As Figure 2.7 shows, these mirrors are placed right after the NIRSpec fold mirror assembly and before NIRC2. M1 is the first mirror which folds the beam in an appropriate angle to direct the desired field's chief ray to the optical axis of M3. The M3 tilt compensates the M1 tilt in addition to the field angle to pass the desired field beam on the optical axis. M2 is just a static relay and does not have any role in the steering process.

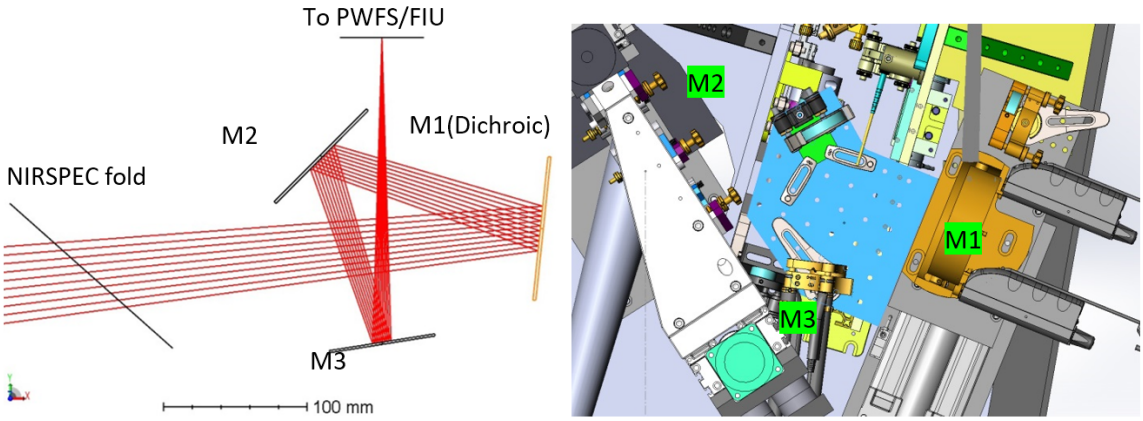

Figure 2.7: Fields Steering Mirrors position on K2AO.

2.2.1 First Approach: Geometric Optics

The simplest approach for calculating field steering mirror motion is to use geometric optics. With this approach, the field itself and each steering mirror is considered to have two orthogonal degrees of freedom. Because of symmetry, unit tilt and tip

motion of each mirror steers the field by the same amount in different orthogonal directions, so the motion of mirrors could be modeled by two linear equations.

The steering range typically depends on the angular separation and M1's diameter. For this system, the maximum safe steering angle is 32 arcseconds from the optical axis to prevent vignetting. Figure 2.8 shows the beam footprint on the M1 surface for the maximum field separation.

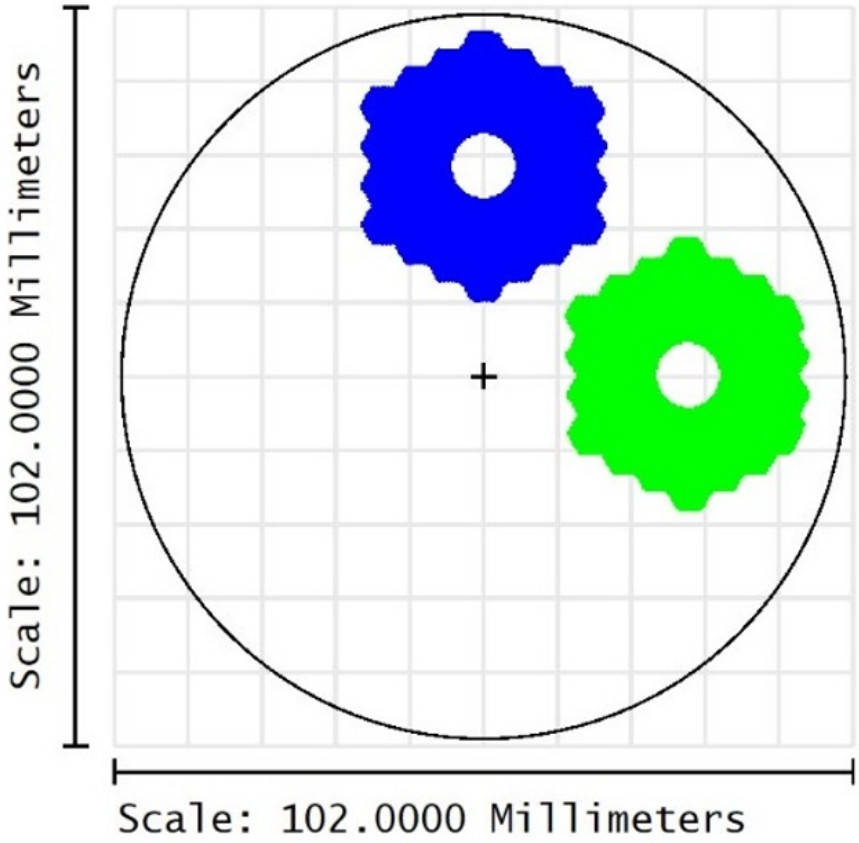

Figure 2.8: Beam profiles on M1 for steering limits.

Figure 2.9 shows the incident perpendicular projection of the chief ray position on M3, for the field range. By a simple fitting, we would have:

$$\frac{\Delta X_{M3}}{\Delta field} = 2582.6\ \frac{mm}{deg}, \frac{\Delta Y_{M3}}{\Delta field} = 2627.3\ \frac{mm}{deg} \tag{2.1}$$

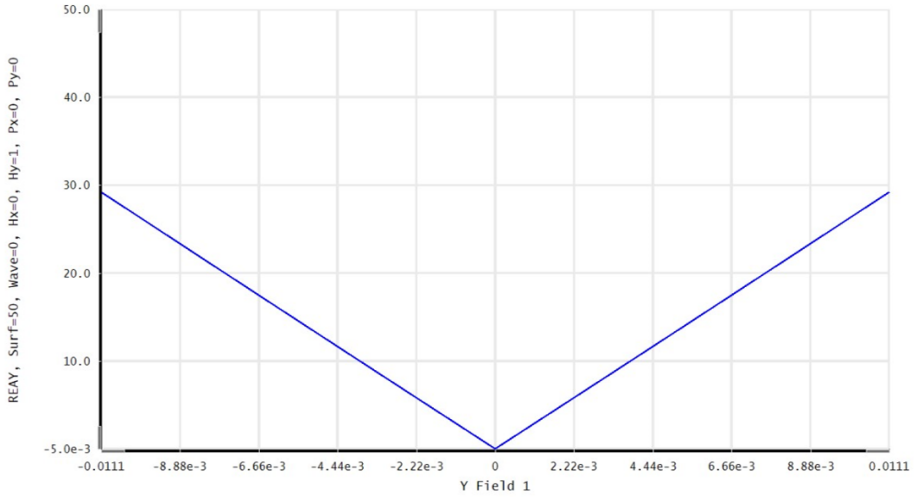

Figure 2.9: Chief ray position on M3 for the field range.

The behavior of the data is >99.9% linear and the y-intercept is negligible. The M1 distance relative to M3 is 295 mm, so the necessary amount of tilt and tip for M1 to eliminate the steered field caused by M3 could be calculated as:

$$M1_{[T/T]} = \frac{\tan^{-1} \frac{\Delta[\frac{X}{Y}]_{M3}}{295}}{2} \tag{2.2}$$

Based on this equation, Figure 2.10 shows the necessary tilt for the M1 mirror over the desired range of the steered field.

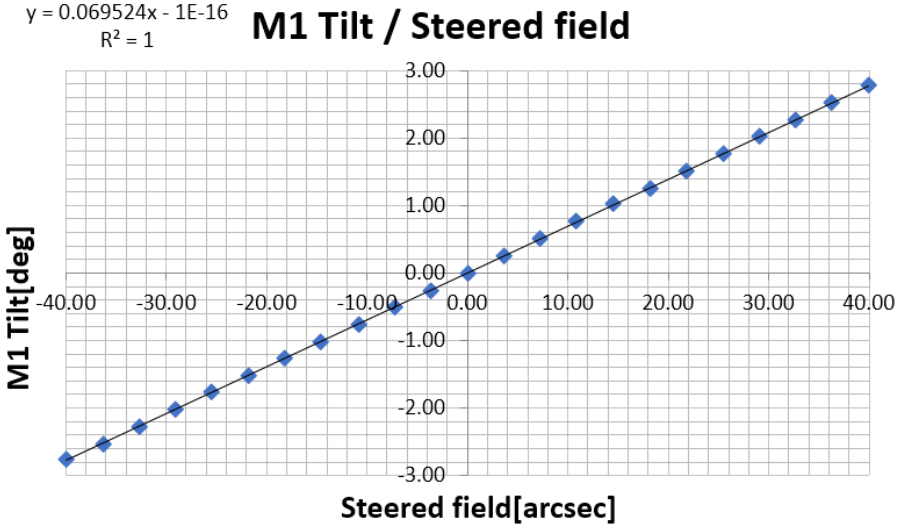

Figure 2.10: M1 tilt.

M3's main function is to eliminate the angle between the desired field's chief ray and the system's optical axis. This angle has two components. One is the tilt that is applied to the beam on the M1 surface and the other is the angle between the chief ray of the desired field and the chief ray of the zero field (main optical axis of the system) as described in Equation 2.3.

$$M3_{[T/T]} = M1_{[T/T]} + \frac{[Chief\ ray\ incident\ angle\ offset]_{M1}}{2} \tag{2.3}$$

Although this system is almost telecentric, there is still a non-negligible amount of field dependency of the incident angle of chief rays. Figure 2.11 shows this dependency.

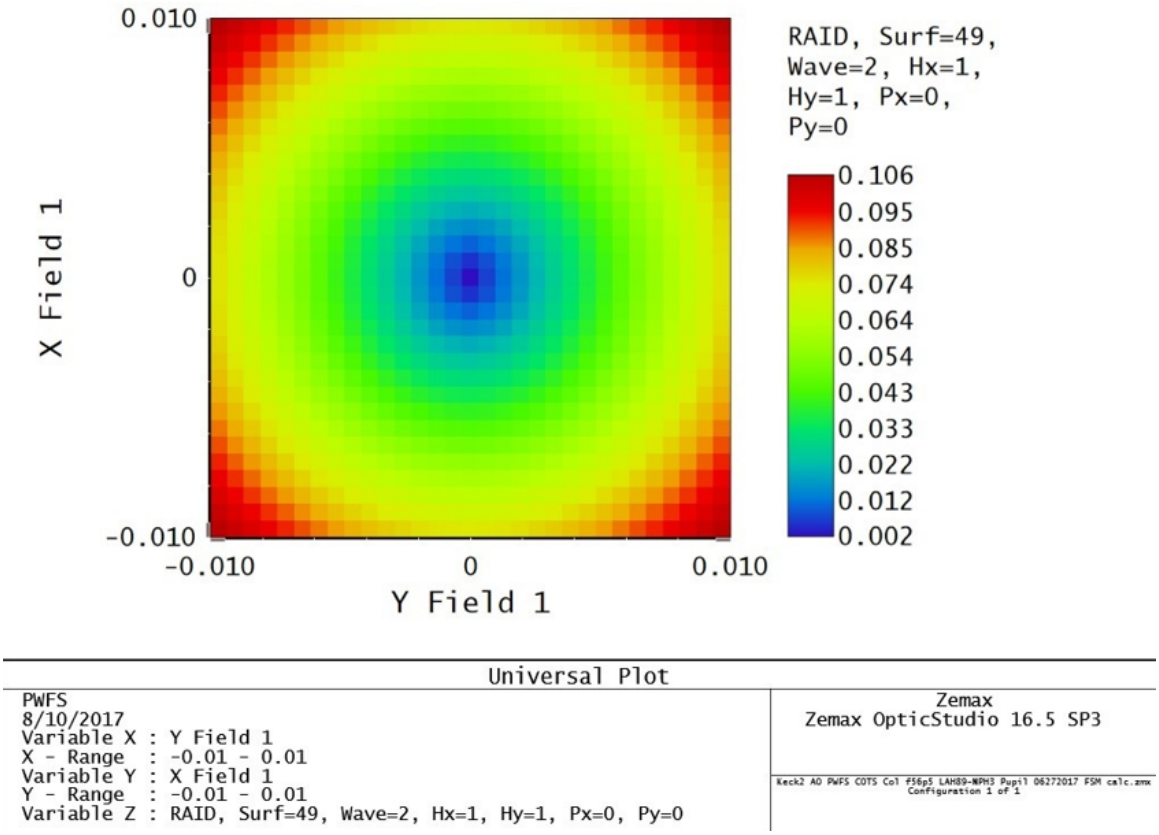

Figure 2.11: Chief ray incident angle offset for the required field range.

The direction of the field dependent chief ray tilt is outward from the center. Considering these two components, the M3 tilt is shown in Figure 2.12.

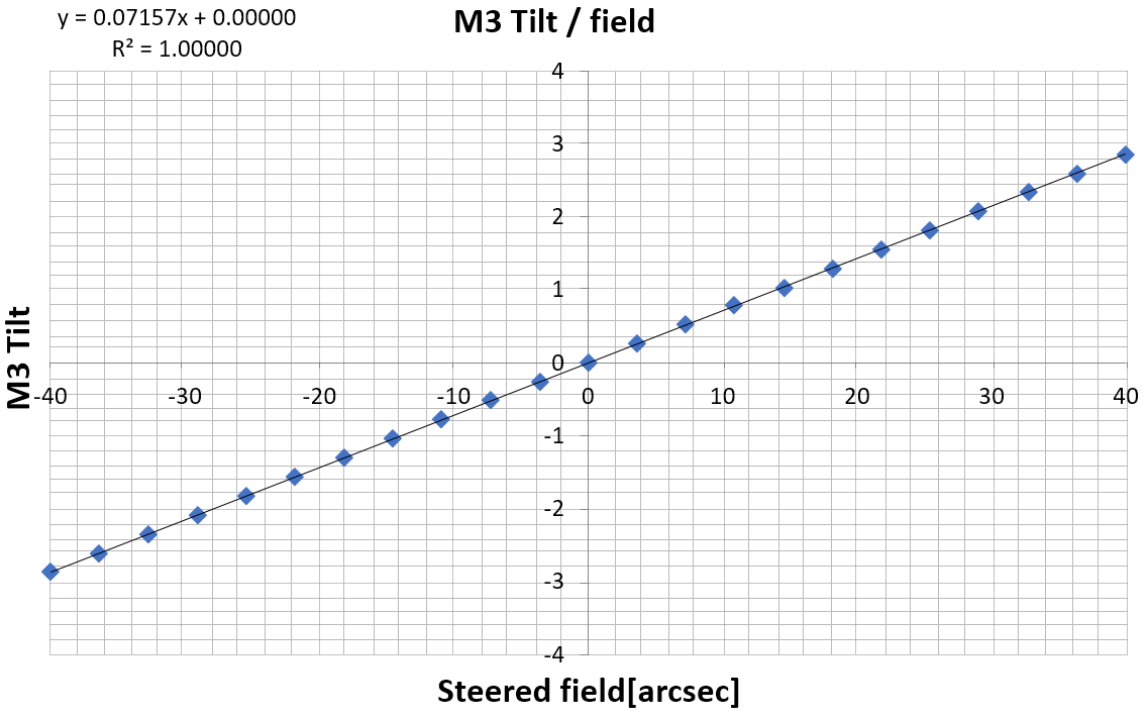

Figure 2.12: M1 tilt.

2.2.2 Verification of the Geometric Approach

Lack of Accuracy in Geometric Approach

The tilt/tip accuracy requirement for field steering mirrors is bound by the field stop size (the maximum acceptable) and actuator accuracy on each mirror (minimum expected). The field stop angular diameter is 2 arcseconds on sky. The first steering mirror uses a Newport 605-4 gimbal mount and two LTA-HS precision motorized actuators. The guaranteed accuracy for each axis in this configuration is $\pm 7\ \mu m$, and the distance from each actuator point of contact to the center of the gimbal is 50 mm. So, T/T accuracy for this mirror would be 30.9 arcseconds on each axis. The second steering mirror uses a Newport U100-G gimbal mount and two TRB-12CC compact motorized actuators. The guaranteed accuracy for each axis in this configuration is $\pm 4\ \mu m$, and the distance from each actuator point of contact to the center of the gimbal is 35 mm. So, T/T accuracy for this mirror would be 23.57 arcseconds on each axis.

It is important to note that using these numbers, the maximum guaranteed field angle error caused by actuator accuracy on both field steering mirrors, would be

±0.38 arcseconds on sky, which is less than the radius of the field stop. This demonstrates that the selected actuators' accuracy should support the maximum field error requirement, which is the field stop radius.

I used the Zemax model of K2AO to verify the accuracy of functions calculated in Section 2.2.1. As shown in Figure 2.13, the primary results show that accuracy requirements were not met. Steering the field based only on the geometric calculation will cause displacements greater than allowed by the requirements, especially for large steering angles. My further investigation showed that a non-linear factor, which became greater with increasing steering angle, is expected in the system. This non-linearity makes the geometrical approach unsuitable for this calculation, so we moved to a numerical solution and model fitting.

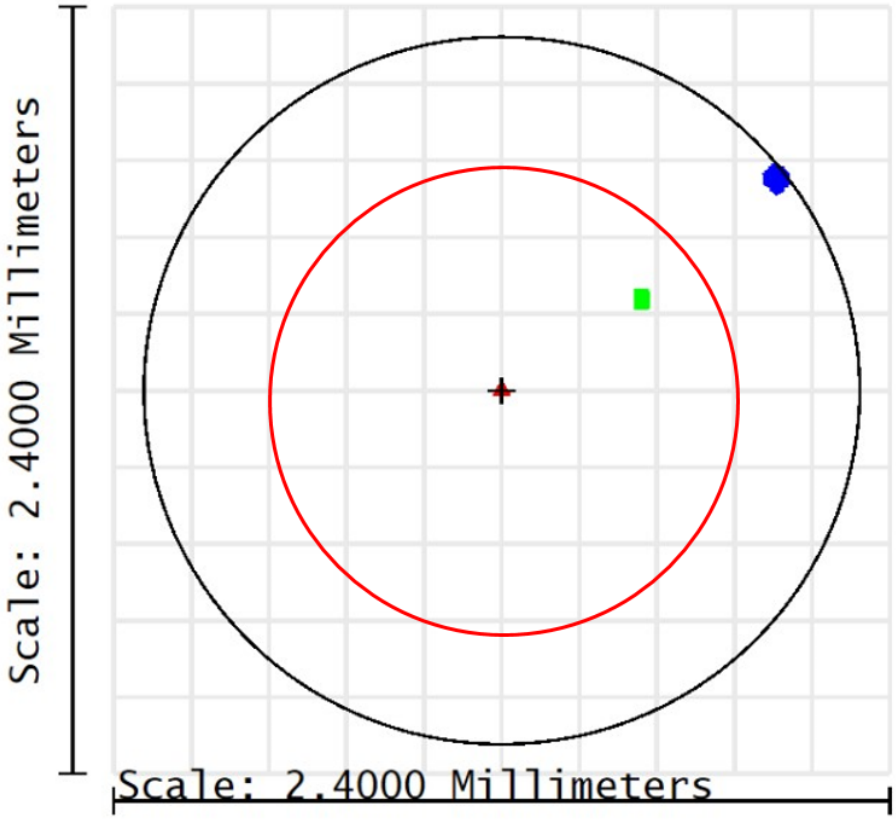

Figure 2.13: Beam profile for steered field on field stop surface. The plate scale is 0.725 mm/arc second. Field angle is 0, 1.2 and 2.4 arc seconds for red, green and blue points and the field is already steered based on section 1 equations (geometric approach). It can be seen that the steering error is more than both expected hardware accuracy (±0.38 arcsecond, 0.27 mm on this surface) and requirement accuracy (±1 arcsecond, 0.725 mm on this surface as shown by the red circle).

Second Approach: Numerical Simulation and Model Fitting

In this approach, the optimized tilt and tip are calculated for a grid of field points. The result is four 2-variable data sets which are used for polynomial fitting. The final result is four nonlinear equations for each degree of freedom of each mirror. Although Zemax is a powerful software for optical design and optimization, it is not the best tool for providing grids and fits of data. Fortunately, there is a relatively new feature added to Zemax which enables it to be controlled by Matlab. This powerful option was used for acquiring the data and fitting the model.

In 2016, Matlab interactive extension API was added to the Zemax optical studio software. This feature lets users control a Zemax session and utilize most of the analyzing and optimization tools directly from the Matlab environment. Differing from previous standalone connection modes, the interactive extension mode makes it possible to modify desired parameters, apply analysis and import data using Matlab and monitor results using the Zemax optical studio interface in real time.

For this application, providing a field grid and feeding it to Zemax, gathering data from Zemax, and fitting polynomials was done in the Matlab environment. Design and optimization of steering mirrors' angles was done using Zemax. The merit function is simple for this application. There are two main conditions: the position of the incident beam for both X and Y, and the chief ray incident angle (the angle between chief ray and surface normal) on the field stop surface. All of these parameters are targeted to be zero as a steered field beam should be identical to non-steered zero fields.

A 21×21 field grid over ± 36 arcseconds domain was used as the input. The output is 4 matrices with the same size as the output for the tilt and tip of both mirrors. Figure 2.14 shows a sample set of data fitted by a linear equation along with the residual plot. The results for such a fit are shown in Table 2.1.

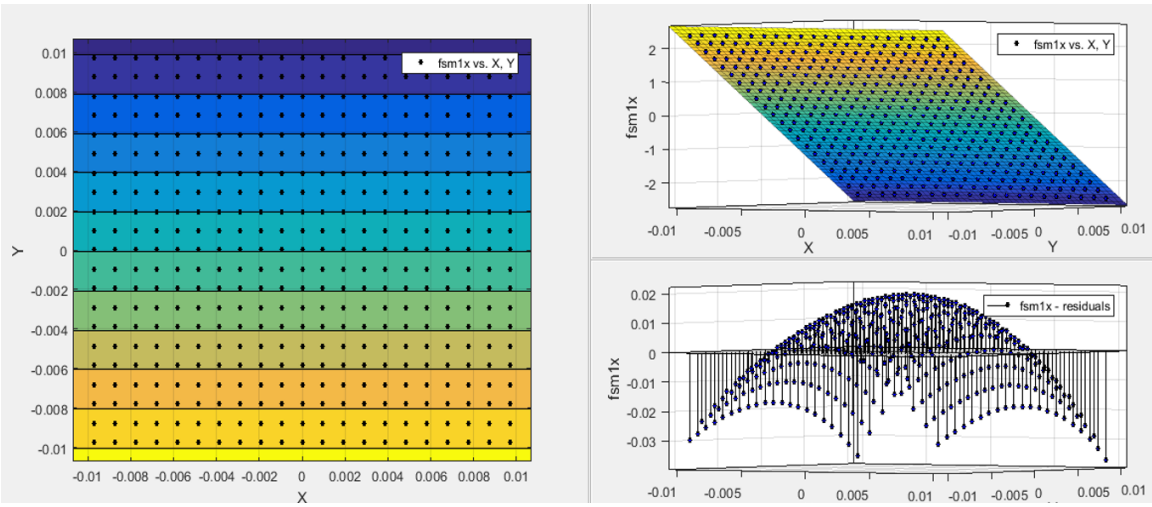

Figure 2.14: Sample set of tilt data fitted by a linear polynomial for the first steering mirror. The diagram in the bottom right is the fit residual, which shows nonlinearities. It is good to note the scale of the z axis, which is almost one order of magnitude larger than the expected accuracy of the tilt and tip actuator, which shows that linear equations are not suitable for this model.

The fit residual (especially at the edge of the field) is greater than the actuating accuracy. There are also situations where the accumulated error is greater than the accuracy requirement. These results explain why the geometric approach failed to model mirror motions.

	Maximum deviation from linearity [deg]	Adjustment accuracy [deg]	Equivalent field error [asec]
Tilt FSM 1	0.0369	0.0085	0.89
Tip FSM 1	0.0245	0.0085	0.58
Tilt FSM 2	0.0405	0.0063	0.41
Tip FSM 2	0.0293	0.0063	0.29
Maximum possible field error	-	-	1.43

Table 2.1: Accuracy of the steering for linear model compared to adjustment accuracy (expected accuracy) and the requirement accuracy.

To make a more accurate model, it is possible to add higher degree terms to the polynomial fit. This should be done until the maximum deviation from the

polynomial becomes less than the adjustment accuracy. Any higher degree terms with magnitudes significantly less than the adjustment accuracy could be neglected to simplify the equations. So, the simplest polynomials which satisfy accuracy conditions are presented in Table 2.2. Equations are described as:

$$f(x,y) = P_0 + P_x \cdot x + P_y \cdot y + P_{xy} \cdot xy + P_{x^2} \cdot x^2 + P_{y^2} \cdot y^2 \tag{2.4}$$

where x and y are the desired field and $f(x,y)$ is the respective tilt/tip of each mirror in the same units.

$f(x,y)$	P_0	P_x	P_y	P_{xy}	P_{x^2}	P_{y^2}	D_1 $[deg]$	D_2 $[deg]$
Tilt FSM 1	0	0	-251	0	-392.5	-162	0.0037	0.0085
Tip FSM 1	0	256.7	0	-235.6	0	0	0.0022	0.0085
Tilt FSM 2	-1.1e-3	0	247.3	0	450.4	166.7	0.0035	0.0063
Tip FSM 2	0	-250.4	0	287.2	0	0	0.0022	0.0063
Maximum field steering error caused by model [arcsec]								±0.12
Maximum field steering error caused by actuators accuracy [arcsec]								±0.38

Table 2.2: Polynomial model for tilt and tip motion of each mirror in addition to compared field steering error budget for the model and actuating accuracy. D_1 and D_2 are "maximum deviation from polynomial" and "adjustment accuracy", respectively.

2.2.3 Results and Verification

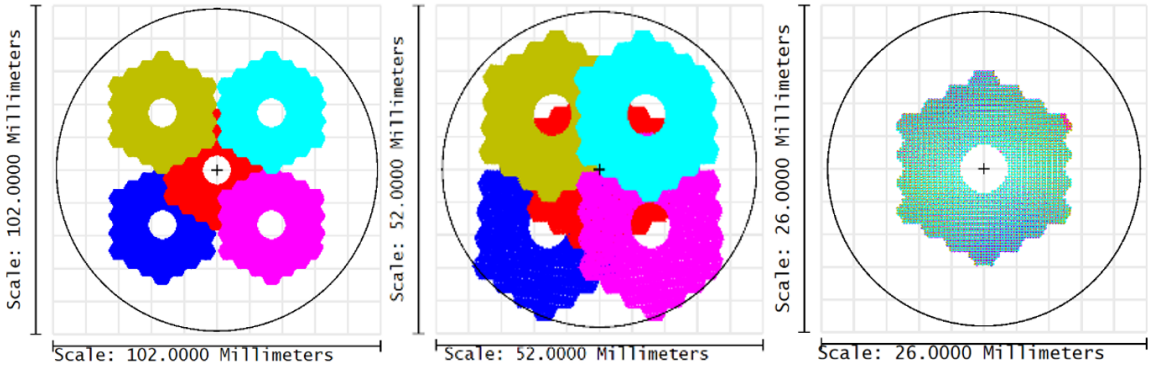

Figure 2.15: From left to right: Beam profile on FSM mirror 1, the static relay mirror and FSM mirror 2 for various fields with 24 arc seconds angular distance from the zero field. It was shown that that beam profile is placed on the boundary of the static relay mirror even though there is still more room on FSM mirror 1.

In typical FSM systems, the diameter of the first mirror defines the steering range. However, while performing simulations in Zemax, it was noticed that in this system the static relay mirror (see Figure 2.16) is the restricting factor. Figure 2.15 shows the beam profile on FSM mirror 1 and 2 and the static relay mirror for various fields with 24 arcseconds angular distance from the zero field on each axis (33 arcseconds from the center). The middle diagram shows that the surface of the 2" mirror is beginning to vignette even though there is still more room on the first mirror. So, in this system the static mirror specifies the steering radius which is ± 33 arcseconds.

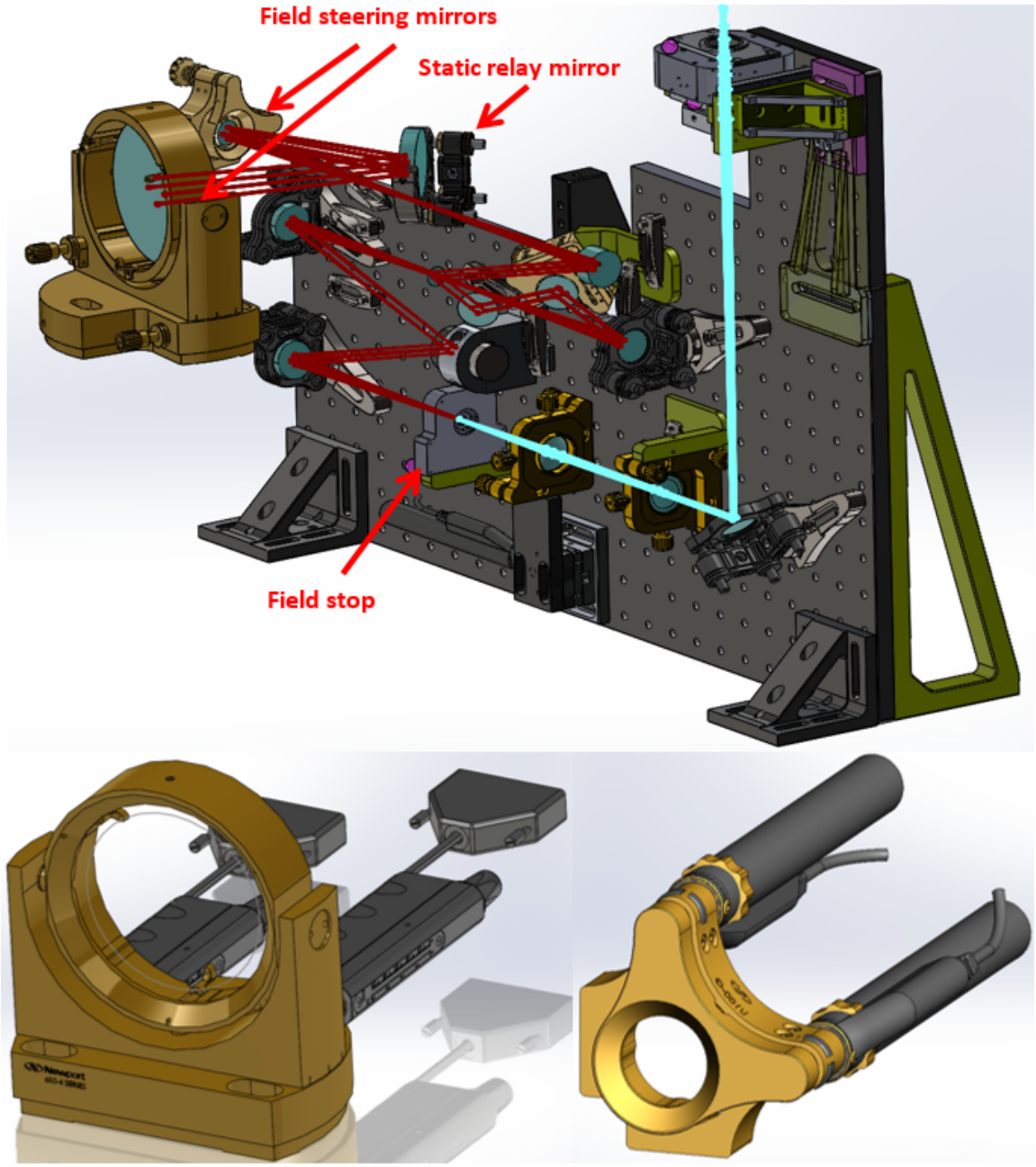

Figure 2.16: Top: A layout of the PWFS plate. Note there is one stationary mirror between two FSMs which acts as a stationary relay. Bottom-Left: Newport 605-4 gimbal mount and LTA-HS precision motorized actuators adjust the position of the first steering mirror, Bottom-Right: Newport U100-G gimbal mount and TRB-12CC compact motorized actuators adjust the position of the second steering mirror.

Finally, the performance of the polynomial model was verified by steering the field in the Zemax model. Figure 2.17 shows the field stops for three steered fields based

on the polynomial model. By repeating this simulation for many randomly selected fields and the field boundaries, I successfully verified that the steered field is always within accuracy requirements.

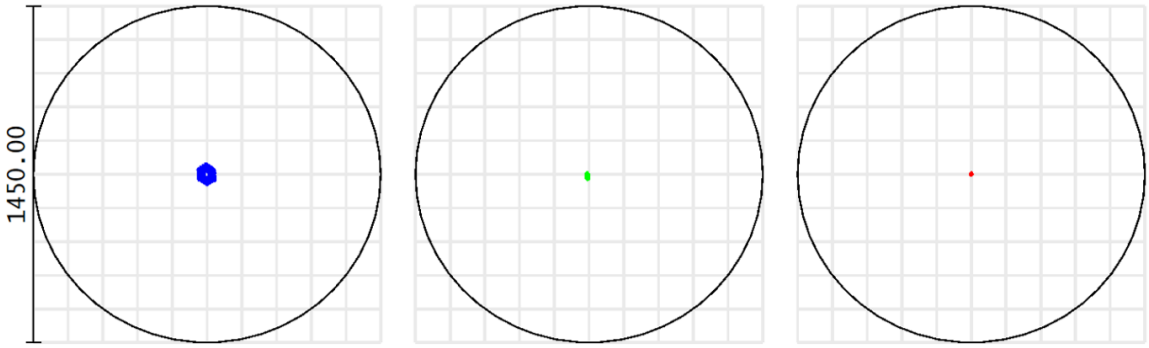

Figure 2.17: Field stops for three steered fields based on the polynomial model. The black circle has the angular diameter equivalent to a 2 arcseconds field. The blue, green and red are steered fields for 24, 12 and 0 fields, respectively.

2.3 Designed Alignment Plan and Assisting the Replacement Procedure of the K2AO NIRSpec Fold Mirror

As very limited space remained on the K2AO bench for installing PWFS and FIU plates, it was necessary to replace the old and large fold mirror assembly with a smaller one to provide more space for the new IR-PWFS and KPIC FIU benches. This replacement process required a precise alignment plan to ensure that the new mirror was oriented accurately and in the same place as the old one. It was also essential to ensure that the mirror assembly, motors, and encoders were working properly. In summary, the tasks I collaborated on were:

- Assembled new NIRSpec fold mirror assembly and tested its motor and encoders.
- Designed an alignment procedure and set up alignment optics.
- Removed old fold mirror assembly.
- Installed new fold mirror assembly.

- Verified cable connections, motor, and encoder performance.
- Performed alignment verification.

The old stage that folded AO light to NIRSpec was the old Interferometer Science Fold Mirror (ISM). This device used a 250 mm linear stage to translate an 8-inch diameter flat mirror. The light for NIRSpec does not require such a large mirror so the entire stage assembly was replaced with a smaller one to make room for PWFS/NIRSpec FIU. The newer stage uses a 150mm linear stage to translate a 6-inch diameter flat mirror. Figure 2.18 shows the Solidworks model of the new NIRSpec fold assembly and its position relative to the other elements on the K2AO bench.

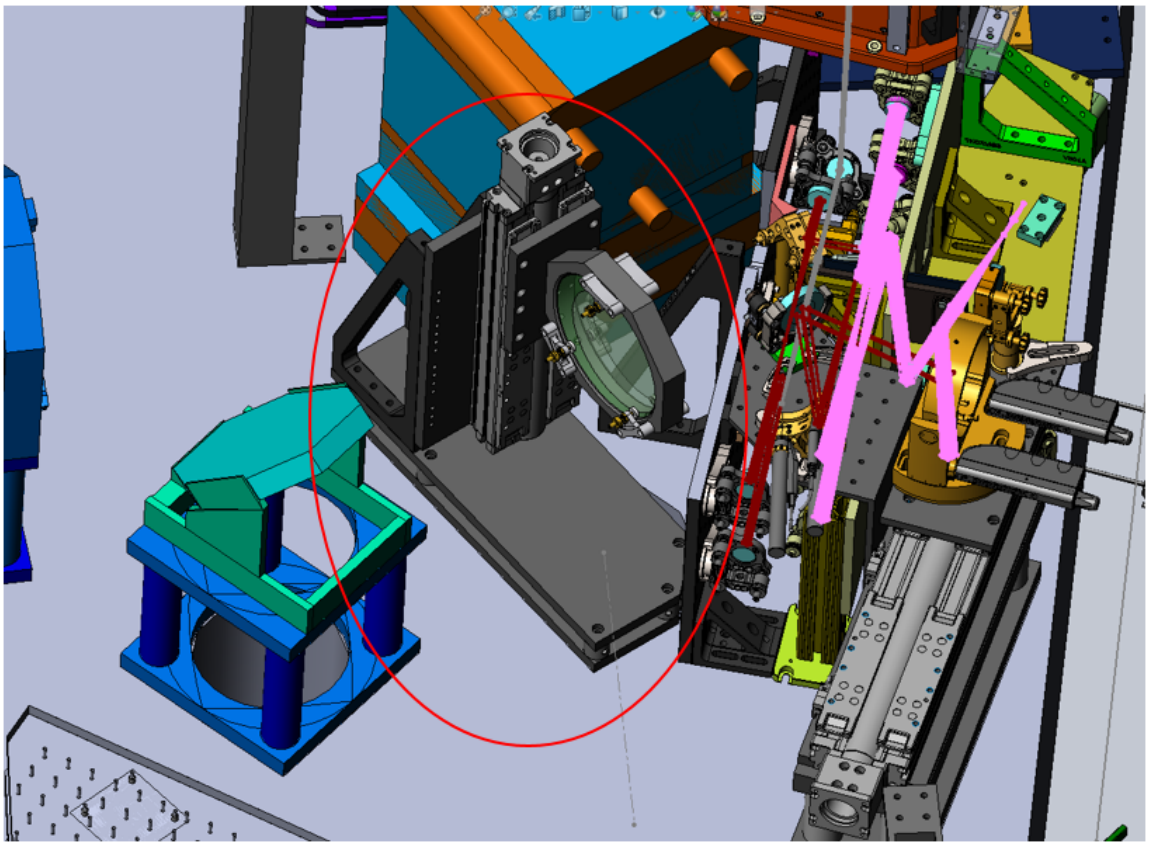

Figure 2.18: K2AO PWFS/FIU and the relative position of the new fold mirror stage.

The new stage was designed to provide a fold mirror for NIRSpec in as little space as possible. NIRSpec has a relatively small FoV, but the new 6-inch fold can accommodate a full 60 arcseconds diameter FoV. The 150mm linear stage is enough to

fully remove the fold mirror without vignetting any light going to NIRC2. Figure 2.19 shows the new stage assembly, also its relative position to the incoming AO beam in the "open" position from the top and front view, considering rays for the full 60 arcseconds FoV.

The 6-inch mirror for the new stage is held in the mount radially by two spring-loaded pushers that push the mirror against a support rod. Spring-loaded pushers are used on the back surface of the mirror to push it against 100 TPI adjusters on the reflective side of the mirror. This allows for fine tip/tilt adjustment of the mirror. The new stage re-uses the ISM cabling and motor. This made the transition to the new stage fairly easy from an operational standpoint.

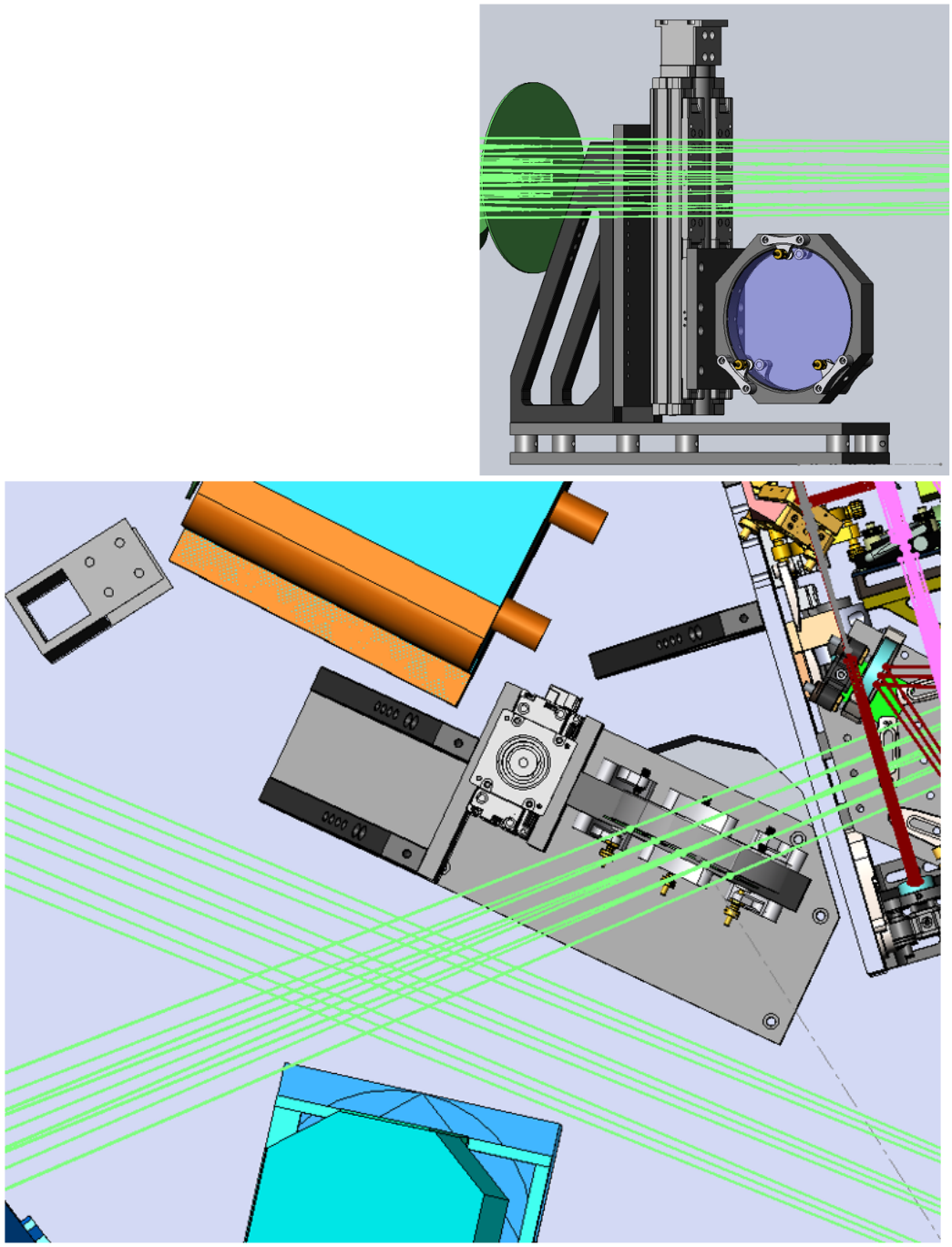

Figure 2.19: Top-left: The new NIRSpec fold stage assembly. Top-right: The front view of the stage in the "open" position and the relative position of the AO beam. Bottom: Same as the top-right but from the top view.

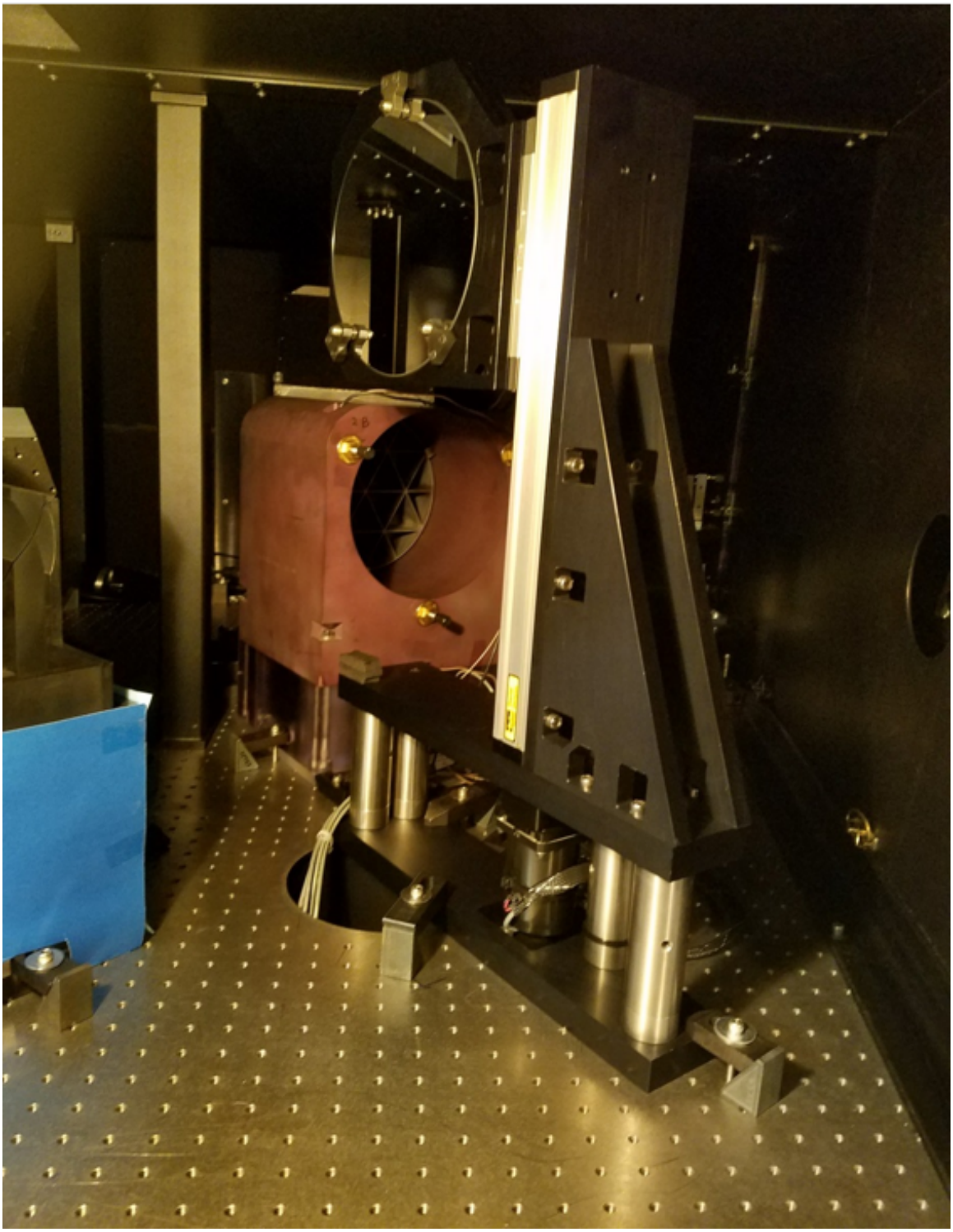

Figure 2.20: ISM assembly needs to be removed before installation of the new stage.

Removal of the ISM assembly (Figure 2.20) was straightforward. It was easily

accessible through the front of the AO bench as shown in Figure 2.19. However, several steps needed to be taken to ensure the new stage can be properly aligned. The difficult part about monitoring the alignment quality was that at the time, there was no instrument available at the focus of the AO system as NIRSpec was not available when the stages were swapped. I designed two different alignment plans based on available devices to perform the replacement procedure.

This plan was based on using two lasers in two non-parallel planes, reflecting from one point on the surface of the mirror. This provided three points of reference which covered all degrees of freedom for adjusting position and tilt. Figure 2.21 shows a schematic of this setup. Reference points R3 is sensitive to mirror translation along the Z direction (perpendicular to the mirror surface) and R2, R3 are sensitive to both translation and tilt/tip. In addition to the three reference points, we also used the focal point of the NIRSpec re-imaging plate and the fiber source to verify the alignment quality.

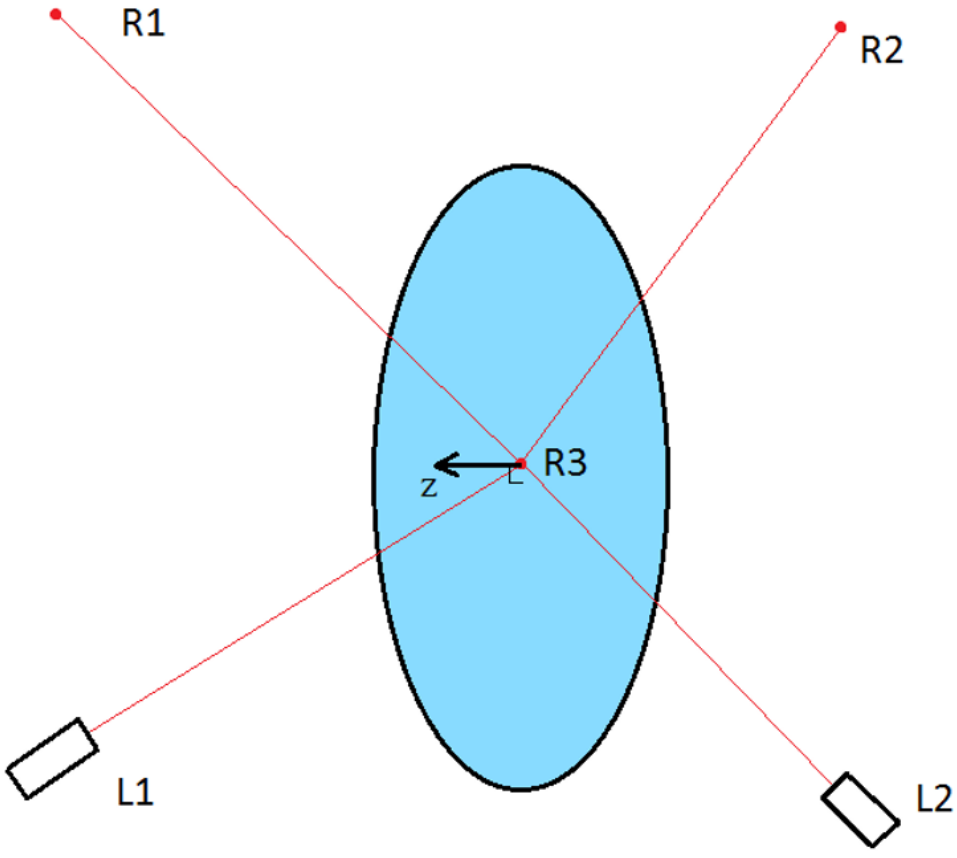

Figure 2.21: The schematics of the alignment setup for plan B.

Before starting the alignment procedure or moving the old mirror, it was necessary to set up and adjust lasers and reference points (see Figure 2.22). We used two sturdy pedestal pillar posts and kinematic mounts for setting up lasers on the K2AO bench. We note that:

- Sensitivity for translation along the Z axis was increased by increasing the incident angle of the lasers.
- Sensitivity to the tilt and tip was increased by increasing R3-R1 and R2-R1 distances and keeping the angle between the two planes containing lasers as perpendicular as possible.

We tried to separate the first two points as much as the spacing on the bench allowed. Also, we installed apertures on the output of laser beams to reduce the diameter of the beam from 5 mm to 1 mm to increase the measurement precision.

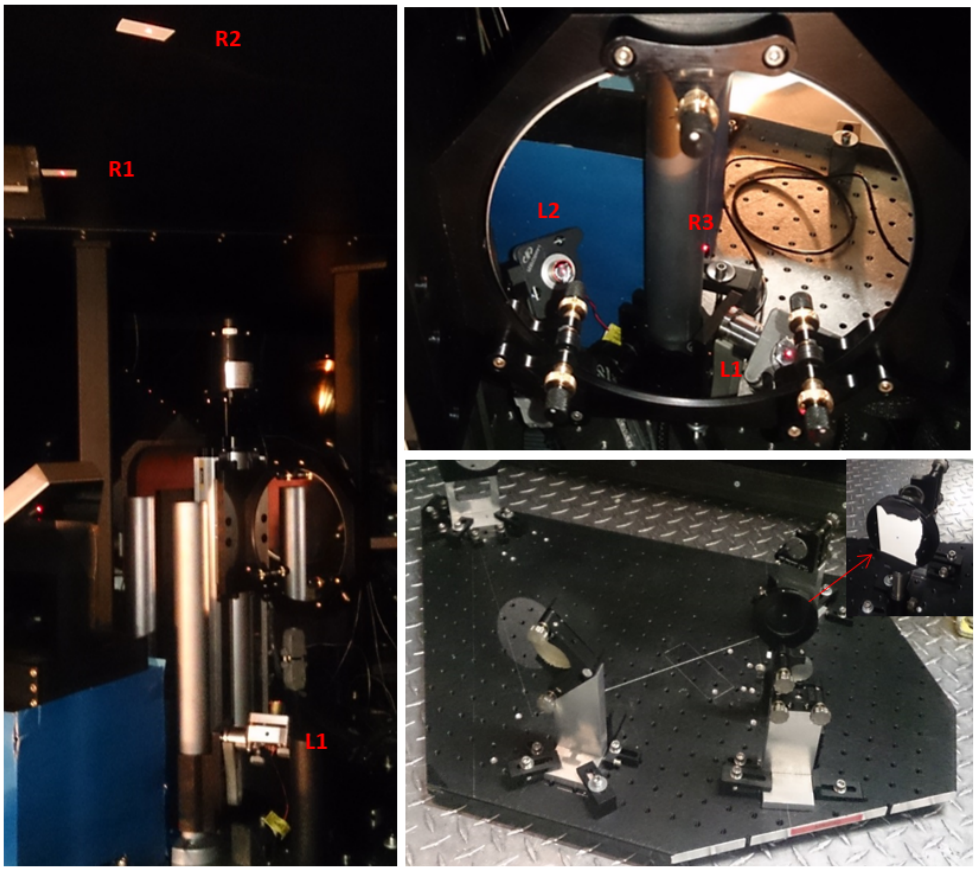

Figure 2.22: Left: A view of new fold mirror assembly, one of the lasers and reference points. Right-Top: Reflected image of lasers and R3 point in the new fold mirror. Right-Bottom: NIRSpec re-imaging plate and the focal plane screen.

2.3.1 Implementation of the Alignment Plan on K2AO

On 16th August 2017 the NIRSpec fold mirror assembly was successfully replaced with the new stage based on Plan B. No significant mishap or misalignment issues occurred during or after the process. This process was performed by Scott Lilley and myself.

Figure 2.23: During the replacement procedure, the author carefully crawling in the confined space of the Keck 2 AO bench positioned on the Nasmyth focus of the telescope, preparing alignment setup ready to remove ISM.

2.4 Design and Fabrication of a New, Very High-Order, SHWFS

Shack-Hartmann Wavefront Sensors (SHWFSs) are the oldest and most frequently used WFSs at astronomical observatories. SHWFSs were originally developed to address a problem that was introduced by the US air force in the late 1960s to improve the images taken from satellites orbiting the Earth. Aden Mienel [73] came up with the idea of enhancing satellite images by limiting the exposure time in a

way that wavefront error caused by the atmospheric turbulence would not exceed $\lambda/10$. This is similar to taking snapshots rather than long exposure times in order to prevent the accumulation of the blurring effect of the atmosphere. He also used measurements of the Optical Transfer Function (OTF) of the atmosphere at the same time of the exposure to use it in post-processing in order to improve the sharpness of acquired images. As an astronomer, he was familiar with the standard Hartmann test, which he used to capture a snapshot of atmospheric aberration. At this point, several other scientists including Ronald Shack, joined the project. The experimental setup that the team was working on finally evolved to the first Shack-Hartmann sensor. The term "Shack-Hartmann" was first coined in 1984 by Ray Wilson at the Optical Sciences Center, University of Arizona [73].

The SHWFS is the most common type of wavefront sensor used in AO systems. In addition to their role in AO systems, SHWFSs can also be used to measure the optical quality of a system in a way similar to that of interferometers [35]. Physical dimensions, sensitivity to vibration, and broader dynamic range are a few of the reasons why SHWFSs might be chosen over interferometric measurements for some applications.

The TMT has contracted with Cilas to build the DMs for NFIRAOS. As part of that work, Cilas provided a prototype DM for testing. There are 616 actuators in the prototype DM (28 actuators across the diameter) while the NFIRAOS DMs will have 60 and 75 actuators across their diameters on a square grid [43]. A sampling resolution of at least 4 is sufficient to study high frequency artifacts between the actuators. Figure 2.24 shows the difference in spatial resolving power between HASO-128, the highest resolution WFS commercially available at NRC's disposal, and SSH-WFS measurements. This would translate to a SHWFS with 252 for DM0 and 300 for DM 11 sub-apertures/lenslets. Such a SHWFS is not available commercially, which motivated the in-house design of our Super SHWFS (SSH-WFS). In addition to the unprecedented resolution of this sensor, we considered cost as an important design factor, resulting in the fabrication cost of the final device to be less than 30k USD. This device is also able to record the wavefront at 50 frames per second at full resolution and up to 4 kHz for cropped regions of interest, making it possible to study the dynamics of the DM actuators. I also designed and performed verification tests to ensure that the SSH-WFS performance met its requirements.

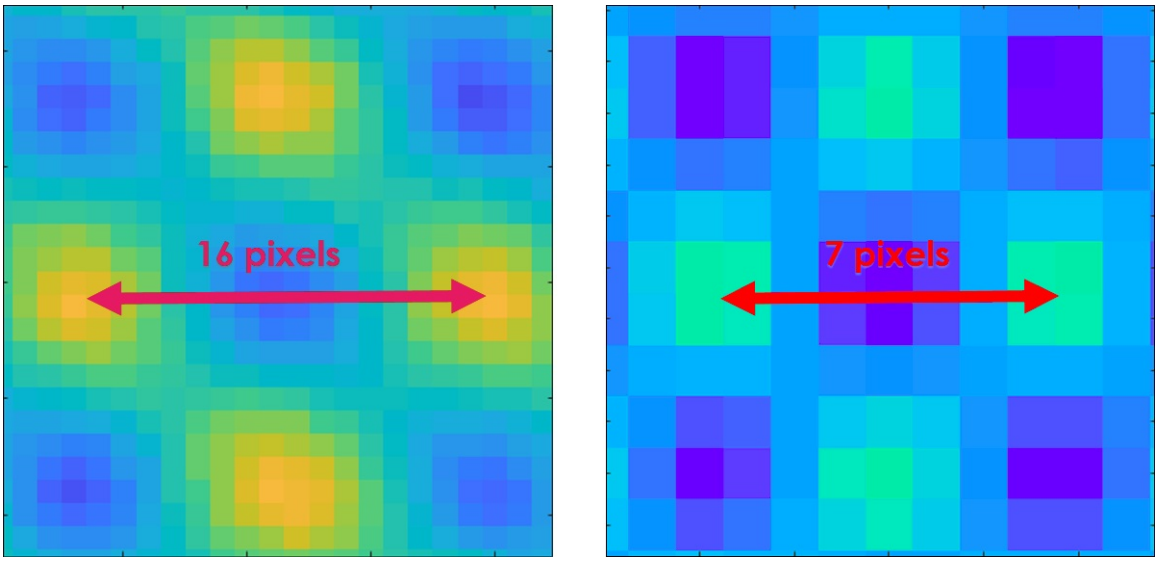

Figure 2.24: Small crop of simultaneous WFS measurements of a waffle pattern on the Cilas prototype DM with HASO-128 on the right, and SSH-WFS on the left panel. Note the difference in resolving power between the two measurements. The red double arrow line indicates the distance equal to two actuator pitches on the DM surface.

In this section, we present the design considerations and fabrication of the SSH-WFS device using low-cost solutions and commercial off-the-shelf components. We also present the opto-mechanical design as well as the results of differential tests and surface measurements down to 5 nm RMS error with this sensor.

2.4.1 Design Outline

Figure 2.25 shows a schematic of the optical design of this device. This system consists of:

- The detector/imager
- The lenslet array
- The optical relay/imaging lens
- The field lens

Below is more information about the design and function of each main component.

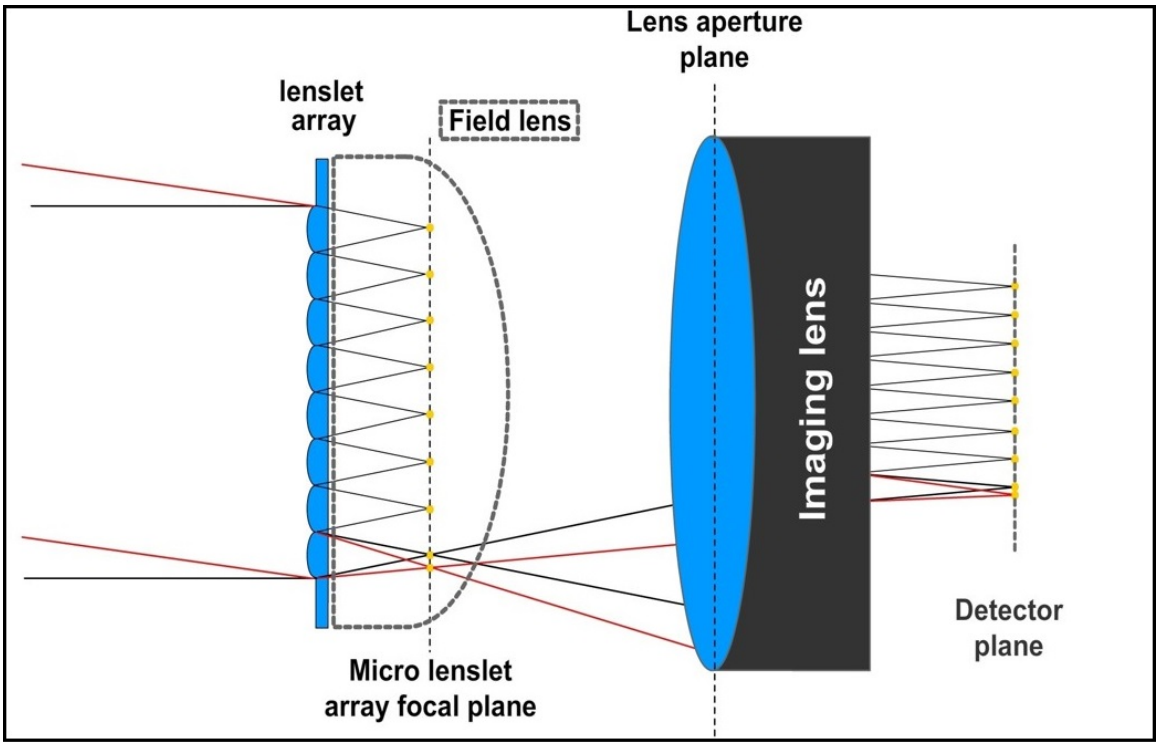

Figure 2.25: The schematic of the design. The system consists of (from left two right): the lenslet array, field lens, imager lens which provides 0.69 magnification, and the detector.

The Super SHWFS incorporated the Andor Zyla 4.2 sCMOS camera. This camera provides 2048x2048 pixels array and full-frame reading frequency of up to 50 frames per second. We use multiple exposures for creating each single wavefront measurement to increase wavefront precision. This makes the high FPS and high quantum efficiency of this detector very desirable as it decreases the total duration of data acquisition. The read noise and linearity of the detector are respectively 0.9 e- and 99.8% which also makes it a suitable option for this application.

For the lenslet we used a SUSS MicroOptics 75 μm pitch, circular sub-aperture lenslet array (see Figure 2.26). Based on the design requirement, each sub-aperture (75 μm) spanned 8 pixels ($8 \times 6.5 = 52$ μm) which means an optical relay with the projection magnification of 0.69 is necessary between the lenslet and the imaging detector. More information about the camera and the lenslet array is presented in Table 2.3.

Figure 2.26: The Zyla 4.2 camera and the schematic of the used lenslet array.

Table 2.3: Specification of detector and lenslet array for SSHWFS.

Detector specification		Lenslet array specification	
Active pixels	2048 × 2048	Dimension	23.1 × 23.1
Sensor size	13.3 × 13.3 mm	Grid type	Square
Pixel size	6.5 um × 13.3 mm	Aperture type	circular
Read noise	0.9 e-	Pitch	75 um
Dark current	0.14 e-/pixel/sec	Focal length	1.18 mm
Max QE	82%	Focal ratio	15.73
Max dynamic range	33000:1	Refraction index	1.458
Max frame rate	53 fps	Thickness	1.2 mm

2.4.2 Role of the Optical Relay

As discussed in the previous section, an optical magnification of 0.69 is required to project a lenslet to 8 pixels of the detector. I considered designing and fabricating this optical relay, but first considered commercially available, high-quality photography lenses to find a potential match for this application. The main criteria for choosing the right imaging relay are:

- Equipped with an aperture larger than the cross section of the diverging beam (passing through the lenslet array), at the distance corresponding to the linear magnification equal to 0.69 times.
- Provide a circular flat focal plane with the radius of 18.8 mm.
- Reasonable low field distortion across the field to maintain linearity of phase measurements, meeting the required wavefront measurement precision of less

than 5 nm across the field.

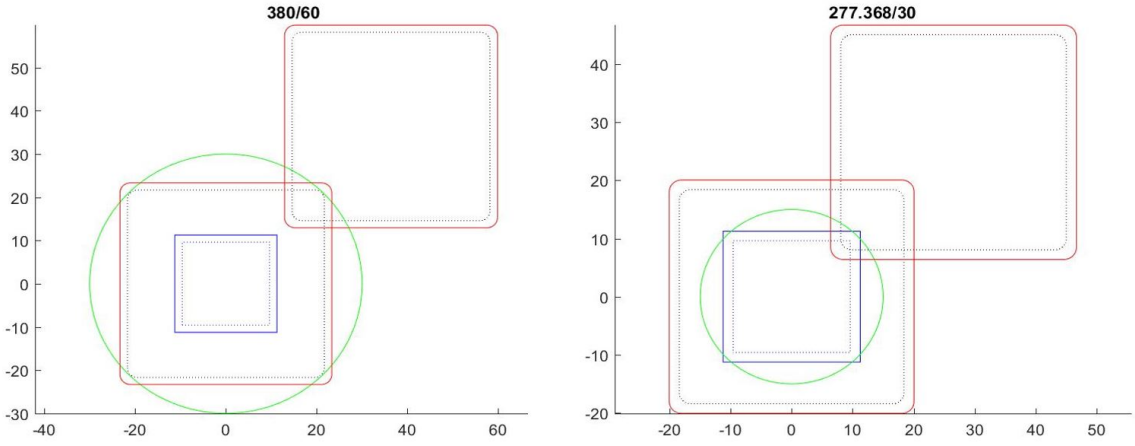

Figure 2.27: Examples of simulation results for the two lenses. The blue rectangle shows the overall size of the lenslet array and the dashed blue square shows the area of interest on the lenslet array (256 sub-apertures wide). The green circle represents the lens aperture and the red squares are the beam footprint on the lens aperture plane in zero and maximum tilt/tipped condition. The blue squares are on the plane of the lenslet array and the rest are on the plane of the lens aperture. Although the chosen lens can fit the zero field beam (central red square) in its aperture (the left panel), none of the lenses in the survey were able to contain the tilt/tipped beam footprint without additional considerations in the design. I resolved this issue by utilizing a field lens (see Section 2.4.3) right after the lenslet array position.

The first option to provide such an optical relay, is to look at commercially available options in order to keep costs as low as possible. I gathered information for 35 commercially available lenses and input their characteristics into a simulation I designed. The simulation takes the projected size of the lenslet array illumination pattern at the distance to the lenses that corresponds to the magnification of 0.69 for the center of the field and compares this with the cross section to the lens input pupil size. The result of this study determined that the Canon EF 24-70mm f/4 lens (see Figure 2.28) is the best choice for this application. The selected lens is able to contain the footprint of the zero-tilted beam passing through the lenslet array and projects it to the detector at the suitable magnification. However, as Figure 2.27 shows, there are still challenges with tilted rays. We address this issue in the next section, by introducing a field lens (see Section 2.4.3) to the design. The combination of using a field lens and off-the-shelf options for the optical relay significantly decreased the overall cost of the project.

To position the Canon lens on the Zyla camera and to install the system on the optical bench, I also designed the lens adaptor and mounting structures. These designs were fabricated at NRC machine shop facilities and installed on the bench. The 3D CAD design of these parts can be seen in Figure 2.28.

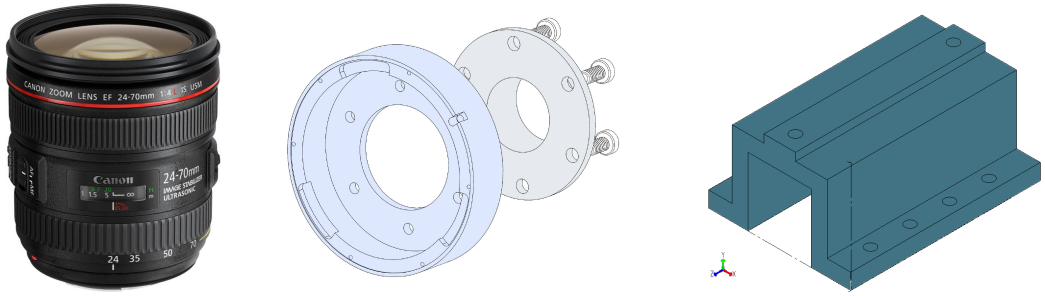

Figure 2.28: Left: The Canon EF 24-70mm f/4 lens chosen for the design of SSH-WFS. Middle: The CAD design of the adaptor, which mounts Canon lens on the Zyla camera. Right: The CAD design of the mount which places the Zyla camera on the optical plate of SSH-WFS.

2.4.3 The Field Lens: Low-Cost Solution for the Field Illumination Challenge

Although the chosen lens pupil is large enough to contain the beam footprint created by the lenslet array, it is unable to catch the incoming beam in the maximum tilt/tipped angle dictated by the requirement. To resolve this issue, I found an inexpensive and efficient solution which is to add a field lens immediately after the lenslet array. This plano-convex lens causes tilted beams to converge into the aperture of the lens without having major effects on the other optical properties of the system. To estimate the specification for the field lens, I provide a Zemax model of the lenslet array and analysed the performance of the system for a range of tilt of the incoming rays (see Figure 2.29).

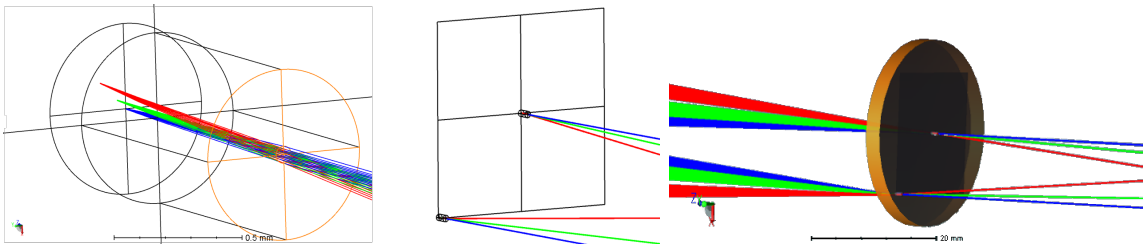

Figure 2.29: Left: The Zemax model I provide for a single lenslet based on the SUSS MicroOptics specifications. Middle: The lenslet array model with a lenslet on the center and one on the farthest lenslet from the center. Right: The Zemax model of the lenslet array in the presence of the Field lens (orange transparent object). The different ray colour represents a range from minimum to the maximum tilt of the incoming beam. Combining maximum tilt with the position of the lenslet right on the corner of the array, represent the worst case illumination scenario that the field lens design should be able to handle.

Figure 2.30 shows the effect of the field lens using the system model designed in the Zemax environment. By incorporating a proper field lens into the design, the aperture of the optical relay could be smaller by a factor of 3.5 and still gather the tilted beam footprint. This dramatically decreases the cost and complexity of the system.

In addition to the optical design, a practical mechanical design was also needed to correctly hold the field lens and the lenslet array in place. The lenslet array is extremely fragile and sensitive to touch, so therefore careful consideration was necessary to design a mechanism to keep it in place. I intentionally chose the field lens to be a plano-convex, so the flat side of the lenslet array could be fixed on the flat side of the field lens. Both optical elements are then fixed by a custom designed mechanical piece to a tilt/tip adjustable mirror mount. Such a design ensures the safety of the featured side of the lenselet array, as well as places both optical elements as close as possible to the pupil conjugation plane which is essential for the correct performance of the SSH-WFS. Figure 2.31 shows the mechanical design of the lenslet array-field lens installation.

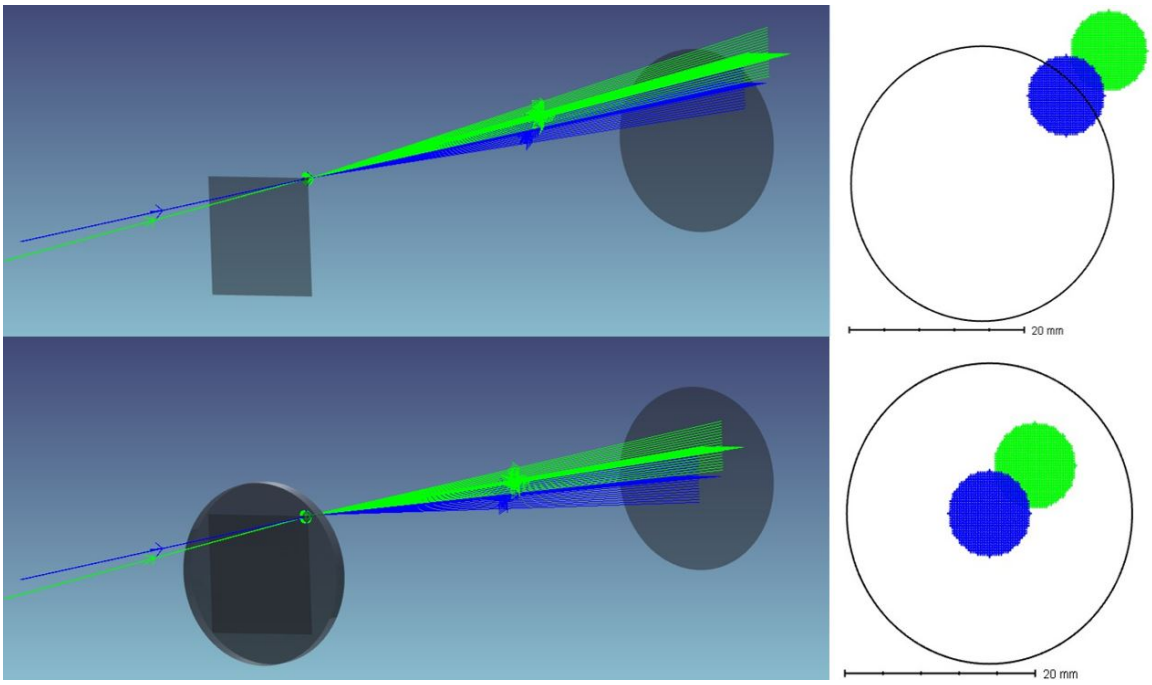

Figure 2.30: Zemax designs showing the effect of the field lens for a sub-aperture on the corner sub-aperture for the zero and maximum tilt/tipped beam (blue and green respectively). The green scenario represents the most tilted and shifted beam considered in the requirements relative to the zero field central beam. The beam profile on the lens aperture plane could be seen on the right. Top: No field lens: the tilted beam would fall outside the lens aperture so the sensor would not be able to sense the wavefront on some sub-pictures in the tilted situation, as well as miss some light in the zero tilt scenario for the edge sub-apertures. Bottom: using a field lens immediately after the lenslet array: even the footprint of the tilted beam hitting the lenslets on the corner of the array would be captured by the imaging lens entrance pupil.

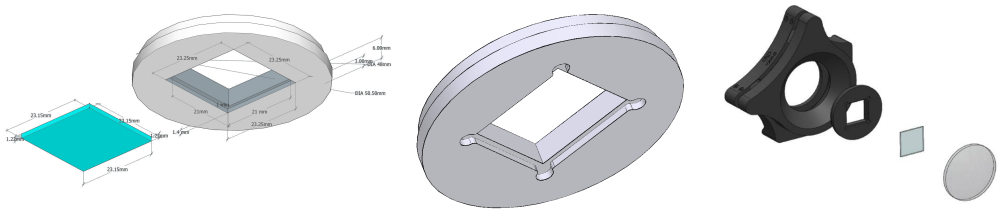

Figure 2.31: Left: The CAD design of the mechanical part that fixes the lenslet to the flat part of the field lens. The blue box represents the mechanical model for the lenslet array. Middle: The final design of the same part before fabrication. Note the round edges on the corner that were added to simplify the machining process. Right: The CAD model of the whole assembly. The flat side of the lenslet array is outward and the field lens inward relative to the page. The custom-made part holds the lenslet array inside the rectangular edge, then presses it to the flat side of the field lens. The whole assembly then screws on the tilt/tip mount which secures the edge of the curved side of the field lens against the flat area of the custom made piece.

2.4.4 Image Reduction and Slope Measurement

I also developed a code package exclusively for the SSH-WFS which reads the WFS detector, applies necessary considerations (i.e applying pupil masks, removes illumination gradient, etc.), and calculates the measured wavefront. A view of what the Zyla detector measures can be seen in Figure 2.32.

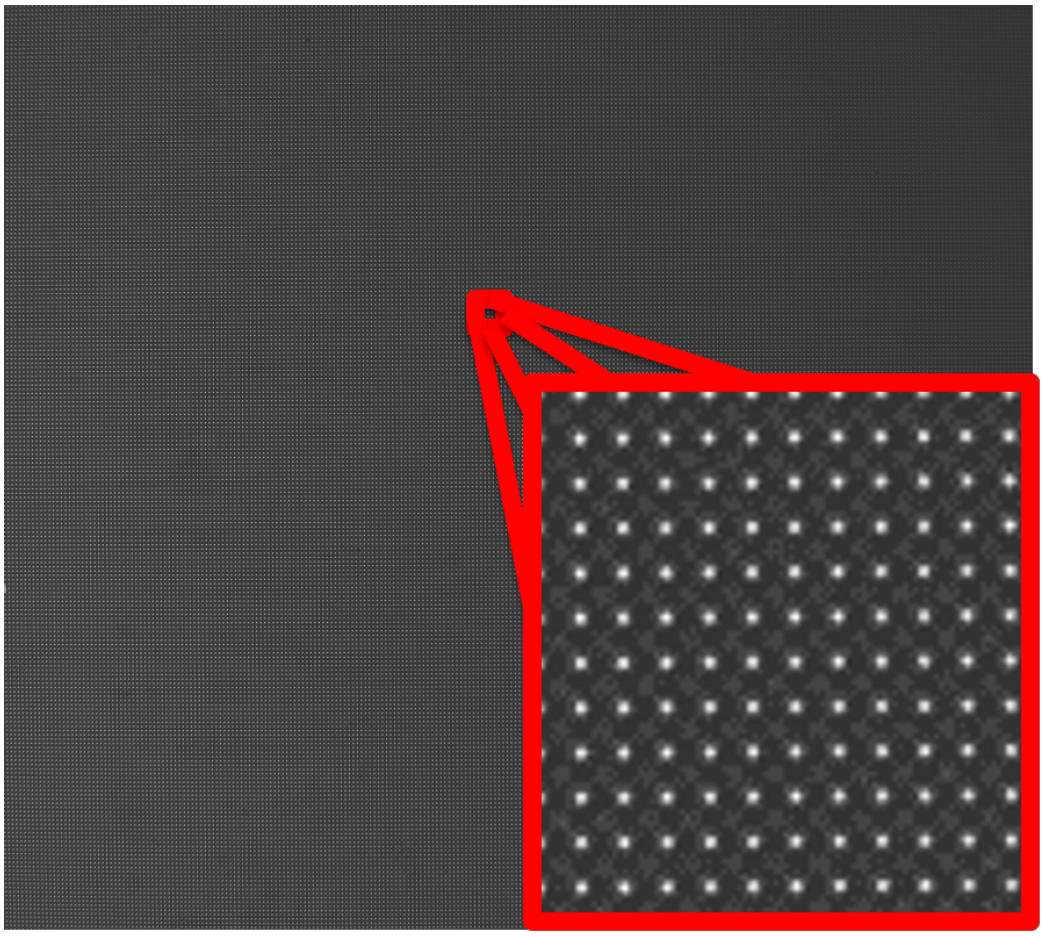

Figure 2.32: A raw image of the Zyla detector while measuring wavefront. The grid of dots is created in the focal plane of the lenslet array. A small region is shown magnified.

The precision of the final wavefront is dependent on the process that determines each sub-aperture spot position. Therefore, I developed an advanced multi-stage image reduction method. I use a zonal, 32x32 segment histogram thresholding algorithm as the phase-one reduction process to roughly find the position of active sub-apertures and recognize the grid connecting them. This method is robust against intensity changes across the field of view, which is one of the main sources of cen-

troiding error in such measurements. In phase two, a more sophisticated histogram thresholding applies specifically to each sub-aperture detected in phase one. The final position is calculated by the intensity-weighted average of validated pixels, which passes through the phase two thresholding process.

In the next step, the precise grid connecting all illuminated sub-apertures is constructed as well as the position of shadowed sub-apertures and the pupil edge are being determined. The code also measures the clocking of the lenslet array (in case it exists) and applies correction to the final positions before the wavefront reconstruction process. Each dataset contains multiple exposures to increase the precision of the spot positions. To reach the 5 nm RMS wavefront residual requirement across the pupil, typically 10-25 exposures per dataset are taken. This means each data acquisition session takes up to 1.2 seconds on the detector in the low-noise mode, which is less than the 5 second requirement of the wavefront measurement.

To measure one set of relative wavefront slopes, the process described above is applied on each exposure of the reference and measurement datasets. The results are two sets of precise measurements of the spot positions for each sub-aperture. A 3-sigma clipping and center-of-gravity algorithm is used to reach the high-precision position of the spot in each sub-aperture. After calculating the spot position map, the effect of potential dust particles is removed by interpolating all the inactive sup-apertures which have more than 3 valid neighbors. Repeating the procedure above provides a set of high-precision measurements of relative movements of spots for all sub-apertures across the field. Using this information and the known physical scale of the system, it is possible to calculate X and Y derivatives of the unknown wavefront relative to the reference measurements and eventually reconstruct the phase wavefront. Figure 2.33 shows the representation of spot displacement between the two measurements (reference and actual measurement) by plotting the difference between the two measurements in addition to the measured slopes.

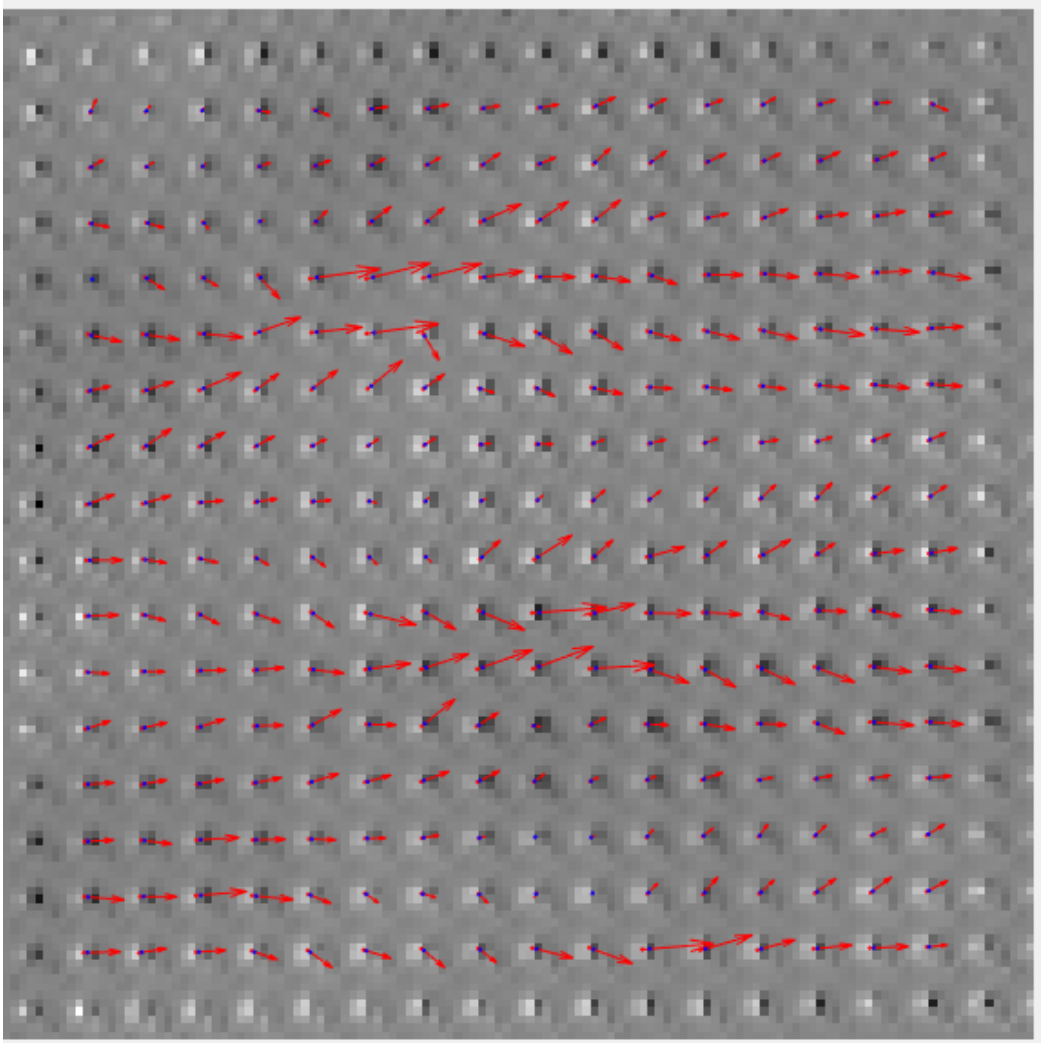

Figure 2.33: This plot shows the difference between a reference and a non-flat measurement for a small region of the detector. The wavefront turbulence is injected into the experiment by placing a transparent plastic CD cover into the pupil conjugation. The measured vectors on the top represent the slope measured on each sub-aperture. The difference between the two spots in the presence of no turbulence should ideally be zero. However, the motion of spots due to the injected wavefront turbulence causes the spots to move. The difference of two spot PSF which are slightly displaced is a sine wave like artifact. Note that more significant difference between the two PSF shaped spots corresponds to a larger slope measurement.

2.4.5 Wavefront Reconstruction

Solutions based on linear decomposition and matrix inversion are the simplest and most common approach for wavefront reconstruction, however they require large

buffer memory for calculations. The number of minimum required memory bytes is usually of the order of [number of sub-apertures]^2 which in this case is 2^{32} bytes. The actual number is even larger than this estimate considering the necessary bytes for storing float precision and other overheads. To make it possible to run our wavefront re-constructor on a typical commercial computer, we used a more complicated approach of iterative wavefront re-construction. I developed an iterative wavefront reconstructor based on the method described by W. Southwell [90]. This method is especially beneficial for reconstructing wavefronts measured from a large number of sub-apertures. This method uses two order of magnitude less memory compared to methods that are based on direct matrix inversion. The iterative core argument is:

$$\phi_{jk}^{(m+1)} = \phi_{jk}^{(m)} + \omega[\overline{\phi}_{jk}^{(m)} + b_{jk}/g_{jk} - \phi_{jk}^{(m)}]$$

where ϕ is the phase, j and k are position indices and m is the iteration counter. Also:

$$b_{jk} = [S_{j,k-1}^{y} - S_{j,k}^{y} + S_{j-1,k}^{x} - S_{j,k}^{x}]h$$

$$\overline{\phi}_{jk} = [\phi_{j+1,k} + \phi_{j-1,k} + \phi_{j,k+1} + \phi_{j,k-1}]/g_{jk}$$

$$\omega = \frac{2}{1 + sin[\pi/(N+1)]}$$

$$g_{jk} = \begin{cases} 2 & j = 1 \vee N; k = 1 \vee N \\ 3 & \begin{cases} j = 1 \vee N; k = 2 \; to \; N-1 \\ k = 1 \vee N; j = 2 \; to \; N-1 \end{cases} \\ 4 & otherwise \end{cases}$$

where h is the grid pitch, N is the number of sub-apertures across the lenslet array, and S_{jk}^{x} is the x-slope in the position j and k. The full description and calculation of the method can be found in Southwell's paper [90].

I also developed a fast Zernike wavefront reconstructor for reconstructing the wavefront from the measured slope matrix. The slope matrix $\begin{bmatrix} X_{slope} \\ Y_{slope} \end{bmatrix}$ can be written as $Zs \times C$, where Zs is the Zernike slope reconstruction matrix and C is the coefficients vector. For creating matrix Zs, the X and Y derivation of the first 30 radial orders are calculated and rearranged to the vector form. Each vector becomes a column in matrix Zs. The result is a matrix of size [number of valid sub-apertures $\times$ 2, number

of reconstructing Zernike modes]. By calculating Zs and measuring $\begin{bmatrix} X_{slope} \\ Y_{slope} \end{bmatrix}$, it is now possible to calculate C using SVD or similar inverse matrix calculation methods. The result, Vector C, contains intensity coefficients for each Zernike mode. The next step is to create matrix *Z*, calculated by the exact same process as matrix *Zs*, except that instead of derivations of Zernike polynomials, it consists of the polynomials themselves. Finally, the reconstructed phase wavefront can be then written as $PWF_{recons.} = Z \times C$.

2.4.6 Verification Tests

Figure 2.34 shows the CAD of the SSH-WFS device as well of the actual device. All parts are installed on a separate optical breadboard to ease moving the device from a bench to another for different experiments and applications.

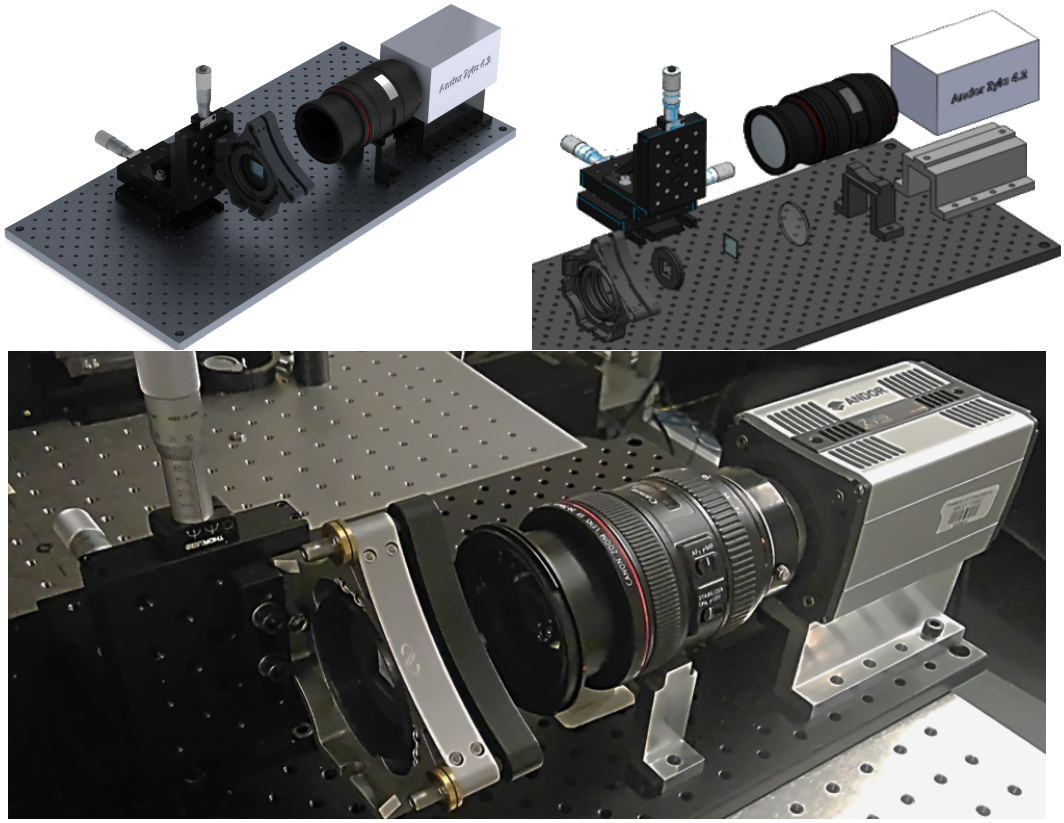

Figure 2.34: Top: The initial CAD design of the device and the exploded view of all components. The CAD design employs precise optical calculations made by the Zemax model of the device. Bottom: Actual fabricated SSH-WFS device.

Before using the SSH-WFS for its ultimate application, it is necessary to characterise and verify its precision and noise propagation behaviour. I designed a series of tests to verify the device performance and confirm that it meets the measurement requirements. The test bench can be seen in Figure 2.35.

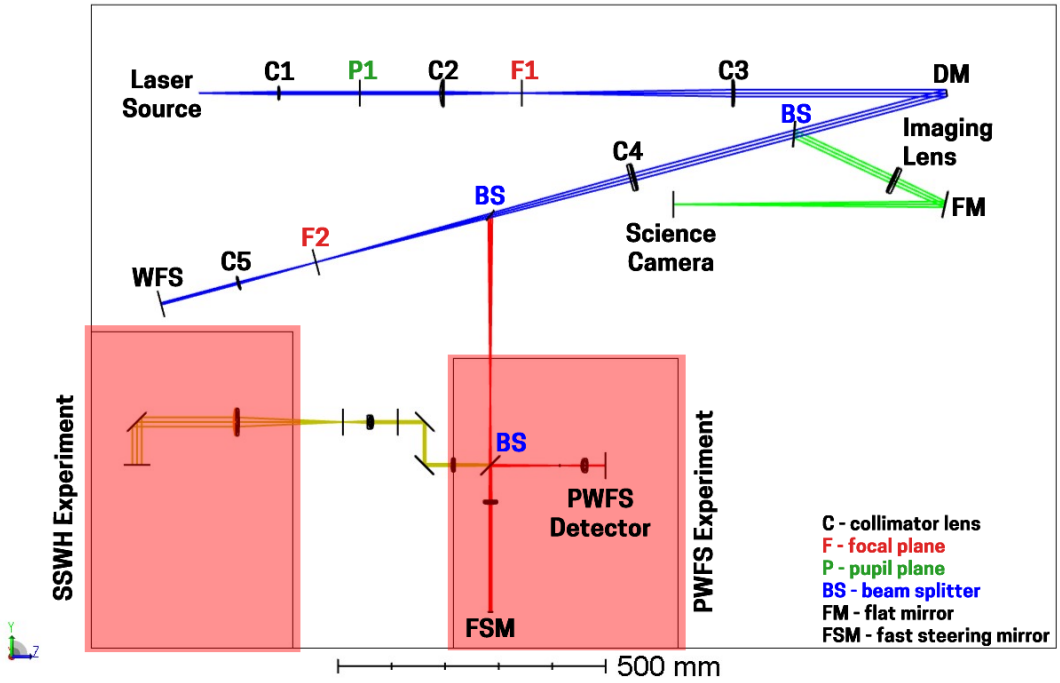

Figure 2.35: Schematic of the test bench used for series of test on SSH-WFS.

On this bench, I used the combination of an Alpao DM 97-15 and HASO 4 broadband SHWFS simultaneously with the SSH-WFS to perform these test scenarios. In some tests, I also used the actual Cilas DM prototype and much higher-order (as compared to HASO4) SHWFS, HASO 128 to compare the abilities of the SSH-WFS to the highest resolution commercial SHWFS at our disposal. The closed-loop design of the test setup gave us the ability of injecting custom wavefronts in a controlled loop scheme.

Stability Test

I also designed a series of tests to measure the stability of the system. These measurements determine how long a single wavefront reference is valid and how frequent the measurement of the reference should be repeated. The stability is determined by the thermal and mechanical properties of the test bench and its environment, and is not

an intrinsic property of the device. For this test, we measured the wavefront residual of a constant wavefront with a delay of one minute up to nine minutes between the reference and measurement data sets. In an ideal situation, all residual measurements should be constant and around the nominal precision of the device. However, internal effects like the randomness of readout noise and environmental effects like the thermal instability of the bench would cause non-zero wavefront residual. It should be noted that we do not use any thermal stabilization solution on the current experimental bench and the temperature on the bench can vary in a range of 10 C. In the case of specific applications, the stability performance could be improved by implementing an athermalized design. Figure 2.36 shows the relation between the RMS residual and the delay between the actual and reference measurements. As expected, these measurements show that the focus mode is changing the most. This is to be expected since slight changes in temperature changes the optical path length during measurements. However, the SSH-WFS device as mentioned previously, is mainly designed to study higher spatial frequency modes such as actuator dynamics and surface behaviour between actuators. Therefore, removing the lowest frequency modes such as tilt, tip and focus does not impact the device's ability to satisfy its design requirements. For a tilt, tip, and focus removed measurements (solid lines) the behavior of our system is favorably comparable to the certified calibrated system.

Combining these results with the precision result of sub-section 2.4.6, I show that this system is capable of providing a minimum of 180/60 (not considering focus applications/considering focus applications) seconds of stability between each reference measurement for the lab environment if 5nm RMS precision requirement is to be satisfied.

Scale Calibration

The scale of the SSH-WFS measurements is calculated based on the optical geometry and the lenslet specifications. I measured a series of differential patterns simultaneously using the HASO 4 and SSH-WFS to check the linearity and scale of the measurements. All measurements were relative to the second reference measurement to eliminate the effect of NCPA on different optical paths between the HASO and our wavefront sensor. Based on the manufacturer's specification, the repeatability of the HASO wavefront sensor in the range of experiment is 3 nm RMS. The pupil size for the SSH-WFS is a circle with a diameter of 256 sub-apertures and for the HASO it

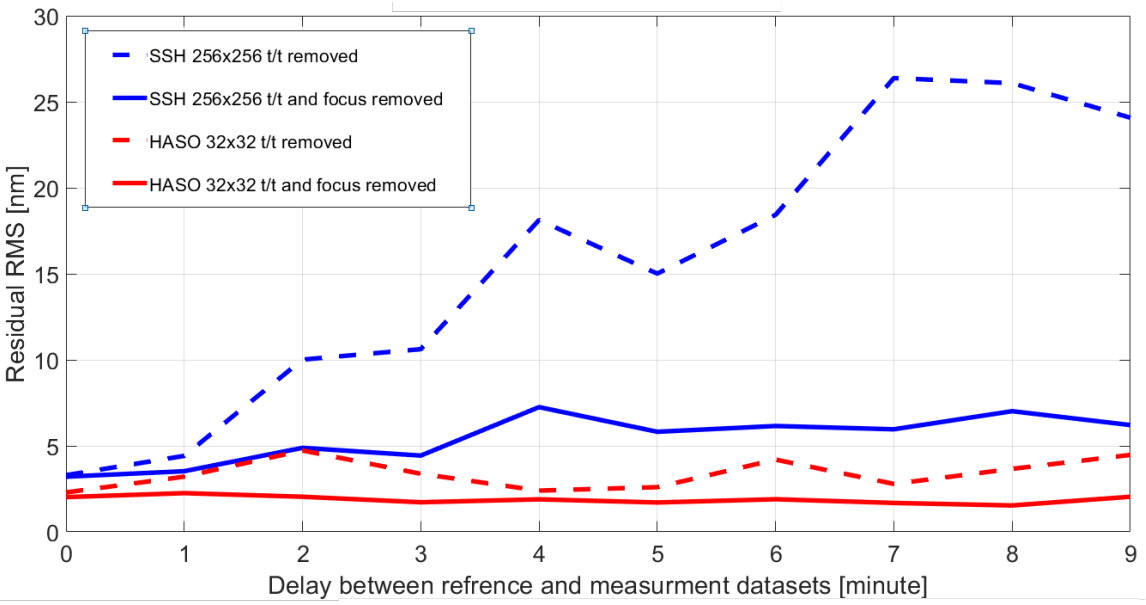

Figure 2.36: The stability test result. Blue solid line describes the response of our 256×256 Shack-Hartman sensor on the experimental bench. The solid line is for tilt/tip and focus removed performance, and the dashed line is for tilt/tip removed performance. The red lines are the same data for the 32×32 HASO Shack-Hartmann device for means of comparison.

is the same physical size but with 32 sub-apertures across. The resolution of the two sensors are very different, so to avoid aliasing on the HASO WFS, I only used very low spatial frequency patterns for this test. Results are shown in Figure 2.37. The red line represents $X = T$. The fit to the data has a correlation of 0.9996 and the RMS deviation from the fit is 4.2 nm, which shows the acceptable level of precision in the scale calibration.

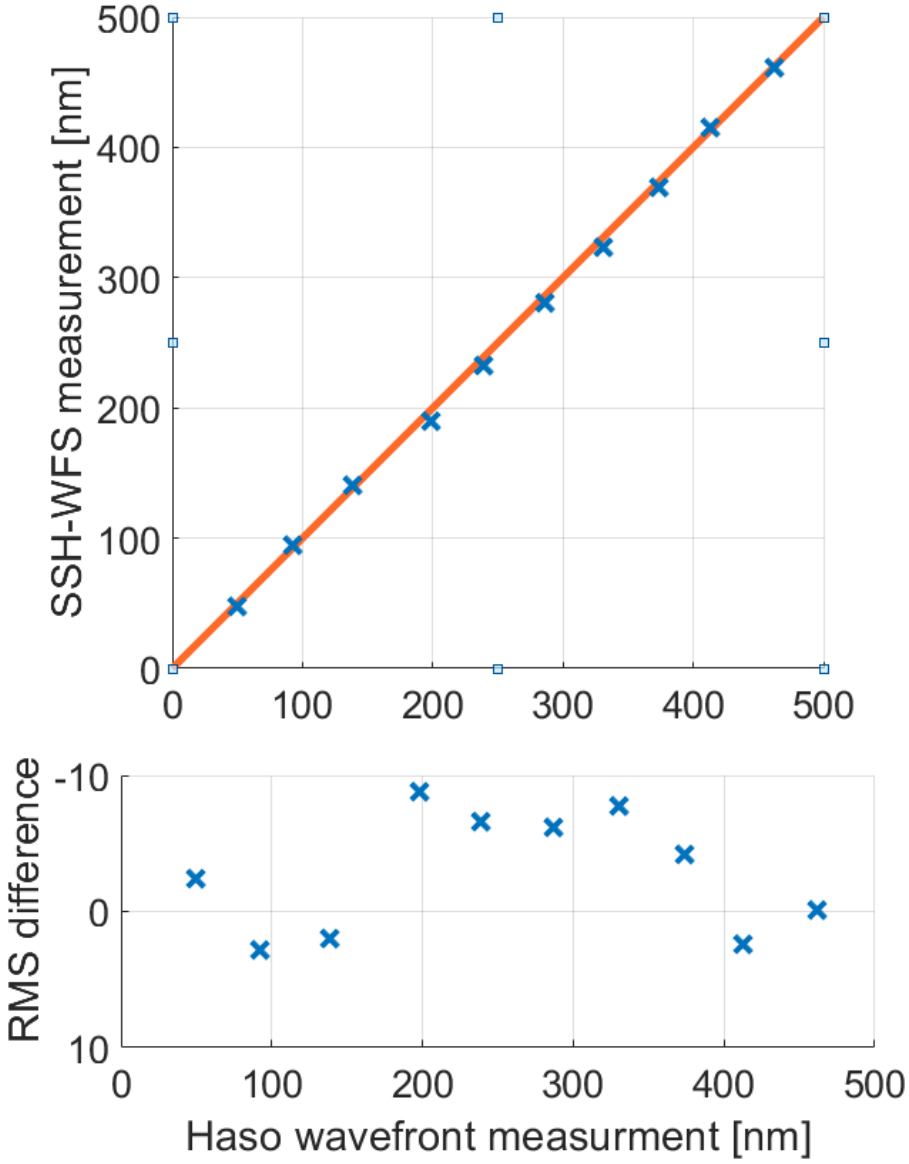

Figure 2.37: The correlation between HASO and SSH-WFS measurement. This result shows the scale of SSH-WFS is well calibrated for a large range of wavefront input.

Noise characteristics

The precision of the measurements are dependent mostly on two factors, the number of stacked exposures for each data set and the signal to noise ratio of the measurements. I performed a series of tests to characterize the noise floor based on these two factors. For these tests, three series of 25 consequent exposures (0.01 second each) of a constant

wavefront were recorded for different light source intensities. The intensity of the light source was set to full well of the detector for the first series, and then was dimmed by a factor of 10x and 100x on the subsequent two sets of exposures. For this scenario, I utilized the Zyla detector in the low-noise, slow read (28 fps) and full well capacity (16-bit) mode to reduce the read noise as much as possible.

Before measuring the relative wavefront, a number of frames are typically stacked to increase the effective exposure time and increase the precision of the final measurements. Figure 2.38 shows the RMS wavefront residual for a different number of stacked exposures and different source intensities. The results of this test demonstrated that the precision of the device is better than the required 5 nm across the pupil for any number of stacked images higher than 15 for the source intensity corresponding to the full well capacity of the detector. This is equivalent to 0.6 second of data acquisition for each data set which is also less than 5 second defined by our requirement on data acquisition time.

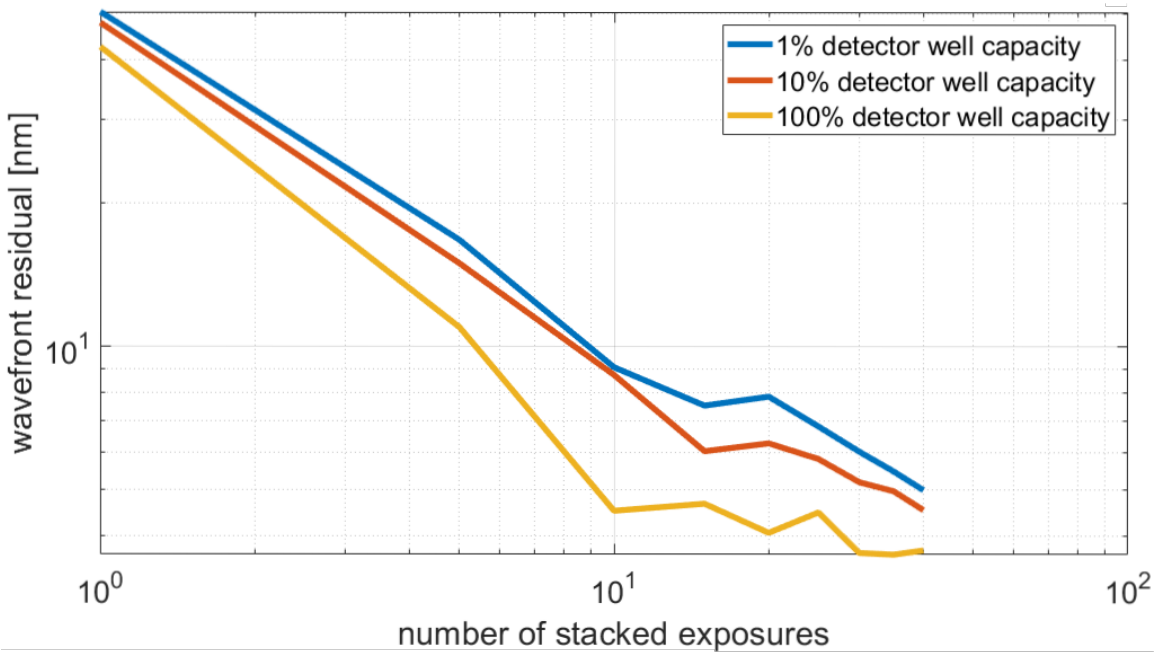

Figure 2.38: The wavefront residual for two sets of consequent SSH-WFS measurements. Ideally the residual should be zero, however, detector and photon noise provide a noise floor in a realistic situation. Different color lines show the relation between full-well capacity utilization and the wavefront residual caused by noise.

2.4.7 Performance comparison

I performed a series of performance comparison tests to represent the advantages of the SSH-WFS over commercially available SHWFSs for certain applications. For these tests, I had the opportunity to use a prototype of the NFIRAOS DM produced by Cilas on a different test bench. The main relative advantages of the SSH-WFS are measurement resolution and dynamic range. Figure 2.39 and 2.40 are representing a real case of such advantage for the SSH-WFS over the HASO 128 SHWFS.

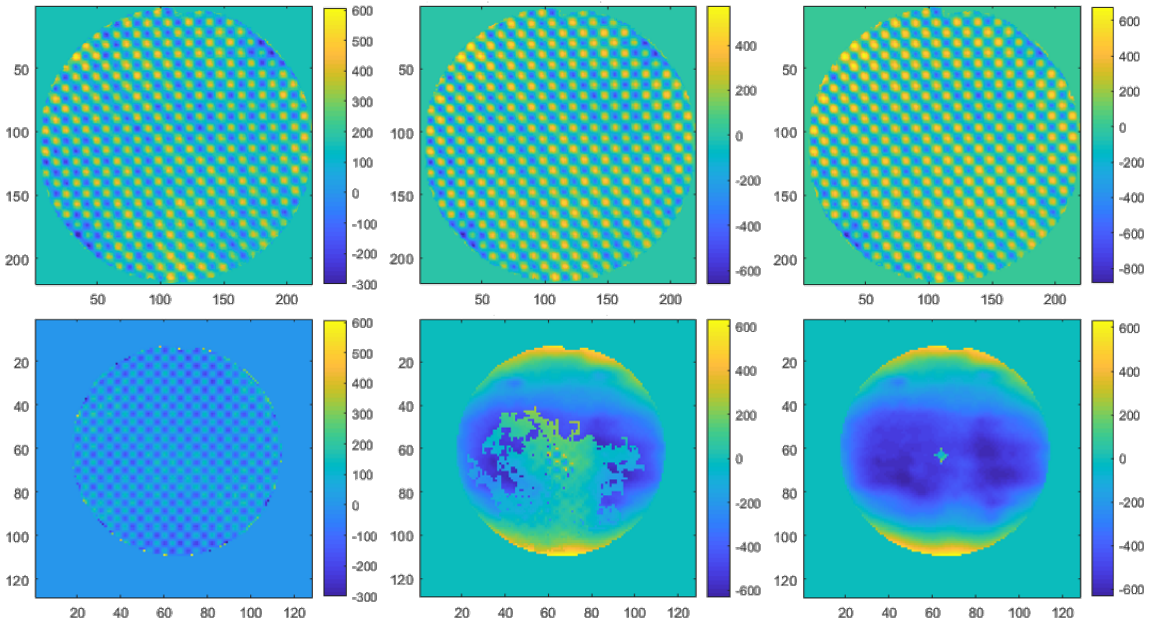

Figure 2.39: Measurement of the waffle pattern on the Cilas DM prototype by SSH-WFS (top) and HASO 128 (bottom). The actuator push increased from left to right by 25%, 50% and 75% of the maximum actuator stroke. Both WFSs are performing similarly on a 25% stroke. However, the HASO dynamic range is saturated in the middle and right panels which caused corrupted measurement.

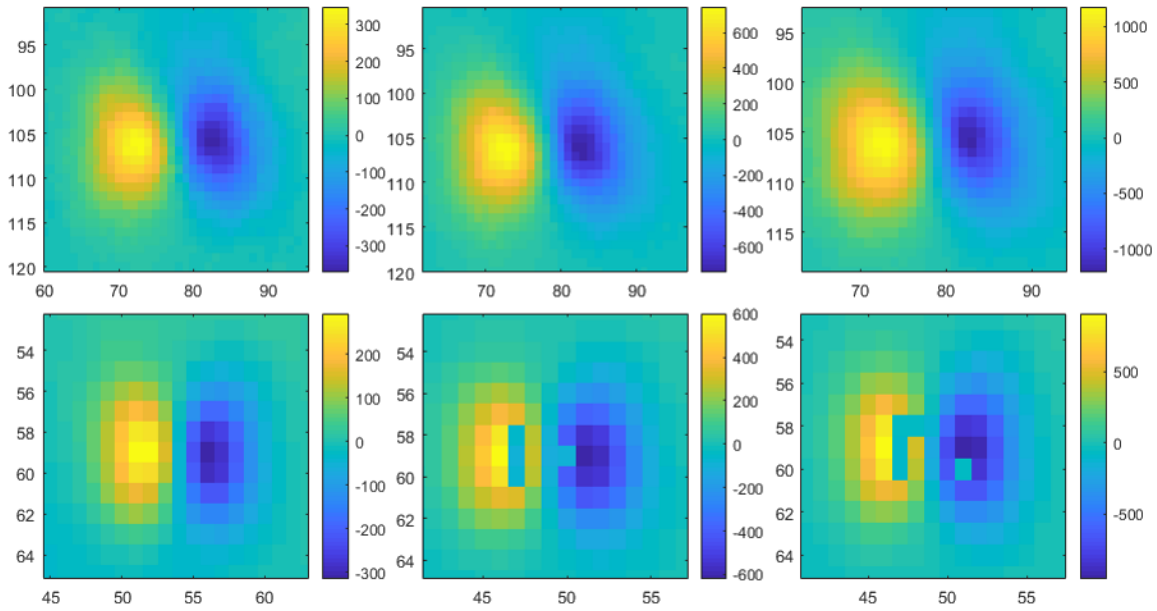

Figure 2.40: Measurement of the single push-pull pattern on the Cilas DM prototype by SSH-WFS (top) and HASO 128 (bottom). Push-pull pattern consists of pushing and pulling a pair of neighbor actuators. The actuator push increased from left to right by 25%, 50% and 75% of the maximum actuator stroke. Also, both WFSs are performing similarly on a 25% stroke, the HASO dynamic range is saturated in the middle and right panels, which caused corrupt measurement. Additionally, the difference in resolving power between the two WFSs are well represented in this figure.

2.5 Summary

In this chapter, I explained my contribution to the design and implementation of new wavefront sensors during the course of my PhD. A major part of this contribution was collaborating with the Keck Observatory on the development of the new IR-PWFS and KPIC instrument. I provided the opto-mechanical design of multiple components of the instrument, made necessary calculations, and performed simulations of the FSM system. I also assisted in the pre-installation procedure, which involved providing alignment plans, and participated in the K2AO bench modification operation. The Keck IR-PWFS and KPIC instrument are now commissioned and operational on the summit of Mauna Kea in Hawaii. I also designed and fabricated an instance of another type of WFS, the Shack-Hartmann wavefront sensor. The AO lab at NRC facilities was interested in a very high-order SHWFS device to study the prototype DMs for the TMT. Such a device was not commercially available. I provided the opto-mechanical

design of a low-cost solution for such an application and successfully fabricated and verified its differential measurement performance, ensuring it can satisfy the necessary precision and requirements.

Chapter 3

The Spider Shadow: Investigating Effects of SMS on AO Performance

Some material of Section 3.2 is closely based on a technical report KAON-1238 [96] published by Mojtaba Taheri et al. (2018) and is published in a paper [72] co-authored by Mojtaba Taheri (2018). I designed the simulation, programmed the simulation code using the OOMAO platform, and analysed the results. Section 3.3 is closely based on a paper [97] published by Mojtaba Taheri et al. (2020). I proposed the concept, designed the experiment strategy, and led the experiment which proved the feasibility of the method.

3.1 Introduction

AO has become a common subsystem of large ground-based observatories. Laboratory AO benches are the backbone of research and development in the field. These setups provide control over many degrees of freedom which are not possible to control within observatory or on-sky systems (i.e. controlled/slow input turbulence, controlled light intensity and wavelength etc). Almost all AO developments and instruments have a laboratory prototype counterpart [59, 31, 18, 20, 53]. However, emulating AO system performance in a laboratory environment is a challenging task. Mimicking the effect of atmospheric turbulence on the wavefront, the telescope structure and flexure and simulating the environmental conditions of the dome are just a few of these challenges.

One of the important features to include in laboratory AO setups is the ability of providing accurate pupil illumination pattern and structure. Currently, the main

method for fabricating large diameter mirrors for astronomical telescopes is the "*segmented mirror*" (i.e. Keck, the Thirty-Meter Telescope (TMT), the Extremely Large Telescope (ELT) etc). In a segmented mirror telescope, the typical shape of each cell is a hexagon, causing jagged features on the edge of the telescope pupil. Furthermore, all large ground-based telescopes utilise a secondary mirror and its supporting structure (SMS) in front of their aperture. This mirror is supported with a mechanical structure commonly referred to as the "*Spider*" (see Figure 3.1). The impact of spider shadow on the performance of AO systems is an important factor to consider, especially in the error budget of the more sophisticated modern systems [32, 96].

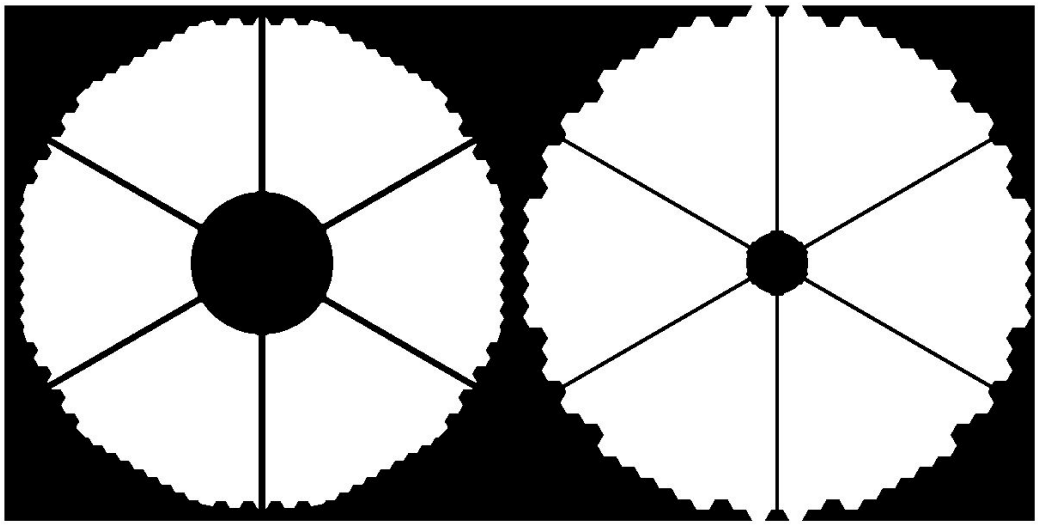

Figure 3.1: Pupil shape and spider shadow for ELT (Left) and TMT (Right). Note the spider structure shadow on the primary and the jagged features on the edge of the pupil. Note that the scale in this figure is arbitrary. ELT and TMT primary mirrors will be 39 and 30 meters in diameter, respectively.

When used with wavefront sensors for AO, shadow patterns on the primary mirror result in only partial illumination of a group of sub-apertures for the SHWFS (or a group of WFS detector pixels in the case of a pyramid). These partially illuminated WFS elements can add a significant error term in the overall WFS error budget which dramatically degrades resolving power. Additionally, the spider shape divides the primary mirror into multiple (generally 4 or 6) discontinuous illuminated segments. In such a case, the AO control system can still flatten the wavefront in each segment, however the WFS is blind to the differential phase delay (Piston mode) between the segments. This makes it impossible for the AO system to flatten the wavefront over

the entire pupil and in some cases even worsening the differential piston between the segments. This undesired effect is often referred to as the “Island” or “Petalling” effect [86]. Without very careful consideration, this can result in large errors in the shape of the wavefront which significantly degrades the AO performance. Other observed effects caused by the presence of the spider is the "*low-wind*" effect. Such an effect happens when a wind passes through the cold spider metallic structure. The thermal exchange between the air flow and the structure composes a layer of air with different temperatures for each segment of the spider structure. This effect induces differential piston or tilt modes in each segment of the pupil, significantly degrading (see Figure 3.2) the AO performance [65].

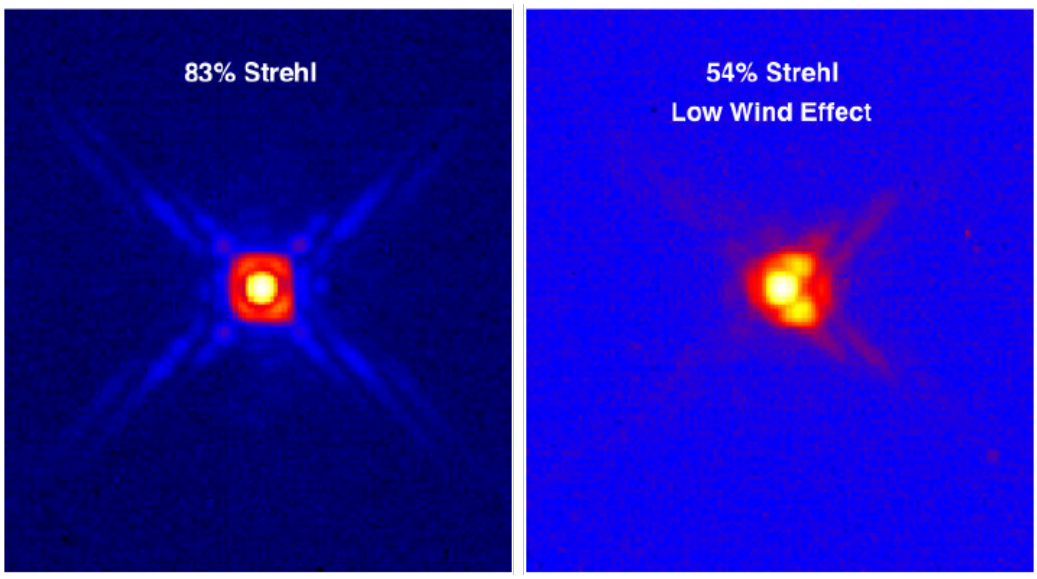

Figure 3.2: Examples of a nominal VLT/SPHERE PSF (left) and PSF affected by a degradation in Strehl caused by pupil differential piston/tilt/tip modes induced by the low wind effect (right). Such a wavefront artifact typically creates two secondary lobes in the PSF form, hence their "Mickey Mouse ears" nickname. (Credit: Milli et al. [66])

These effects and ways to mitigate them are still being studied, especially for extreme AO systems. These studies are mainly built on simulation methods whose results need to be verified on laboratory AO setups. Building a precise, small-scale model of the intensity pattern created by the shadow of the spider structure and the exact shape of the telescope mirror within a laboratory setup is becoming increasingly important for gaining a deeper understanding of AO system performance. The pupil intensity pattern modelling is a particularly challenging task for a few reasons, given

that the ratio of the thinnest element of the spider structure to the pupil diameter can be of the order of 1%, and the size of beams in laboratory setups are typically of the order of few centimeters.

In this chapter, I present a simulation and analysis considering the impact of spider shadow on the performance of Keck and ELT. I also develop and implement a simple, precise and very flexible method to inject and modify custom spider shadow patterns into laboratory AO benches. The results of this work are being transferred to the National Research Council of Canada (NRC) and implemented on the advanced wavefront sensing bench.

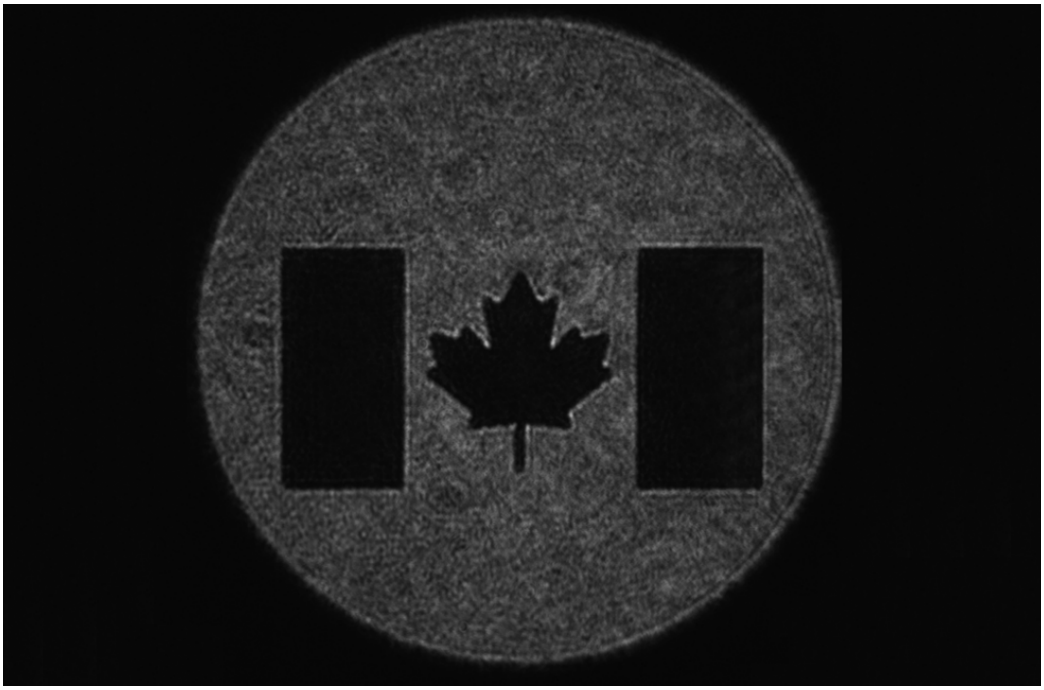

Figure 3.3: For the first test of using the SLM for intensity modulation I used the Canadian flag as the binary intensity mask. In this image the circular white region is the circular pupil of the optical system and the flag pattern is applied by SLM pixels. The process and its applications are explained in Section 3.3.

Laboratory AO benches are essential for the development of new AO instruments such as future extremely large telescope AO systems. One of the key elements for simulating the performance of such systems in a smaller scale laboratory environment is the ability of projecting the precise intensity mask on the pupil plane. This mask often has binary (black or transparent/reflective) patterns that mimic the secondary

obscuration and spider design of the telescope. Precise implementation of intensity masks on the bench is important since studying effects such as petalling are critically dependent on the correct down-scaling and precise representation of the spider structure.

Using a physical mask for such an application is very challenging since including such fine structure in the manufacturing of pupil masks and precisely aligning them is difficult. It is also necessary to build a new physical mask for each telescope system or scale that is desired for the experiment. In this section, I introduce two methods of using a phase-only Liquid Crystal on Silicon Spatial Light Modulator (LCoS-SLM) device as an alternative option to precisely and relatively easily injecting a custom intensity mask into an optical bench. By implementing these methods on the LOOPS bench AO facilities at LAM, we demonstrated that the contrast produced by both methods could be less than 2% (dark/bright ratio), which is sufficient for representing pupil obscuration in the majority of applications. We also show that by using one of these methods, it is possible to inject phase and binary intensity mask simultaneously which could greatly increase the versatility and ease of use of an experimental AO setup.

3.2 Simulation Studies: Keck II and Thirty-Meter Class Telescope Scenarios

Here, I present two simulation studies involving the impact of spider shadows on the AO performance. In Section 3.2.1, I estimate the performance of the new IR-PWFS instrument for the Keck II telescope and compare its performance in the presence of the spider shadow with the calibration mode. In the calibration mode, a laser fed fiber optic illuminates the AO system of the telescope, which means there is no footprint of the spider or the hexagonal shape of the pupil in the measured data. However, this mode is important as the calibration of the AO system can be done in daylight time without the presence of the turbulent effect of the atmosphere. In this simulation, I analyzed the contribution to the error budget caused by using such a calibration method for on-sky use with a pyramid wavefront sensor, which includes the error caused by partially illuminated PWFS pixels caused by the spider shadow. Section 3.2.2 is also a study on the effect of spider shadows on ELT's wavefront control and partial analysis of the effectiveness on proposed mitigation methods like the use

of a synthetic interaction matrix. An interaction matrix is a mathematical element which connects wavefront measurement to the necessary DM commands to flatten it. Using a modified interaction matrix for the shadowed region of the DM, or using a synthetic one are a few different ways of improving the AO performance in the presence of non-circular (or wobbling) pupils and the spider shadows.

3.2.1 Simulation of Partially-Illuminated PWFS Pixels and Using a Modified Interaction Matrix

In this study, we used a detailed simulation to compare a modified interaction matrix approach with a partially illuminated pixel with a baseline performance that does not face these issues. The results show the nominal RMS closed-loop wavefront difference between the two scenarios is $124 \pm 27\ nm$. However, the analysis unexpectedly demonstrates that the main source of error is not the non-linearity caused by partially illuminated PWFS pixels but the control algorithm performance near the removed regions shaped by the interaction matrix modification procedure. This study focuses on the details of the simulation, results and the analysis which lead to this new explanation for the difference between the two scenarios.

Technical Challenges

The Keck calibration pupil (OSP) is larger than the actual primary mirror pupil, which helps to deal with the 10-meter telescope pupil wobbling. As a result, the interaction matrices that are measured in calibration mode need to be modified before being applied on the on-sky wavefront. Adding a pupil mask in the calibration path might seem like the immediate and most simple solution for this issue, but because of the slight pupil wobbling the result would not be desirable. This is the first time that this calibration and interaction matrix modification procedure have been done with a pyramid wavefront sensor. The main aim of this study is to simulate the impact of this process on the Keck AO closed-loop performance and to investigate other probable source of errors which might have been overlooked.

The Keck primary mirror pupil shape is not smooth or circular and contains many sharp features. In addition, there is the fine structure of the spider, creating a shadow on the primary mirror. These features cause partially-illuminated regions on the wavefront sensor. The effect of these partially illuminated sup-apertures were well considered and practically dealt with for the Keck Shack Hartmann sensor. Given

that this is the first-time the Keck AO is using a PWFS, the other aim of this study is to determine the effect of partially illuminated PWFS pixels on the closed-loop performance of the Keck AO system.

Simulation Code and Input Parameters

There are different codes available for performing AO simulation. For this study OOMAO (Object Oriented Matlab Adaptive Optics) toolbox was chosen. The main reasons for this selection where:

- Good collaboration and connections with developers.
- The standard and flexible object-oriented environment.
- Widely accepted and used within the AO community, including the Keck Observatory.

The flowchart in Figure 3.4 shows the general structure of the code and its modules.

The Keck influence function and Keck pupil mask are taken as the simulation inputs. Further explanation about most modules and initial variable values are given below.

Table 3.1 contains all variables that effect the outcome of the simulation, their valid range and description.

Variable name	Range	Value	Type	Notes
res_coef	> 3	17	OV	Simulation sampling resolution coefficient, [sampling resolution] = (res_coef)×(number of lenslets)/ (detector pixels)
res	-	731	OV	Simulation sampling resolution
opwave	-	H-band	OV	Operation source wavelength (baseline and restricted set source wavelength)
strkcoef	-	0.01	OV	Stroke size for IM measurement, the unit is 1 wavelength
lirat	0-1	0.5	OV	Minimum light ratio for validating sub-aperture/PWFS pixel

calwave	-	H-band	OV	Calibration source wavelength
nthd	0-ndm	2	CC	Number of modes that are removed in command matrix calculation process
loopcount	-	-	CC	Number of steps for the close loop cycle
gain	0-1	0.25	CC	Close loop gain
Loop_freq	-	1000	CC	Frequency of the loop, the unit is Hz
Tempo_lag	-	1	CC	Temporal lag between WFS and DM, unit is loop cycle
wfstype	'p', 's'	'p'	WC	'p' for pyramid and s for the shack-Hartmann wavefront sensor
C	-	1.5	WC	PWFS four pupil sampling ratio
calmag	-	4	WC	Calibration source magnitude
opmag	-	4	WC	Operation source magnitude
Photon_noise	0 or 1	1	WC	WFS detector photon noise
Readout_noise	0 or 1	1	WC	WFS detector readout noise
Modulation	-	3-5	WC	PWFS modulation (lambda/D)
nlens	-	43	WC	Number of WFS sub-apertures/PWFS pixels in diameter
gpu_step	-	1-15	CM	Number of parallel GPU threads for PWFS calculations
Showparam1	0 or 1	-	CM	Level 1 diagnostic plots
Showparam2	0 or 1	-	CM	Level 2 diagnostic plots
D	-	11.732	TC	Conjugated size of the DM on the telescope primary [m]
pupil_type	'r','k'	'k'	TC	'r' for smaller circular pupil, 'k' for The Keck pupil mask
dmtype	'if','mr', 'zr'	'mr'	DC	'mr' for keck IF, 'if' for OOMAO monotonic IF, 'zr' for Zernike DM
dmcop	0-1	-	DC	DM mechanical coupling coefficient, only for 'if' dmtype
ndm	-	21	DC	Number of DM actuators in diameter

Table 3.1: List of variables that is used in the simulation. These variables are categorised based on their type: Code maintenance (CM), telescope configuration (TC), DM configuration (DC), WFS configuration (WC), closed-loop configuration (CC), and other variables (OV).

This simulation utilizes three main object sets for:

- A) measuring the Keck calibration pupil (OSP) interaction matrix
- B) measuring the closed-loop baseline scenario performance (BLS)
- C) measuring the Keck pupil closed-loop scenario performance (KPS)

Each object set contains a WFS, source, DM and telescope.

The atmosphere is modeled by the OOMAO atmosphere object. Model atmosphere parameters are shown in Table 3.2. These parameters match the typical seeing conditions on the summit of Mauna Kea.

Variable name	Value
R_0	$0.165\ m$
L_0	$75\ m$
Number of turbulence layers	7
altitude	$0, 500, 1000, 2000, 4000, 8000, 16000\ m$
R_0 fraction per layer	$0.517, 0.119, 0.063, 0.061, 0.105, 0.081, 0.054$
Wind speed	$6.7, 13.9, 20.8, 29, 29, 29, 29\ m/s$
Wind direction	$0, \pi/3, -\pi/3, -\pi, -4/3\pi, -\pi/6, \pi/8$

Table 3.2: Atmospheric parameters and their value for the simulation.

Atmospheric data is used slightly differently in this simulation in comparison with the common use of OOMAO. Typically, each frame of atmosphere is created at the beginning of each cycle of the AO loop. In this case, however, identical atmospheric behavior for set B and C is required to make the comparison valid. Therefore, "loopcount" sequences of the atmosphere are simulated and stored at the beginning of the simulation. These sequences will be used later in the input phase. This guarantees

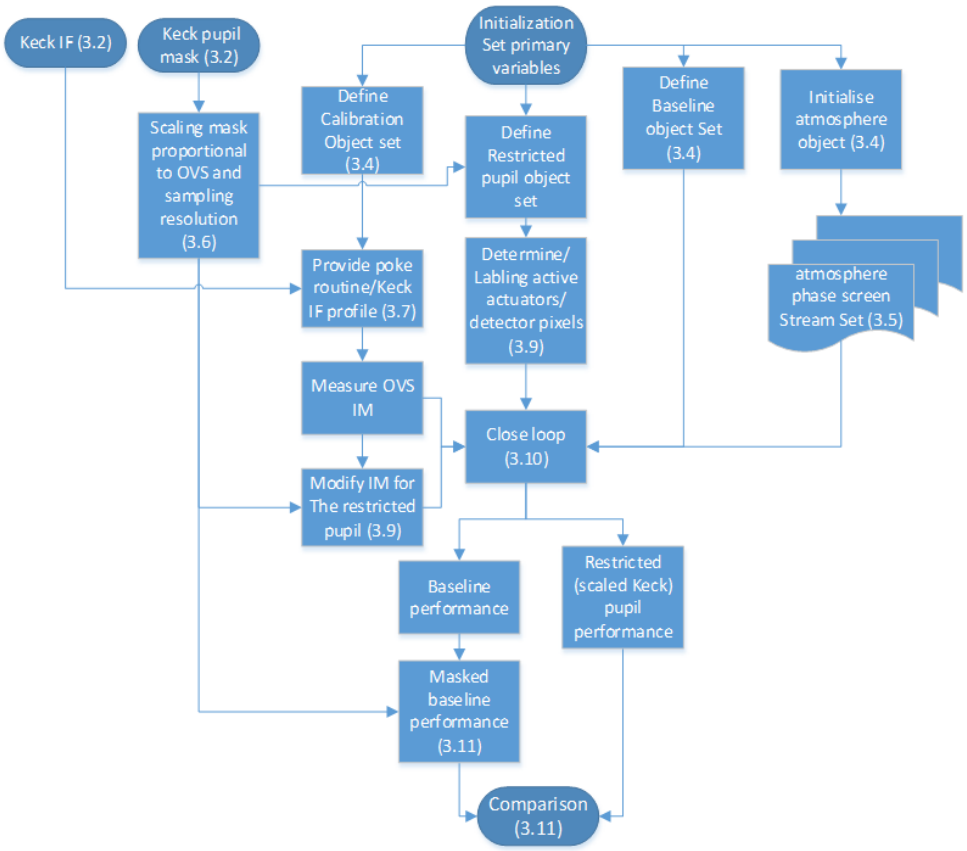

Figure 3.4: The main structure of the simulation code.

that both Baseline and Keck pupil experiments would receive identical input wavefronts.

There are also other important considerations involved in creating the Keck pupil mask. The main constraints are:

1. OOMAO only accepts integer number pixels as sampling resolution.

2. The sampling resolution should be an integer multiple of the number of pixels for PWFS or sub-apertures for the SHWFS.

3. The sampling resolution should be at least large enough that the smallest feature of the pupil would be represented.

4. The fully illuminated pupil should encircle the Keck pupil. In addition, the ratio of diameters should match the ratio of the physical Keck pupil size (10.95 m) to the conjugated size of the DM on the primary mirror plane (11.732 m).

So, these proportions should be considered simultaneously:

- The ratio between the fully-illuminated pupil and widest feature of the Keck pupil should be 1.0714.
- The widest feature of the Keck pupil is 10.95-meter-long and would be projected onto 40 PWFS pixels. We derive from these two constraints that the fully-illuminated pupil should be 42.85 pixels in diameter. Unfortunately, it is not possible in OOMAO to use a non-integer number as a diameter input. So, it was necessary to use 43 pixels corresponding to a physical diameter of 11.732 meters. Therefore:
  - The thickness of the finest pupil structure (spider thickness) is 3.17 cm.
  - The sampling size should be an integer multiplication of $nlens = 43$.

This means that the ratio of the largest feature to the smallest is equal to ~ 369. This means any simulation that is supposed to consider all the features of the spider structure should have a minimum sampling resolution of 369 pixels in diameter. In practice, to well represent the shadow of the diagonal spiders, we use double that number as it is very close to the `res_coef`=17 situation. Although running this simulation with `res_coef`< 17 would be significantly faster and less resource intensive, and would still represent the sharp features of the pupil, the spider structure would not be well captured in the simulation (see Figure 3.5).

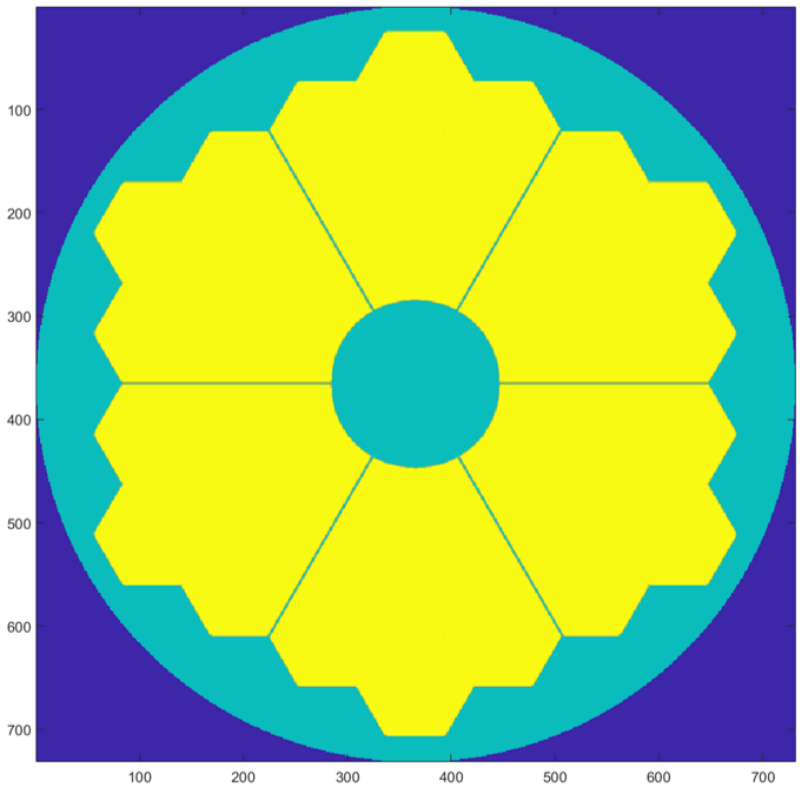

Figure 3.5: Proportionally scaled Keck and OSP. Note that the spider structure is clearly represented. Yellow regions are the Keck pupil, placed in the center of the green fully illuminated pupil that is used for the calibration process. The ratio of number of pixels in the diameter of these two pupils is `res_coef`=17 is 1.718 which is very close to the ratio of 1.714.

The Keck 2 deformable mirror influence function could be described with the function below [1]:

$$\begin{aligned} I(r) &= exp(-p_4 r_e(r)) \cdot (1 + p_5 r_r(r)) \cdot M(r) \\ r_e(r) &= p_6^{e(r)} \cdot (|x|^{e(r)} + |y|^{e(r)}) \\ e(r) &= p_0 + p_1 r^2 + p_2 r^4 + p_3 r^6 \\ M(r) = r^8 < \frac{1}{3p_6^8} &: exp(-150 p_6^8 r^8)], \ otherwise : 0 \end{aligned} \tag{3.1}$$

The profile of the monolithic OOMAO IF with mechanical coupling coefficient of 0.25 is shown beside the Keck IF based on Equation 3.1 in Figure 3.6.

[1] Sam Ragland - KAON 1152-11/3/2016

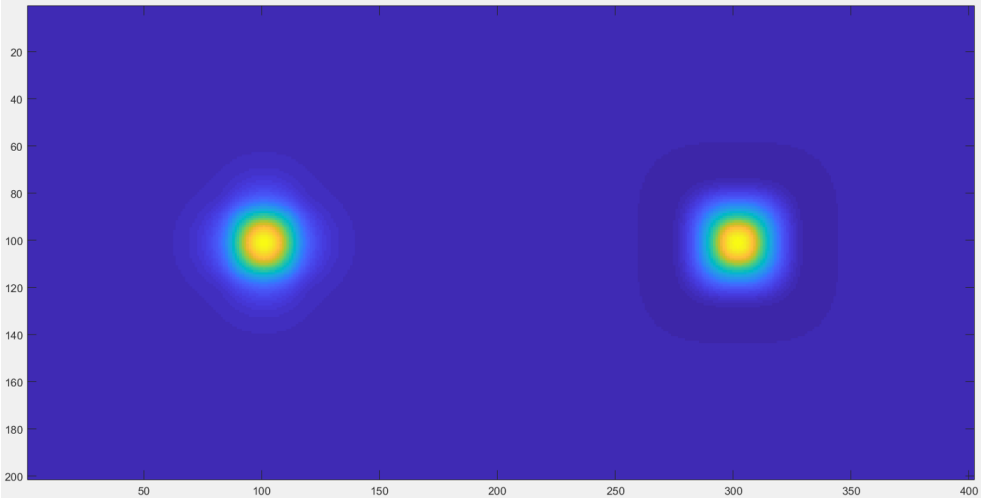

Figure 3.6: Left: OOMAO monolithic IF profile with mechanical coupling of 0.25. Right: Keck DM IF model base on Equation 3.1.

To keep the modeling as precise as possible, we use the Keck IF in the final run of the simulation. However, it turns out that the difference in influence functions does not have a significant effect on the outcome.

During the primary PWFS tests and crosschecks with the Shack-Hartmann closed-loop performance, occasional instability was observed in the function of the OOMAO PWFS module. This instability arose from the way OOMAO dealt with sampling: it was observed in cases which used asymmetric pupil masks or in cases where the sampling resolution would not be easily divisible by the WFS resolution[2]. After intensive probing, it becomes apparent that the PWFS module required modification. Specifically, the few lines of code that set the relative orientation of the valid WFS detector pixels, slopes, and the pupil needed to be modified. This was an important change that future users should be aware of.

The calibrated IM is measured on the oversized pupil. To make it usable for the actual on-sky (restricted) pupil, it was necessary to modify it. It should be noted that this modification should be done before inverting the IM.

[2]More precisely, any ratio that causes asymmetric patterns in the position of the center of WFS sub-apertures/pixels on the sampling grid pixels, i.e. if there were 7 sampling pixels for every 3 WFS pixels.

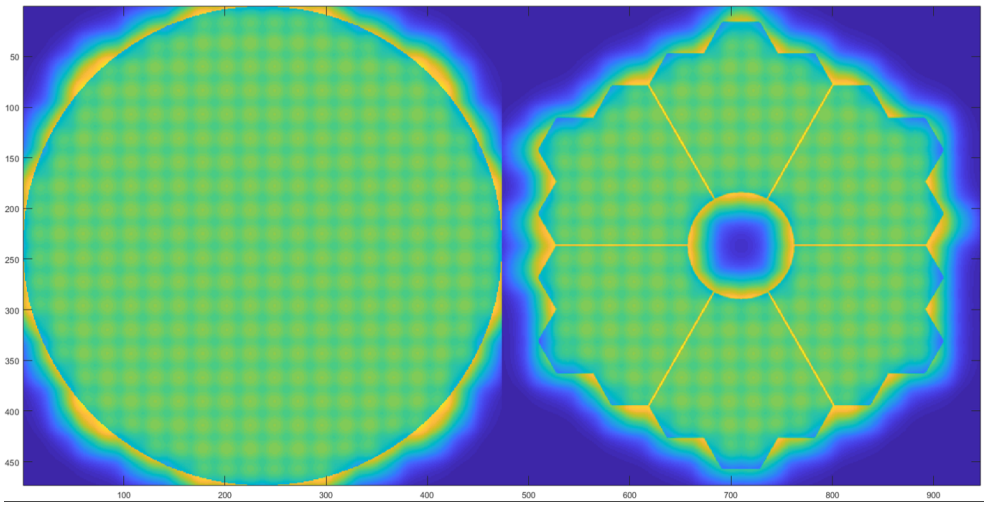

Figure 3.7: The pattern of active actuators for each illumination pattern, OSP on the left and the Keck pupil on the right. For this diagram, all the active actuators are pushed and simultaneously the illumination pattern on the DM is super-imposed on top. It can be seen that all the active actuators in each scenario are correctly chosen to be in the illuminated region and cover it completely.

To apply the modification, it is important to identify and label each active PWFS pixel and its corresponding active actuators on the Keck calibration pupil (OSP). Active actuators are in the illuminated region, and also actuators that surround the illuminated pupil on the DM plane (see Figure 3.7). Each active pixel corresponds to a specific row, and each active actuator corresponds to a specific column of the OSP interaction matrix. By knowing the difference in illumination patterns of the OSP and on-sky mode, it is possible to remove any rows and columns of the OSP IM that correspond to the obscured PWFS pixels and DM actuators respectively. This would derive the modified IM for the on-sky restricted pupil from OSP IM.

There is an important point to consider before comparing the baseline and restricted pupil performances. Some of the regions that have valid AO corrected wavefront values in the baseline scenario (BLS), do not have any valid counter regions on the Keck pupil scenario (KPS). Because of this difference it is not appropriate to directly compare the RMS wavefront residual between the two cases. Before the comparison, it is necessary to apply a binary mask similar to the restricted pupil shape on the AO corrected baseline wavefront residual and then calculate the wavefront RMS. This way the two RMS are comparable. It is important to note that the mask should be applied only after AO correction and not before (see Figure 3.8).

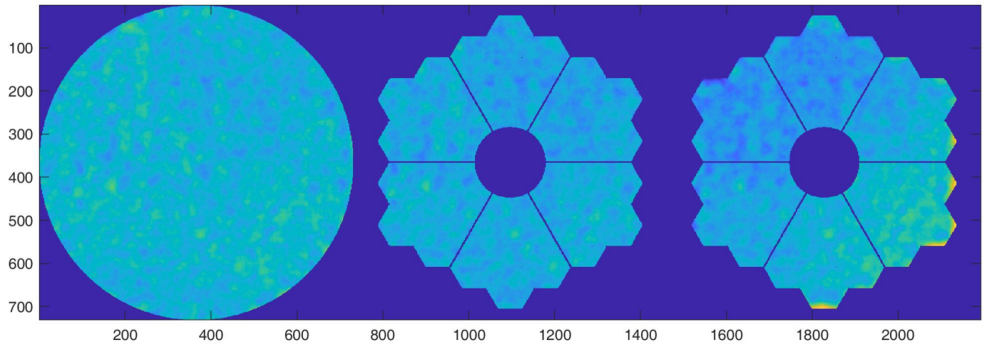

Figure 3.8: Left: OSP wavefront residual after AO correction. Middle: mask applied on the OSP wavefront residual. Right: the wavefront residual for restricted pupil scenario. The binary mask applies on the OSP residual before calculating RMS error to consider lack of data in shadow regions on Keck pupil. Although the middle and right pupils are very similar, one can see slight differences which is the performance difference between the two scenarios.

Carefully considering all points mentioned above, it is now possible to close the loop to produce the results. The schematics of the closed-loop structure are shown in Figure 3.9.

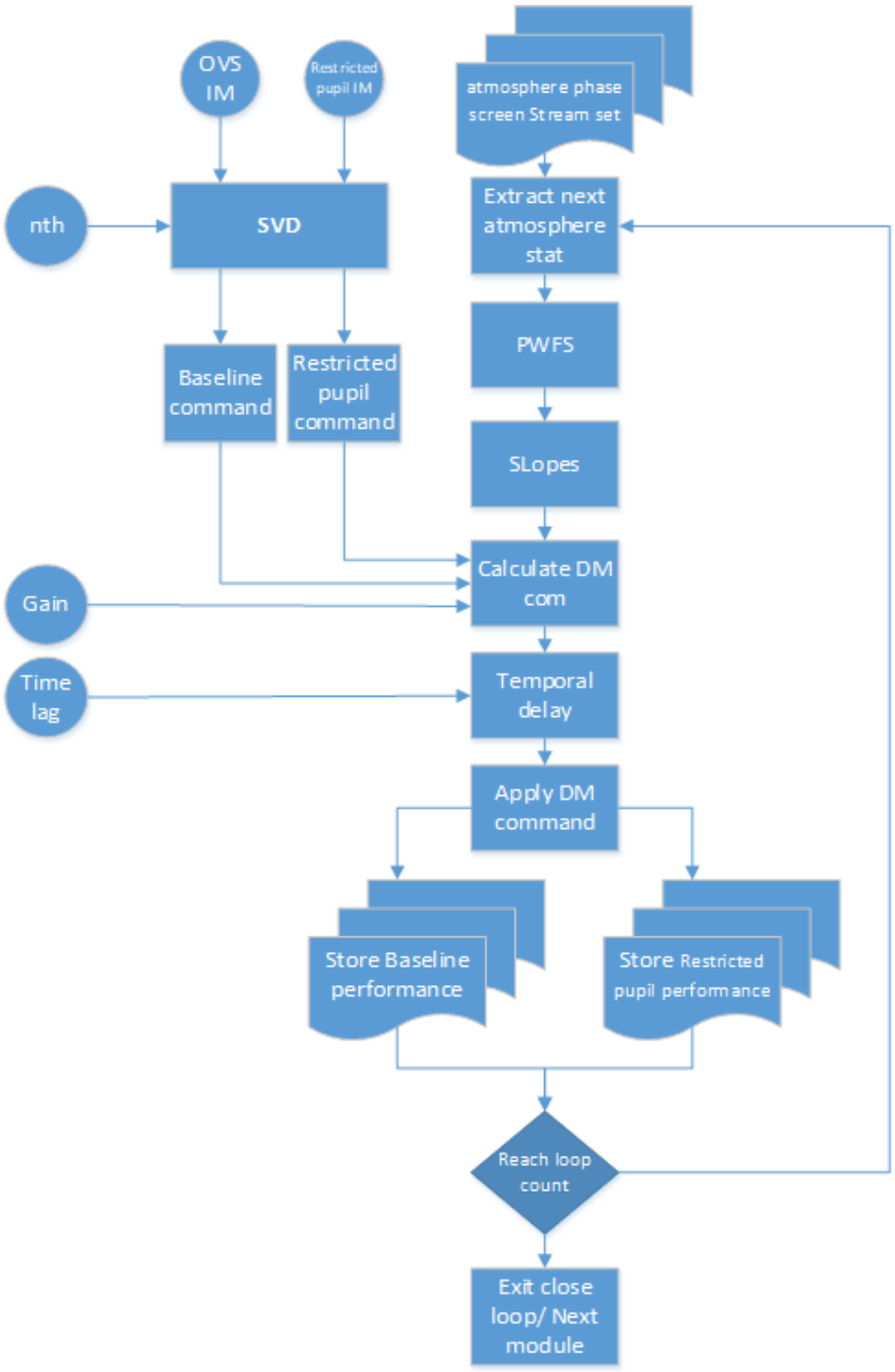

Figure 3.9: The main structure of the closed-loop module.

Results

A sample of the simulation results for the input variables described in Table 3.1 and Table 3.2 can be seen in Figure 3.10. Figure 3.10 shows the closed-loop performance for 2400 steps (2.4 seconds in real time). Figure 3.11 shows different phase measurements for one random step during this time series. The difference of the two scenarios are statistically significant. During these series of simulations, the quadratic phase residual difference between the two scenarios measured is $124 \pm 27\ nm$. This result was unexpected, so we investigated multiple scenarios which could explain this difference. This issue is discussed in the next section, but in summary, we find that the major part of the error is caused by the current control algorithm performance on the edge of the modified pupil and not the IM modification process or non-linearity of the partially illuminated pixels.

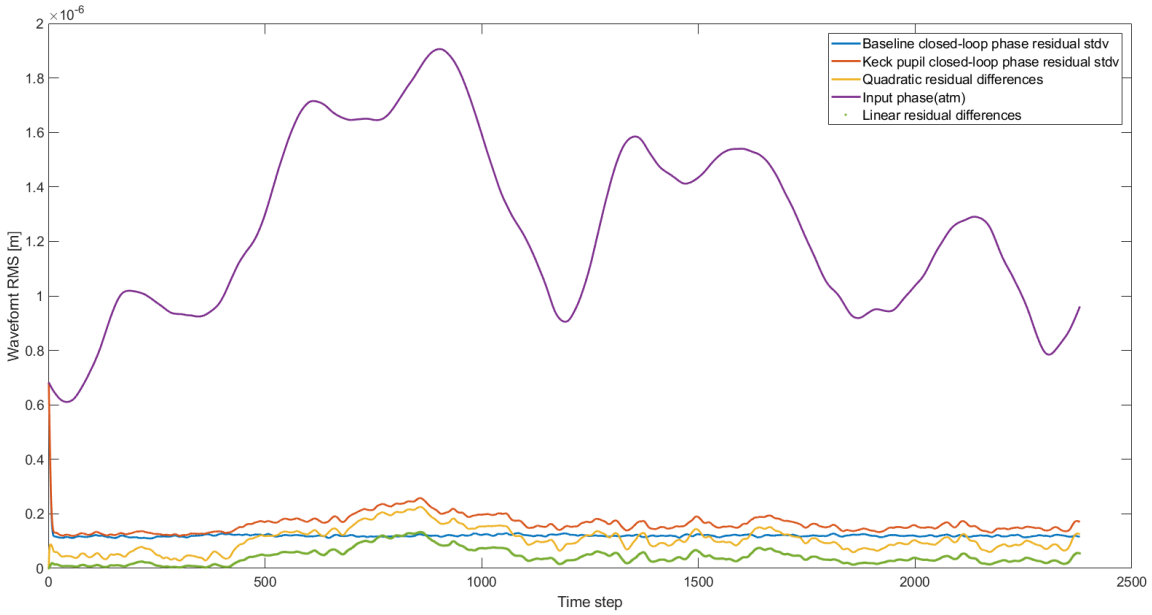

Figure 3.10: Sample simulation results including input atmospheric phase error, BLS and KPS performances in addition to the quadratic and linear differences between the two scenarios.

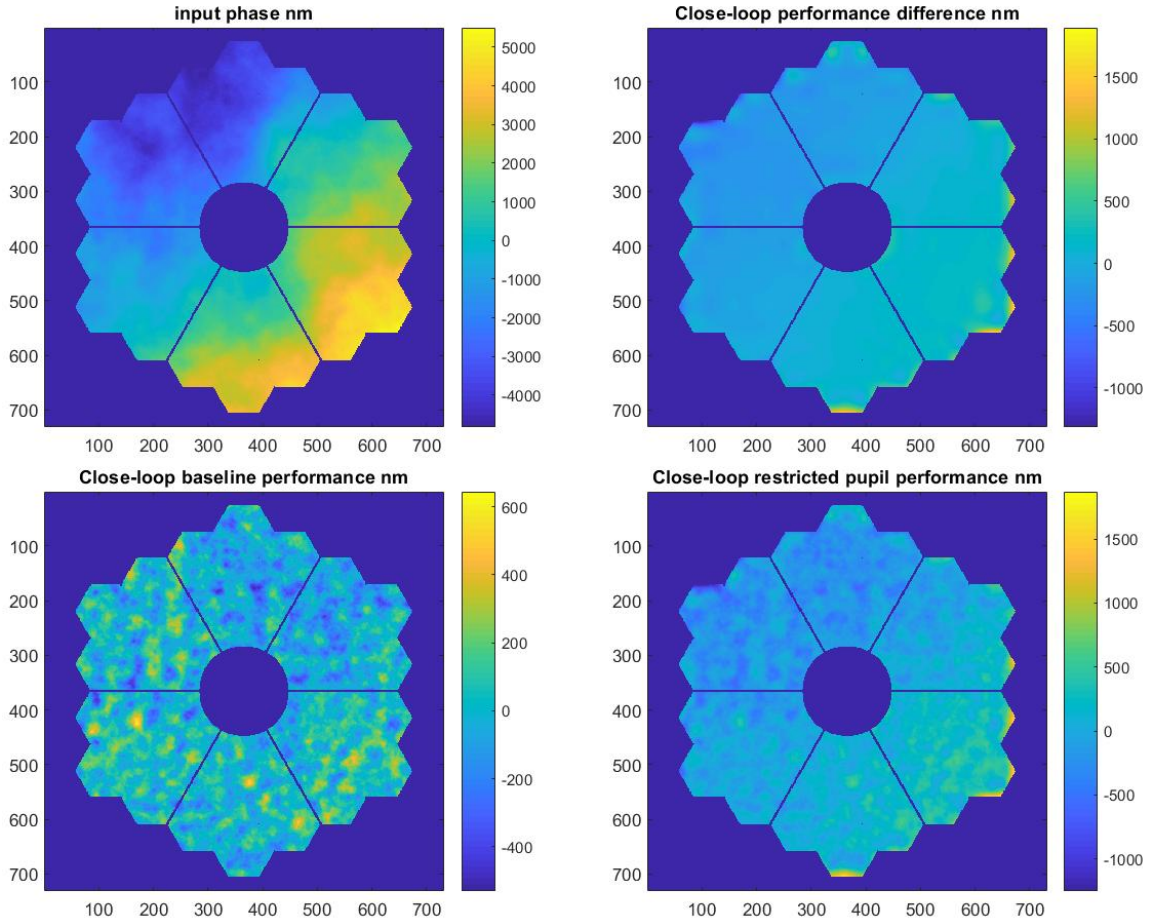

Figure 3.11: Sample frame, comparing closed-loop performance of the two scenarios.

There are different possible factors which can cause different close-loop wavefront residual between the baseline scenario (BLS) and the Keck pupil scenario (KPS). The expectation was that the dominant terms of this difference originate from i) the method of IM reduction and ii) the non-linearity of partially illuminated pixels of the PWFS. However, further analysis showed that the effect of the spider shadow on the control system performance, particularly in the regions close to the edges of the pupil is the major source of error. Analysis of the residual phase pattern and distribution shows that a few percent of pixels/regions are responsible for the majority of the error. Figure 3.12 shows the difference between the two scenarios considering the removal of specific percentiles of sampling pixels with the highest phase difference value between the two scenarios.

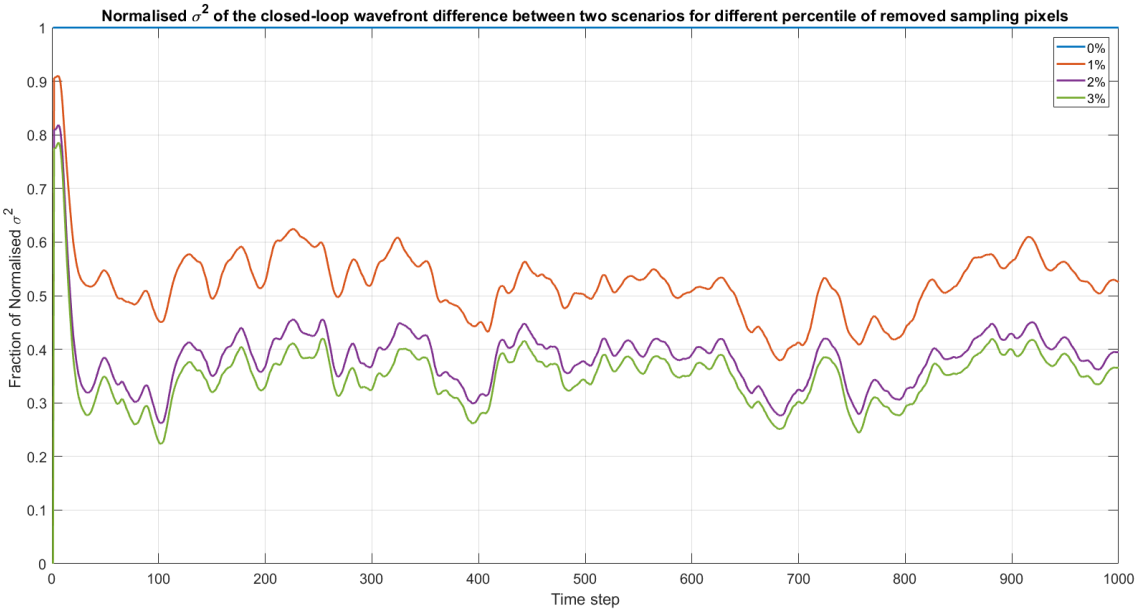

Figure 3.12: This figure shows the quadratic wavefront residual difference between the two scenarios in the case that the specific percentage of sampling region/pixels with the most mean error are not considered. The blue line (Y=1) represents the situation in which all the pixels are considered and used for normalizing other instances. The numbers on the legend show the percentage of the removed sampling pixels for each specific plot. This graph clearly shows that close to 65% of the error budget is caused by only 2% of pixels in the pupil region.

As demonstrated in Figure 3.12, almost 65% percent of the total error budget is caused by only 2% of the total sampling pixels. Combining this analysis with the mean absolute phase residual difference map (Figure 3.13) reveals that more than 60% of the total error budget is created by only 2% of the regions placed on the edge of the modified pupil.

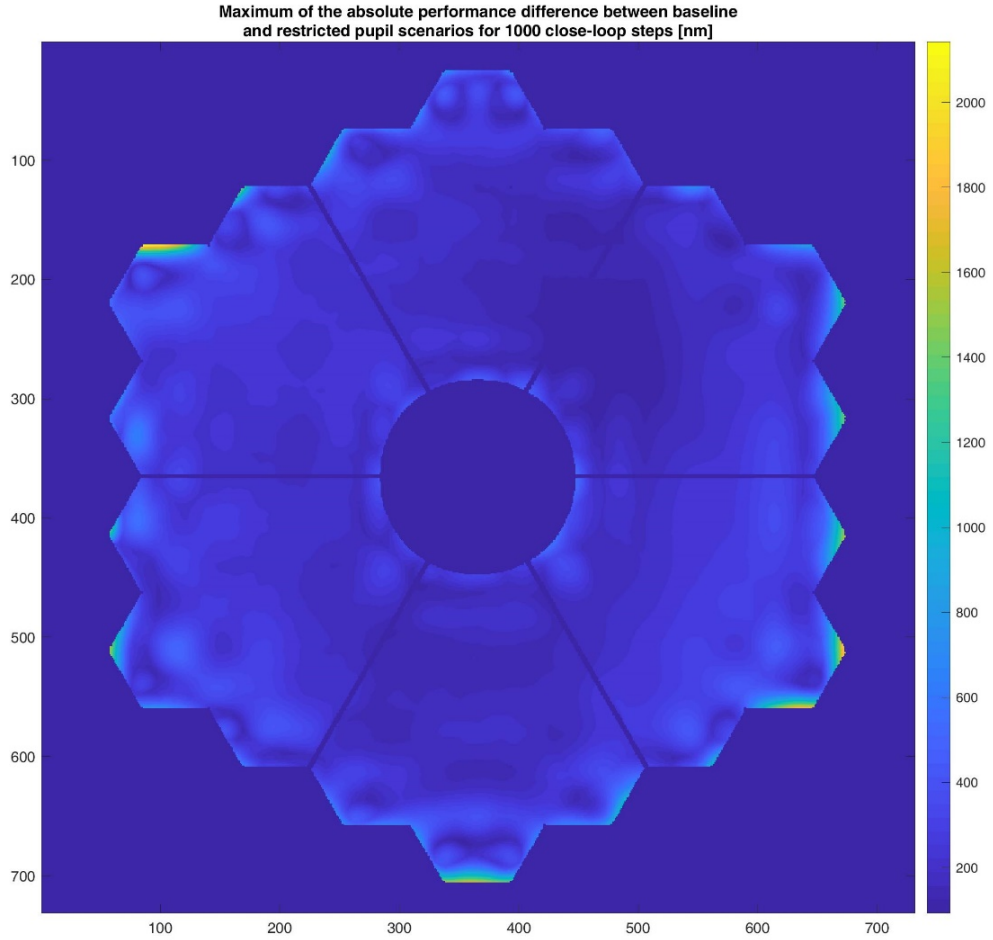

Figure 3.13: Mean absolute wavefront difference between the two scenarios for 1000 closed-loop instances [nm].

Tolerancing of different variables and modules examined factors including: the Keck DM IF model that is being used, the minimum light ratio for activating PWFS pixels, and the threshold of the number of modes for the SVD process. The results show that none of the above factors contribute significantly to the $\sim$ 100 nm RMS difference in the wavefront error. The effect of changing the minimum light ratio on this difference was particularly revealing as it directly ruled out a theory about the origin of this error. This previous theory suggested that the main component of the edge effect comes from the fact that when we reduce the pupil shape to the restricted pupil in the IM modification process, we are creating a specific illumination pattern on the edge PWFS pixels which makes their response dramatically different than the fully-illuminated pixels.

I tried a range of minimum light ratios between 50% to 100%. With a 100%

illumination ratio, only PWFS pixels that received the same amount of light in both BLS and KPS were considered. Tests showed no significant differences in the error between the two scenarios respective to the light ratio. This result suggested that the previous theory might not be accurate and there should be a different explanation for this error. This simulation suggested there is an important wavefront error term associated with the control algorithm in the presence of the spider shadow. This effect is much more significant compared to the effect of partially illuminated PWFS pixels, contrary to previous thoughts.

Overall, regarding the required error budget for the Keck IR-PWFS, the simulation demonstrates that [72]:

- There is tolerable impact on the Keck PWFS performance solely due to the presence of the spiders, as they are small compared to the WFS pixel size, but there should be a more sophisticated control algorithm used at the edge of the illuminated area.
- It is feasible to calibrate the interaction matrix for the PWFS, taking into account differences in the pupil shape between the true Keck pupil and the calibration source, without exceeding the required wavefront residual budget.

3.2.2 Impact of Spider Shadows and Use of Synthetic IM on the Performance of PWFS

I also studied the impact that spider shadows and the application of synthetic IMs have on the performance of Extremely Large Telescope (ELT) and Thirty-Meter Telescope (TMT) AO systems. One aspect of pyramid wavefront sensor performance requiring more study is the impact of spider shadows on the wavefront measurements. Here, I first discuss the simulation used to initially attack this problem, and then in Section 3.3, I provide a practical method to verify the result of this study on a AO bench.

Simulating Extremely Large Telescope AO Systems

I used the OOMAO (Object Oriented Matlab Adaptive Optics [19]) simulation platform to simulate PWFS AO systems for two future thirty meter class telescopes, ELT and TMT. The precise pupil and spider shape for these two telescopes are shown in Figure 3.14. These masks represent the precise form of the shadow that falls on the

telescope primary mirror, preserving the aspect ratios of different structures of the shadow and pupil shape, such as the spider structure and pupil rough edges.

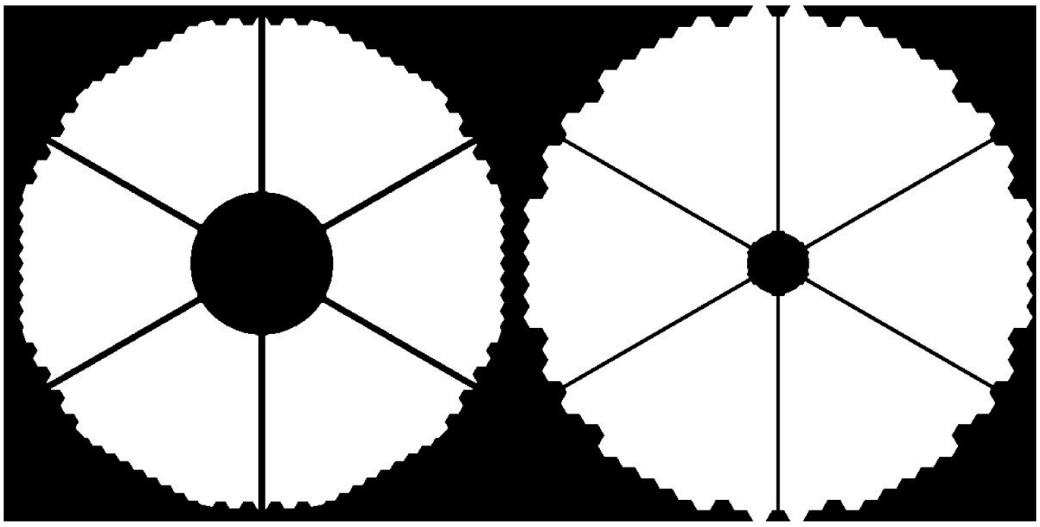

Figure 3.14: The pupil layout and spider structure shadow for ELT and TMT, respectively. Note, the projection scale for each telescope pupil is arbitrary.

While running the initial tests, we noticed an unlooked for issue was interfering with our study - the petalling effect caused by spider arms. As described in Section 3.1, the petalling effect is caused by the discontinuity between different sections of the primary mirror as a result of the thick spider legs. The ELT spider structure is supporting a much heavier secondary mirror (particularly the M4 mirror assembly) compared to the TMT design. ELT's heavier payload requires the spider legs to be significantly thicker, as shown in Figure 3.14. This thicker shadow on the wavefront sensor creates six separate segments instead of one continuously illuminated pupil. This in turn causes artifacts an order of magnitude larger (see Figure 3.15) than the finer impacts of spider shadow on PWFS and use of synthetic IM on AO system performance. To avoid the petalling effect, we focused our study only on the TMT scenarios. The island effect for ELT can be suppressed using special consideration in the control algorithm, which is outside the scope of this study [12, 15]. The result of our study will still be valid for the island-free case of ELT scenarios.

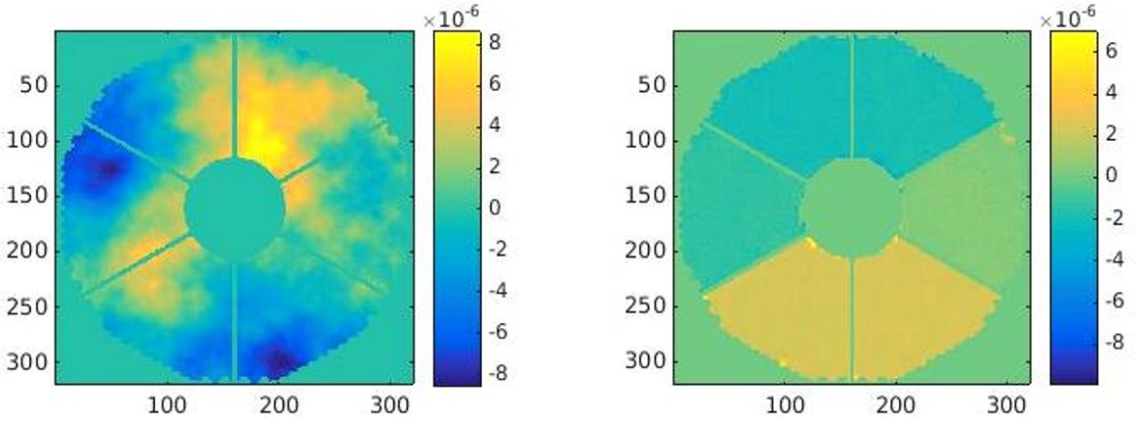

Figure 3.15: Left: The input wavefront. Right: the output (corrected) wavefront for scenario B2 (see next chapter) for ELT pupil layout. Note the significant piston difference between pupil segments. This is the island effect which is covering the artifacts of the effects that we aim to study for the ELT pupil layout. The units of the wavefront in the colour bar are meters and pixels for the X and Y axis.

Simulation Scenarios

I carefully designed different scenarios to compare as part of this simulation, and these are described in Table 3.3.

		Calibration IM		
Pupil status		No mask	Masked	Rotated mask
	No mask	B1	n/a	n/a
	Masked	SC1-SC1mod	B2-B2mod	n/a
	Rotated mask	SC2-SC2mod	SC3-SC3mod	B3-B3mod

Table 3.3: Simulation Scenarios: The "B" scenarios represent the baselines. The "SC" scenarios are the ones which are utilized an interaction matrix for different scenario without any modification. The "mod" scenarios are the ones where the interaction matrix would get modified before use.

Each row represents the status of the pupil plane and the presence of the spider or rotated spider. Each column represents different ways of utilising the interaction matrix to account for the effect of the spider shadow. The interaction matrix is the mathematical element that describes the interaction between the deformable mirror command and the wavefront sensor measurements. We considered different methods

to compensate for the effect of the shadowed region on the wavefront sensor on the AO system performance.

The "B" scenarios represent the baseline performance, meaning that we use each interaction matrix for its relative pupil scenario without any modification. The "SC" scenarios used interaction matrices for each different cases, but without any modification. For example, SC1 scenario represents measuring an interaction matrix, then applying it to a case in which the telescope pupil includes the spider obstruction without any modification. This scenario is especially important as it represents the typical realistic condition for AO systems in which the interaction matrix is measured using the calibration source and then used for on-sky corrections. The calibration source in these kinds of systems is typically injected into the input of the AO system by a fiber fed laser source. Since such a source does not pass through the spider structure, it does not contain the shadow pattern and illuminates the full disk on the WFS detector.

The "mod" scenarios use interaction matrices for different cases that are modified before use on a masked or rotated simulation. To modify the interaction matrices, we remove the rows of the interaction matrix that correspond to the shadowed pixels on the wavefront sensor detector. We identify these pixels by resizing the pupil binary mask to the size of the wavefront sensor detector size and use the nearest neighbour pixel algorithm to identify if the pixel falls on the vignetted or illuminated area.

In contrast with the initial expectations, the simulations suggest that modifying the interaction matrix to account for the presence of spiders in the pupil, at least in the TMT scenarios, may not be critical (Figure 3.16). These results so far provide a better understanding of the modified interactions matrix approach and highlight additional scenarios that need study.

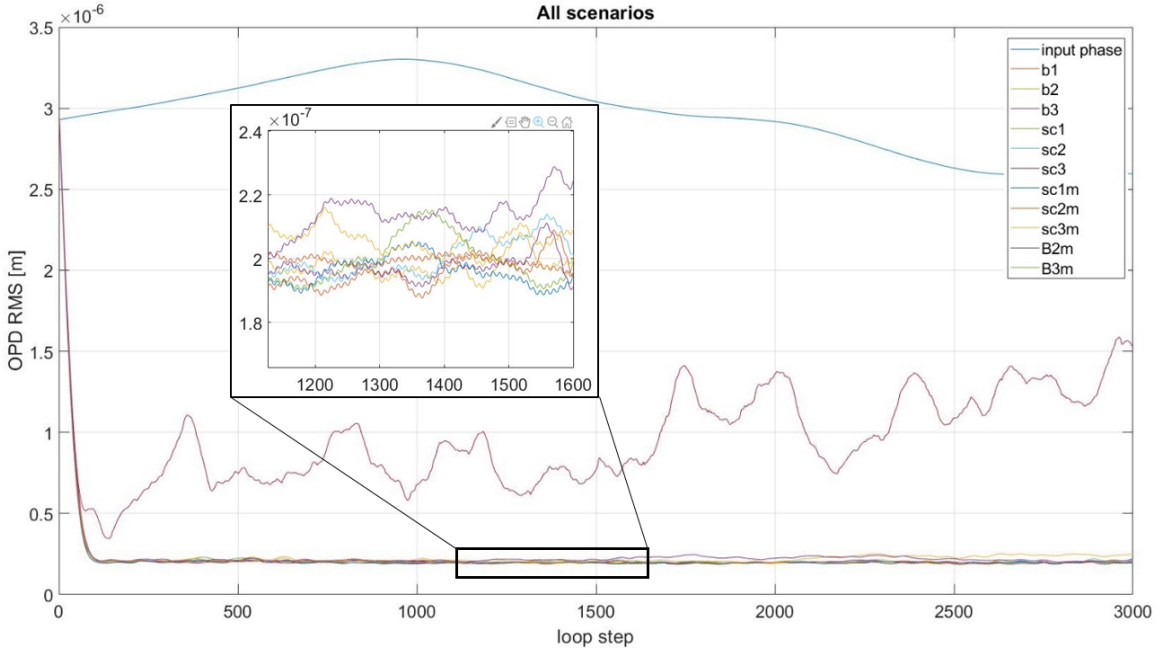

Figure 3.16: The primary result of the simulation. Except for the SC3 scenario, all other modified and unmodified scenarios are almost provided the same wavefront residual.

In all scenarios (except SC3), the modified, unmodified and baseline scenarios provided nearly equivalent close-loop performance. The SC3 scenario is an exception as it represents the case in which the masked interaction matrix is used for a rotated mask pupil configuration without any modification. The output of this particular case is predicted to be poor, but for the sake of completeness, it is still included in the simulation.

While the primary results are interesting, this research is still ongoing. An on-bench demonstration of these scenarios for the TMT case is planned for the updated advanced wavefront bench based on a SLM implementation at NRC facilities in Victoria. The details of this effort are presented in Section 3.4.

3.3 New Method for Injecting Pupil Binary Intensity Pattern into the Experimental Adaptive Optics Benches

The current method for injecting pupil intensity patterns into laboratory benches is to fabricate an intensity mask [44] and place such a structure in a pupil-conjugated plane. Considering the scale of a typical laboratory bench and beam size, this can easily translate to sub-millimeter elements in the pupil mask structure which are hard to fabricate, and are also expensive and difficult to work with. Additionally, the precise control of the position and clocking of the mechanical mask on a laboratory setup for emulating pupil rotation or wobbling is also a challenge with this approach. Finally, with the mechanical fabrication approach, each mask is built for a specific intensity pattern. This means that a new mask is necessary to model each different telescope. In this section, we propose a new solution to this challenge based on SLM technology. This solution does not need any mechanical fabrication and provides ultimate flexibility to shift or rotate or change the intensity pattern.

3.3.1 Methodology

There are different types of SLM devices with different physical properties. The most common and commercially available devices are the phase-only LCoS-SLMs [106]. The refraction index of some special materials such as liquid crystals can be changed by applying voltage. By utilizing such a material, LCoS-SLMs devices are able to control the phase of the reflected wavefront. Originally, SLM technology has been used in optical communication and optical projection applications [84], but is being used more commonly for phase modulation on AO laboratory benches [49, 79, 48, 1]. SLMs can provide similar functionality as deformable mirrors (DMs) in such setups. The main differences between the two are:

- Typically, SLM devices have many more controllable phase units than DMs and are significantly cheaper.
- Since deformable mirrors have reflective mirror surfaces, they are achromatic. The performance of SLM devices are a function of wavelength and therefore are typically used in monochromatic setups.

- The response time of commercial SLMs is on the order of 10 ms, which is significantly slower than typical deformable mirrors.
- The stroke of each controllable phase unit (i.e. actuator, liquid crystal pixel) of SLM devices is significantly smaller than deformable mirrors, however there are methods to emulate high dynamic range phase patterns with SLMs by using phase wrapping.

Although SLM technology is not yet suitable for on-sky applications, it is an ideal choice to serve as a high-resolution, affordable deformable mirror on monochromatic laboratory benches. Utilising two SLMs conjugated to the pupil and focal plane, the LAM/ONERA Pyramid Sensor (LOOPS) optical bench [48, 14, 51] (see Figure 3.17) in Marseille provides a comprehensive testbed for AO studies.

The focal plane-conjugated SLM makes it possible to extensively study Fourier-based wavefront sensing techniques such as generalised forms of Pyramid WaveFront Sensors (PWFS) [49, 79] while the pupil-conjugated SLM is used for phase modulation purposes such as injecting atmospheric or custom phase turbulence into the optical path [99]. This architecture along with the utilisation of the parallel Shack-Hartmann WaveFront Sensor (SHWFS) and advanced detectors provides the LOOPS bench with the flexibility for a wide range of AO research and studies. In collaboration with LAM, we designed and demonstrated two experimental approaches to use the pupil-conjugated SLM for intensity pattern injection, adding new abilities to the LOOPS bench.

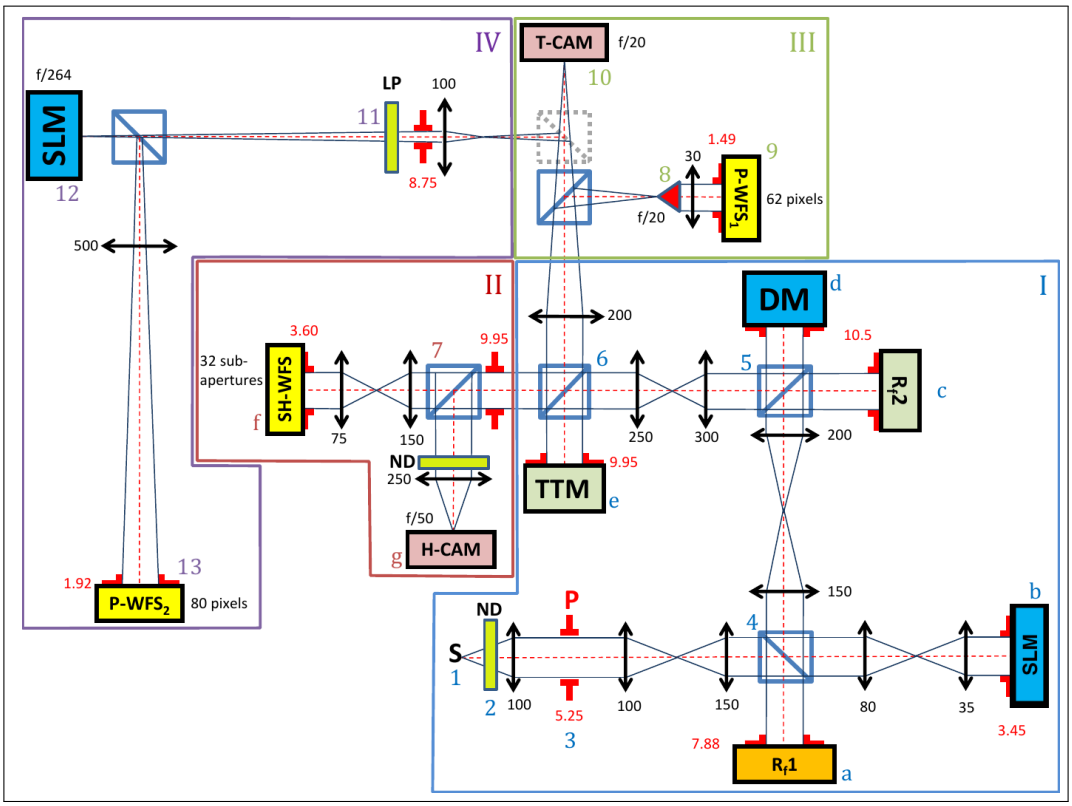

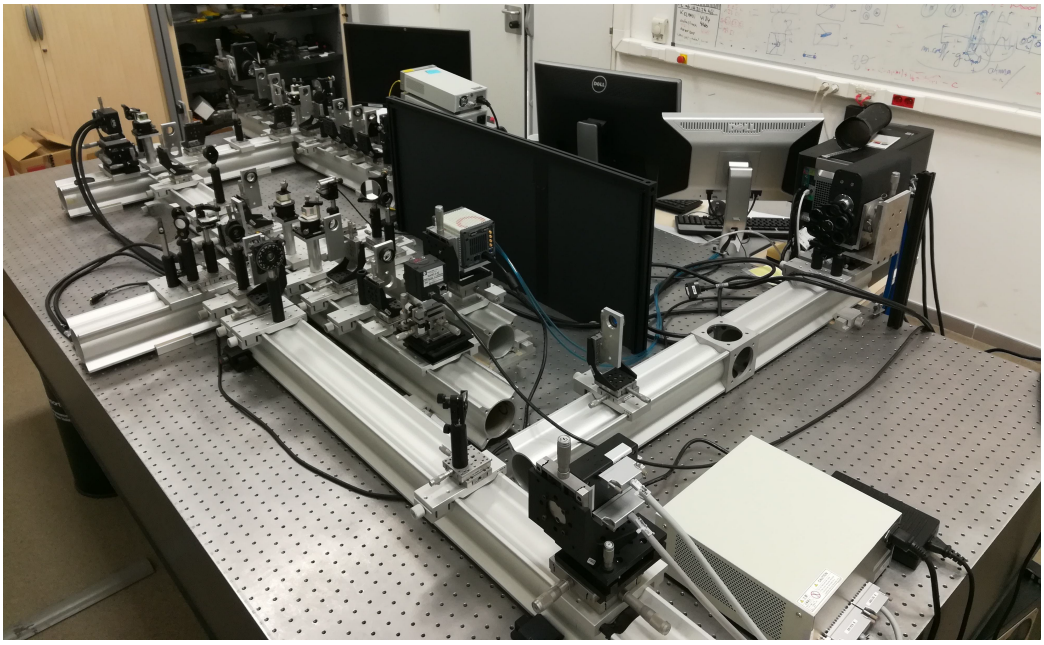

Figure 3.17: The LOOPS bench: Schematic design and laboratory setup.

3.3.2 Approach A: Cross Polarization

LCoS-SLM devices modulate the phase only across a certain polarization vector. The perpendicular polarization component of the beam would remain untouched and should be filtered from the system. In the cross polarization approach, the device is placed between two perpendicular linear polarisers with 45° between the polarization vector of the SLM and filters. The first polariser is placed before the SLM device, turned 45° respective to the working vector of the SLM. The second polariser is placed after the SLM, turned 45° respective to the working vector of the SLM and 90° respective to the first polariser filter. Without modulation, no light would pass through the system. However, applying voltage to the SLM pixels changes the polarization between the two perpendicular filters, hence allowing some of the light to pass through. The schematic of this method is shown in Figure 3.18.

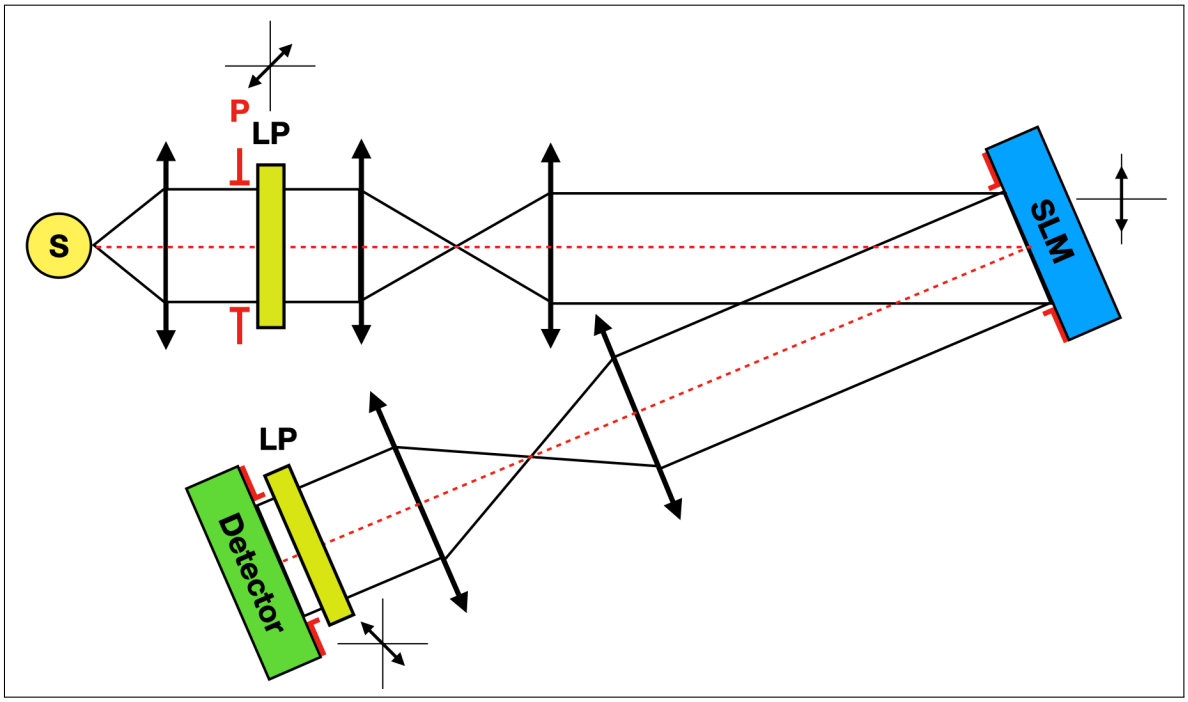

Figure 3.18: The schematic of the cross polarization approach.

3.3.3 Approach B: Focal-Plane Filtering

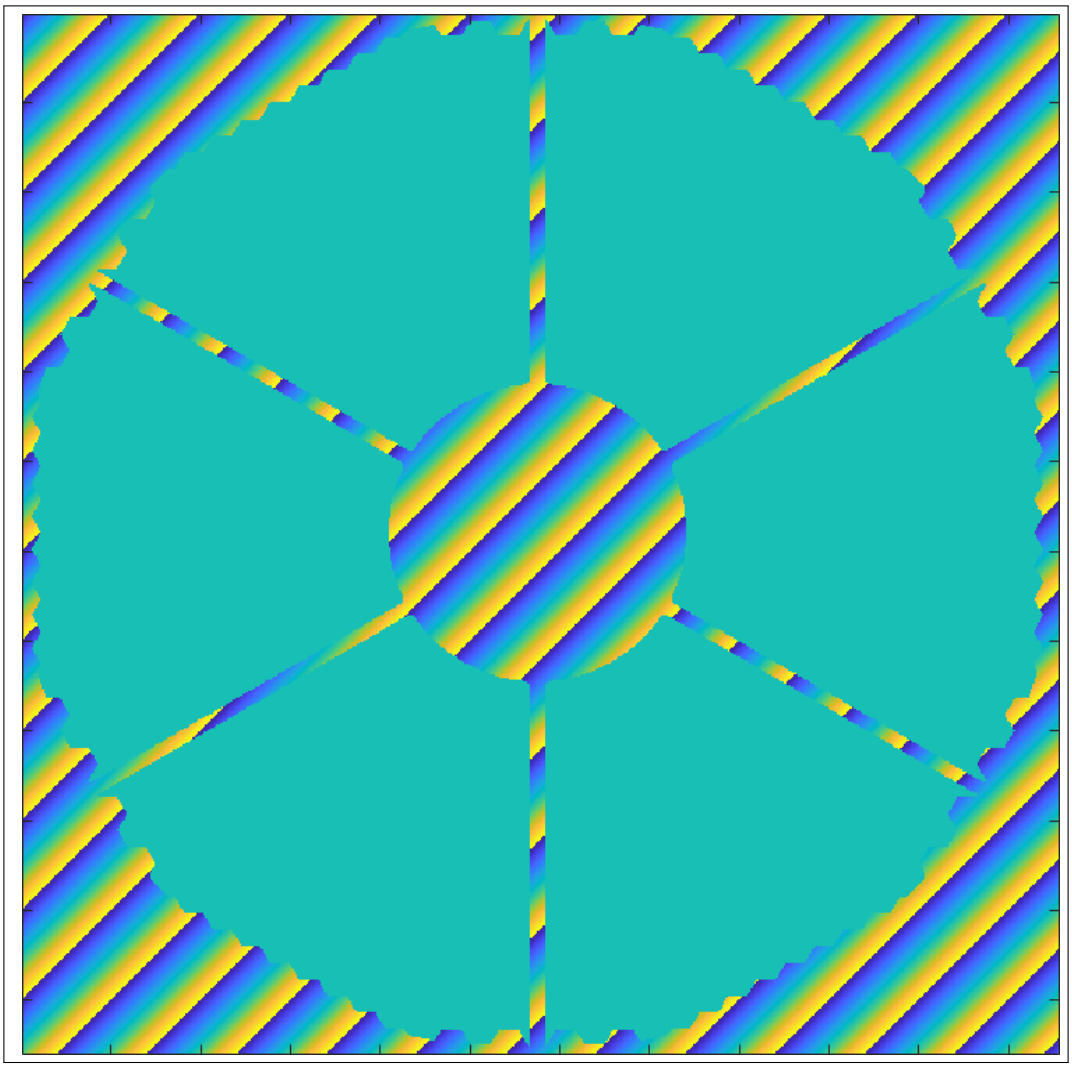

Figure 3.19: An example of pupil SLM phase modulation pattern for ELT pupil and spider structure. The light from the shadow region is diverted to a large separation of the optical axis using a phase wrapped high angle tilt-tip pattern. The illuminated region of the pupil (the flat green region) can be used to inject a custom phase pattern into the system.

In the focal plane filtering approach, the light in the shadowed region is diverted to a certain point in the focal plane by applying an intense tilt/tip pattern (see Figure 3.19). The off-axis illumination pattern is then filtered in the focal plane using a spatial filter such as an iris. This approach also filters out the non-modulated

and non-polarised portion of the light resulting from the realistic SLM fill factor. SLM pixels are not ideal and there are typically 4-10% of the surface area that are not optically active. The reflected light from this region reduces the contrast and increases the noise of the experiment results. To filter out this residual, it is possible to add a tilt to the desired phase modulation pattern and filter the non-modulated part using an off-axis iris. It is possible to add intensity pattern injection by utilising the same concept, diverting shadow light to the opposite direction of the focal plane and filter it the same way. A simple schematic of such a layout is presented in Figure 3.20.

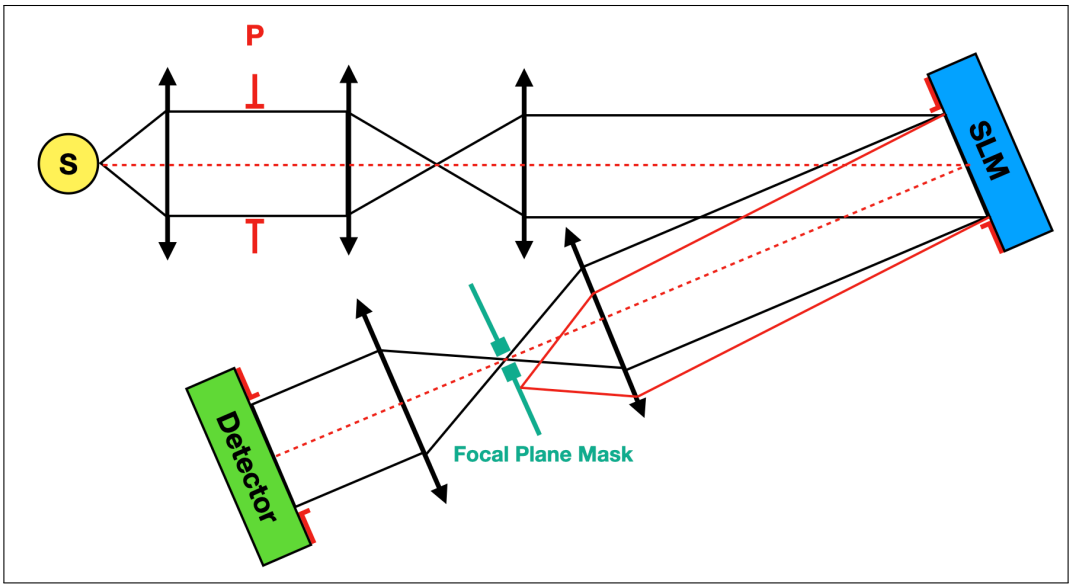

Figure 3.20: Schematic of the focal plane filtering approach. The red beam contains the light from the shadow area which is tilted and filtered in the focal plane.

3.3.4 Results and Method Comparison

I successfully implemented both methods on the LOOPS bench. Both methods provide similar contrast (the ratio of the normalised flux in the shadow to the illuminated region) sufficient for the majority of AO applications. However, the other considerations such as complexity and the ability of simultaneous phase and intensity modulation make them distinct.

The result for the cross polarization method is shown in Figure 3.21. By fine tuning the phase shift of SLM pixels and the angle between linear polarisers, a contrast

of 2% is achieved. This method is easier to implement, but two focal plane conjugated SLMs are necessary for simultaneous phase and intensity control. It should be noted that producing gray scale illuminated patterns (i.e. simulating atmospheric scintillation effects) is not possible with this approach as any shift in intensity would be accompanied by an undesired phase modulation.

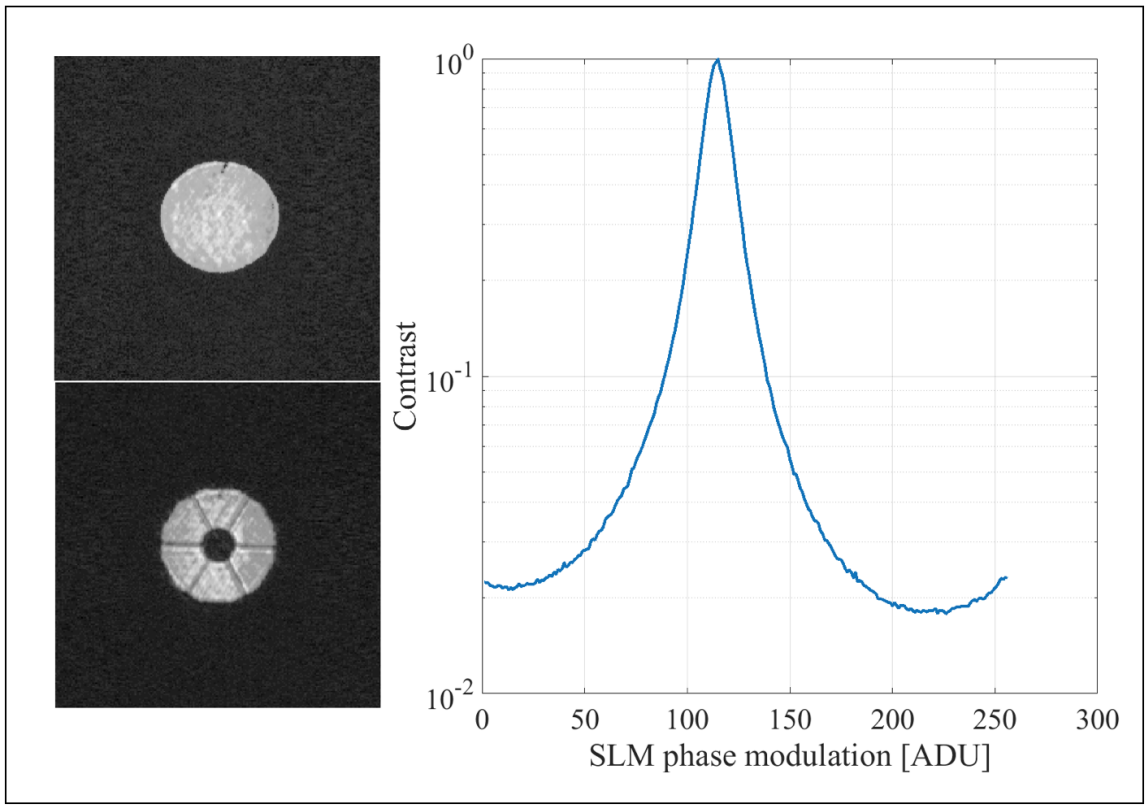

Figure 3.21: The result of the cross polarisation approach. Left: the pupil intensity before and after injecting the intensity pattern. Right: The contrast per SLM phase input. The contrast of 2% is achieved through this method. The E-ELT pupil shape and spider shadow (see Figure 3.1) is used as the intensity pattern.

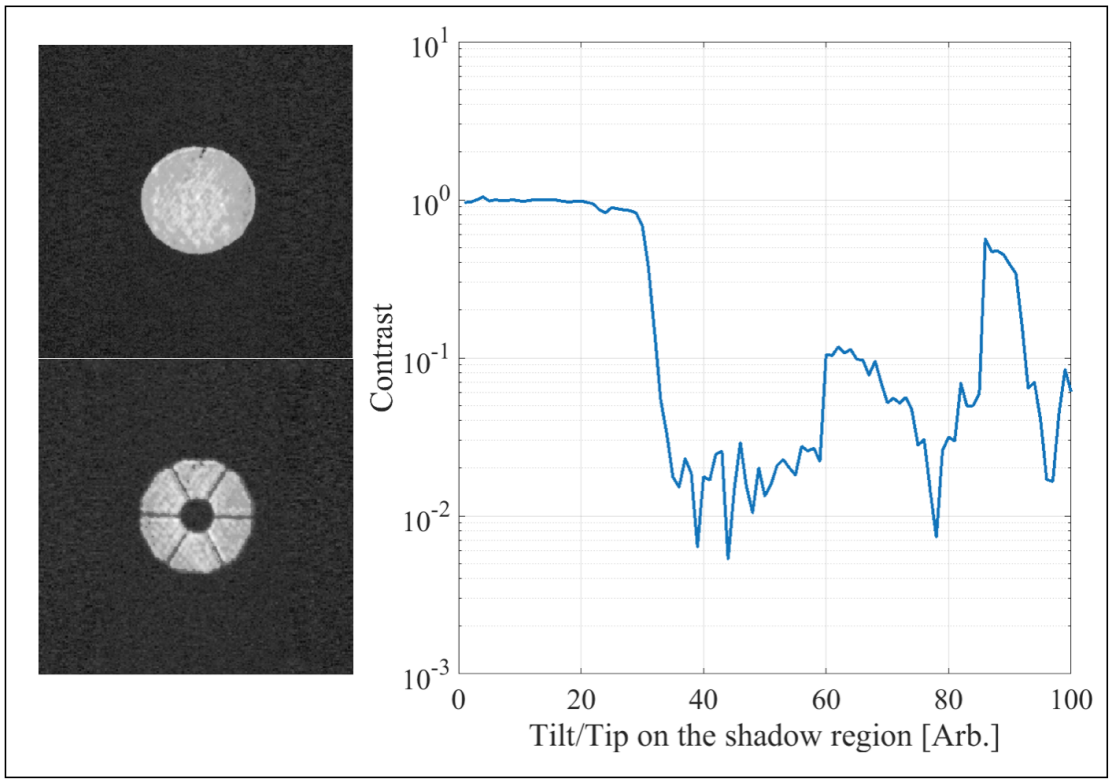

Figure 3.22: The result of the focal plane filtering approach. Left: The pupil intensity before and after injecting the intensity pattern. Right: The contrast per input tilt for the shadow region. In the optimum configuration, contrast of 0.5% is achieved. The ELT pupil shape and spider shadow (see Figure 3.1) is used as the intensity pattern. Note that the contrast curve is irregular in comparison with the cross polarisers approach. This is due to higher order diffraction pattern caused by the SLM phase wrapping. This particularly makes the fine tuning focal plane approach relatively more challenging.

Using the focal plane filtering approach, an improved contrast of 0.5% can be achieved. However, this method requires more fine tuning. The most sensitive alignment aspect is to correctly account for the tilt/tip of the shadow region and the size of the off-axis pupil in a way to filter out undesired light and simultaneously pass the light of the desired Point Spread Function (PSF) and its wings. This is more difficult especially when dealing with higher-order diffraction spots caused by phase wrapping. An example of such spots can be seen in the top left panel of Figure 3.23. The amount of tilt/tip for the shadow region should be carefully chosen so that the off axis spot be moved significantly far from the main PSF wings and at the same

time, there be no high-order diffraction spot on the top of the main PSF. The major benefit of this method is the ability of using the same SLM for simultaneous phase and intensity modulation. The result for this approach can be seen in Figure 3.22.

Since simultaneous phase modulation is possible in this approach, we also closed the loop while injecting ELT's pupil structure and spider pattern. The simulated and on-bench PSFs can be seen in the top panel of Figure 3.23, as well as high-resolution images of the pupil intensity pattern for ELT and TMT in the bottom panel.

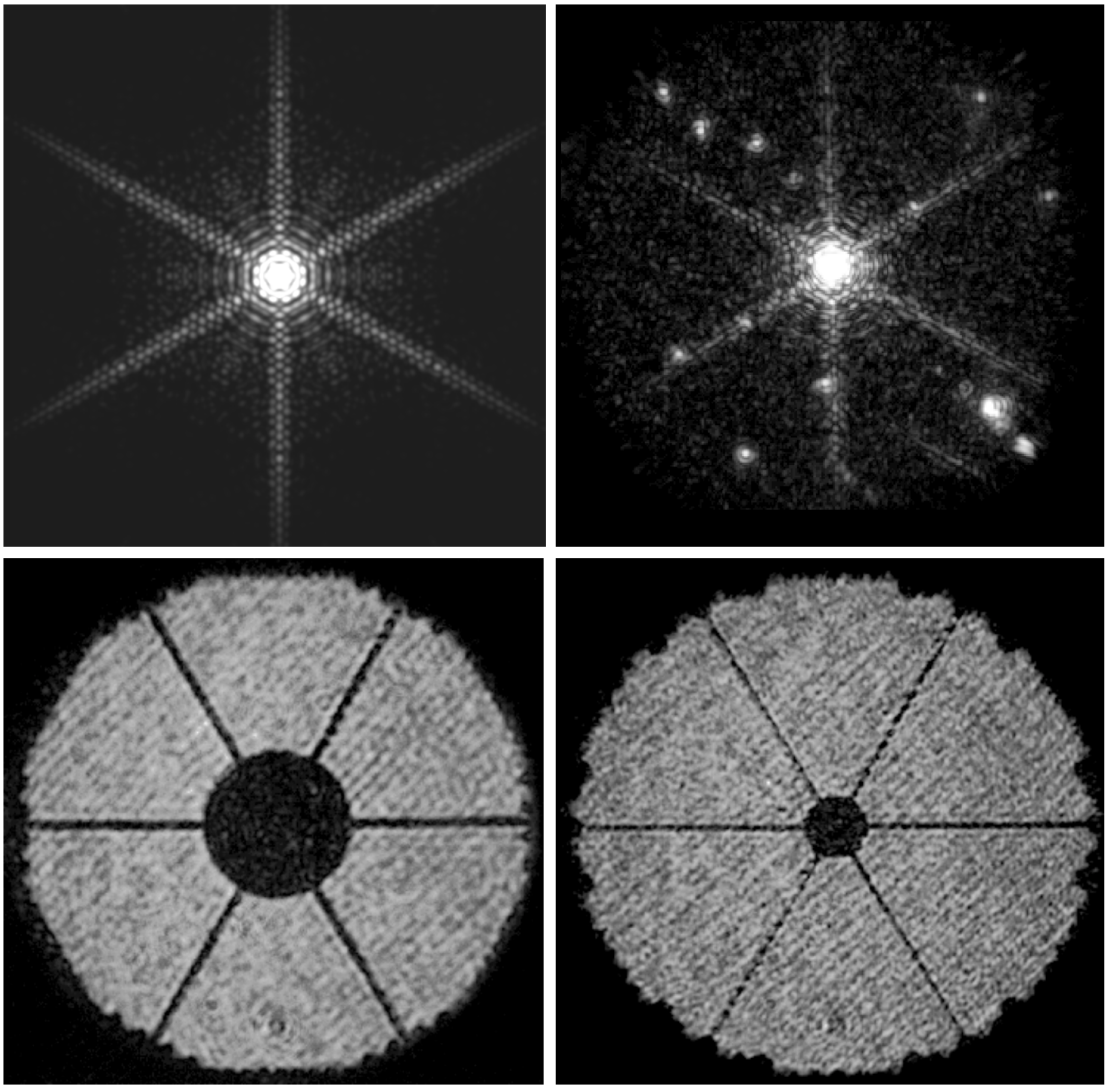

Figure 3.23: Top panel: Simulation and close loop demonstration of the PSF shape for ELT pupil structure. The close similarities between the two PSF demonstrates the success of the intensity pattern injection using the SLM device. The vignetting on the top tight image is caused by the focal plane filter/iris. Note the few fainter spots at 4 and 10 o'clock of the main PSF. They are ghosts of high-order diffraction spots caused by the SLM phase-wrapped tilt/tip pattern. Bottom panel: The high resolution pupil images demonstrated on the LOOPS bench for the intensity structure of ELT (left) and TMT (right) pupils. The faint diagonally striped pattern is caused by the internal diffraction of the beam splitters and is not related to SLM or intensity pattern injection.

3.3.5 Summary and Discussion

We successfully demonstrated two different approaches to inject high-precision intensity patterns into the LOOPS AO bench. These methods are based on phase-only LCoS SLM technology. This technology has some limitations such as wavelength dependent modulation coefficient, however the significantly higher resolution and affordability makes it a desirable substitute for deformable mirrors for a wide range of experiments. The ability of emulating the precise pupil shape and the effect of spider shadows on the performance of the AO system and PSF shape is essential for advanced AO instrument laboratory setups. Study of important challenges such as the effect of partially illuminated pixels on the performance of PWFS and PSF shaping for high-contrast imaging are strongly dependent on such an ability.

In comparison, the focal plane filtering method has two major benefits: the ability of simultaneous phase and intensity control using only one SLM device and the removal of non-modulated light leaked by the not-ideal fill factor of SLM pixels. However, tighter alignment tolerances make it relatively more difficult to implement. This is because two simultaneous effects should be considered in the alignment of the focal plane iris in this method. On the one hand, the iris should be as wide as possible to not filter the wings of the desired PSF, which is particularly difficult in cases where intense high-tilt phase patterns are used. On the other hand, the size of the pupil should be smaller to not let any of the higher order diffraction pattern caused by SLM phase wrapping pass through the focal plane or superimposed by the desired PSF. This limitation makes this method more suitable for the tilt/tip removed or closed-loop residual phase scenarios.

The cross-polarization method on the other hand is more straight forward to setup, although in our experience the resulted contrast is slightly less than the focal plane filtering approach. It should be noted that both approaches provide the ability of injecting binary intensity patterns only and neither are suitable for emulating gray scale intensity phenomena such as the atmospheric scintillation.

3.4 Accommodating SLM: The new Design of Advanced Wavefront Sensing Bench

In Section 3.3, I successfully demonstrated injecting precise binary intensity patterns using a SLM on laboratory AO benches. The solution is not only inexpensive and

precise, but it also does not require any mechanical fabrication and can easily apply any custom spider shadow. It also provides the ability of implementing real-time dynamic patterns such as the rotation of the spider pattern relative to the WFS detector and pupil wobbling effect. This was demonstrated on the LOOPS bench at the Laboratoire d'Astrophysique de Marseille facilities in France. The ultimate goal after proving the feasibility of this SLM application was to transfer and implement this solution on the Advance Wavefront Sensing (AWS) Bench at NRC facilities in Victoria, B.C., Canada.

The AWS is NRC's testbed for new WFS technologies, including the PWFS. One of the interesting questions to look at in the error budget of NFIRAOS is the effect of spider shadows on the performance of the pyramid truth WFS, which is responsible for monitoring and compensating for the fluctuation of the high-altitude sodium layer. Inspired by the LOOPS bench (see Section 3.3.1), I re-designed the AWS bench to enable the capability of having SLM technology and PWFS on the same bench. The new optomechanical design provides extra capabilities such as a pupil monitoring camera, as well as pre-allocated space to accommodate future experiments. I designed the Zemax model of the previous arrangement of the AWS as shown in Figure 3.24. This relatively simple setup provided room for two, or in the case of small devices, three simultaneous experiments.

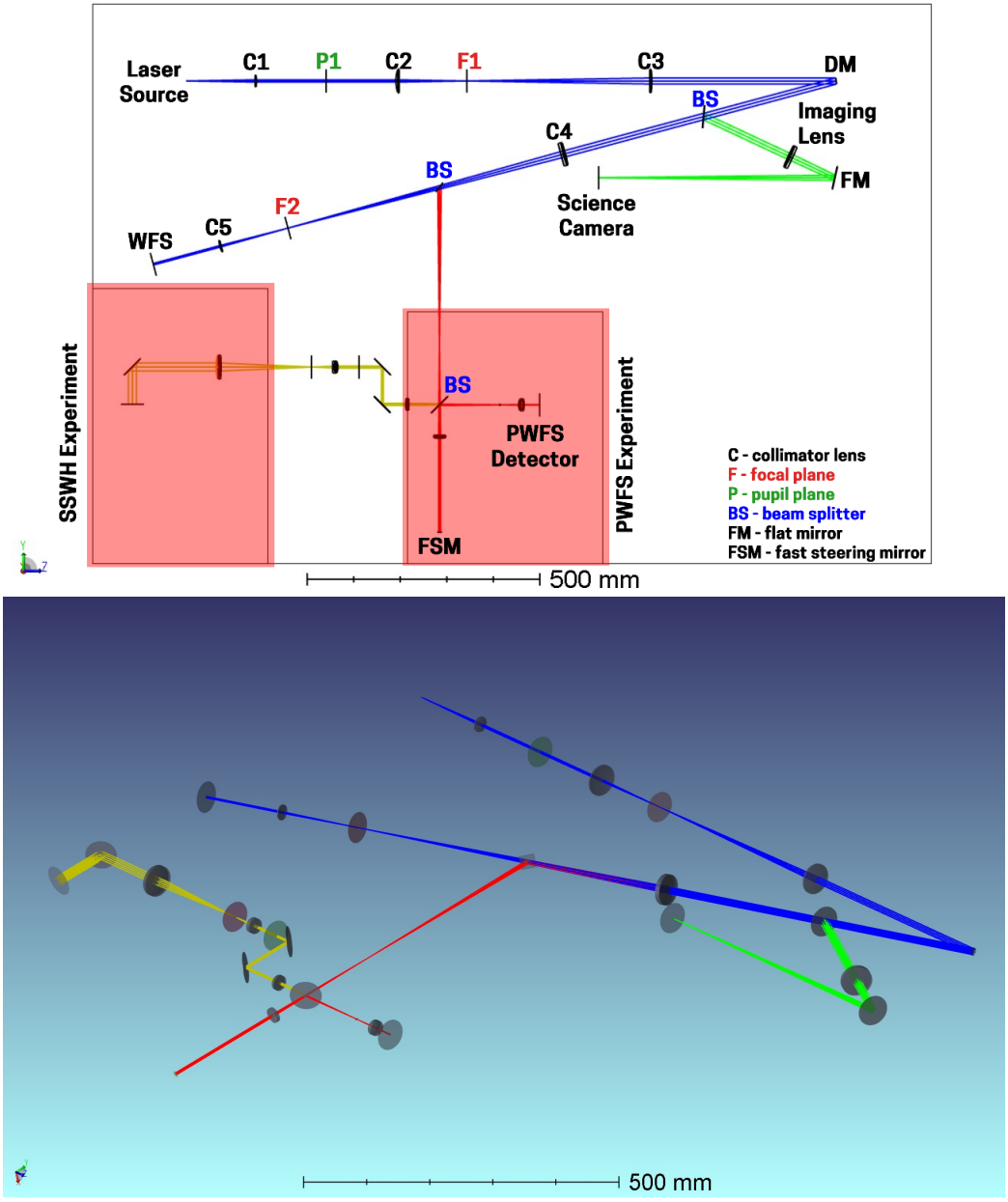

Figure 3.24: The Zemax design of the initial state of the AWS bench.

The new design of the AWS bench is presented in Figure 3.25. In the new design, in addition to accommodating the SLM, other important factors are considered as explained below:

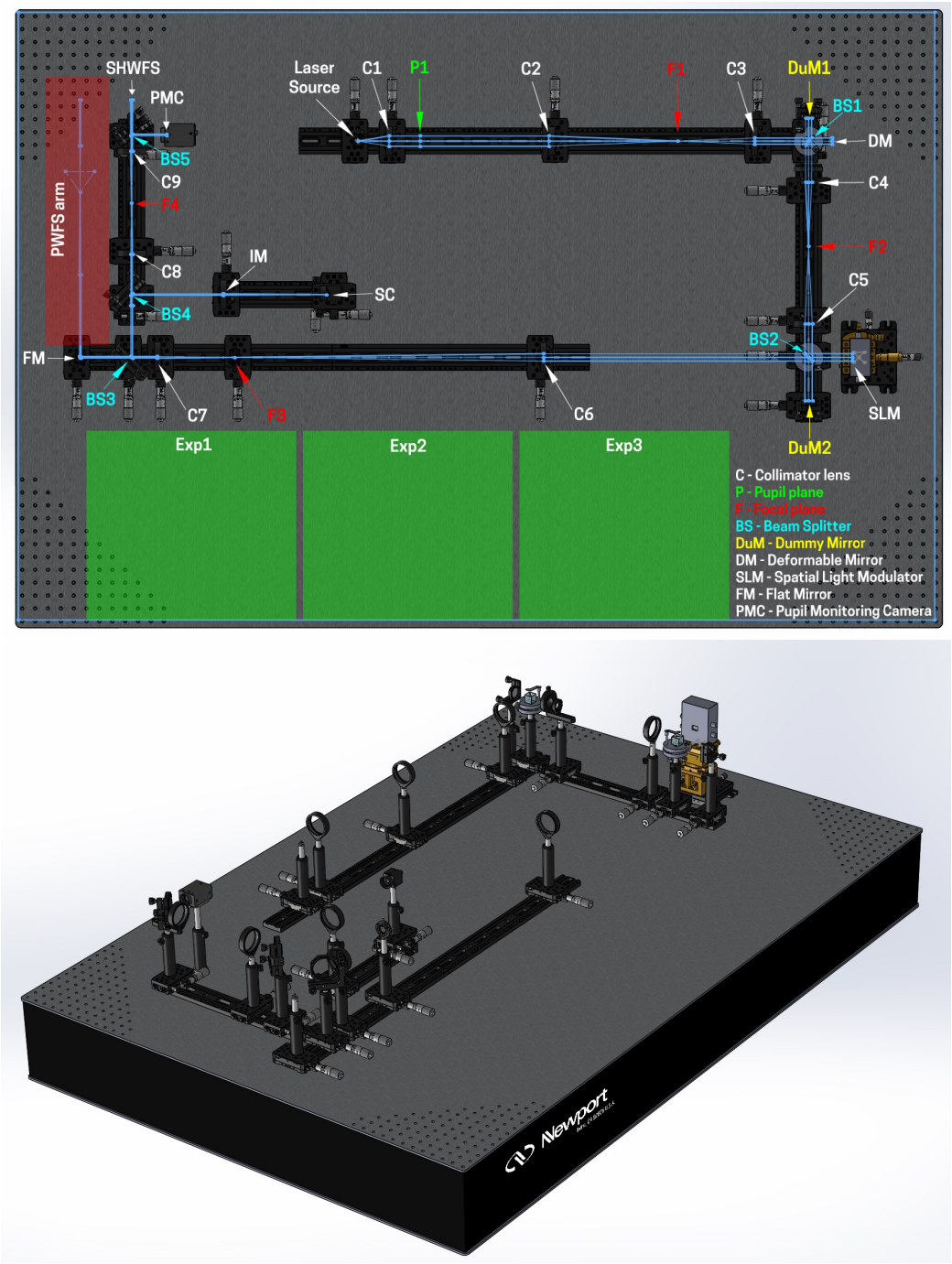

Figure 3.25: The CAD design of the new AWS bench arrangement. The light blue lines on the top panel indicate the optical path.

- Instead of using post holders as in the previous design, I used 2" wide dovetail rails and compact quick connect linear stages from Thorlabs. This makes

alignment of each arm and future modifications easier and more robust (see Figure 3.26).

Figure 3.26: The 2" wide dovetail rails and compact quick connect linear stages. The stage can only move along the rail which makes the alignment of each arm considerably simpler compared to using the traditional free-to-place stages for this application.

- In the previous design, the DM was tilted ~ 25 degrees to eliminate the use of a beam splitter. Although it is simpler to implement, such a tilt will change the projection of the circular shape of the DM to an ellipse. In the case of an SLM, it can additionally reduce the reflection and efficiency of phase modulation. In the new design, I used cube beam splitters at two points of the optical design providing perpendicular angles of incidence for both DM and SLM surfaces.

- In addition to the previous point, using beam splitters in front of active optical elements such as the DM and SLM has another advantage, which is providing placement positions for implementing dummy surfaces. Dummy surfaces, as placed in the new design, are extremely handy during initial alignment as well as monitoring alignment over time. Also, they provide the option of easily removing active optical elements from the path simply by covering and uncovering the dummy mirror.

- I added a pupil monitoring camera in the new design of the bench. Such a

camera is essential for experiments which utilise the SLM for intensity injection into the pupil, such as emulating the spider shadow, and studying the pupil rotation on the performance of the AO system.

- All optical components have one-dimensional micrometer adjustment (X direction) as well as smooth motion along the graduated rails (Z direction).
- The science camera stage is provided with two-dimensional micrometer adjustment in the direction of X and Z. This feature proves to be very useful as it provides very accurate manual focusing capability, as well as one-dimensional adjustments for the placement of the PSF on the science detector.
- A stop (on the position of F3 in Figure 3.25) is designed after active elements and before WFSs to remove ghosting effects from the optical path as well as the higher order SLM diffraction pattern (see focal plane filtering in Section 3.3.3).
- I designed a special mount for the SLM. The SLM requires very accurate adjustments not only on XYZ, but the tilt angle as well. This is essential to make the focal plane filtering process (see focal plane filtering in Section 3.3.3) possible along the optical axis. Without considering this degree of freedom for the placement of the SLM, all optical elements after it should be individually aligned after each focal plane filtering adjustment which is difficult and very time consuming (see Figure 3.27).

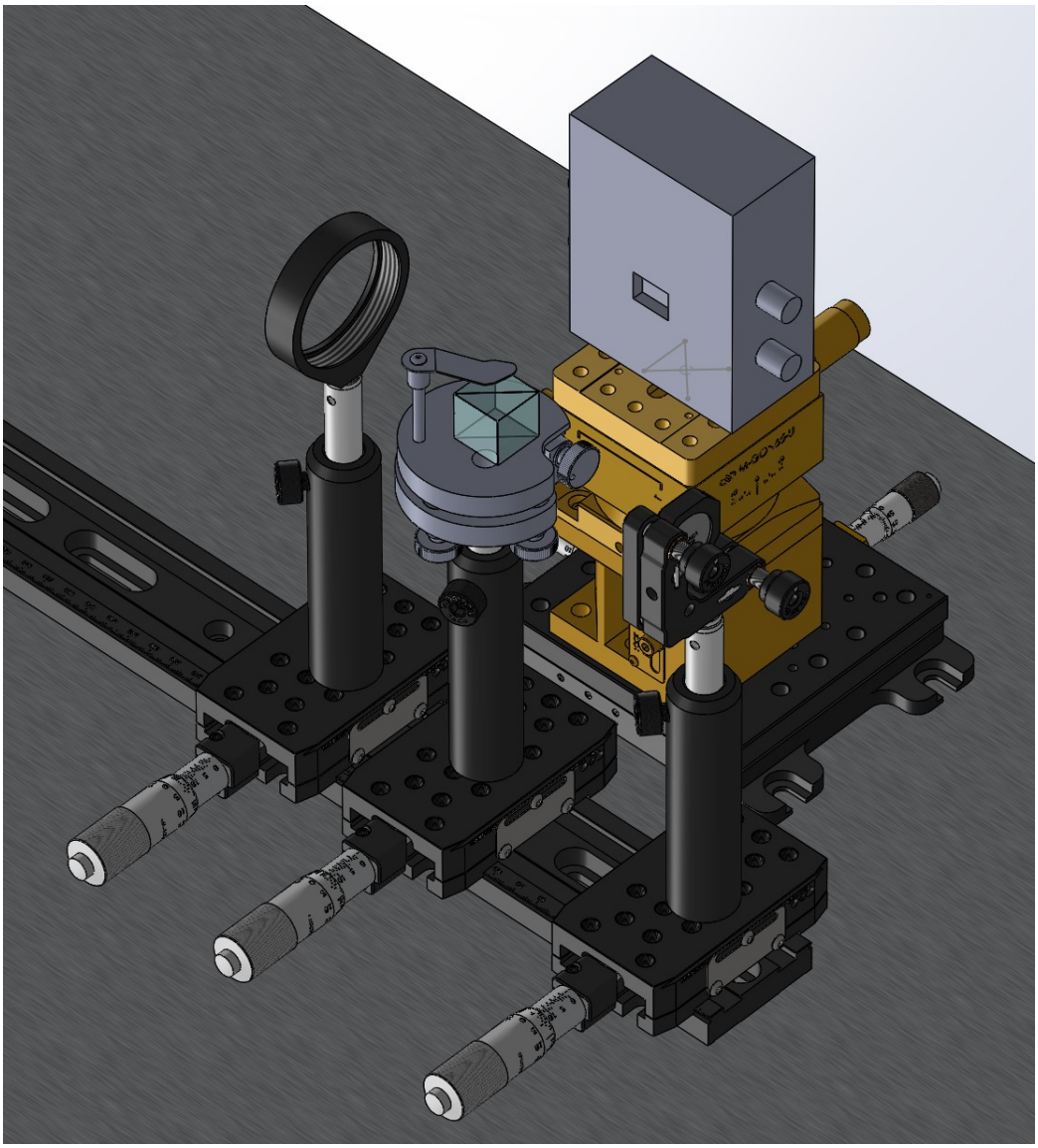

Figure 3.27: The gray SLM box on top of the yellow XYZ and tilt mount in my design. The dummy mirror and cube beam splitter also can be seen in the foreground.

- This new design also provides extra room for three simultaneous experiments in addition to simultaneous SHWFS and PWFS measurement capabilities.

I also specified the requirements for the SLM used in the new bench design. Table 3.4 provides the technical specification for the most suitable models from different manufactures. I narrowed down these four final competitors carefully from over 50 different options.

Model	PLUTO2 15	PLUTO2 11	1950x1152 series with 600-1300 coating	x10468-07
Manufacture	Holoeye	Holoeye	Medowlark	Hamamatsu
Type	ref	ref	ref	ref
Modulation	phase	phase	phase	phase
Fill factor	%93	%93	%95.70	%98
Reflectivity	%65-73	%65-%75	%78	%79
Frequency	60hz	60hz	31 hz	30hz
Resolution	1920x1080	1920x1080	1920x1152	800x600
Active area	15.3x8.6	15.3x8.6	17.6x10.7	15.8x12
Pixel size	8 μm	8 μm	9.2 μm	20 μm
Max phase shift(p/v)	∼1700nm	∼1100nm	∼640nm	∼700nm
Dynamic range	8-bit	8-bit	8-bit	8-bits
Matlab compatibility	Y	Y	Y	Y
Price	∼15K USD	∼15K USD	∼15K USD	∼17K USD
Wavelength range	650-11008 nm	420-1100 nm	600-1300 nm	620-1100 nm
Notes	High Retardation Version-Low phase flicker	”Broadband Use Fast Response Time”	-	-

Table 3.4: Table of four most suitable options for AWS AO bench application. The selected device should be as versatile as possible, having the capability of supporting a wide range of experiments considering available laser sources, reflectivity and fill factor.

After careful consideration, I chose the Hamamatsu x10468-07 for the AWS bench. In addition to other factors mentioned in Table 3.4, the important reasons that led

to this choice was the higher fill factor[3] compared to the other options.

The design of the new bench was finalised in February 2020 and I placed the order for all the components. Unfortunately, soon after that, laboratories at NRC closed as a result of the COVID 19 pandemic. This experiment will be set up in the future at NRC and I hope to be involved, but this will have to be done after the completion of my thesis.

3.5 Summary

The multiple effects caused by the spider structure in large-scale, ground-based telescopes can degrade the performance of their AO systems. The Island/Petalling effect, the effect of partially illuminated sub-apertures/pixels and the low-wind effect are three examples of such effects. The error budget of such effects on AO performance is still under investigation, and it is especially important for this to be well understood for the design and fabrication of ELT AO systems. The research methodology to study such a phenomena is typically based on simulation and lab verification cycles. The lab verification for the spider shadow effect has always been a difficult challenge to face, as fabricating precise shadow masks of such a fine structure in addition to installing and adjusting it on an AO laboratory bench is not an easy procedure. In this chapter, in addition to performing simulations on real-world systems, I introduced a method to inject precise binary intensity patterns into laboratory AO benches using phase only LCoS-SLM devices. In addition to being inexpensive and precise, this method is extremely flexible for inputting different spider patterns as well as applying adjustments such as rotation on a pattern. In collaboration with the Laboratoire d'Astrophysique de Marseille, I proved the feasibility of this method on the LOOPS bench. Finally, I provide a new opto-mechanical design for the AWS bench to enable such a valuable ability at NRC's AO facilities in Victoria, Canada.

[3]fill factor is the ration of area of each SLM pixel which is optically active. The small region of each pixel which is not active acts as flat mirror. It is possible to filter the effect of non-active area to reach better SLM response as explained in section 3.3.3

Chapter 4

High precision, arcminute wide field, astrometry for MCAO-aimed ground-based observatories

This chapter is closely based on a paper [98] published by Taheri et al. (2022).

4.1 Introduction

The relatively wide, corrected, fields-of-view of the next generation of MCAO telescopes makes them ideal facilities to study the dynamics of dense stellar fields like the core of globular clusters [64, 30, 38, 82]. Critical to this science is the determination of residual astrometric errors that act to reduce the precision of astrometric data gathered by these systems, in order to develop methods to correct for them. Our group has previously examined GeMS data to determine the optimal methods for obtaining precision stellar photometry that takes into account the variation in the structure of the point spread function resulting from the MCAO performance [67, 101, 69]. Reference [62] also looked into the astrometric limits of GeMS/GSAOI in tandem with HST and compared the results to HST-HST proper motion measurements. Here, I use similar datasets to understand the global distortions of the MCAO system and their impact on science-based astrometric measurements across the field.

In astrometric studies, the principal scientific measurement is that of the position of stars (or other astronomical objects) in each observation/epoch relative to some invariable frame of reference. Although the array detectors used for these ob-

servations have linear spatial geometry, other factors - for example optical design imperfections, telescope structure flexure under a varying gravity vector and the AO performance [76, 7, 70] - can distort the linearity of the ideal field of view and degrade the precision of astrometric measurements. The resulting distortion field can typically be described by a complicated vector field that could be significantly time-variable depending on instrument structure design. For example, in the case of Gemini South and the GeMS/GSAOI system, the time variable changes are more significant due to the Cassegrain mounting of the AO system and the imager. The Cassegrain mounting increases the structure flexure effect caused by the varying gravity vector and eventually causes time-variable field distortion. This will be less of a problem for TMT and ELT as their designs mount these systems on the significantly more stable Nasmyth platform [47, 75].

In addition to flexure, another important factor that can contribute to the intensity of the distortion field is the optical design of the instrument. For example, the number of off-axis parabola (OAP) mirror relay pairs are an important design factor that affects the distortion field, since it is necessary to use two pair of OAPs in order to simultaneously eliminate phase and field distortion. However, GeMS only uses one pair of OAPs [70]. This causes the instrument to suffer from a field distortion component induced by the optical design. This is an important design lesson from GeMS that is now considered in the optical design of the TMT and ELT [45]. The net intensity of the overall distortion field caused by different factors can be much larger than the actual proper motion that is being measured for GeMS/GSAOI, as I will demonstrate later. Therefore, it is essential to develop methods to efficiently compensate for the distortion field of current and future generations of MCAO systems, in order to perform astrometry-focused science. I note that part of this methodology may include developing techniques that allow for the direct, on-sky, measurement of any remaining distortions in the optical system simultaneous to the science observations.

There have been many prior efforts to characterise and correct for the field distortion of AO instruments and improve the resulting astrometry. Some of these efforts are based on decomposing the field distortion into different components. Reference [17] was one of the first studies that efficiently decomposed different components of field distortion and astronomical uncertainties for an AO-assisted observation. This paper provided a complete analysis of the astrometric precision for a dataset that was taken using the Hale 200-inch telescope equipped with a classical AO system. In this

study, they found that differential tilt jitters are one of the most significant sources that degrades the precision of astrometric measurement. They also showed that it is possible to reach an astrometric precision of order 100 microarcseconds using three 2-minute observations for narrow angular separation and bright stars. A similar study was performed by [36] for the crowded field of the Galactic Center which reached similar conclusions.

However, these results are not necessarily valid for other flavors of AO systems. In MCAO devices, the tilt jitter effect is different compared to single-conjugate systems as multiple guide stars are being used. The field of view of the observation is also significantly wider (arcminutes rather than arcseconds). Reference [94] conducted one of the first studies for GeMS, and examined the absolute astrometric accuracy using background galaxies as a reference frame. They concluded that GeMS has an overall astrometric accuracy of order 400 microarcseconds. Reference [94] also provides a relatively detailed astrometric error budget for GeMS observations, and similar effort for characterising the error budget for an MCAO system have been done by [85]. These authors evaluated a comprehensive error budget for NFIRAOS/IRIS (the analogous instruments to GeMS/GSAOI for TMT; see [46, 47]. Based on this study, the expected differential astrometric precision for TMT in crowded narrow fields in K-band could be as small as 37 microarcseconds. Of course, results of this study have yet to receive on-sky validation.

Another approach for measuring the distortion field and improving the astrometric performance of AO systems is to use an internal calibration grid. Here, internal grid pinholes are illuminated to provide a reference measurement to study the distortion of the AO system. In this approach, the net distortion caused by the internal instrument optics is measured and can be compensated for. This method was originally considered for use in GeMS/GSAOI, and results of initial tests of the calibration grid are reported in [76]. However, it has not seen regular use in science operations thus far. Reference [76] suggests that distortion calibration can be done across the field of view with a precision of 170 microarcseconds RMS. More sophisticated technologies to fabricate and implement calibration masks are being considered for future improvements of GeMS [27] and large aperture telescopes like TMT [60]. Such techniques are more efficient in comparison to on-sky measurements considering the demands on telescope time, but by design they do not consider the entire system simultaneously. Cross-check and validation of these measurements with on-sky results will remain an essential component of astrometric studies.

In the absence of a precise distortion model for the relevant ground-based MCAO instrument, the main approach used to perform high-precision astrometry is to calibrate to on-sky observations that are "distortion-free". Typically, HST observations are used since this instrument and telescope are extremely well calibrated and the field distortions are well understood, and this approach has been used heavily with GeMS observations [37, 3, 24, 62, 10, 4]. Of course, in planning for the future, it is necessary to move towards precise methods that do not rely heavily on auxiliary observations (especially expensive space-observations), since it is just not practical to be dependent on space-based imaging for ground-based AO observations. It is with an eye to this era that I undertake the present study.

The work described in this chapter is one of the first steps to move towards independent, high-precision astrometry for the new generation of giant telescopes. I present a new methodology for the analysis, measurement and removal of astrometric distortions for GeMS, using HST/ACS as an auxiliary, first-epoch, dataset. This is a necessary, intermediate step, moving towards the ultimate goal of enabling precision proper motions from dual epoch MCAO ground based observations. As part of this analysis, I show how GeMS/GSAOI observations can be used to make empirical measurements of the optical distortion of the system that could be of use in understanding the behaviour of the system over time.

The target observations are of the globular cluster NGC 6723, taken as part of the observational program first presented in [22, 101] (GS-2013A-Q-16, PI: A. McConnachie). All globular clusters observed as part of this program also have HST/ACS observations [83]. The short term goal of this program is to study the space motion and stellar content of Galactic satellites seen with GeMS/GSAOI, and the long-term goal is to prepare for the exciting photometric and astrometric potential of the extremely large telescopes.

4.2 Data Acquisition and Preparation

4.2.1 Observations

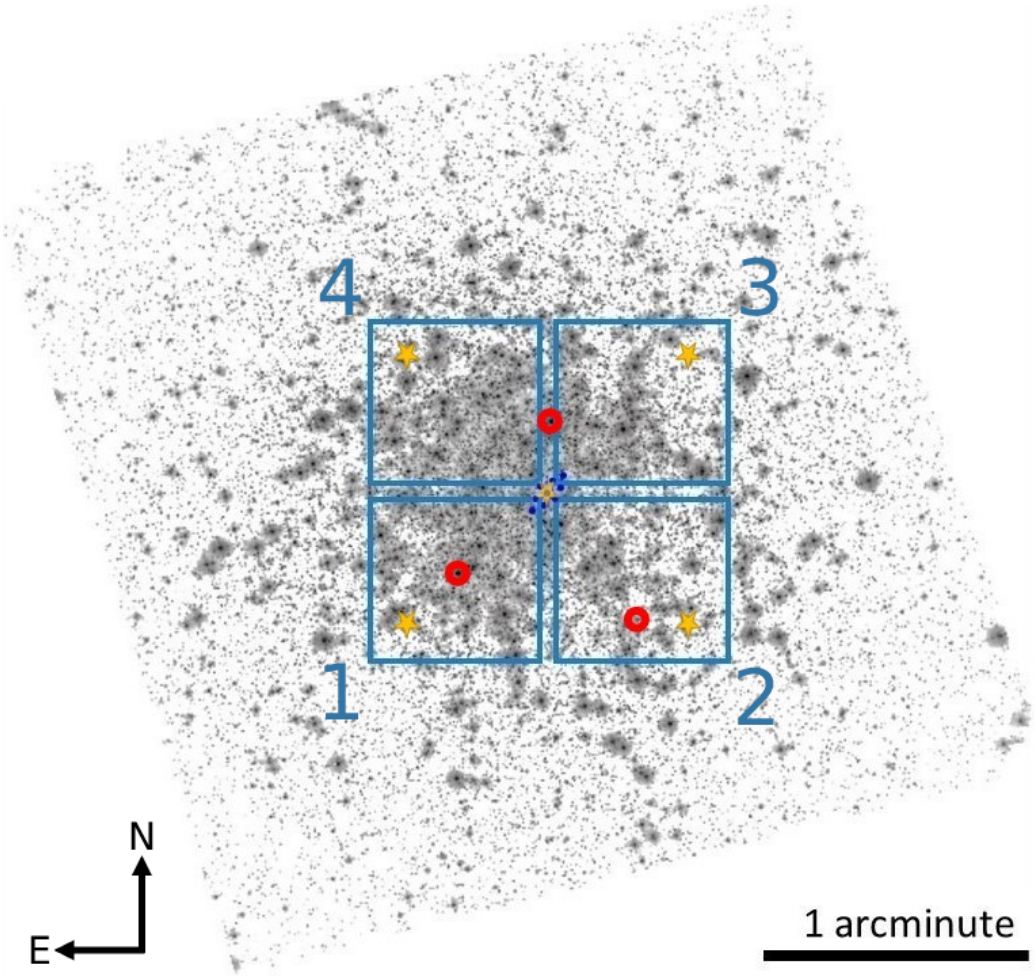

Figure 4.1: The HST/ACS image from [83]. Overlaid as blue squares is the field of view of GeMS/GSAOI. The dark blue constellation of points shows the set of field centers used for the set of dithered sub-exposures. The red circles indicate the positions of the NGSs and the five yellow stars represent the positions of the LGSs.

My analysis is based on data from the Gemini South GeMS/GSAOI, the only MCAO imager system in regular science operation. GSAOI consists of 2x2 Rockwell HAWAII-2RG arrays arranged in a square configuration. Each chip has 2048×2048 pixels with a total field of view of 85”×85” and a pixel scale of 0.02” pixel^{-1}. Chips are separated by a 2 mm gap. Figure 4.1 shows the geometry of the GSAOI chips, including their numbering scheme.

Observations took place on 2013/04/18 7:55 to 9:28 UTC and consisted of 8×160, 1×90 and 1×25.5 seconds exposures in each of the K_S and J bands. Table 4.1 shows the observational log. For this study, I only use the K_S band observation which benefits from the better AO correction and provides better astrometric precision compared to the J band. The average airmass for the K_S 160 seconds observations is 1.05. Exposures are dithered in a grid pattern which fills in the gaps between detector chips and also improves the photometric precision. The grid pattern offset step is $\sim$ 3" with a maximum offset of 5.6" in each axis. Dither positions are shown in Figure 4.1 which also shows the positions of the LGSs and NGSs.

In Figure 4.1, the background image is an HST/ACS image that was observed as part of the ACS Survey of Galactic Globular Clusters [83]. I use this catalogue as the first epoch measurements, which provides us with a temporal baseline of 6.75 years. The photometric and astrometric reduction process of this catalogue is explained in detail in [5]. Specifically, these authors identify stars simultaneously in the multiple dithered exposures for each cluster and measures their positions and magnitudes using the best available point-spread function models, correcting for distortion and placing the stars on an astrometric reference frame that is cross-matched to 2MASS. The publicly available catalog of HST/ACS data that I use[1] contains two parameters, `xsig` and `ysig`, that correspond to the expected astrometric measurement error in units of 50 mas pixels. These were derived based on the average position of each star in the $\sim$ 4 F606W and $\sim$ 4 F814W observations. An RMS about that average was determined, such that `xsig`, `ysig` correspond to the RMS/$\sqrt{8}$ (J. Anderson, *private communication*). I adopt these as the random uncertainties on the positions of the stars in the HST catalog. As discussed in [5], the remaining distortion-related positional uncertainties are at the level of $\sim$ 0.01 pixels (0.5 mas) across the field.

[1] https://archive.stsci.edu/prepds/acsggct/

UT time	Band	Exposure time [sec]	Airmass	Exposure ref.
2013-04-18 8:50	J	21.5	1.03	
2013-04-18 8:51	J	90	1.03	
2013-04-18 8:56	J	160	1.03	
2013-04-18 9:00	J	160	1.03	
2013-04-18 9:03	J	160	1.02	
2013-04-18 9:06	J	160	1.02	
2013-04-18 9:10	J	160	1.02	
2013-04-18 9:13	J	160	1.02	
2013-04-18 9:17	J	160	1.02	
2013-04-18 9:20	J	160	1.01	
2013-04-18 8:00	K_S	21.5	1.1	
2013-04-18 8:01	K_S	90	1.1	
2013-04-18 8:05	K_S	160	1.09	#1
2013-04-18 8:17	K_S	160	1.07	#2
2013-04-18 8:27	K_S	160	1.06	#3
2013-04-18 8:31	K_S	160	1.05	#4
2013-04-18 8:34	K_S	160	1.05	#5
2013-04-18 8:38	K_S	160	1.05	#6
2013-04-18 8:41	K_S	160	1.04	#7
2013-04-18 8:45	K_S	160	1.04	#8

Table 4.1: Observing log for the GeMS/GSAOI observation

4.2.2 Data Preparation

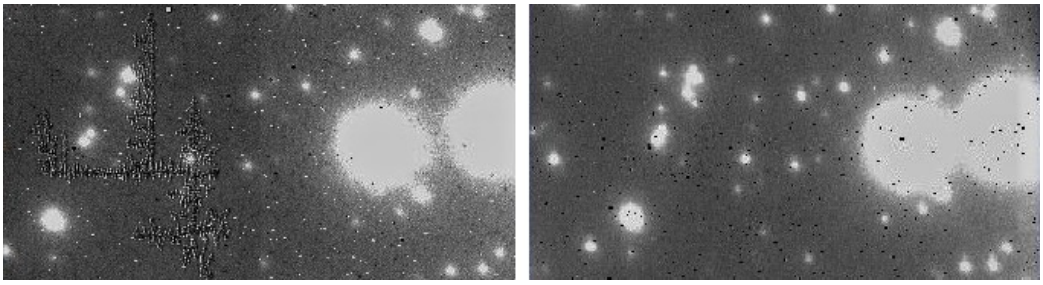

Figure 4.2: Small region of chip number 1 before (left) and after (right) primary data processing. See text for details.

I follow the method described in [69] for data preparation and photometric reduction. This method is carefully tailored for the GeMS/GSAOI observations. In brief, I use the IRAF Gemini package for performing primary data reduction. For flat fielding, I combine the dome and twilight flats for each chip individually. The dome flat provides high signal to noise information, however, its spectral response is different than that of the twilight flat. I combine the two by applying a high-pass filter on the dome flat to exclude high-spatial resolution features that may be caused by the dome flat acquisition mechanism. A 3-sigma clipping and a median is then used to add the information from the twilight flat. The output of this process is a "super flat" frame that is used for flat fielding raw exposures.

The GSAOI detector also suffers from some dead and bright pixels. The Gemini IRAF package provides a map of these pixels and removes them from the image, preventing their destructive effect on the accuracy of the photometry. I correct for the non-linearity of each detector chip by applying a quadratic polynomial correction measured during the GSAOI commissioning process [33]. I do not use dark frames since the dark current is ~ 0.01 e.s^{-1} px^{-1}, which is totally negligible for the exposure times I used. I also did not use sky frames, since this only introduces an additional systematic uncertainty into the photometry. Instead, I evaluate the sky background at the position of each star by measuring the sigma-clipped median value of pixels in an annulus surrounding each of them. Figure 4.2 shows a before-and-after image of part of the GSAOI field following all these procedures.

4.2.3 Photometric reduction

High-accuracy astrometry on multi-epoch data requires determining the precise positions of each star. To achieve this, I use a careful PSF photometric analysis using the DAOPHOT II [93] suite of programs. The use of two discrete DMs conjugate to two different altitudes to correct the full 3D volume of turbulence above the Gemini telescope will lead to field dependent wavefront errors that cause spatial variations in the PSF [62, 101, 7]. This must be carefully considered while performing any kind of photometric analysis, and was the focus of earlier contributions in [69]. Critically, DAOPHOT II can vary the PSF model for stars across the field using either a bi-linear or cubic model, which makes it an ideal tool for analyzing MCAO and GeMS data.

The first step of the photometric analysis is to find the stars using Gaussian

profile convolution. All star-like objects in the field are filtered by their sharpness and roundness parameters. This helps to distinguish stars from cosmic rays, extended objects and other artifacts. The next step, based on [69], is to combine all exposures to create a master frame. This practice is primarily to reach fainter magnitudes, critical for accurate and deep photometry. However, I do not recommended this for astrometric analyses where working with the raw positions per exposure reduces systematic errors, at least prior to correction of the astrometric distortion. For the current analysis, I therefore combine information from all frames after individual distortion corrections on each exposure. Thus, in contrast with [69], the rest of the photometric analysis summarised below is performed on each individual exposure and each chip.

The next step in the photometric analysis is to choose suitable stars to provide a PSF model, and calculating the look-up table that determines the variation of the PSF across the field. Choosing stars for PSF fitting is typically accomplished by using the `PICK` command in the DAOPHOT II suite. The `PICK` command tries to delineate the number of stars across the field which are bright and isolated enough to be used for PSF modeling. I noticed that in some very crowded regions of the field, the `PICK` command fails to find enough sufficiently isolated stars. Selecting a large number of isolated stars in a dense field is challenging but necessary. It ensures that the effect of photon noise and other artifacts like bad pixels on the final PSF profile are minimized and the look-up table has enough data points to efficiently interpolate the whole field of view. Therefore, I developed a script specifically designed to pick stars from more crowded fields. This script uses Gaussian fitting and the average distance between stars to ensure that the picked star profile is not significantly disturbed by neighbouring bright objects. Eventually, I chose 100 stars for each chip. This process is repeated for each exposure and each chip separately.

I used the Lorentzian function for the analytic part of the PSF model. It is typically the best match for the AO PSF [50]. I also choose cubic interpolation for modeling the look-up table that corrects for the variation of the PSF across the field. The eventual output of the PSF photometry procedure is a catalogue containing the precise position and instrumental magnitude of each star for each exposure and each chip. This catalogue is used in the rest of this work to represent star positions measured by GeMS/GSAOI.

4.2.4 Photometric Calibration

The last step of the photometric analysis is the photometric calibration. I calibrate the photometric data using the 2MASS catalogue [89, 21]. The process of matching stars between my catalogue and the 2MASS photometric reference is challenging. Firstly, the resolution of the two catalogues is very different, and this causes multiple resolved stars in my catalogue to be seen as one star in the 2MASS catalogue. This is discussed at length in [69] and they correct explicitly for this effect. I do not require the same photometric precision as [69] and I find good results from hand-picking the most isolated stars in both catalogues. Secondly, the depth of the two catalogs is quite different, which makes finding common non-saturated stars very difficult. I checked each pair of stars by eye for the final calibration process. After verifying the matched stars, I use a maximum likelihood estimator (MLE) algorithm to find the best estimates of the zero points and the uncertainty of the calibration for each chip. Table 4.2 shows the results of this process.

Chip#	Zero-point (GSAOI-2MASS)	Zero-point uncertainty
1	-5.33	0.02
2	-5.62	0.04
3	-5.20	0.02
4	-5.01	0.03

Table 4.2: K_s-band zero-point magnitudes for each GSAOI chip, calibrated to the 2MASS catalogue.

4.3 Astrometric Analysis

4.3.1 Overview

While AO technology helps compensate for the degrading effect of the Earth's atmosphere on the resolving power of telescopes, MCAO observations can suffer from field distortion. Field distortion can be described as a vector field of the difference between the real (relative) positions of astronomical objects and what the instrument records for these objects across the field of view. Precise knowledge of the field distortion for a specific observation/instrument allows astrometric measurements to be made with greatly reduced systematic errors.

It is important to compensate for the relative distortion fields between the two epochs, specifically the AO-based catalog and the HST/ACS catalog. However, the fact that these are taken at two different epochs is a complicating factor. While this allows for the measurement of the proper motion of stars, it creates a new challenge in the ability to distinguish between the displacements in position due to the telescope/instrument distortion, and displacements due to actual physical movement of the stars. An additional factor that is important to consider is that not all sources present in one catalog are present in the other, and indeed the initial AO-based catalogs include all the usual spurious detections that are obtained in single frame photometric analysis (e.g, additional sources in the halos of bright stars, etc). However, the methodology that I develop is robust to these effects, and indeed will be shown to be highly effective at removing spurious sources.

The astrometric pipeline I have developed exploits specific characteristics of instrumental distortion maps to separate these two components. The main distinction between the distortion component and the proper motion component is the difference in the statistical spatial frequency of the displacement vector field (DVF). The DVF is the vector field created by spatially connecting the same stars between the two different observations that have been matched to each other using only shift, scale and rotation. The distortion map intrinsically has a continuous nature with low-spatial frequencies changing across the field of view for each detector chip. This is in contrast with the relative proper motion component which is statistically dominated by higher spatial frequency motion and random behavior. By modeling the distortion field based on the low-spatial frequency behaviour of the DVF, I capture the majority of the distortion field component without losing any significant proper motion information. The pipeline I developed measures and models the low-spatial frequency behaviour of the DVF by analysing local neighbourhoods of vectors, and eventually builds the field distortion model based on this information. I now present this method in more detail.

4.3.2 Finding Common Stars Between Catalogs

After performing the photometric analysis described in the previous section, I produce a catalog of precise positions of detected objects for each chip of each exposure. The first step is to do a preliminary match of each of these catalogs to the HST/ACS catalog that gives us the first epoch measurements.

I have written a vote-based star pattern matching algorithm to do this match, which works for two catalogs that have completely different coordinate systems, in terms of offset, scale and rotation. I initially use a small subset of each catalogue consisting of the highest luminosity members from each catalog, in order to have a good chance of having common stars in each catalog and to optimise the processing speed of the algorithm. I also filter both subsets to remove stars with very nearby neighbours in order to reduce the probability of incorrect matches.

The two sub-catalogues feed into a voting-based star pattern matching module. This module uses angles of triangles that can be formed in each sub-catalogue as a feature to find match candidates between the two catalogues. For any three stars in either of the sub-catalogs, I form a triangle (see Figure 4.3) and compare it to the triangles formed in the other sub-catalog. If the difference between the angles of the triangles in both sub-catalogs is below a certain threshold, then this is recorded as a matched triangle pair. This creates three "votes" for the three pairs of stars contributing to the triangles. Many triangles are considered and compared, and votes accumulate in a votes matrix, where element $n_{i,j}$ represent the number of votes for the ith star in one sub-catalogue being matched to the jth star in the other sub-catalogue. The end result is that the votes matrix reveals the best candidates in the two sub-catalogues to be the same stars. Figure 4.3 shows an example of matched triangles between the two data sets.

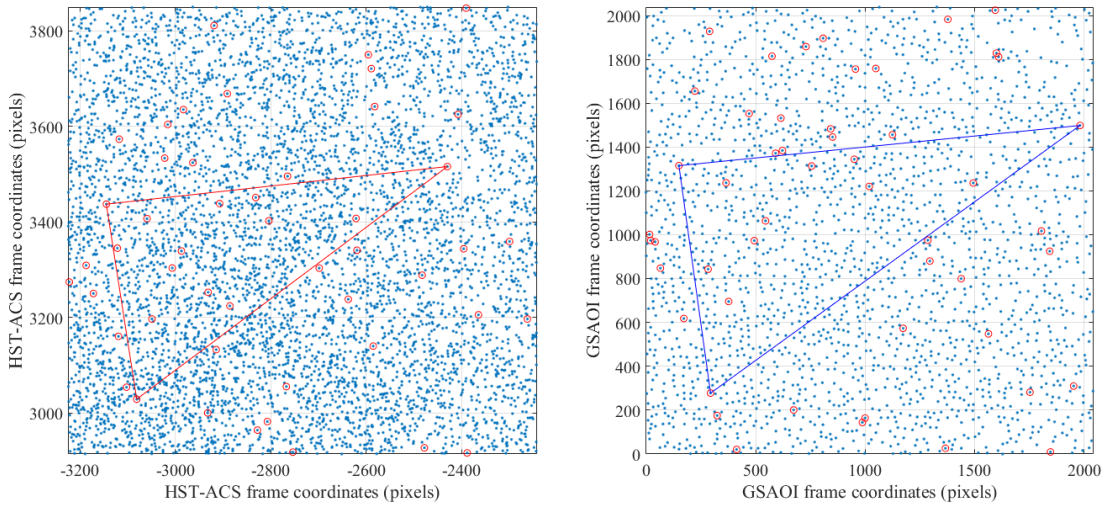

Figure 4.3: Each blue point represents a star in the HST catalog (left panel) and GeMS chip number 4 (right panel). These sub-catalogs have already been filtered to ensure they do not have any very nearby neighbours, to avoid unnecessary confusion. The brightest stars of each sub-catalogue are indicated by red circles. One of the matched triangles between the two data sets is plotted: each matched triangle provides three votes for the three pairs of stars. The origin of the coordination system and the scales in x and y between these two panels are totally different, but it is clear that by finding many of these matched triangles it is possible to robustly find matching stars between the two catalogues.

4.3.3 Coordinate Transformation

The previous step has identified common stars between the two catalogs, which I can now use to define the appropriate transformations between catalogs. While the vote-based star pattern matching method is very robust against false-positive matches, I add a second stage analysis to increase the robustness even more. Specifically, I calculate all possible transformations (correcting for offset, scale and rotation) for every combination of four matched pairs. The star pairs that I use are the highest voted matches between the two catalogues found in the voting process. Assuming the two catalogues are not reflected relative to each others, each similarity transformation is described by four parameters; two degrees of freedom for x and y translation, scale and rotation. Any false positive match that passes through this process from the previous step will cause a family of wrong and inconsistent transformations. However, all combinations of correct 4-pair sets will produce a unique, correct transformation. Repeated *correct* transformations will result in the same set of four parameters "piling up", whereas any incorrect transformations will scatter throughout the 4-dimensional

space of all possible transformations. I use a 4D histogram analysis to recognize the most repeated transformations between all the possible ones. This method is particularly resistant against wrongly identified pairs that may pass through the previous step. I then only use those star pairs that contributed to these correct transformations, and calculate the final similarity transformation between the two catalogs based on these stars (by minimising the RMS scatter). Using this transformation, I convert all the positions in both the GSAOI catalog and the HST catalog into the same frame of reference. Stars in the transformed GSAOI positions are matched to their HST counterparts based primarily on their spatial proximity in this new frame of reference. Using all matched pairs, I am able to produce the first version of the DVF.

4.3.4 Calculating the Distortion Model

The initial DVF for chip 4 of GSAOI observation using the match between the GSAOI and HST catalogs described in the previous subsection is presented in the top row of Figure 4.4. This DVF contains all raw displacements measured between the two epochs, including distortion effects, proper motions and incorrect matches (either between stars that do not actually match or including "stars" that are actually spurious detections). I remind the reader that these diagrams have already been corrected for shift, scale and rotation using the similarity transformation.

To extract the distortion model from the initial DVF, I have developed a zonal analysis method, specifically an algorithm that looks at the behaviour of each vector compared to its neighbours. In contrast to previous approaches, such as [52, 30], my methodology does not require that I spatially bin any of the data or take averages, since I want to keep the intrinsic spatial resolution of the catalogs to probe the distortion field (which is set by the density of matched star pairs). It works on any matched catalog of objects. In essence, if the size and direction of the vector is consistent with its neighbours, the vector is kept, and if not, it is removed. To make this decision for each vector, the algorithm considers multiple features. These features are calculated based on the analysis of the histogram of differences between the DVF and each individual vector in its local neighbourhood. This is done iteratively: the *first loop* cycle starts with the first DVF and scans the field repeatedly until the number of remaining stars and the RMS of the vector field reach an asymptote. Figure 4.4 shows a sample of the DVF before and after the first loop cycle. In the

case of the DVF before the first loop cycle, there are clearly many mismatched stars that have large vectors pointing in random directions, and which contribute to the high spatial frequencies in the map. Clearly, the high-spatial frequency behaviour of the DVF is removed and only low-spatial modes remain after application of the first-loop cycle.

The similarity transformation (that accounts for the scale-shift-rotation of the two fields) is recalculated at the completion of the first loop cycle, based now on only those pairs of stars that remain in the distortion map. The whole process then repeats in the *second loop* cycle. Like the first loop, the second loop cycle continues until the RMS of the DVF and the number of participating star pairs reach an asymptote.

At the end of the second loop cycle, the information remaining in the DVF is the basis for the distortion model. For the example shown in Figures 4.4 , there are 3251 star pairs with an RMS displacement of 167 *mas* prior to applying the first loop cycle. After the first loop cycle, 2502 star pairs remain with an RMS displacement of 135 *mas*. Figure 4.5 show the final result after the second-loop cycle, where there are now 2581 star pairs with an RMS displacement of 130 *mas*. Although this figure and the bottom right panel of Figures 4.4 looks very similar, there are subtle differences between the two, since the second-loop cycle acts like a fine adjustment to the matching. In this specific example, 79 more star-pairs are recovered by the end of the second loop cycle compared to the first, and the RMS is reduced by 5 *mas*. This increase in the number of pairs of stars, and the reduction in the RMS, is due to the fact that the similarity transformation between the two fields is recalculated at the start of the second-loop cycle. The sample results shown in Figure 4.5 are calculated by 5 iterations of the second loop cycle, with an average of 4 iterations in the first-loop cycle. The same result for all the chips in exposure number 4 (see Table 4.1 for exposure reference numbers) is presented in Figure 4.6.

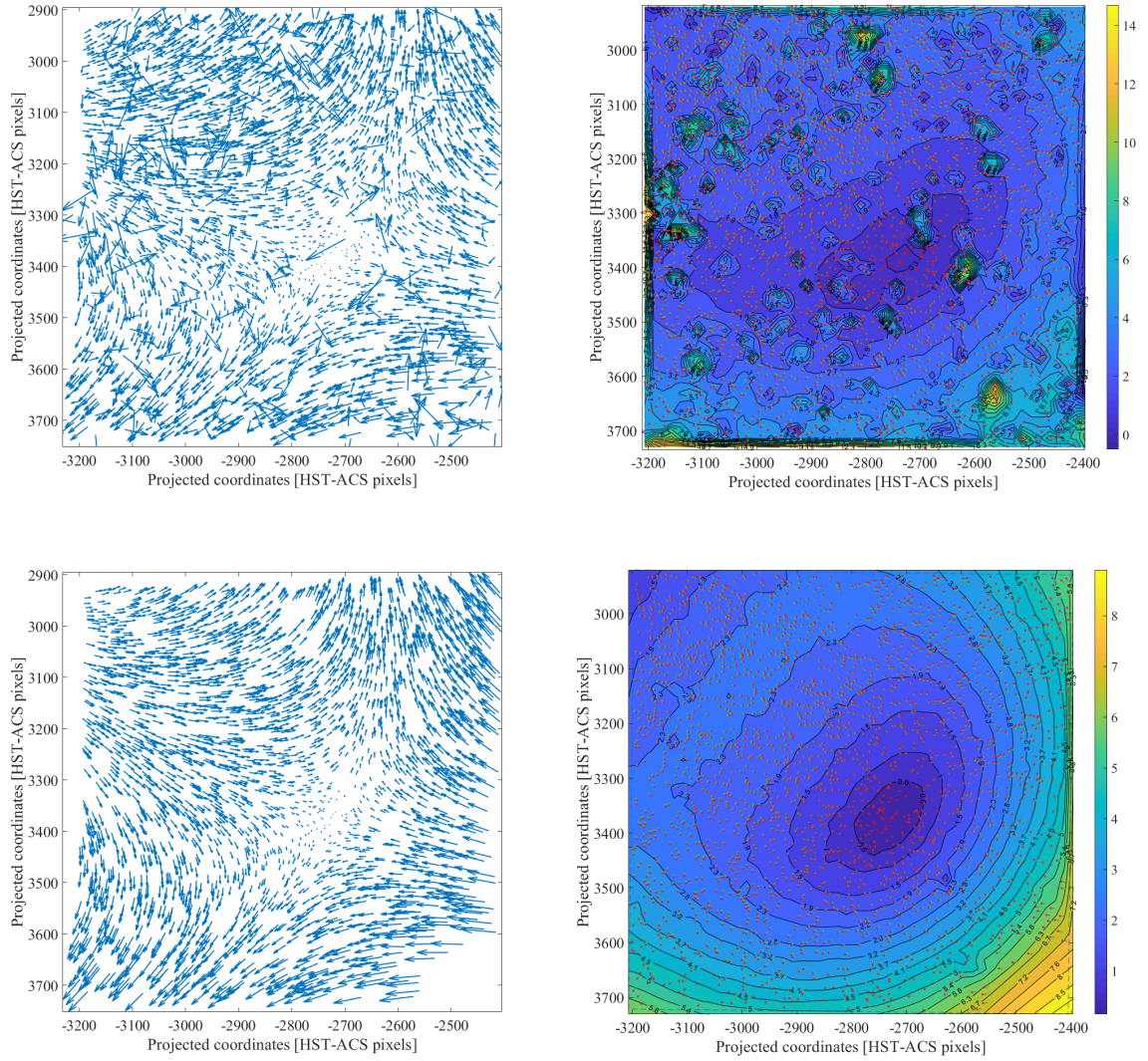

Figure 4.4: Top: the initial DVF for exposure 1 and chip 4, prior to the first loop cycle of the zonal analysis. The left panel shows the vector field, and the right panel shows the magnitude. Each red-green pairs of dots in the right panel represent one pair of stars matched between the two catalogues. There are 3251 star-pairs with an RMS displacement of 167 *mas* in this map. The spatial units of the color bar is HST/ACS pixels ($\sim 50\,mas$). Bottom: Same as top panel after the first-loop cycle. 2502 star-pairs with an RMS displacement of 135 *mas* remained in the field. Note that only low spatial frequency components remain and all higher frequency components have been removed.

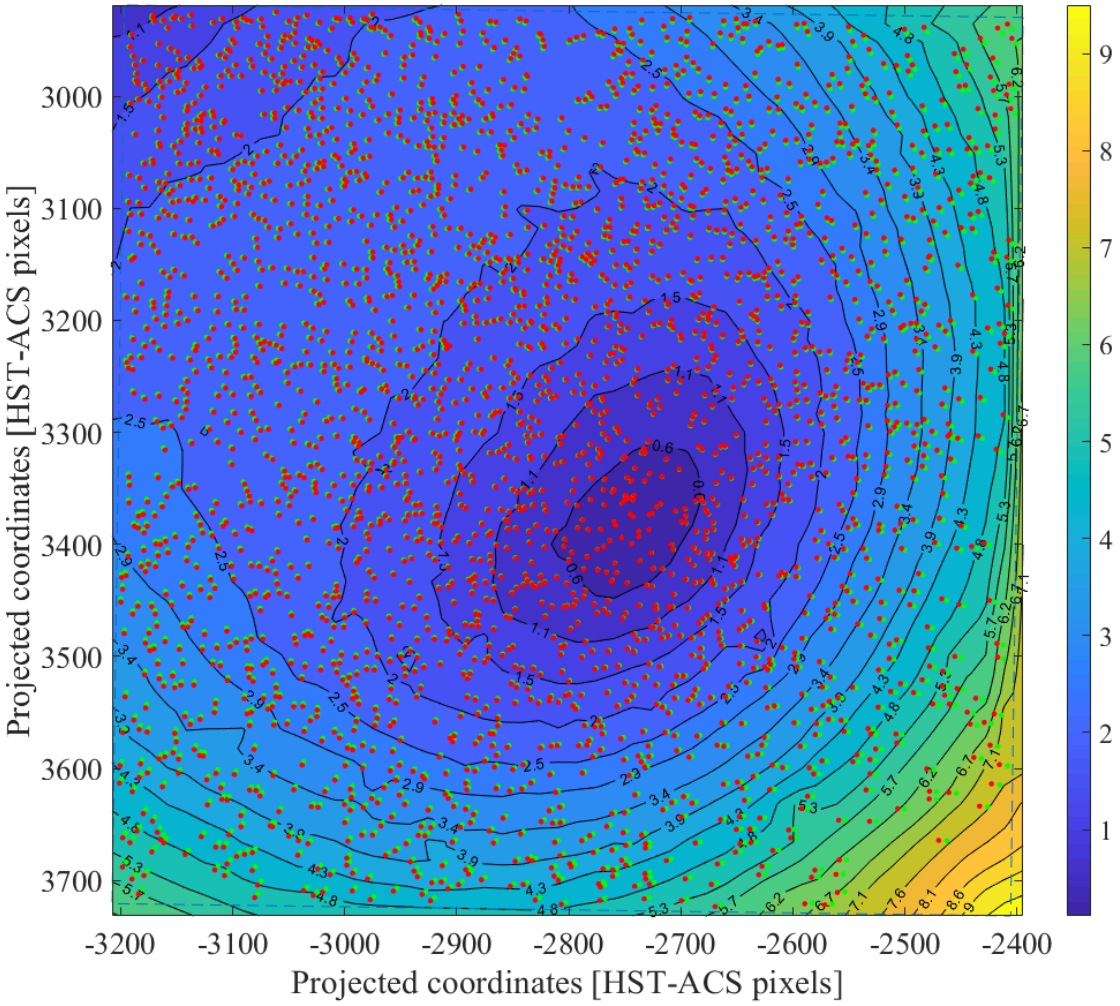

Figure 4.5: The final displacement map after the completion of the second-loop cycle, for the same exposure as Figure 4.4. After the second-loop cycle, 79 more pairs of stars are recovered and the RMS reduced by 5 *mas* compared to the end of the first loop cycle. Each GSAOI pixel is equivalent to 0.02 arcsecond.

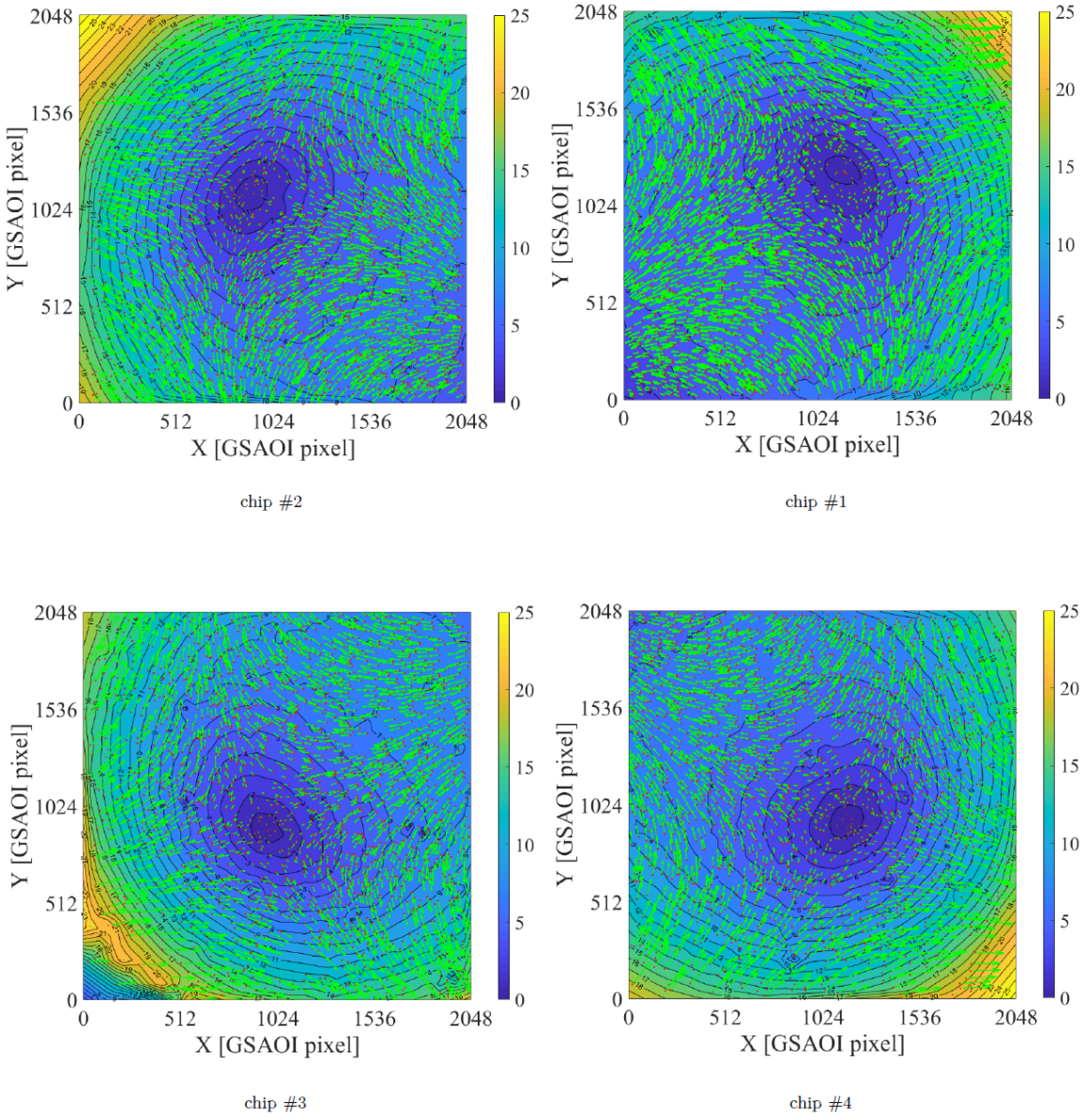

Figure 4.6: All four final displacement vector fields (DVFs) for exposure #4. The background color represent the intensity of the displacement between the two catalogs for each point in the field. The green vectors show the direction of the displacement. Each GSAOI pixel is equivalent to 0.02 arcsecond.

4.3.5 The Final Match Between Catalogs

The GSAOI dataset consists of multiple dithered exposures. The dither pattern covers the gap between the detector chips, and increases the precision of the photometric and astrometric measurements. The analysis thus far has been performed on each

chip and each exposure individually, for a total of 32 DVFs. To combine data sets, it is easy to transform all exposures to the same frame of reference and to match stars in close proximity. Here, I use all stars in the GSAOI dataset. However, given the different epochs of the HST and GSAOI data, this could result in incorrect matches for high proper motion stars.

To consider this issue I first use the nearest neighbour match only for star pairs that were already confirmed as matching pairs in the second loop cycle of the zonal analysis in the previous subsection. These pairs are used to form an initial color-magnitude diagram (CMD). To match the rest of the stars, including high proper motion stars, I use this initial CMD in combination with a nearest neighborhood algorithm. Specifically, I ensure that the colors and magnitudes of the matched stars are consistent given the CMD. Any star which cannot be matched with a candidate from the catalog is identified as noise and removed from the process.

4.4 Distortion Maps

The previous section describes in detail how I match different catalogs and use the resulting DVFs to create distortion maps. This information is essential to correct the proper motion measurements I am trying to make, and I describe that process in Section 4.4.1. My method differs markedly from previous approaches in the literature (e.g., [52, 30]). Specifically, I use all photometrically identified sources in this analysis, regardless of magnitude (i.e., I do not limit ourselves to only analysing the brightest stars), and I do not bin or average the data. In this way, I use data with the highest spatial resolution possible (set by the density of matched star pairs) on which to fit the distortion model, making maximal use of the data. The only assumption is that the distortion model be continuous and dominated by low spatial frequencies. The methodology described in Section 4.3.4 can be applied to any two catalogs that have been matched; however, how the resulting distortion field is subsequently interpreted needs careful consideration and depends on the catalogs that have been matched.

In the case of the GSAOI and HST/ACS catalogs that form the basis of the analysis so far, the distortion map is actually a *differential* distortion map. That is, it provides a map that contains the difference in position caused by the *relative* distortion that exists between the two instrument systems: it includes distortion from the entire Gemini/GeMS/GSAOI system (i.e. atmosphere, telescope and instrumentation) as well as any distortions that remain present in the HST/ACS instrument

system (telescope plus instrument). This means that each single differential map does not give any direct information about the astrometric performance of each system independently, but rather they reveal the entangled displacement effect caused by the distortion fields of both instruments.

In this section, I discuss how I use distortion models to enable the science and, uniquely, to understand the behaviour of GSAOI observatory system. In Section 4.4.1, I first discuss the differential distortion maps, and how I apply these as a correction for proper motion analysis. Section 4.4.2 then shows how I can us these maps to monitor changes in the observatory system with time. In Section 4.4.3, I then demonstrate how it is possible to extract the distortion map due *only to GSAOI* using the data in hand, and I argue that this type of analysis can be used as an important diagnostic tool to test, measure and monitor the system performance.

4.4.1 Differential Distortion Map and Distortion Compensation

With the creation of the differential distortion map, I can model and subtract the effect of distortion on astrometric measurements. I fit degree-5 polynomials [23] on each dimension of the processed DVF using all the stars pairs which passed the process described above. This allows us to create the distortion model for any particular chip and exposure. There are two reasons to fit a model on the DVF to form the distortion model:

- The DVF includes the distortion information only for the points which a pair of stars that survive previous steps exists. To interpolate at any point across the field of view requires some type of model.
- Because of the discreet nature of the DVF (the fact that there are only pairs of stars at some and not all positions in the field), a small component of random relative proper motion can pass through the multiple iteration process. This component originates from the internal motion of stars relative to the rest frame of the globular cluster. Fitting a continuous low spatial frequency model on the DVF therefore acts as a way to fit over these (small) residuals.

Armed with the fitted distortion model, it is trivial to calculate the distortion-correction vector field by inverting the distortion model functions. Figure 4.7 provide

a visual representation of the effect of the distortion compensation on proper motion measurements represented as a vector point diagram (VPD). The VPD is a diagram in proper motion space, where each point represents the proper motion of a star. The top left panel shows the "raw" VPD for stars on chip #4, exposure 1 of GSAOI. Note the scale of the proper motions is of order tens of $mas\ yr^{-1}$, and is irregular. The top right panel is the differential distortion maps for this chip, corresponding to the first exposure. The inverse polynomial fit to this map is applied on the DVF and the results are shown in the lower panels. Here the distribution of points is much more regular, and has a scale of less than 1 $mas\ yr^{-1}$, i.e., the relative distortion between Gemini/GSAOI and HST/ACS is an order of magnitude larger than the science measurements that I seek to make.

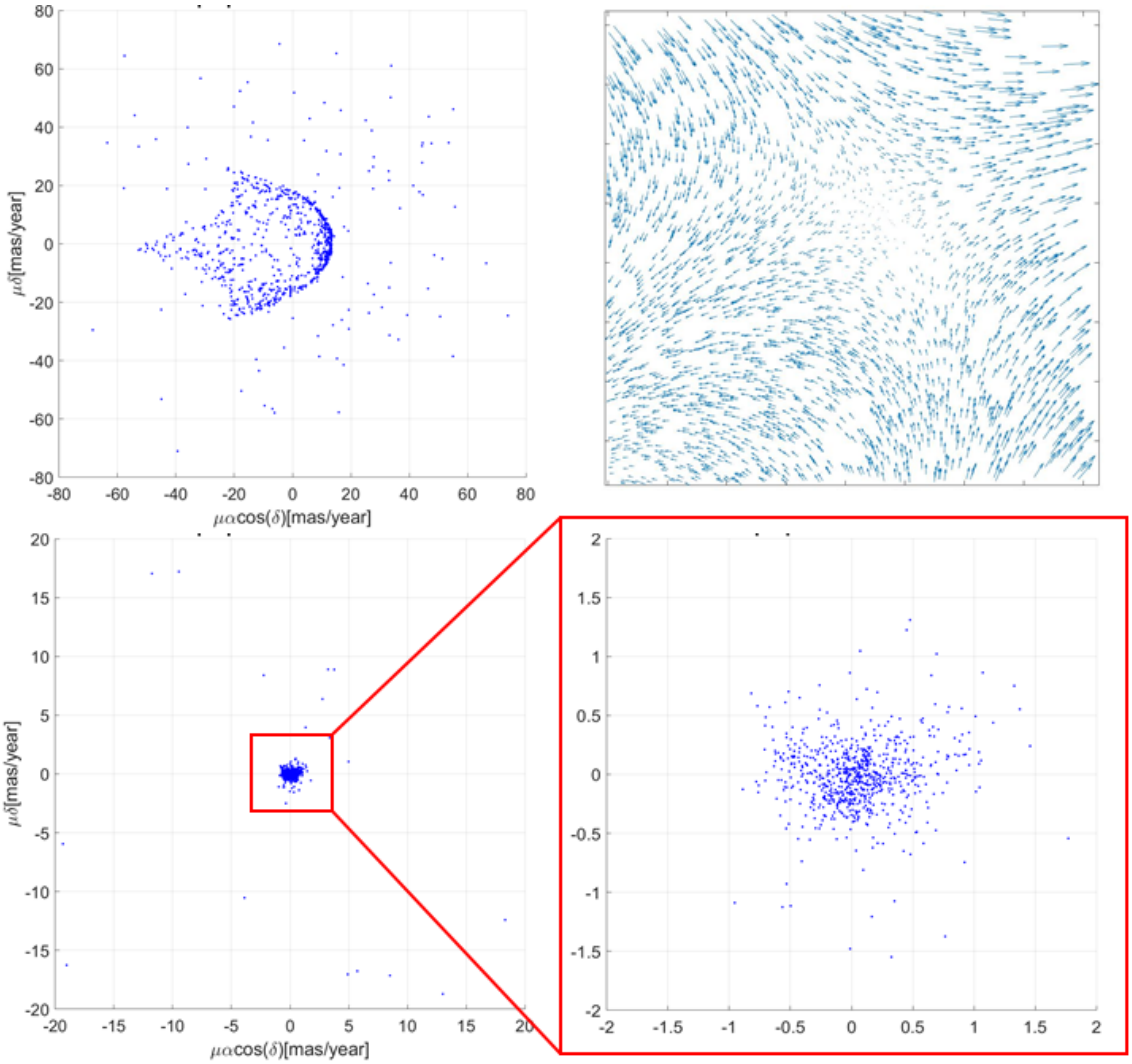

Figure 4.7: Top left: the proper motion VPD for NGC 6723 obtained by simple matching of stars between the GeMS and HST/ACS catalogs before the distortion compensation procedure. Top right: the differential distortion map for the first exposure for chip 4. Bottom row: the proper motion distribution after applying the distortion correction (inverse of the top left panel).

4.4.2 Time-Variable Distortion Maps

In addition to distortion compensation for astrometric analysis, differential distortion maps such as those discussed above have a great potential for monitoring instrument performance over time with the aim of improving astrometric performance.

I illustrate the utility of this idea by measuring the time varying component of the distortion field over the course of GSAOI observations. I perform this analysis by

fixing the similarity transformation between the two catalogs for all 8 GSAOI exposures and look at the *difference* of the differential distortion map for each exposure relative to the first one. The result is presented in Figure 4.8 for a few of the exposures. The top row shows the vector fields, and the bottom row shows the histograms of the magnitude of the vectors in the top panels. Typically, the magnitude of the temporal distortion residual is of order 0.1 pixel (2 *mas*), although for exposure 2 the magnitudes of the residuals are larger. This is in broad agreement with the temporal distortion residual value found by [62].

Examination of the vector fields in the top row of panels in Figure 4.8 reveals that the majority of this time-varying distortion component over the course of GSAOI observations consists of rotational modes. The effect is at the sub-pixel level, and points quite convincingly to the field rotator as the dominant sources of this time-varying distortion, an interpretation that is consistent with an independent study by [76]). Clearly, examination of the differences between the differential distortion maps of an instrument system taken at different times can provide a potentially very powerful diagnostic of time-varying distortions, enabling a better understanding of the scale and sources of systematics in astrometry that will otherwise dominate astrometric error budgets.

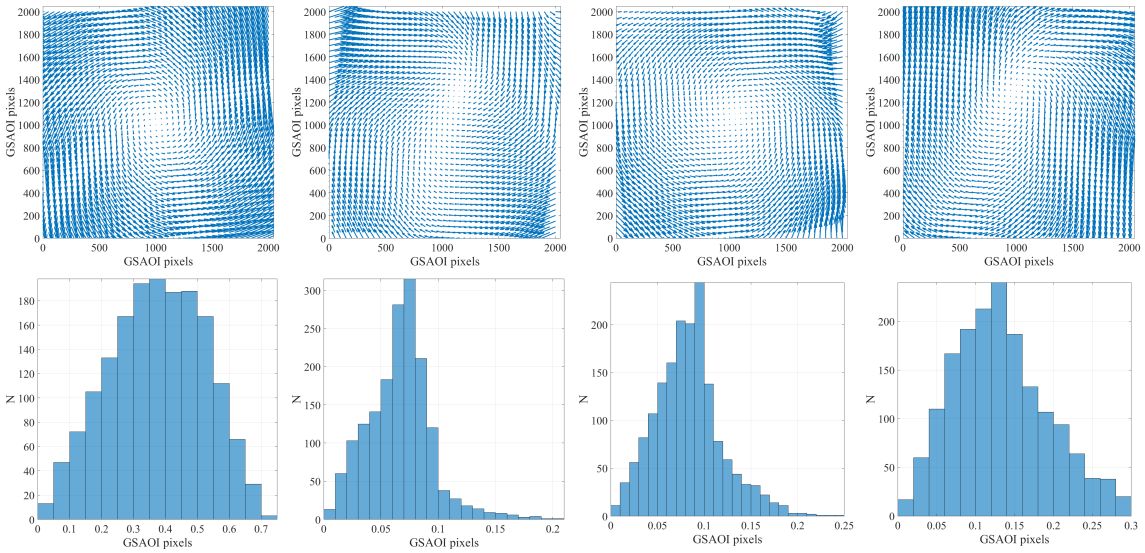

Figure 4.8: Four instances of the measured time variability in the relative distortion maps for chip #4. These diagrams represent the difference of the differential distortion map for exposures 2, 3, 6 and 7 (left to right, see Table 4.1 for exposure reference numbers) and the first exposure. All these exposures are taken within a period of 15 minutes. The top panel shows the vector field and the bottom panel shows the histogram of the intensity of the magnitude of the distortion. Each GSAOI pixel projects to 20 microarcseconds on sky. Note that the intensity of the time variable component is an order of magnitude smaller than the static distortion map shown in Figure 4.11.

4.4.3 On-Sky Measurement of Static Distortion Maps

Using the same concept as described for the creation of the differential distortion map between the GSAOI data and HST/ACS, it is also possible to create a "static" distortion map, that is, a map showing the common distortions between all of Gemini/GeMS/GSAOI observations. In contrast with the differential distortion map, the static distortion map only contains distortion components which are fixed relative to the field of view of the instrument and are preserved, quasi-static, during the on-sky dithering process.

To make the "static distortion" measurement, I only use the dithered GSAOI observations. In this way, the procedure becomes similar to the well-known auto-calibration methods used by [4, 11] and others, albeit formulated in a different way as I utilize the knowledge of the dither pattern in the process for estimating some low-order distortion modes. I follow the same procedure described earlier, but now

applied only to the overlapping regions of each pair of dithered exposures. I also use a "shift-only" transformation model instead of a similarity transformation, since I only expect a shift due to the dithering process, and any rotation or scale in this analysis are considered as components of the instrument distortion. Figure 4.9 shows the differential distortion field for the overlapping sections of chip number 4 for exposures 4 and 5.

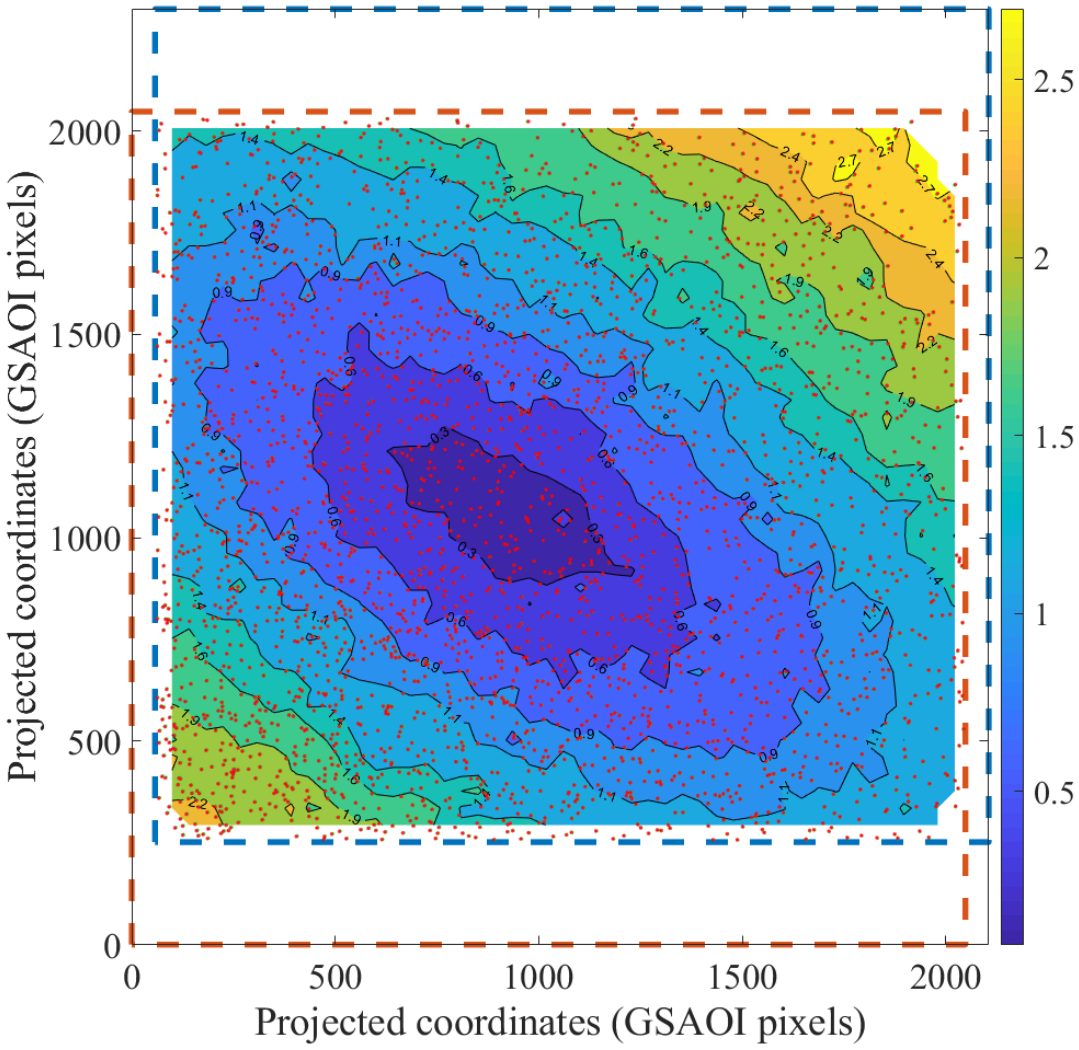

Figure 4.9: The relative DVF between exposure 4 and 5 for chip 4 of GSAOI. The dashed orange and blue squares indicate the relative positions of chip 4 in exposure 4 and 5 respectively. The color bar represents the displacement of star-pairs in units of GSAOI pixels (20 miliarcsecond). The obvious shift between the two dashed-line frames is caused by the telescope dither between the two exposures. The overlapped region contains 2850 verified star-pairs.

A differential distortion field like Figure 4.9 can be calculated for each pair of dithered exposures. Using each differential distortion field, I then solve a non-linear differential vector field problem, where the goal is to reconstruct a static distortion field that can provide all the differential distortion fields over the specific dithering vector for each pair of exposures.

The outer seven panels of Figure 4.10 show the input differential distortion maps for chip 4, where there are seven differential distortion maps because there were eight individual exposures. The central panel is the reconstructed static distortion field: that is, the elements of the distortion field that are common to all the exposures. If this derived static distortion field is displaced along the dithering vector and subtracted relative to itself, it would produce each of the seven observed differential distortion maps shown in Figure 4.10. The complete static distortion map and displacement histograms for each chip are shown in Figure 4.11.

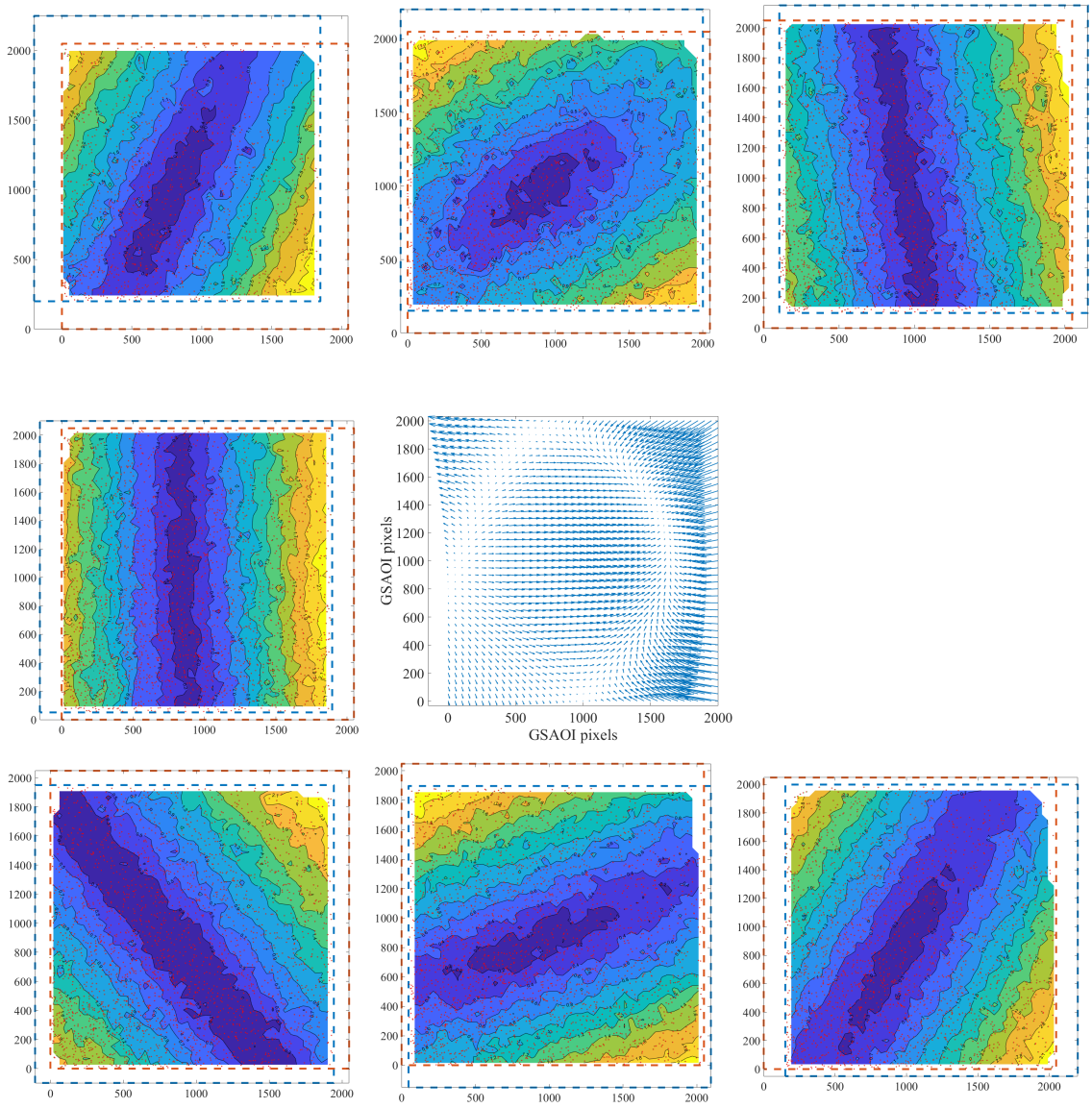

Figure 4.10: Each panel around the outside represents the differential distortion field of chip #4, relative to exposure #5. Each DVF is approximately positioned relative to the central panel by its dithered field location. Combining these maps allows us to construct the static distortion map (central panel). If the static distortion map is displaced relative to itself and subtracted, it would create the differential distortion maps that are observed.

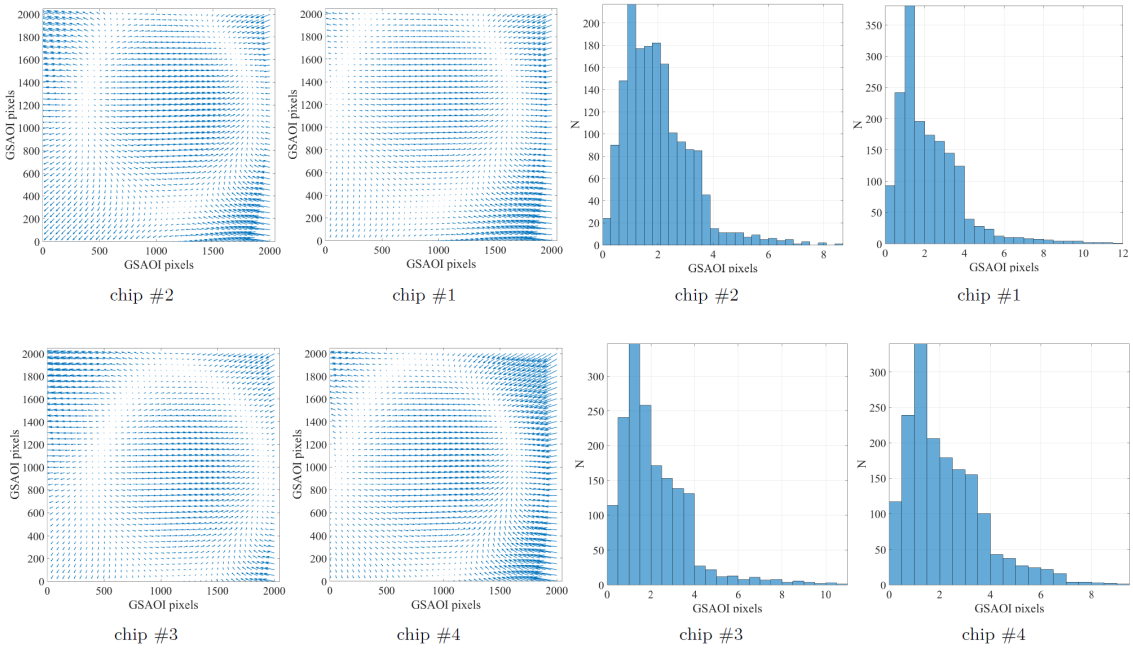

Figure 4.11: The static distortion map and the displacement histograms for all four chips of GSAOI. The vector field average of each chip is removed.

Given the duration of the exposures, very rapidly changing effects with temporal frequencies of order seconds and minutes will be averaged out, and will not be a significant contributor to the static distortion maps visible in Figure 4.11. Thus, these maps are a suitable tool to study the effects of instrument flexure, optical design, some aspects of MCAO system performance like residual modes between two DMs, and other parameters affecting instrument performance. This procedure has the same short-comings as the auto-calibration method used by [4, 11] and others. Specifically, the input data that I have used are not equally sensitive to all the spatial distortion modes that might be of relevance, since this is set by the dither pattern of the input images, and the spatial scale of the offsets that each pair of images probes. Ideal observations for derivation of the static distortion map of GeMS/GSAOI would include a much more extensive dither pattern, possibly including rotational dithers.

It is revealing to compare the results of this work with Figure 3 of [70]. These authors derive the expected distortion map of GeMS/GSAOI due solely to its optical design. Despite unequal sensitivity to all spatial modes, it is striking that, although the map applies to the entire observing system (i.e., including the telescope and the AO system), the general behaviour and intensity of on-sky measurements are in very good agreement with this study. This implies that the optical design of GeMS/GSAOI

is the dominant term in the static distortion component for this observing system.

I believe that these techniques described in this section could become essential tools for future generations of astronomical instruments, especially the ELTs, to monitor, diagnose, and understand the actual astrometric performance of these observing systems. This will be especially true when used in conjunction with internal calibration micro-aperture grids [60, 46, 39] as an on-sky verification of measurements. One clear advantage of the methodology presented here, is the reliance on on-sky observations, matching closely the set-ups required for actual science measurements (indeed, these diagnostic tools can be produced from the actual science observations).

4.5 Proper Motion Measurements

4.5.1 Relative Proper Motion Measurements

By combining data from all exposures and chips using the method explained in Section 4.3, it is possible to calculate the relative proper motion VPD for the cluster. I require that each star is observed a certain number of times across all GSAOI exposures, and this acts as an additional quality control criteria. By increasing this threshold, the precision and reliability of the data increases, but at the cost of smaller numbers of stars meeting the cut. Increasing the verification threshold decreases the number of data points in semi-linear trend, but increases the measurement precision of each data point. I adopt a verification threshold of three independent detections, which results in a total of $\sim$12500 data points. I measure the proper motion of each star by calculating its mean position in the distortion-corrected GSAOI exposures, and comparing them with the corresponding first epoch HST positions. The uncertainty in the proper motion of each star is estimated as the random error in the mean of the multiple measurements for GSAOI, combined with the random error in the HST positions described in Section 4.2.1. As discussed in the previous section, the displacement caused by combined systematic uncertainties of GSAOI and HST have been removed by application of the *differential* distortion correction, and I will later examine the scale of any remaining systematic effects not accounted for by this correction. The VPD for NGC 6723 analysed in this way is shown in Figure 4.12.

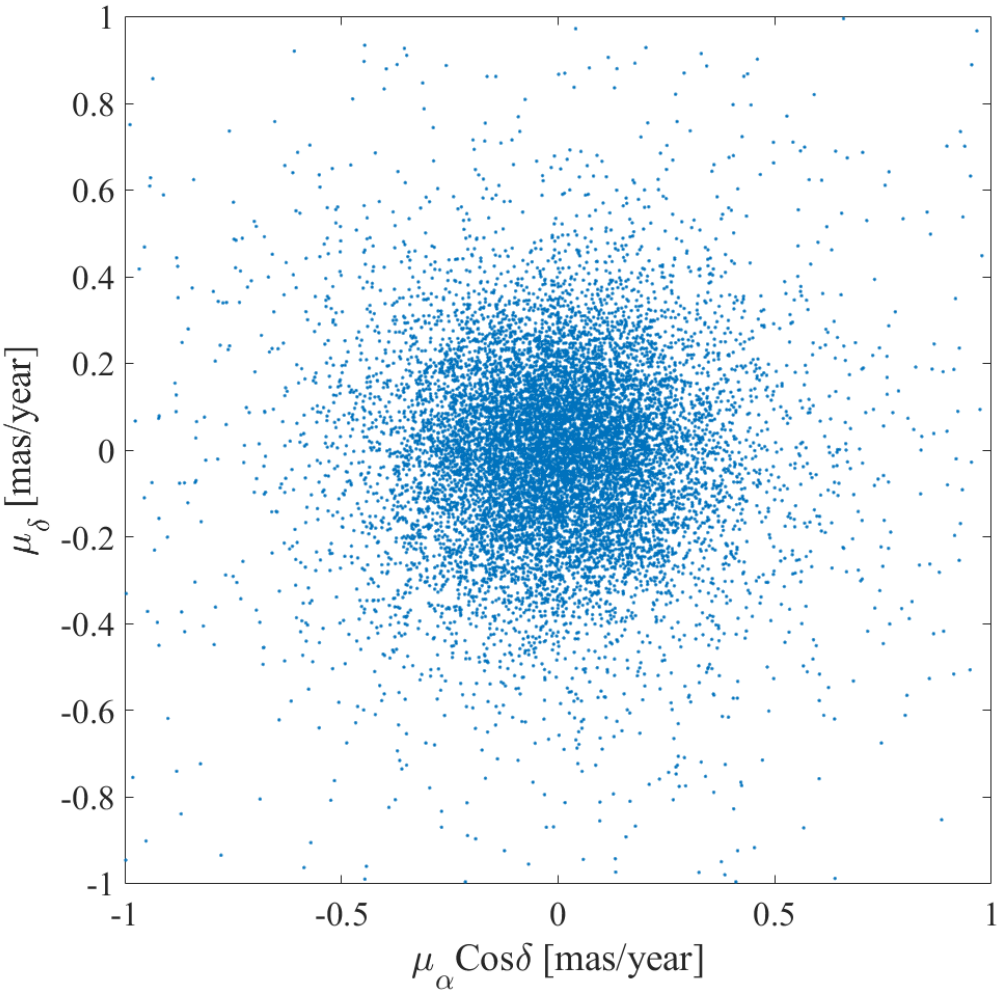

Figure 4.12: The proper motion diagram for NGC 6723. Each point in this diagram represents the proper motion of one star. This representation is for the verification threshold of 3, containing ∼12500 data points.

4.5.2 Systematic Sources of Uncertainty

I check the existence of systematic trends in proper motion with magnitude and color. Figure 4.13 shows these diagrams. The red line in these figures represents the average value in each bin. The error bars are the standard in the error of the mean for each bin. No significant trend between magnitude and proper motion values are evident.

I looked at maps of the residual distortion plots to check if any low frequency spatial trends remain after distortion correction. Figure 4.14 and 4.15 represent the distortion map for multiple chips for exposure 4. Figure 4.14 shows the distortion

map binned by x and y position prior to correction for the distortion correction, where vectors have been enlarged by a factor of 20. Figure 4.15 shows the corresponding residual distortion map after correction for the distortion, where now vectors have been enlarged by a factor of 2500. The random behaviour of the residual distortion maps shows that the distortion reduction process provides good distortion compensation. It should be noted that the final differential distortion model is measured based on the combination of data for all 8 exposures, where each chip has been corrected for distortion individually. Therefore, I expect that the error budget for the residual distortion in the final result will be less than what is presented in Figure 4.15 by a factor of $\sqrt{8}$. I also show the overall dependency of the residual distortion as a function of x and y before and after the correction process. Figure 4.16 and Figure 4.17 showed the result of this analysis for exposure 4. In line with the 2D maps, I see no evidence for significant spatial dependency in the residual plots for any of the exposures and/or chips.

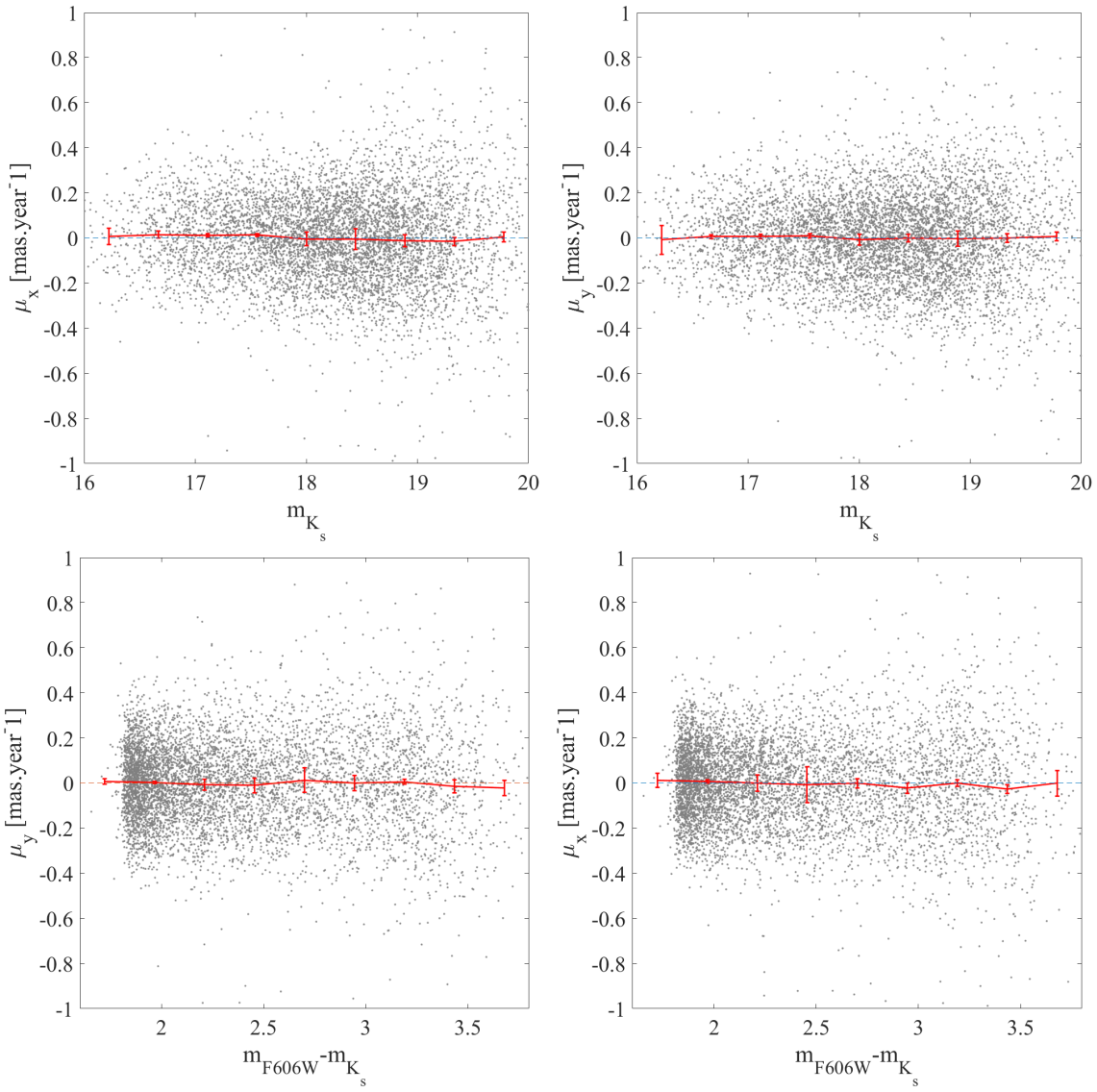

Figure 4.13: Top panel: proper motion components in the x and y directions versus K_S magnitude. Bottom: proper motion components versus optical-infrared color. The red line and error bars indicate the mean and the standard error in the mean for each bin, respectively. No significant systematic trend can be seen between magnitude/color and proper motion.

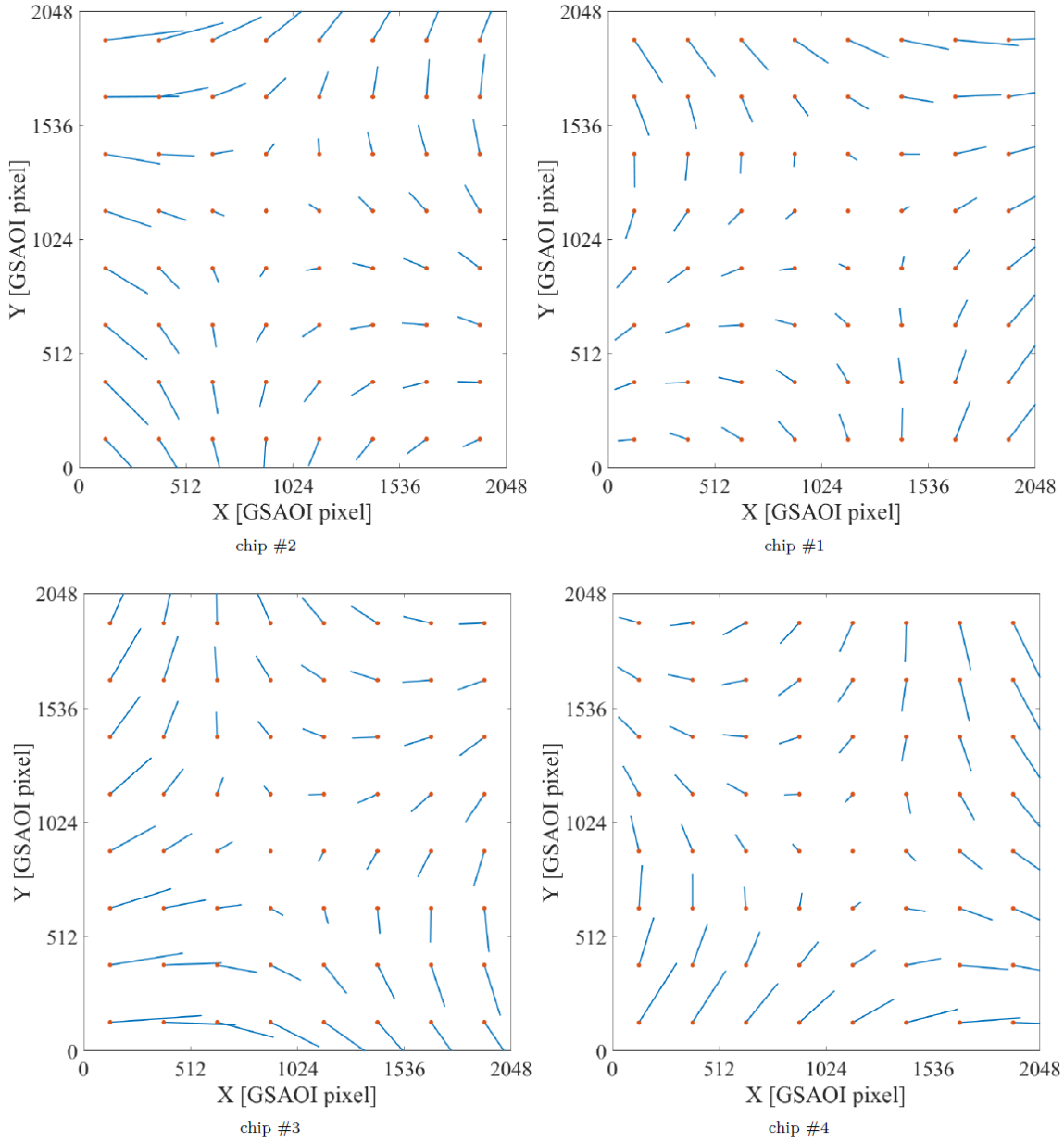

Figure 4.14: The GSAOI distortion map for the exposure 4 before the distortion correction, magnified by a factor of 20.

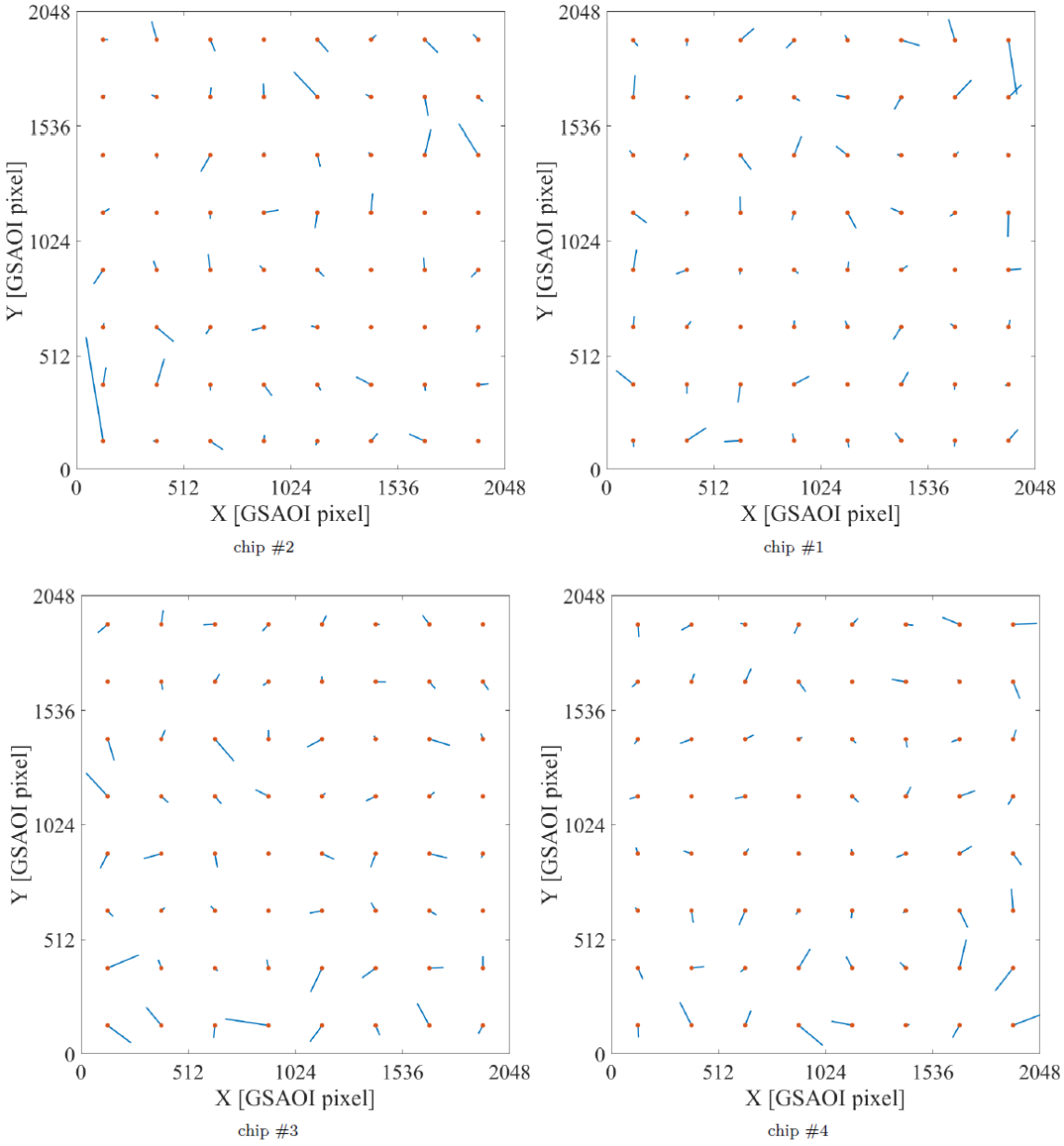

Figure 4.15: The residual distortion map for the exposure 4 after the reduction process, magnified by the factor of 2500. No significant systematic trend can be seen in the residual distortion map.

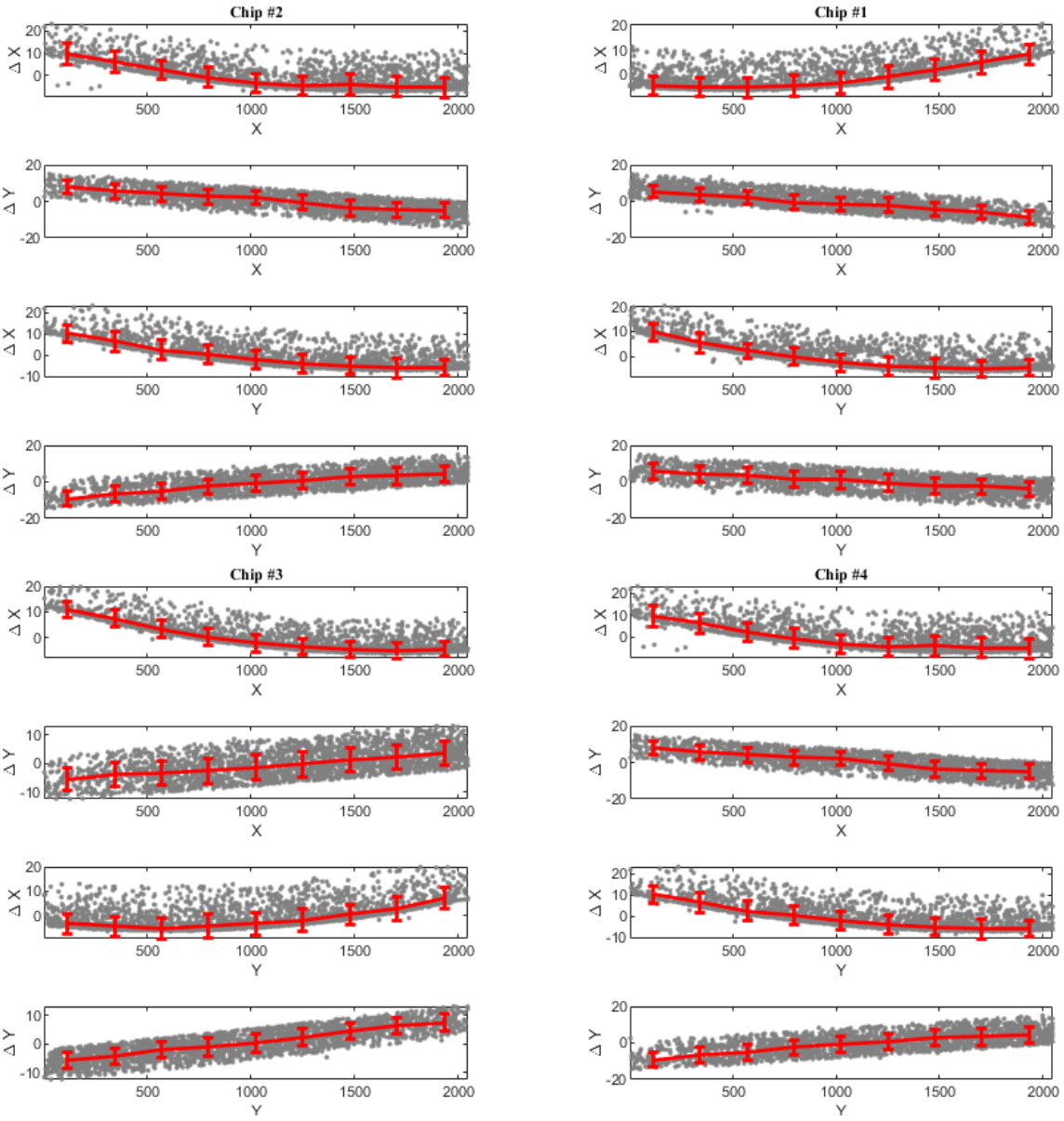

Figure 4.16: The spatial dependency of the distortion before the distortion compensation process for all chips of exposure #4. The unit of the Y axis is GSAOI pixels (0.02").

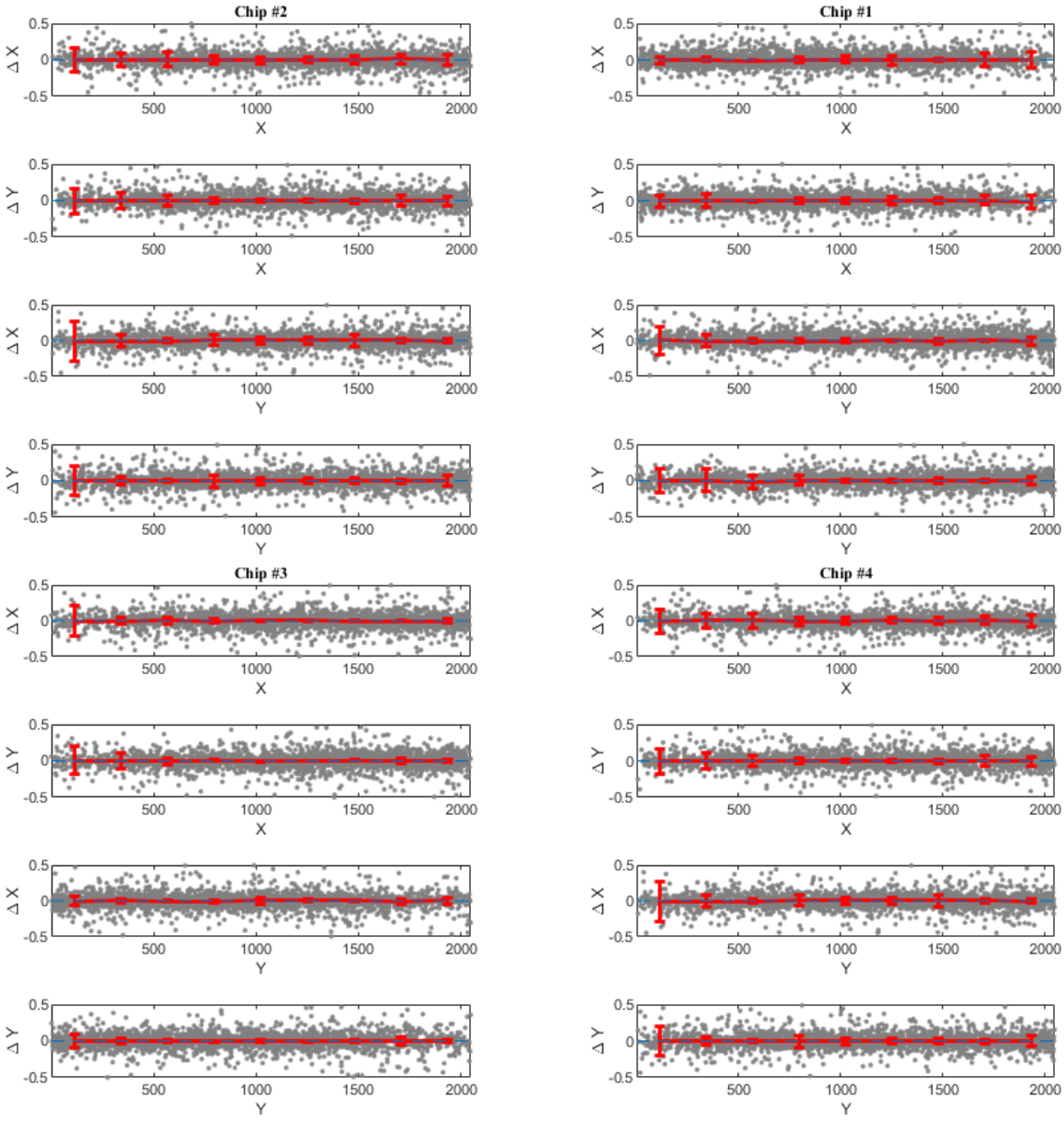

Figure 4.17: The spatial dependency of the residual distortion after the distortion compensation process for all chips of exposure #4. The unit of the Y axis is GSAOI pixels (0.02").

4.5.3 The Tangential Velocity Dispersion Profile

To calculate the dispersion in the proper motions, I adopt a maximum likelihood technique in order to disentangle the contribution of measurement errors from the intrinsic dispersion of the cluster. I follow the method of [61] and others, by seeking

to maximize the likelihood function,

$$L(\mu_T, \sigma_T) = \prod_{i=1}^{N} \frac{1}{\sigma_{\rm tot}} \exp\left[-\frac{1}{2}\left(\frac{\mu_T - \mu_i}{\sigma_{\rm tot}}\right)^2\right] \tag{4.1}$$

where μ_i are the individual proper motions of each star ($\mu^2 = (\mu_\alpha \cos\delta)^2 + \mu_\delta^2$), μ_T is the mean proper motion of the entire cluster and is zero by design, and $\sigma_{\rm tot} = \sqrt{\sigma_T^2 + \sigma_i^2}$ is the sum of the dispersion from measurement errors, σ_i (that includes both the GeMS and HST positional uncertainties) and the intrinsic tangential dispersion, σ_T. Applied to the entire dataset, I find that $\sigma_T = 0.148^{+0.002}_{-0.002}$ $mas\ yr^{-1}$. This corresponds to a tangential velocity dispersion of $\sigma_T = 5.84^{+0.07}_{-0.07}$ $km\ s^{-1}$. Error bars are random errors only, and are small because of the large number of stars involved in the analysis. For calculation of the velocity dispersion, I have assumed a distance to NGC 6723 of 8.3 ± 0.47 kpc [9].

Additional confirmation of the absence of any significant sources of systematic uncertainties as a function of magnitude or crowding can be obtained by recalculating the velocity dispersion using only brighter stars, or less crowded stars. The left panel of Figure 4.18 shows the result of recalculating the velocity dispersion using different magnitude limits, for stars brighter than m_{F606W} of 20^{th} to fainter than 24^{th} magnitude. Whatever magnitude cut is used, the result is consistent to well within the 1-σ uncertainties to that obtained using all of the stars.

The right panel of Figure 4.18 shows the recalculated velocity dispersion using stars in different local environments, as defined by their separation from their nearest neighbour as determined from the HST catalog, in units of the HST-ACS F606W filter PSF half-width-at-half-maximum (HWHM) [2]. Here, I expect stars that are more widely separated from their nearest neighbours to be least affected by any residual systematics caused by crowding in the HST data, and as discussed in Section 7.1 of [5]. I go out to 10 HWHMs, at which point I have excluded approximately 50% of the stars. While a small trend is present, as expected, the derived velocity dispersion changes by only a small amount. I conclude that the global velocity dispersion and its uncertainties derived above is a good representation of the data, even accounting for residual crowding effects.

[2]Nominal HST-ACS F606W filter PSF FWHM is equal to 74 mas or 1.48 pixel [104].

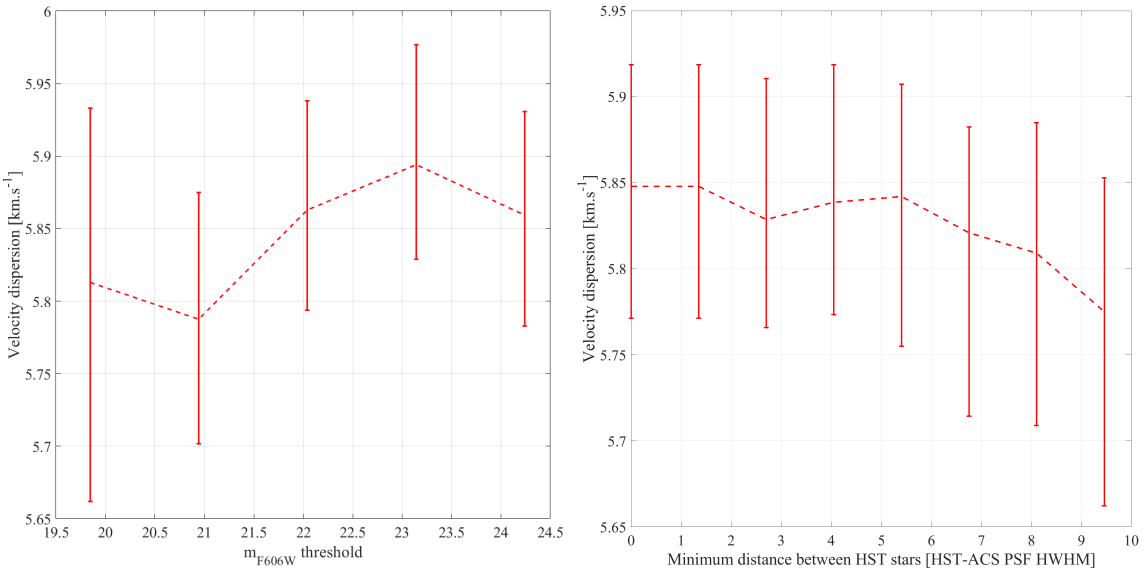

Figure 4.18: Left: Global velocity dispersion and its uncertainty as a function of limiting magnitude as seen in HST. Right: Global velocity dispersion and its uncertainty as a function of the local environment of the stars used, defined in terms of their nearest neighbour separation as determined from the HST data. See text for discussion.

Given the spatial extent of this data, it is possible to repeat this analysis but now examining the tangential velocity dispersion as a function of radius. To do this, I divided the cluster into concentric regions around the center with equal numbers of stars in each annulus. The centroid of the cluster is adopted from [9]. I measured the velocity dispersion in each annulus using the same maximum likelihood (MLE) algorithm as before. The position of these annuli superimposed on the HST and Gemini datasets are shown in the left panel of Figure 4.19. In the right panel, the blue data points (dots) show the derived proper motion dispersion profile for NGC 6723. Also shown are the proper motion dispersion measurements from Gaia DR2, and the line of sight velocity measurements, both from [9][3]. The values of the data points that contribute to the right panel of Figure 4.19 are given in Table 4.3. In this table, R_{med} is the median distance of stars to the center of the GC in each annulus alongside the inner (R_{in}) and outer (R_{out}) bounds of the annulus, σ_{1D} is the one dimensional equivalent proper motion dispersion, and V is the corresponding dispersion in $km\ s^{-1}$.

[3]Data is extracted from https://people.smp.uq.edu.au/HolgerBaumgardt/globular/fits/NGC 6723.html

R_{in} ["] | [pc]	R_{med} ["] | [pc]	R_{out} ["] | [pc]	σ_{1D} [mas yr^{-1}]	V [$km\ s^{-1}$]
0.0 | 0.0	11.6 | 0.5	15.2 | 0.6	$0.159^{+0.005}_{-0.006}$	$6.24^{+0.19}_{-0.22}$
15.2 | 0.6	18.0 | 0.7	20.2 | 0.8	$0.151^{+0.005}_{-0.005}$	$5.97^{+0.20}_{-0.20}$
20.2 | 0.8	22.3 | 0.9	24.1 | 1.0	$0.153^{+0.005}_{-0.004}$	$6.01^{+0.22}_{-0.17}$
24.1 | 1.0	26.3 | 1.1	27.9 | 1.1	$0.148^{+0.005}_{-0.005}$	$5.85^{+0.20}_{-0.18}$
27.9 | 1.1	30.0 | 1.2	31.7 | 1.3	$0.147^{+0.005}_{-0.005}$	$5.80^{+0.18}_{-0.21}$
31.7 | 1.3	33.7 | 1.4	36.3 | 1.5	$0.143^{+0.004}_{-0.005}$	$5.64^{+0.18}_{-0.20}$
36.3 | 1.5	38.0 | 1.5	58.5 | 2.4	$0.140^{+0.005}_{-0.005}$	$5.53^{+0.20}_{-0.19}$

Table 4.3: Velocity dispersion profile for NGC 6723.

Inspection shows that the GSAOI dataset is able to probe to considerably smaller radius than either the Gaia or radial velocity datasets, due to the superior image quality of GSAOI. Further, the uncertainties are comparable to, or better than, either of the other two datasets. Finally, I note that the absolute values I obtain are very comparable to the proper motion measurements from Gaia at larger radius, and the radial velocity measurements. I conclude that GeMS is able to provide very precise velocity measurements for NGC 6723 to relatively small radius from the center of the cluster.

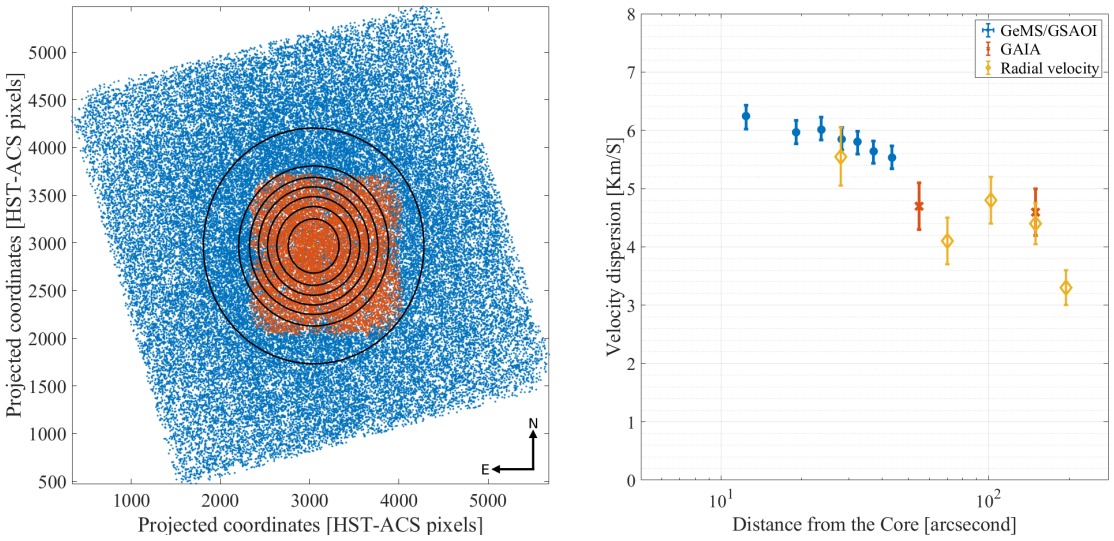

Figure 4.19: Left: The blue and red dots represent stars in the HST/ACS and GeMS/GSAOI catalogues, respectively. The black circles show the boundary of the radial bins, where I have an equal number of stars per annulus. Right: The proper motion dispersion profile for NGC 6723. The blue (dot) data points are the 1D equivalent velocity dispersion from this work. Also shown are the velocity dispersion measurements from Gaia DR2, and line of sight velocity measurement, both taken from [9].

4.5.4 Comparison to Previous Works

I compare the proper motion precision of the measurement to our group's earlier study using NGC 6681 by [62], i.e., using data from the same program and with a very similar time baseline (6.9 years compared to 6.75 years for this work). Figure 4.20 shows this comparison as a function of instrumental magnitude. I use the instrumental magnitude here since the astrometric precision is primarily related to the number of photons that the detector receives, rather than the apparent magnitude of stars (clearly the latter is a factor in determining the number of photons received, but it is not the only factor, e.g., observing conditions, exposure times, etc.). Each dot in this plot represent the precision of a proper motion measurement for a star in NGC 6723 (this work, blue) and NGC 6681 (yellow). The solid lines are the 3 σ-clipped mean of each dataset, and are color-coded red and purple for NGC 6723 and NGC 6681, respectively. It can be seen that the uncertainty floor for this work is given by the bright stars, and is approximately $\sim 45\ \mu as\ yr^{-1}$.

The precision of these two studies is comparable, as should be expected for such

similar data. Critically, however, the methodology presented in this work does not require any additional information or assumptions about the HST/ACS data other than the first-epoch *relative* positions of the stars. In contrast, [62] first used the HST-HST proper motion data to propagate the first epoch HST positions to the second epoch GeMS data and subsequently removed the distortion field. The methodology presented in this chapter is more flexible in being able to derive proper motions from GeMS data that does not require extensive auxiliary data other than (relative) first-epoch positions, and that data is used to construct a DVF that probes the cluster and instrument at the highest possible spatial frequencies. This is a necessary step in moving towards precision proper motions using only ground-based MCAO observations. I also refer the reader to other relevant work for other globular clusters, for example [52, 30], that also do not require propagating stars to different epochs from which they were observed.

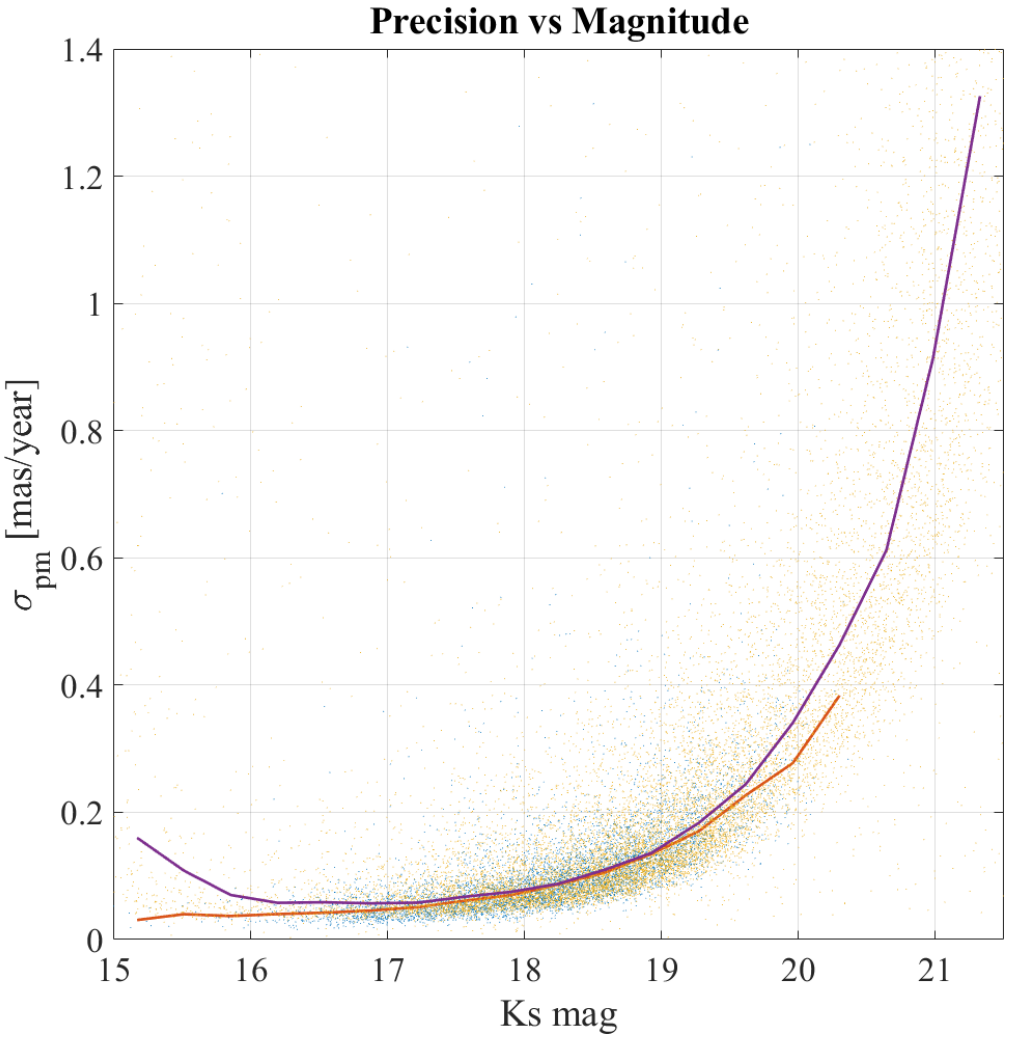

Figure 4.20: Comparison of astrometric precision as a function of instrumental magnitude for this NGC 6723 (this work, blue dots) and NGC 6681 [62]; yellow dots). The solid lines are the 3σ-clipped mean of each dataset, and are color coded red and purple for NGC 6723 and NGC 6681, respectively. The precision of these two studies is comparable, as should be expected for such similar data. Critically, however, the methodology presented in this work does not require any additional information or assumptions about the HST/ACS data other than the first-epoch positions of the stars. See text for details.

4.5.5 The Optical - Near-Infrared Color-Magnitude Diagram

Figure 4.21 shows the optical-near-infrared color-magnitude diagram for NGC 6723. I note that my technique for identifying matched stars between GSAOI and HST/ACS automatically cleans the CMD of spurious detections or poor matches (i.e., no ad-

ditional photometric criteria or quality control was needed to create this CMD, and it relies only on the astrometric methods described earlier). As such, the shape and features of the CMD provides strong validation of the matching procedure. In this analysis I have used only the 160 second Gemini exposures, and did not use the short exposures. As such, the final CMD saturates at the approximate level of the horizontal branch. The left panel shows the CMD including ground-based data from 2MASS (used in the photometric calibration discussed earlier), and the right panel shows just the Gemini-HST data. The continuity of the CMD in the transition region between GSAOI to 2MASS demonstrates that the photometric calibration is reasonable. I also note the beautiful extreme horizontal branch stars that are present in the GSAOI data at a color of $m_{\mathrm{F606W}} - m_{K_{\mathrm{S}}} \sim 0$ and the main sequence knee located at $m_{K_{\mathrm{S}}} \sim 20$.

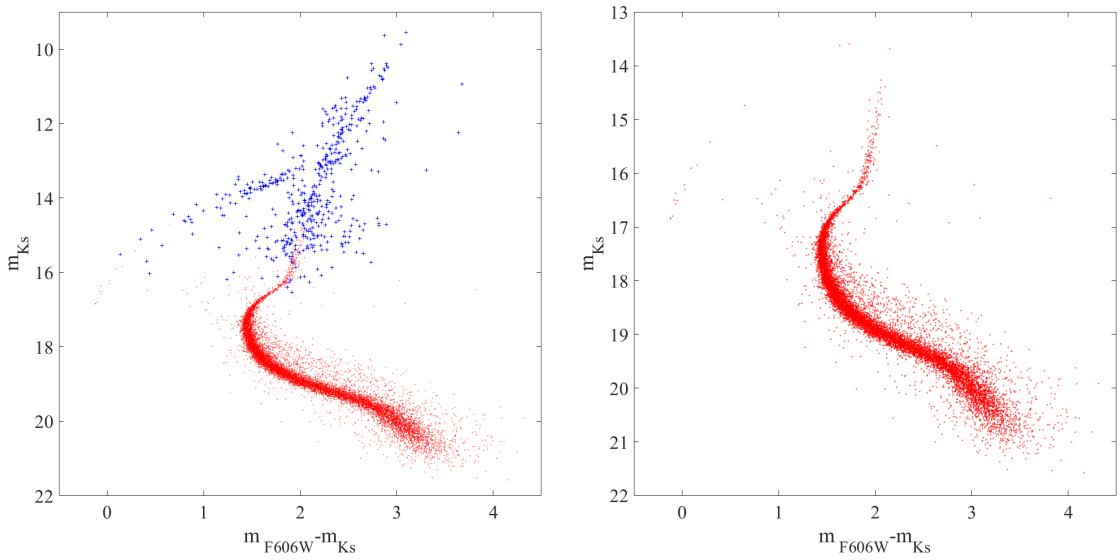

Figure 4.21: The optical-near-infrared CMD for NGC 6723. The red points represent the GSAOI-HST and the blue point are from the 2MASS-HST catalogues. The continuity of the CMD in the transition region between GSAOI to 2MASS suggests that the photometric calibration is reasonable.

4.6 Summary

I used GeMS/GSAOI on the Gemini South Telescope to better understand the on-sky astrometric performance of MCAO. I developed a pipeline that can be used to measure and compensate for the relative distortion field between the MCAO observations and

any secondary catalog. To validate the performance of the pipeline I used observations of the core of globular cluster NGC 6723 that ultimately produce a high quality tangential velocity dispersion profile for the cluster to small radius as well as a deep optical-near-infrared CMD. In order to do this, I had to deal with the adverse effect of the distortion field. I derived the relative distortion maps between the two catalogues by developing a novel method that uses the maximal amount of information to probe the distortion fields at the highest possible spatial resolution (set by the density of stars). I demonstrate how these maps can be used to trace both the time-variable and static components of the distortion. In this way, I am able to show the effect of the Gemini field rotator at the sub-pixel level, and I can reproduce the distortion caused by the optical design of GeMS/GSAOI. I believe these kinds of measurements will be a valuable tool to diagnose and monitor the telescope/AO system astrometric performance for future generations of large ground-based telescopes.

The methodology presented in this chapter does not require any additional information from other sources, other than the *relative* first-epoch positions of the stars being studied. This is a necessary step towards the high precision MCAO-only proper motions. In the future, this pipeline will be applied to multi-epoch MCAO data, an important next step towards enabling future telescopes like TMT and ELT to reach their astrometric potentials.

Chapter 5

Conclusions and Future Directions

Throughout my PhD, my main direction was to simultaneously increase my knowledge of astronomical instrumentation as well as the knowledge necessary to optimally utilise instruments for astrometric applications. Having experience in both how an instrument is designed and built, in addition to how it is used in action, provides a rare and crucial insight into the field. Therefore, this thesis includes involvement in the design and fabrication of new science-class instruments by tackling key issues of wavefront sensors with their hardware (Chapter 2), their response to real-world problems such as uneven pupil illumination (Chapter 3), and then examined practical consequences of real-world AO systems as pertaining to the key issue of astrometry, which is a key capability for future ELT facilities (Chapter 4). This work aims to pave the path for future laboratory AO models, while at the same time moving towards using future generation of MCAO facilities on ELTs for optimum astrometric studies.

The focus of Chapter 2 is on developing new wavefront sensing instruments at Keck and NRC. My collaboration with the Keck Observatory resulted in the fabrication and commissioning of the new IR-PWFS system as well as the KPIC instrument. This instrument is now operational, enabling astronomers to look into the composition of the atmosphere of exoplanets. The IRP-PWFS significantly improves the number of faint NGSs that could be used as WFS target, increasing coverage and AO performance across the sky. I also built the SSH-WFS for NRC's AO lab. The device design and fabrication met the requirements for differential measurement and was successfully completed. This device will be necessary to study the surface behaviour of the new DMs for TMT, as well as characterizing the influence function of actuators and surface behaviour between neighbouring actuators. Preparing the device for absolute measurements is a future goal for this project. Before Covid 19 restricted

my access to the laboratory facilities, I had begun to make the necessary efforts to provide this additional capability. However, a mis-conjugation in the DM prototype experimental setup prevented me from being able to demonstrate the expected accuracy. Therefore, the absolute measurement capabilities for SSH-WFS are scheduled for future opportunities when the laboratory and the bench are fully accessible.

In Chapter 3, I focused on improving AO laboratory models by attacking a specific problem: the convenient and precise solution to model the spider shadow in a laboratory environment. This is an important challenge to overcome especially when ensuring the requirements of ELTs in terms of wavefront error will be satisfied. I performed simulation studies for real-world scenarios of these effects for specific scenarios. Particularly, I looked at the expected error budget caused by partially illuminated pixels of IR-PWFS for Keck. The result of this study showed that for this case, the error would not be a major term, but this would be different for ELTs as their error budget requirements are an order of magnitude tighter. A sufficient and accurate study of spider structure related issues such as the effect of partially illuminated sub-apertures/pixels, low wind effect and petalling are dependent upon resolving this challenge. My solution to this issue was successfully demonstrated and provided satisfactory results. Additionally, I provided an opto-mechanical design for the AWS bench at NRC facilities in Victoria to implement this new solution. Due to the COVID 19 restrictions, reconfiguration of the AWS remains to be done in the future.

In Chapter 4, I focused on the implementation of MCAO systems for astrometric studies. The new generation of extremely large telescopes are just on the horizon. These giants use sate-of-the-art MCAO facilities, enabling them to perform diffraction-limited observation in a relatively wide field of view. This makes them an ideal tool for very high-precision dynamic measurements such as the dynamics of stars in the core of our galaxy, or hunting for IMBHs in the core of globular clusters. However, to reach the real astrometric potential of these instruments, there are some challenges that need to be addressed, namely, the characterisation of the distortion pattern that MCAO systems can introduce and efficient methods to mitigate it. I used the only MCAO system currently in science operation to address this problem. The method I developed for high-precision MCAO differential astrometry was successfully demonstrated on the globular cluster NGC 6723. I also provided a method for on-sky measurements of the distortion field to complement shortcomings of pinhole-mask calibration strategies. Finally, I presented a deep and precise $K_s - Visible$ CMD as

well as proper motions of over 6000 stars near the core of NGC 6723 and the velocity dispersion profile for the cluster. There are few future directions for this work:

- The data we gathered from the vicinity of the NGC 6723 will be used to place dynamical limits on the presence of a possible intermediate-mass black hole (IMBH). In particular, the velocity dispersion profile close to the core of the GC – enabled by MCAO – provides critical information on the dynamics close to the center where a black hole could dominate. Understanding the limits provided by the current generation of MCAO capabilities will be essential information that can help guide expectations and possibly design choices for future generations of MCAO on the TMT and ELT.

- I was the PI of observation program GS-2019A-Q-203 that successfully observed the core of NGC 5904 in 2019. This means deep MCAO-aimed observations with a baseline of 13 and six years HST-GSAOI, and six years GSAOI-GSAOI now is at our disposal. This valuable data set opens the path for the ultimate goal; the independent (without auxiliary space-based data) very high-precision ground-based astrometry. This is important since no space telescope would be able to compete with the resolving power of diffraction-limited observation of ELTs. This makes it essential to develop advanced astrometric techniques that are solely dependent upon MCAO-aimed, ground-based observations. I took the first step on this path through my research described in Section 4 of this thesis, providing the second epoch MCAO-aimed, ground-based observation of a core of a globular cluster, the reduction method, as well as its astrometric reduction pipeline. In the future, I will use this combination to take future steps towards very high-precision astrometry with ELTs.

- I also provided an on-sky method to accurately measure the distortion field from the combination of a telescope and its imager instrument. For doing so, a set of dithered observations is necessary. During the course of publishing this research, I noticed the lack of an optimum methodology to determine the best dither pattern for this application. I developed a Monte Carlo simulation program which measures the precision of the derived distortion field from a set of simulated observations with a certain dither pattern. One future direction of the research described in this thesis is to add an optimisation component to this simulation. This will provide a method to find the optimum dither pattern for on-sky distortion calibration for a given telescope and imager system.

Bibliography

[1] V. Akondi, A. Jewel, and B. Vohnsen. Closed-loop adaptive optics using a single spatial light modulator for ophthalmic applications. 08 2014.

[2] I. Al-Haytham and A.I. Sabra. *The Optics of Ibn Al-Haytham: Books I-III : on Direct Vision*. Number no. 1 in G - Reference, Information and Interdisciplinary Subjects Series. Warburg Institute, University of London, 1989.

[3] S. Mark Ammons, E. Victor Garcia, M. Salama, B. Neichel, J. Lu, C. Marois, B. Macintosh, D. Savransky, E. Bendek, O. Guyon, E. Marin, V. Garrel, and G. Sivo. Precision astrometry with adaptive optics: constraints on the mutual orbit of Luhman 16AB from GeMS. In Enrico Marchetti, Laird M. Close, and Jean-Pierre Véran, editors, *Adaptive Optics Systems V*, volume 9909, pages 1698 – 1706. International Society for Optics and Photonics, SPIE, 2016.

[4] J. Anderson and I.R. King. An Improved Distortion Solution for the Hubble Space Telescope's WFPC2. *The Publications of the Astronomical Society of the Pacific*, January 2003.

[5] J. Anderson, A. Sarajedini, L.R. Bedin, I.R. King, G. Piotto, I.N. Reid, M. Siegel, S.R. Majewski, N.E. Paust, A. Aparicio, et al. The acs survey of globular clusters. v. generating a comprehensive star catalog for each cluster. *The Astronomical Journal*, 135(6):2055, 2008.

[6] S. M. Andrews, J. Huang, L. M. Pérez, A. Isella, C. P. Dullemond, N. T. Kurtovic, V. V. Guzmán, J. M. Carpenter, D. J. Wilner, S. Zhang, Z. Zhu, T. Birnstiel, X.-N. Bai, M. Benisty, A. M. Hughes, K. I. Öberg, and L. Ricci. The Disk Substructures at High Angular Resolution Project (DSHARP). I. Motivation, Sample, Calibration, and Overview. , 869:L41, December 2018.

[7] B. Neichel, J. Lu, F. Rigaut, S.M. Ammons, E. Carrasco, and E. Lassalle. Astrometric performance of the Gemini multiconjugate adaptive optics system in crowded fields. , 445(1):500–514, November 2014.

[8] E.J. Barton, J.E. Larkin, A.M. Moore, S.A. Wright, D. Crampton, L. Simard, B. Macintosh, P. Côté, A.J. Barth, A.M. Ghez, J.R. Lu, T.J. Davidge, and D.R. Law. The Infrared Imaging Spectrograph (IRIS) for TMT: the science case. In Ian S. McLean, Suzanne K. Ramsay, and Hideki Takami, editors, *Ground-based and Airborne Instrumentation for Astronomy III*, volume 7735, pages 2076 – 2084. International Society for Optics and Photonics, SPIE, 2010.

[9] H. Baumgardt, M. Hilker, A. Sollima, and A. Bellini. Mean proper motions, space orbits, and velocity dispersion profiles of galactic globular clusters derived from gaia dr2 data. *Monthly Notices of the Royal Astronomical Society*, 482(4):5138–5155, 2019.

[10] A. Bellini, J. Anderson, and L. R. Bedin. Astrometry and Photometry with HST WFC3. II. Improved Geometric-Distortion Corrections for 10 Filters of the UVIS Channel. , 123(903):622, May 2011.

[11] A Bellini and LR Bedin. Ground-based ccd astrometry with wide field imagers-iv. an improved geometric-distortion correction for the blue prime-focus camera at the lbt. *Astronomy & Astrophysics*, 517:A34, 2010.

[12] . Bertrou-Cantou, E. Gendron, G. Rousset, F. Vidal, V. Deo, and F. Ferreira. Analysis of the island effect for elt micado maory scao mode. *Proc. AO4ELT6*, 2019.

[13] C.Z. Bond, S. Cetre, S. Lilley, P. Wizinowich, D. Mawet, M. Chun, E. Wetherell, S. Jacobson, C. Lockhart, E. Warmbier, S. Ragland, C. Álvarez, O. Guyon, S. Goebel, J-R. Delorme, N. Jovanovic, D.N. Hall, J.K. Wallace, M. Taheri, C. Plantet, and V. Chambouleyron. Adaptive optics with an infrared pyramid wavefront sensor at Keck. *Journal of Astronomical Telescopes, Instruments, and Systems*, 6(3):1 – 21, 2020.

[14] C.Z. Bond, C.M. Correia, J.F. Sauvage, K.E. Hadi, Y. Abautret, B. Neichel, and T. Fusco. Optimized calibration of the adaptive optics system on the lam pyramid bench. In *Adaptive Optics for Extremely Large Telescopes 5-Conference Proceedings*, 2017.

[15] H. Bonneta, J. Spyromilioa, C. Vérinauda, M. Esselborna, E. Marchettia, M. Le Louarna, S. Lewisa, T. Pfrommera, and F. Biancat-Marcheta. Elt wavefront control strategy.

[16] V. Villalba C., H. Kuiper, and E. Gill. Review on thermal and mechanical challenges in the development of deployable space optics. *Journal of Astronomical Telescopes, Instruments, and Systems*, 6(1):1 – 30, 2020.

[17] P. B. Cameron, M. C. Britton, and S. R. Kulkarni. Precision Astrometry With Adaptive Optics. , 137(1):83–93, January 2009.

[18] C. Colodro-Conde, S. Velasco, J. J. Fernández-Valdivia, R. López, A. Oscoz, R. Rebolo, B. Femenía, D. L. King, L. Labadie, C. Mackay, B. Muthusubramanian, A. Pérez Garrido, M. Puga, G. Rodríguez-Coira, L. F. Rodríguez-Ramos, J. M. Rodríguez-Ramos, R. Toledo-Moreo, and I. Villó-Pérez. Laboratory and telescope demonstration of the TP3-WFS for the adaptive optics segment of AOLI. *Monthly Notices of the Royal Astronomical Society*, 467(3):2855–2868, 02 2017.

[19] R. Conan and C. Correia. Object-oriented Matlab adaptive optics toolbox. In Enrico Marchetti, Laird M. Close, and Jean-Pierre Véran, editors, *Adaptive Optics Systems IV*, volume 9148, pages 2066 – 2082. International Society for Optics and Photonics, SPIE, 2014.

[20] A. Costille, C. Petit, J.M. Conan, C. Kulcsár, H.F. Raynaud, and T. Fusco. Wide field adaptive optics laboratory demonstration with closed-loop tomographic control. *J. Opt. Soc. Am. A*, 27(3):469–483, Mar 2010.

[21] R. Cutri, M. Skrutskie, S. Van Dyk, C. Beichman, J. Carpenter, T. Chester, L. Cambresy, T. Evans, J. Fowler, J. Gizis, et al. Vizier online data catalog: 2mass all-sky catalog of point sources (cutri+ 2003). *VizieR online data catalog*, pages II–246, 2003.

[22] D. Massari, G. Fiorentino, A. McConnachie, G. Bono, M. Dall'Ora, I. Ferraro, G. Iannicola, P.B. Stetson, P. Turri, and E. Tolstoy. GeMS MCAO observations of the Galactic globular cluster NGC 2808: the absolute age. , 586:A51, February 2016.

[23] D. Massari, G. Fiorentino, E. Tolstoy, A. McConnachie, R. Stuik, L. Schreiber, D. Andersen, Y. Clénet, R. Davies, D. Gratadour, K. Kuijken, R. Navarro, J. Pott, G. Rodeghiero, P. Turri, and G. Verdoes Kleijn. High-precision astrometry towards ELTs. In Enrico Marchetti, Laird M. Close, and Jean-Pierre Véran, editors, *Adaptive Optics Systems V*, volume 9909 of *Society of Photo-Optical Instrumentation Engineers (SPIE) Conference Series*, page 99091G, July 2016.

[24] E. Dalessandro, S. Saracino, L. Origlia, E. Marchetti, F. R. Ferraro, B. Lanzoni, D. Geisler, R. E. Cohen, F. Mauro, and S. Villanova. GeMS/GSAOI Photometric and Astrometric Performance in Dense Stellar Fields. , 833(1):111, December 2016.

[25] R. Davies, N. Ageorges, L. Barl, L. Bedin, R. Bender, P. Bernardi, F. Chapron, Y. Clenet, A. Deep, E. Deul, et al. Science and adaptive optics requirements of micado, the e-elt adaptive optics imaging camera. In *1st AO4ELT conference-Adaptive Optics for Extremely Large Telescopes*, page 01002. EDP Sciences, 2010.

[26] R. Davies, J. Alves, Y. Clénet, F. Lang-Bardl, H. Nicklas, J.-U. Pott, R. Ragazzoni, E. Tolstoy, P. Amico, H. Anwand-Heerwart, S. Barboza, L. Barl, P. Baudoz, R. Bender, N. Bezawada, P. Bizenberger, W. Boland, P. Bonifacio, B. Borgo, T. Buey, F. Chapron, F. Chemla, M. Cohen, O. Czoske, V. Déo, K. Disseau, S. Dreizler, O. Dupuis, M. Fabricius, R. Falomo, P. Fedou, N. Förster Schreiber, V. Garrel, N. Geis, H. Gemperlein, E. Gendron, R. Genzel, S. Gillessen, M. Glück, F. Grupp, M. Hartl, M. Häuser, H.-J. Hess, R. Hofferbert, U. Hopp, V. Hörmann, Z. Hubert, E. Huby, J.-M. Huet, V. Hutterer, D. Ives, A. Janssen, W. Jellema, W. Kausch, F. Kerber, H. Kravcar, B. Le Ruyet, K. Leschinski, C. Mandla, M. Manhart, D. Massari, S. Mei, F. Merlin, L. Mohr, A. Monna, N. Muench, F. Müller, G. Musters, R. Navarro, U. Neumann, N. Neumayer, J. Niebsch, M. Plattner, N. Przybilla, S. Rabien, R. Ramlau, J. Ramos, S. Ramsay, P. Rhode, A. Richter, J. Richter, H.-W. Rix, G. Rodeghiero, R.-R. Rohloff, M. Rosensteiner, G. Rousset, J. Schlichter, J. Schubert, A. Sevin, R. Stuik, E. Sturm, J. Thomas, N. Tromp, G. Verdoes-Kleijn, F. Vidal, R. Wagner, M. Wegner, W. Zeilinger, J. Ziegleder, B. Ziegler, and G. Zins. The MICADO first light imager for the ELT: overview, operation, simulation. In Christopher J. Evans, Luc Simard, and Hideki Takami, editors,

Ground-based and Airborne Instrumentation for Astronomy VII, volume 10702, pages 570 – 581. International Society for Optics and Photonics, SPIE, 2018.

[27] K. Dennison, S.M. Ammons, Vi. Garrel, E. Marin, G. Sivo, E. Bendek, and O. Guyon. An engineered design of a diffractive mask for high precision astrometry. In Enrico Marchetti, Laird M. Close, and Jean-Pierre Véran, editors, *Adaptive Optics Systems V*, volume 9909 of *Society of Photo-Optical Instrumentation Engineers (SPIE) Conference Series*, page 99094E, July 2016.

[28] C. d'Orgeville, S. Diggs, V. Fesquet, B. Neichel, W. Rambold, F. Rigaut, A. Serio, C. Araya, G. Arriagada, R. Balladares, et al. Gemini south multi-conjugate adaptive optics (gems) laser guide star facility on-sky performance results. In *Adaptive Optics Systems III*, volume 8447, page 84471Q. International Society for Optics and Photonics, 2012.

[29] T.J. Dupuy, M.C. Liu, W.M.J. Best, A.W. Mann, M.A. Tucker, Z. Zhang, I. Baraffe, G. Chabrier, T. Forveille, S.A. Metchev, P. Tremblin, A. Do, A.V. Payne, B.J. Shappee, C.Z. Bond, S. Cetre, M. Chun, J-R. Delorme, N. Jovanovic, S. Lilley, D. Mawet, S. Ragland, E. Wetherell, and P. Wizinowich. WISE J072003.20-084651.2B is a Massive T Dwarf. *The Astronomical Journal*, 158(5):174, 2019.

[30] E. Dalessandro, S. Saracino, L. Origlia, E. Marchetti, F.R. Ferraro, B. Lanzoni, D. Geisler, and F. Mauro. GeMS/GSAOI performances from a user perspective. In Enrico Marchetti, Laird M. Close, and Jean-Pierre Véran, editors, *Adaptive Optics Systems V*, volume 9909 of *Society of Photo-Optical Instrumentation Engineers (SPIE) Conference Series*, page 99095V, July 2016.

[31] E. Mieda, J-P. Veran, M. Rosensteiner, P. Turri, D. Andersen, G. Herriot, O. Lardiere, and P. Spano. Multiconjugate adaptive optics simulator for the Thirty Meter Telescope: design, implementation, and results. *Journal of Astronomical Telescopes, Instruments, and Systems*, 4:049002, October 2018.

[32] B. Engler, S. Weddell, M. Louarn, and R. Clare. Effects of the telescope spider on extreme adaptive optics systems with pyramid wavefront sensors. page 198, 07 2018.

[33] E.R. Carrasco, M.L. Edwards, P.J. McGregor, C. Winge, P.J. Young, M.C. Doolan, J. van Harmelen, F.J. Rigaut, B. Neichel, G. Trancho, E. Artigau, P.

Pessev, F. Colazo, J. Tigner, F. Mauro, J. Lührs, and W.N. Rambold. Results from the commissioning of the Gemini South Adaptive Optics Imager (GSAOI) at Gemini South Observatory. In Brent L. Ellerbroek, Enrico Marchetti, and Jean-Pierre Véran, editors, *Adaptive Optics Systems III*, volume 8447 of *Society of Photo-Optical Instrumentation Engineers (SPIE) Conference Series*, page 84470N, July 2012.

[34] R. C. Flicker, F. J. Rigaut, and B. L. Ellerbroek. Tilt anisoplanatism in laser-guide-star-based multiconjugate adaptive optics. Reconstruction of the long exposure point spread function from control loop data. , 400:1199–1207, March 2003.

[35] C. Forest, C. Canizares, D. Neal, M. Mcguirk, A. Slocum, and M. Schattenburg. Metrology of thin transparent optics using shack-hartmann wavefront sensing. *Optical Engineering*, 43, 03 2004.

[36] T. Fritz, S. Gillessen, S. Trippe, T. Ott, H. Bartko, O. Pfuhl, K. Dodds-Eden, R. Davies, F. Eisenhauer, and R. Genzel. What is limiting near-infrared astrometry in the galactic centre? *Monthly Notices of the Royal Astronomical Society*, 401(2):1177–1188, 2010.

[37] T. K. Fritz, S. T. Linden, P. Zivick, N. Kallivayalil, R. L. Beaton, J. Bovy, L. V. Sales, T. Sohn, D. Angell, M. Boylan-Kolchin, E. R. Carrasco, G. Damke, R. Davies, S. Majewski, B. Neichel, and R. van der Marel. The Proper Motion of Pyxis: The First Use of Adaptive Optics in Tandem with HST on a Faint Halo Object. , 840(1):30, May 2017.

[38] G. Fiorentino, D. Massari, A. McConnachie, P.B. Stetson, G. Bono, P. Turri, D. Andersen, J-P. Veran, E. Diolaiti, L. Schreiber, P. Ciliegi, M. Bellazzini, E. Tolstoy, M. Monelli, G. Iannicola, I. Ferraro, and V. Testa. Stellar photometry with multi conjugate adaptive optics. In Enrico Marchetti, Laird M. Close, and Jean-Pierre Véran, editors, *Adaptive Optics Systems V*, volume 9909 of *Society of Photo-Optical Instrumentation Engineers (SPIE) Conference Series*, page 990906, July 2016.

[39] G. Rodeghiero, J. Pott, and P. Bizenberger. Study of the impact of E-ELT and MICADO distortion and wavefront errors residuals on the MICADO astrometric observations. In Christopher J. Evans, Luc Simard, and Hideki Takami, editors,

Ground-based and Airborne Instrumentation for Astronomy VI, volume 9908 of *Society of Photo-Optical Instrumentation Engineers (SPIE) Conference Series*, page 99089E, August 2016.

[40] Physikalisch-Technische Reichsanstalt (Germany). *Zeitschrift für Instrumentenkunde*. Springer, 1891.

[41] S. Goebel, D. Hall, O. Guyon, E. Warmbier, and S. Jacobson. Overview of the SAPHIRA detector for adaptive optics applications. *Journal of Astronomical Telescopes, Instruments, and Systems*, 4, 2018.

[42] J. Hardy. *Adaptive optics for astronomical telescopes*, volume 16. Oxford University Press on Demand, 1998.

[43] G. Herriot, P. Hickson, B. Ellerbroek, D. Andersen, T. Davidge, D. Erickson, I. Powell, R. Clare, L. Gilles, C. Boyer, M. Smith, L. Saddlemyer, and J.-P. Véran. NFIRAOS: TMT narrow field near-infrared facility adaptive optics. In Brent L. Ellerbroek and Domenico Bonaccini Calia, editors, *Advances in Adaptive Optics II*, volume 6272, pages 228 – 239. International Society for Optics and Photonics, SPIE, 2006.

[44] S. Hippler, M. Feldt, T. Bertram, W. Brandner, F. Cantalloube, B. Carlomagno, O. Absil, A. Obereder, J. Shatokhina, and R. Stuik. Single conjugate adaptive optics for the elt instrument metis. *Experimental Astronomy*, 11 2018.

[45] J. Atwood, P. Byrnes, G. Herriot, J. Pazder, and S. Roberts. Optical design challenges of NFIRAOS, the first-light adaptive optics system for TMT. In Julie Bentley, Anurag Gupta, and Richard N. Youngworth, editors, *International Optical Design Conference 2010*, volume 7652 of *Society of Photo-Optical Instrumentation Engineers (SPIE) Conference Series*, page 765229, August 2010.

[46] J. Crane, G. Herriot, D. Andersen, J. Atwood, P. Byrnes, A. Densmore, J. Dunn, J. Fitzsimmons, T. Hardy, B. Hoff, K. Jackson, D. Kerley, O. Lardière, M. Smith, J. Stocks, J-P. Véran, C. Boyer, L. Wang, G. Trancho, and M. Trubey. NFIRAOS adaptive optics for the Thirty Meter Telescope. In Laird M. Close, Laura Schreiber, and Dirk Schmidt, editors, *Adaptive Optics Systems VI*, volume 10703 of *Society of Photo-Optical Instrumentation Engineers (SPIE) Conference Series*, page 107033V, July 2018.

[47] J. Larkin, A. Moore, S. Wright, J. Wincentsen, D. Anderson, E. Chisholm, R. Dekany, J. Dunn, B. Ellerbroek, Y. Hayano, A. Phillips, L. Simard, R. Smith, R. Suzuki, R. Weber, J. Weiss, and K. Zhang. The Infrared Imaging Spectrograph (IRIS) for TMT: instrument overview. In Christopher J. Evans, Luc Simard, and Hideki Takami, editors, *Ground-based and Airborne Instrumentation for Astronomy VI*, volume 9908 of *Society of Photo-Optical Instrumentation Engineers (SPIE) Conference Series*, page 99081W, August 2016.

[48] P. Janin-Potiron, V. Chambouleyron, L. Schatz, O. Fauvarque, C. Bond, Y. Abautret, E. Muslimov, K. EL HADI, J-F. Sauvage, K. Dohlen, B. Neichel, C. Correia, and T. Fusco. Adaptive optics with programmable fourier-based wavefront sensors: a spatial light modulator approach to the lam/onera on-sky pyramid sensor testbed. *Journal of Astronomical Telescopes, Instruments, and Systems*, 5:1, 07 2019.

[49] P. Janin-Potiron, V. Chambouleyron, L. Schatz, O. Fauvarque, C. Bond, E. Muslimov, K. El-Hadi, J-F. Sauvage, K. Dohlen, B. Neichel, C. Correia, N. Villard, S. Aïssani, M. Taheri, and T. Fusco. In depth analysis of fourier-based wavefront sensors with the adaptive optics testbed loops. In *6th International Conference on Adaptive Optics for Extremely Large Telescopes, AO4ELT 2019*, Jun 2019.

[50] J.D. Drummond. Adaptive optics Lorentzian point spread function. In Domenico Bonaccini and Robert K. Tyson, editors, *Adaptive Optical System Technologies*, volume 3353 of *Society of Photo-Optical Instrumentation Engineers (SPIE) Conference Series*, pages 1030–1037, September 1998.

[51] K. El Hadi, M. Vignaux, and T. Fusco. Development of a Pyramid Wave-front Sensor. In Simone Esposito and Luca Fini, editors, *Proceedings of the Third AO4ELT Conference*, page 99, December 2013.

[52] L. O. Kerber, M. Libralato, S. O. Souza, R. A. P. Oliveira, S. Ortolani, A. Pérez-Villegas, B. Barbuy, B. Dias, E. Bica, and D. Nardiello. A deep view of a fossil relic in the Galactic bulge: the Globular Cluster HP 1. , 484(4):5530–5550, April 2019.

[53] E. Laag, S. Ammons, D. Gavel, and R. Kupke. Multiconjugate adaptive optics results from the laboratory for adaptive optics mcao/moao testbed. *J. Opt. Soc. Am. A*, 25(8):2114–2121, Aug 2008.

[54] L. Lessard. *Tractability of Complex Control Systems*. PhD thesis, 08 2011.

[55] S. Lilley and M. Taheri. Kaon 1178 - pwfs and fiu field steering mirror (fsm) calculations for k2 ao system. Technical report, W. M. Keck Observatories, Waimea HI, 2017.

[56] S.J. Lilley, P. Wizinowich, D. Mawet, M. Chun, C.Z. Bond, J.K. Wallace, N. Jovanovic, J-R. Delorme, S.M. Jacobson, M. Taheri, et al. Near-infrared pyramid wavefront sensor for keck adaptive optics: opto-mechanical design. In *Adaptive Optics Systems VI*, volume 10703, page 107033G. International Society for Optics and Photonics, 2018.

[57] M. Longair. *High Energy Astrophysics*. Cambridge University Press, 1992. ISBN: 0-521-38374-9.

[58] J. Lozi, N. Jovanovic, O. Guyon, M. Chun, S. Jacobson, S. Goebel, and F. Martinache. Visible and near-infrared laboratory demonstration of a simplified pyramid wavefront sensor. *Publications of the Astronomical Society of the Pacific*, 131(998):044503, mar 2019.

[59] J. Lozi, N. Jovanovic, O. Guyon, M. Chun, S. Jacobson, S. Goebel, and F. Martinache. Visible and near-infrared laboratory demonstration of a simplified pyramid wavefront sensor. *Publications of the Astronomical Society of the Pacific*, 131(998):044503, mar 2019.

[60] J. Lu, M. Chun, R. Suzuki, M. Schoeck, J. Atwood, D. Andersen, G. Herriot, et al. Geometric distortion calibration with photolithographic pinhole masks for high-precision astrometry. *Journal of Astronomical Telescopes, Instruments, and Systems*, 5(3):039005, 2019.

[61] A. Martin and S. Koelfgen. A maximum-likelihood algorithm for reduction of Langmuir probe data. *Review of Scientific Instruments*, 78(10):103508–103508–6, October 2007.

[62] D. Massari, G. Fiorentino, A. McConnachie, A. Bellini, E. Tolstoy, P. Turri, D. Andersen, G. Bono, P.B. Stetson, and J-P. Veran. Astrometry with mcao: Hst-gems proper motions in the globular cluster ngc 6681. *Astronomy & Astrophysics*, 595:L2, 2016.

[63] E. Mieda, M. Rosensteiner, M. van Kooten, J-P. Veran, O. Lardiere, and G. Herriot. Testing the pyramid truth wavefront sensor for nfiraos in the lab. In *Adaptive Optics Systems V*, volume 9909, page 99091J. International Society for Optics and Photonics, 2016.

[64] B. W. Miller, T. H. Puzia, S. Monty, E. R. Carrasco, M. Simunovic, and GCS Team. G4CS: GeMS/GSAOI Galactic Globular Cluster Survey. *Boletin de la Asociacion Argentina de Astronomia La Plata Argentina*, 61:116–118, August 2019.

[65] J. Milli, M. Kasper, P. Bourget, C. Pannetier, D. Mouillet, J-F. Sauvage, C. Reyes, T. Fusco, F. Cantalloube, K. Tristram, Z. Wahhaj, J. Beuzit, J. Girard, D. Mawet, A. Telle, A. Vigan, and M. N'Diaye. Low wind effect on vlt/sphere: impact, mitigation strategy, and results. 07 2018.

[66] J. Milli, D. Mouillet, T. Fusco, J.H. Girard, E. Masciadri, E. Pena, J.F. Sauvage, C. Reyes, K. Dohlen, J.L. Beuzit, et al. Performance of the extreme-ao instrument vlt/sphere and dependence on the atmospheric conditions. *arXiv preprint arXiv:1710.05417*, 2017.

[67] S. Monty, F. Rigaut, R. McDermid, J. Cranney, G. Agapito, C. Plantet, D. Greggio, J. Trevor Mendel, M. Taheri, D. Vassallo, C. Schwab, G. Fiorentino, G. Bono, and D. Haynes. The MAVIS Image Simulator: predicting the astrometric performance of MAVIS. In Christopher J. Evans, Julia J. Bryant, and Kentaro Motohara, editors, *Ground-based and Airborne Instrumentation for Astronomy VIII*, volume 11447, pages 1063 – 1071. International Society for Optics and Photonics, SPIE, 2020.

[68] A. Nikitin, I. Galaktionov, J. Sheldakova, A. Kudryashov, V. Samarkin, A. Rukosuev, and V. Toporovsky. Focusing laser beam through pinhole using high-resolution stacked-actuator deformable mirror. In Vladimir S. Ilchenko, Andrea M. Armani, Julia V. Sheldakova, Alexis V. Kudryashov, and Alan H. Paxton, editors, *Laser Resonators, Microresonators, and Beam Control XXIII*,

volume 11672, pages 122 – 132. International Society for Optics and Photonics, SPIE, 2021.

[69] P. Turri, A.W. McConnachie, P.B. Stetson, G. Fiorentino, D. Andersen, G. Bono, D. Massari, and J-P. Véran. Optimal Stellar Photometry for Multi-conjugate Adaptive Optics Systems Using Science-based Metrics. , 153(4):199, April 2017.

[70] M. Patti and G. Fiorentino. Unveiling the nature of Gemini multiconjugate adaptive optics system distortions. , 485(3):3470–3475, May 2019.

[71] C. Pernechele. Imaging — adaptive optics. In Robert D. Guenther, editor, *Encyclopedia of Modern Optics*, pages 127–134. Elsevier, Oxford, 2005.

[72] C. Plantet, C.Z. Bond, C. Giordano, G. Agapito, M. Taheri, S. Esposito, and P. Wizinowich. Keck ii adaptive optics upgrade: simulations of the near-infrared pyramid sensor. In *Adaptive Optics Systems VI*, volume 10703, page 1070335. International Society for Optics and Photonics, 2018.

[73] B. Platt and R. Shack. History and principles of shack-hartmann wavefront sensing. *Journal of refractive surgery (Thorofare, N.J. : 1995)*, 17(5):S573—7, 2001.

[74] R. Ragazzoni. Pupil plane wavefront sensing with an oscillating prism. *Journal of Modern Optics*, 43(2):289–293, February 1996.

[75] S. K. Ramsay, M. M. Casali, J. C. González, and N. Hubin. The E-ELT instrument roadmap: a status report. In Suzanne K. Ramsay, Ian S. McLean, and Hideki Takami, editors, *Ground-based and Airborne Instrumentation for Astronomy V*, volume 9147 of *Society of Photo-Optical Instrumentation Engineers (SPIE) Conference Series*, page 91471Z, August 2014.

[76] H. Riechert, V. Garrel, J. Pott, G. Sivo, and E. Marin. GeMS/GSAOI: towards regular astrometric distortion correction. In Christopher J. Evans, Luc Simard, and Hideki Takami, editors, *Ground-based and Airborne Instrumentation for Astronomy VII*, volume 10702 of *Society of Photo-Optical Instrumentation Engineers (SPIE) Conference Series*, page 1070232, July 2018.

[77] F. Rigaut, B. Neichel, M. Boccas, C. d'Orgeville, G. Arriagada, V. Fesquet, S.J. Diggs, C. Marchant, G. Gausach, W.N. Rambold, J. Luhrs, S. Walker, E.R. Carrasco-Damele, M.L. Edwards, P. Pessev, R.L. Galvez, T.B. Vucina, C. Araya, A. Gutierrez, A.W. Ebbers, A. Serio, C. Moreno, C. Urrutia, R. Rogers, R. Rojas, C. Trujillo, B. Miller, D.A. Simons, A. Lopez, V. Montes, H. Diaz, F. Daruich, F. Colazo, M. Bec, G. Trancho, M. Sheehan, P. McGregor, P.J. Young, M.C. Doolan, J. van Harmelen, B.L. Ellerbroek, D. Gratadour, and A. Garcia-Rissmann. GeMS first on-sky results. In Brent L. Ellerbroek, Enrico Marchetti, and Jean-Pierre Véran, editors, *Adaptive Optics Systems III*, volume 8447, pages 149 – 163. International Society for Optics and Photonics, SPIE, 2012.

[78] F. Roddier. Curvature sensing and compensation: a new concept in adaptive optics. *Appl. Opt.*, 27(7):1223–1225, Apr 1988.

[79] A. Rudy, L. Poyneer, S. Srinath, M. Ammons, and D. Gavel. A laboratory demonstration of an LQG technique for correcting frozen flow turbulence in adaptive optics systems. *arXiv e-prints*, page arXiv:1504.03686, April 2015.

[80] s. Ragland, D. Mawet, C. Alvarez, K. Matthews, C. Bond, S. Cetre, J-R. Delorme, S. Lilley, N. Jovanovic, G. Ruane, et al. High contrast imaging upgrades for the keck adaptive optics imager. *AO4ELT 2019-Proceedings 6th Adaptive Optics for Extremely Large Telescopes*, 2019.

[81] G. Sanders. The thirty meter telescope (tmt): An international observatory. *Journal of Astrophysics and Astronomy*, 34(2):81–86, 2013.

[82] S. Saracino, E. Dalessandro, F. R. Ferraro, D. Geisler, F. Mauro, B. Lanzoni, L. Origlia, P. Miocchi, R. E. Cohen, S. Villanova, and C. Moni Bidin. Ultra-deep GEMINI Near-infrared Observations of the Bulge Globular Cluster NGC 6624. , 832(1):48, November 2016.

[83] A. Sarajedini, L.R. Bedin, B. Chaboyer, A. Dotter, M. Siegel, J. Anderson, A. Aparicio, I. King, S. Majewski, A. Marín-Franch, et al. The acs survey of galactic globular clusters. i. overview and clusters without previous hubble space telescope photometry. *The Astronomical Journal*, 133(4):1658, 2007.

[84] N. Savage. Digital spatial light modulators. *Nature Photonics*, 3:170–172, 03 2009.

[85] M. Schöck, T. Do, B. Ellerbroek, L. Gilles, G. Herriot, L. Meyer, R. Suzuki, Lianqi. Wang, and S. Yelda. Thirty Meter Telescope astrometry error budget. In Enrico Marchetti, Laird M. Close, and Jean-Pierre Vran, editors, *Adaptive Optics Systems IV*, volume 9148 of *Society of Photo-Optical Instrumentation Engineers (SPIE) Conference Series*, page 91482L, July 2014.

[86] N. Schwartz, J.F. Sauvage, C. Correia, C. Petit, F. Quiros Pacheco, T. Fusco, K. Dohlen, K. EL HADI, N. Thatte, F. Clarke, J. Paufique, and J. Vernet. Sensing and control of segmented mirrors with a pyramid wavefront sensor in the presence of spiders. 01 2017.

[87] R. V. Shack and F. Dow Smith. Production and use of a lenticular Hartmann screen. *Journal of the Optical Society of America (Oral presentation)*, 61(5):656, 1971.

[88] I. Shatokhina, V. Hutterer, and R. Ramlau. Review on methods for wavefront reconstruction from pyramid wavefront sensor data. *Journal of Astronomical Telescopes, Instruments, and Systems*, 6(1):1 – 39, 2020.

[89] MF Skrutskie, RM Cutri, R Stiening, MD Weinberg, S Schneider, JM Carpenter, Capps Beichman, R Capps, T Chester, J Elias, et al. The two micron all sky survey (2mass). *The Astronomical Journal*, 131(2):1163, 2006.

[90] W.H. Southwell. Wave-front estimation from wave-front slope measurements. *JOSA*, 70(8):998–1006, 1980.

[91] B. Steffens. *Ibn Al-Haytham: First Scientist*. Profiles in Science. Morgan Reynolds Pub., 2007.

[92] C.C. Steidel, S. Kulkarni, D.C. Martin, J.G. Cohen, M.M. Kasliwal, F.A. Harrison, J. Liu, and E.N. Kirby. Thirty meter telescope detailed science case: 2015. 2015.

[93] P.B. Stetson. Daophot: A computer program for crowded-field stellar photometry. *Publications of the Astronomical Society of the Pacific*, 99(613):191, 1987.

[94] T. Fritz, N. Kallivayalil, E. Carrasco, B. Neichel, R. Davies, R. Beaton, D. Angell, S. Linden, P. Zivick, S. Majewski, G. Damke, M. Boylan-Kolchin, R. van der Marel, and T. Sohn. Astrometry with MCAO at Gemini and at ELTs.

In *Adaptive Optics for Extremely Large Telescopes IV (AO4ELT4)*, page E90, October 2015.

[95] M. Taheri and C. Bond. "kaon 1179 - k2 ao nirspec instrument fold mirror replacement plan". Technical report, W. M. Keck Observatories, Waimea HI, 2017.

[96] M. Taheri and C. Bond. impact of partially-illuminated pwfs pixels and using modified interaction matrix on k2ao performance. Technical report, W. M. Keck Observatories, Waimea HI, 2018.

[97] M. Taheri, P. Janin-Potiron, B. Neichel, D. Andersen, J-P. Veran, J-F. Sauvage, V. Chambouleyron, K. El Hadi, and T. Fusco. Injecting pupil binary intensity map into the laboratory adaptive optics bench using phase-only LCoS-SLM device. In Laura Schreiber, Dirk Schmidt, and Elise Vernet, editors, *Adaptive Optics Systems VII*, volume 11448, pages 1278 – 1287. International Society for Optics and Photonics, SPIE, 2020.

[98] M. Taheri, A.W. McConnachie, P. Turri, D. Massari, D. Andersen, G. Bono, G. Fiorentino, K. Venn, J-P. Véran, and P.B. Stetson. Optimal differential astrometry for multiconjugate adaptive optics. i. astrometric distortion mapping using on-sky gems observations of ngc 6723. *The Astronomical Journal*, 163(4):187, 2022.

[99] J.S. Tharp and R. Tyson. Measurement of the optical path difference over an atmospheric turbulence phase plate. In Domenico Bonaccini Calia, Brent L. Ellerbroek, and Roberto Ragazzoni, editors, *Advancements in Adaptive Optics*, volume 5490, pages 805 – 809. International Society for Optics and Photonics, SPIE, 2004.

[100] A. Tokovinin. http://www.ctio.noirlab.edu/ atokovin/tutorial/.

[101] P. Turri, A. W. McConnachie, P. B. Stetson, G. Fiorentino, D. R. Andersen, J. P. Véran, and G. Bono. Toward Precision Photometry for the ELT Era: The Double Subgiant Branch of NGC 1851 Observed with the Gemini/GeMS MCAO System. , 811(2):L15, October 2015.

[102] M. van Kooten, C. Bradley, J.-P. Véran, G. Herriot, and O. Lardiere. Fast modulation and dithering on a pyramid wavefront sensor bench. In *Proceedings of the SPIE*, volume 9909, 2016.

[103] C. Wilcox, S. Restaino, and G. Tkachenko. *New Developments in Liquid Crystals*. Intechopen, 2009. DOI: 10.5772/9684.

[104] R.A. Windhorst, S.H. Cohen, N.P. Hathi, P.J. McCarthy, R.E. Ryan, H. Yan, I.K. Baldry, S.P. Driver, J.A. Frogel, D.T. Hill, et al. The hubble space telescope wide field camera 3 early release science data: panchromatic faint object counts for 0.2–2 μm wavelength. *The Astrophysical Journal Supplement Series*, 193(2):27, 2011.

[105] P. Wizinowich, D.S. Acton, C. Shelton, P. Stomski, J. Gathright, K. Ho, W. Lupton, K. Tsubota, O. Lai, C. Max, et al. First light adaptive optics images from the keck ii telescope: a new era of high angular resolution imagery. *Publications of the Astronomical Society of the Pacific*, 112(769):315, 2000.

[106] Z. Zhang, Zheng. You, and D. Chu. Fundamentals of phase-only liquid crystal on silicon (lcos) devices. *Light: Science & Applications*, 3(10):e213, 2014.